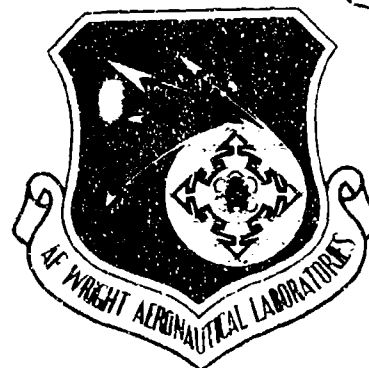


AD-A177 491

AFWAL-TR-86-3070



RESEARCH AND DEVELOPMENT OF AIRCRAFT CONTROL ACTUATION
SYSTEMS

Carl N. Albright
Gavin D. Jenney
Harry W. Schreadley
William G. Talley

Dynamic Controls Inc.
7060 Cliffwood Place
Dayton, Ohio 45424-2929

DTIC
ELECTE
MAR 05 1987
S D

December 1986

Final report for Period May 1979 - February 1985

Approved for public release; distribution unlimited.

DTIC FILE COPY

FLIGHT DYNAMICS LABORATORY
AIR FORCE WRIGHT AERONAUTICAL LABORATORIES
AIR FORCE SYSTEMS COMMAND
WRIGHT-PATTERSON AIR FORCE BASE, OHIO 45433-6553

87 3 2 032

UNCLASSIFIED

SECURITY CLASSIFICATION OF THIS PAGE

ADA177491

REPORT DOCUMENTATION PAGE

1a REPORT SECURITY CLASSIFICATION UNCLASSIFIED			1b RESTRICTIVE MARKINGS NONE	
2a SECURITY CLASSIFICATION AUTHORITY N/A			3 DISTRIBUTION/AVAILABILITY OF REPORT Approved for Public Release; distribution unlimited.	
2b DECLASSIFICATION/DOWNGRADING SCHEDULE N/A				
4 PERFORMING ORGANIZATION REPORT NUMBER(S)			5. MONITORING ORGANIZATION REPORT NUMBER(S) AFWAL-TR-86-3070	
6a NAME OF PERFORMING ORGANIZATION Dynamic Controls, Inc.		6b. OFFICE SYMBOL (If applicable)	7a NAME OF MONITORING ORGANIZATION Flight Dynamics Laboratory (AFWAL/FIGL) Air Force Wright Aeronautical Laboratories	
6c ADDRESS (City, State and ZIP Code) 7060 Cliffwood Place Dayton, OH 45424			7b. ADDRESS (City, State and ZIP Code) Air Force Systems Command Wright-Patterson AFB, OH 45433-6553	
8a NAME OF FUNDING/SPONSORING ORGANIZATION Flight Dynamics Laboratory		8b. OFFICE SYMBOL (If applicable) AFWAL/FIGL	9. PROCUREMENT INSTRUMENT IDENTIFICATION NUMBER F33615-79-C-3602	
8c ADDRESS (City, State and ZIP Code) Wright-Patterson AFB, OH 45433-6553			10. SOURCE OF FUNDING NOS	
			PROGRAM ELEMENT NO	PROJECT NO
			62201F	2403
11 TITLE (Include Security Classification) Research & Development of Aircraft Control Actuation Systems			TASK NO	WORK UNIT NO
			02	90
12. PERSONAL AUTHOR(S) Carl N. Albright, Gavin D. Jenney, Harry W. Schreadley, William G. Talley				
13a. TYPE OF REPORT Final		13b. TIME COVERED FROM 05/79 TO 02/85		14 DATE OF REPORT (Yr, Mo, Day) 12/86
15 PAGE COUNT 168				
16 SUPPLEMENTARY NOTATION NONE				
17 COSATI CODES			18 SUBJECT TERMS (Continue on reverse if necessary and identify by block number)	
FIELD	GROUP	SUB GR	Digital Interface; Direct Drive; Energy Storage; Flight Control Hydraulics; Force Motor; Force Enhancement, Flutter Suppression.	
01	03			
19. ABSTRACT (Continue on reverse if necessary and identify by block number)				
<p>This report describes the design and test of a multipurpose actuation test rig to be used for loaded evaluation of actuation systems with rotary outputs and/or integrated as part of a wing structure.</p> <p>This report also describes a hydromechanical flutter damping module for an F-4 stabilator actuator. The module incorporates design improvements based on previous test results. The result of laboratory tests on the improved module are presented.</p> <p>Also present are the development and test results of a linear force motor based upon a moving magnet concept. The report presents the measured performance characteristics of the concept over a range of parameter variations.</p> <p>(continued on reverse)</p>				
20 DISTRIBUTION AVAILABILITY OF ABSTRACT UNCLASSIFIED/UNLIMITED <input checked="" type="checkbox"/> SAME AS RPT <input type="checkbox"/> DTIC USERS <input type="checkbox"/>			21 ABSTRACT SECURITY CLASSIFICATION Unclassified	
22a NAME OF RESPONSIBLE INDIVIDUAL Mr. Gregory Cecere			22b TELEPHONE NUMBER (Include Area Code) (513)-255-2831	22c OFFICE SYMBOL AFWAL/FIGL

DD FORM 1473, 83 APR

EDITION OF 1 JAN 73 IS OBSOLETE

UNCLASSIFIED
SECURITY CLASSIFICATION OF THIS PAGE

Block 19 (Continued)

A method of force enhancement for direct drive force motors and the corresponding test results applied to a moving coil force motor are described. The concept is based upon applying a limited time duration pulse to the force motor in order to increase the force output when required. The logic technique used to initiate the pulse application is presented. Applying a digital computer as a controller for an analog electrohydraulic control system requires consideration of the interface used. A study of the effect of a pulse width modulation interface on the life of analog electrohydraulic hardware is presented.

There is a potential for reducing the pumping capacity of an aircraft's flight control hydraulic system by using accumulators to store hydraulic energy. The results of a study using this approach and an F-16 simulation are presented. *See page 10*

FOREWORD

The effort described in this document was performed by Dynamic Controls, Inc. of Dayton, Ohio under Air Force Contract F33615-79-C-3602. The work under the contract was carried out in the Flight Dynamics Laboratory, Air Force Wright Aeronautical Laboratories, Wright-Patterson Air Force Base, Ohio. The work was administered by Mr. Gregory Cecere, AFWAL/FIGL Program Manager.

The authors wish to express their appreciation to Dynamic Controls, Incorporated personnel: Mr. Heinrich J. Weig for his contribution in the areas of analysis, design and fabrication of the Multipurpose Actuation System Test Rig (MASTR) and flutter suppression hardware, and Mrs. Linda Pytosh for her extensive efforts in the report preparation.

This report covers work performed between May 1979 and February 1985. The technical report was submitted by the authors in June 1986.



Accession For	
NTIS GRA&I	<input checked="checked" type="checkbox"/>
DTIC TAB	<input type="checkbox"/>
Unannounced	<input type="checkbox"/>
Justification	
By	
Distribution /	
Availability Codes	
Dist	Availability for Special
A-1	

TABLE OF CONTENTS

<u>SECTION</u>	<u>PAGE</u>
I MASTR	1
General Discussion	1
System Specification	1
Hydraulic System Supply Description	4
Servovalve Selection	7
Hydraulic Manifold Description	7
Control Actuator Description	9
Instrumentation Transducers	11
Control Console Description	11
Load Control Module Description	14
Surface Position Signal Conditioner	20
Channel Failure and Signal Monitor	23
Solenoid Driving Relay Description	26
Data Logger Description	26
Input Signal Panel	26
Power Supplies Description	26
Interface Wiring Description	27
Load Control Loop Description	27
MASTR Component Design Verification	27
MASTR Final Assembly and Check-Out	35
Conclusion	35
II FLUTTER SUPPRESSION ACTUATOR	41
General Investigation Description	41
Hydromechanical Pressure Feedback Characteristics	43
Undamped Actuator & Surface Mass Response	43
Actuator & Surface Mass Response with Load	
Pressure Feedback	45
Actuator & Surface Mass Response with Load	
Pressure Feedback Plus Washout Circuit	46
Washout Transfer Function Description	48
F-4 Stabilator Actuator Sizing Calculations	50
F-4E Damping Circuit Summary	52
Optimized Flutter Suppression Actuator Description	52
General Test Procedure	56
Isolation & Damping Spool Differential Pressure	
Response	62
Individual Damping Section Dynamic Load Response	70
Dual Damping Sections Dynamic Load Response	77
Flow Gain Excitation Sensitivity	88
Conclusions & Recommendations	91

TABLE OF CONTENTS (CONTINUED)

<u>SECTION</u>	<u>PAGE</u>
III MOVING MAGNET FORCE MOTOR	92
General Discussion	92
Technical Approach	92
Magnetic Circuit Calculation	94
Permanent Magnet Size	95
Evaluation Procedure	97
Test Results	99
Summary & Recommendations	110
IV DIRECT DRIVE FORCE MOTOR ENHANCEMENT	112
General Discussion	112
Technical Approach	112
Mechanical Design	118
Electronic Design	118
Test Procedure	122
Test Results	122
Conclusion and Recommendations	128
V DIGITAL INTERFACE STUDY FOR HYDRAULIC CONTROL SYSTEMS	130
General Discussion	130
Interface Overview	130
Update Rate	132
Throughput Time	132
Resolution	132
PWM Interface	133
Technical Approach	133
Interface Evaluation System	135
Electronic Control Description	135
Test Valve Description	138
Hydraulic Circuit	140
Test Results	140
Conclusions and Recommendations	150
VI AIRCRAFT ENERGY STORAGE STUDY	152
Objective	152
Background	152
Investigation Technique	153
Data Analysis	154
Data Analysis Results	157
Discussion of Results	166
Conclusions & Recommendations	167

LIST OF ILLUSTRATIONS

FIGURE	TITLE	PAGE
1	MASTR Reaction Structure and Load Actuators	2
2	Electronic Control Console	3
3	Load Actuator Location and Channel Number	5
4	MASTR Hydraulic Distribution Schematic	6
5	Manifold Hydraulic Schematic	8
6	Actuator Rod Seal Modification	10
7	Rear View of Console	12
8	Rear Console Construction	13
9	Load Control Module Front View	15
10	Load Control Module Rear View	16
11	Load Controller Schematic	19
12	Position/Rate Module Front View	21
13	Position/Rate Module Rear View	22
14	Position/Rate Module Schematic	24
15	Control Channel Schematic	28
16	Servo Valve Pressure Gain - Typical	30
17	Servo Valve Flow Gain - Typical	31
18	Reaction Structure	32
19	Load Actuator Dynamic Response	33
20	Load Actuator Static and Dynamic Threshold	34
21	Test Structure in MASTR	36
22	Load Channel #5L Linearity/Hysteresis	37
23	Load Channel #15L Linearity/Hysteresis	38
24	Channel #4L Frequency Response	39

LIST OF ILLUSTRATIONS (CONTINUED)

FIGURE	TITLE	PAGE
25	Channel #1 Frequency Response	40
26	Hydromechanical Damping Circuit Schematic	49
27	Modified F-4 Actuator with Add-on Damping Modules . . .	53
28	Modified F-4 Actuator with Integrated Control Package	54
29	Integrated Control Package Housing (End View)	57
30	Integrated Control Package Housing (Side View)	58
31	Plastic Machining Aid of Control Package Housing (End View)	59
32	Plastic Machining Aid of Control Package Housing (Side View)	60
33	Integrated Control Package and Actuator in GPATR . . .	61
34	Test Setup Schematic for Measuring Pressure Response	63
35	P ₁ Isolation & Damping P Response at 1,720 Lb Load	64
36	P ₁ Isolation & Damping P Response at 3,612 Lb Load	65
37	P ₁ Isolation & Damping P Response at 6,192 Lb Load	66
38	P ₂ Isolation & Damping P Response at 2,064 Lb Load	67
39	P ₂ Isolation & Damping P Response at 3,784 Lb Load	68
40	P ₂ Isolation & Damping P Response at 5,504 Lb Load	69
41	Damping Flow Response, P ₁ Section, Hand Held Input, ± 1200 psi P	72
42	Damping Flow Response, P ₁ Section, Mechanical Ground Input, ± 1200 psi P	73

LIST OF ILLUSTRATIONS (CONTINUED)

FIGURE	TITLE	PAGE
43	Damping Flow Response, P ₂ Section, Mechanical Ground Input, <u>+1200</u> psi P	74
44	Damping Flow Response, P ₁ Section, Hand Held Input, <u>+2100</u> psi P	75
45	Damping Flow Response, P ₂ Section, Mechanical Ground Input, <u>+2200</u> psi P	76
46	Damping Flow Response, P ₁ Section, Mechanical Ground Input, <u>+2000</u> lb. Load	78
47	Damping Flow Response, P ₂ Section, Mechanical Ground Input, <u>+2000</u> lb. Load	79
48	Damping Flow Response, P ₁ Section, Mechanical Ground Input, <u>+5000</u> lb. Load	80
49	Damping Flow Response, P ₂ Section, Mechanical Ground Input, <u>+5000</u> lb. Load	81
50	Chart Data, Dynamic Flow Response at 12 Hz	83
51	Flow Gain Response, Undamped, <u>+4,000</u> lbs.	84
52	Flow Gain Response, Undamped, <u>+7,500</u> lbs.	85
53	Flow Gain Response, Undamped, <u>+2,000</u> lbs.	86
54	Flow Gain Response, Undamped, <u>+4,000</u> lbs.	87
55	Flow Gain Response, Damped, <u>+7,500</u> lbs.	89
56	Damping Flow Gain Vs Differential Pressure at Hz	90
57	Force Motor Crosssection	93
58	Typical Demagnetization Curve RAECO-i6	95
59	Photo of Assembled Force Motor	98
60	Photo of Force Motor Partially Disassembled	100
61	Air Gap Control Flux Density	102
62	Schematic for Test Setup	103
63	Magnet Location Definition	104

LIST OF ILLUSTRATIONS (CONTINUED)

FIGURE	TITLE	PAGE
64	Bias Force Output Test Results	105
65	Output Force Measurements - 0.116" Gap	107
66	Output Force Measurements - 0.187" Gap	108
67	Output Force Measurements - 0.258" Gap	109
68	Force Vs Current, ± 10.0 Amp Input	114
69	Enhancement Logic Tree	117
70	Force Enhancement Test Setup	119
71	Direct Drive Force Enhancement Schematic Diagram . . .	121
72	Suspension Resonant Frequency	123
73	Force Vs Current, ± 3.0 Amps D.D. Modified Suspension	125
74	Force Vs Current, ± 1.5 Amps D.D. Modified Suspension	126
75	Negative Current-Force Enhancement	127
76	Positive Current-Force Enhancement	129
77	Analog-Digital System Interface	131
78	PWM Signal	134
79	Interface Test System	136
80	Interface System Test Setup	137
81	Electronic Schematic	139
82	Servo valve Crosssection	141
83	Hydraulic Schematic	142
84	Base Line No. 120 Feedback Ball Photo 35X Actual . . .	143
85	Base Line No. 120 Control Spool Photo 2X Actual	143
86	Base Line Pressure Gain, S/N 120	144
87	Base Line Pressure Gain, S/N 128	145

LIST OF ILLUSTRATIONS (CONTINUED)

FIGURE	TITLE	PAGE
88	Base Line Flow Gain, S/N 120	147
89	Base Line Flow Gain, S/N 128	148
90	Pressure Land Polishing Effect	149
91	Sample History - 3G Reversing Target Chase	155
92	Sample History - Landing With Turbulence	156
93	0-20 Secs., 3G Reversing Target Chase	158
94	20-40 Secs., 3G Reversing Target Chase	159
95	40-60 Secs., 3G Reversing Target Chase	161
96	60-70 Secs., 3G Reversing Target Chase	162
97	0-20 Secs., Landing With Turbulence	163
98	20-40 Secs., Landing With Turbulence	164
99	Accumulator Sizing	165

SECTION 1. MASTR

General Discussion

The Multipurpose Actuation System Test Rig (MASTR) was designed to evaluate the performance of flight control actuation systems that are integral with the control surface under static and dynamic load conditions. Examples of such systems are mission adaptive wings, hinge line actuation systems and actuation systems with rotary outputs. The components of the MASTR are the reaction structure and the individual load channels consisting of load actuators and their associated control electronics. Thirty six individual load channels are provided with the MASTR.

Figure 1 is a photograph of the reaction structure and the load actuators. The load actuators are attached to a test plate used in verification tests of the load channel performance. The reaction structure provides a mounting table for the test specimen and rigid reaction points for the 36 hydraulically operated load channels. The load actuators are divided into 18 upper and 18 lower units. For each 18 actuators, 12 are provided for distributed loading on the trailing edge of a test specimen and 6 actuators for the leading edge. The trailing edge of the test specimen would be located at the left of the specimen mounting table shown in Figure 1 and the leading edge located to the right. The attach points of the loading actuators are moveable in the horizontal plane in order to adapt to configurations requiring different loading directions and load points.

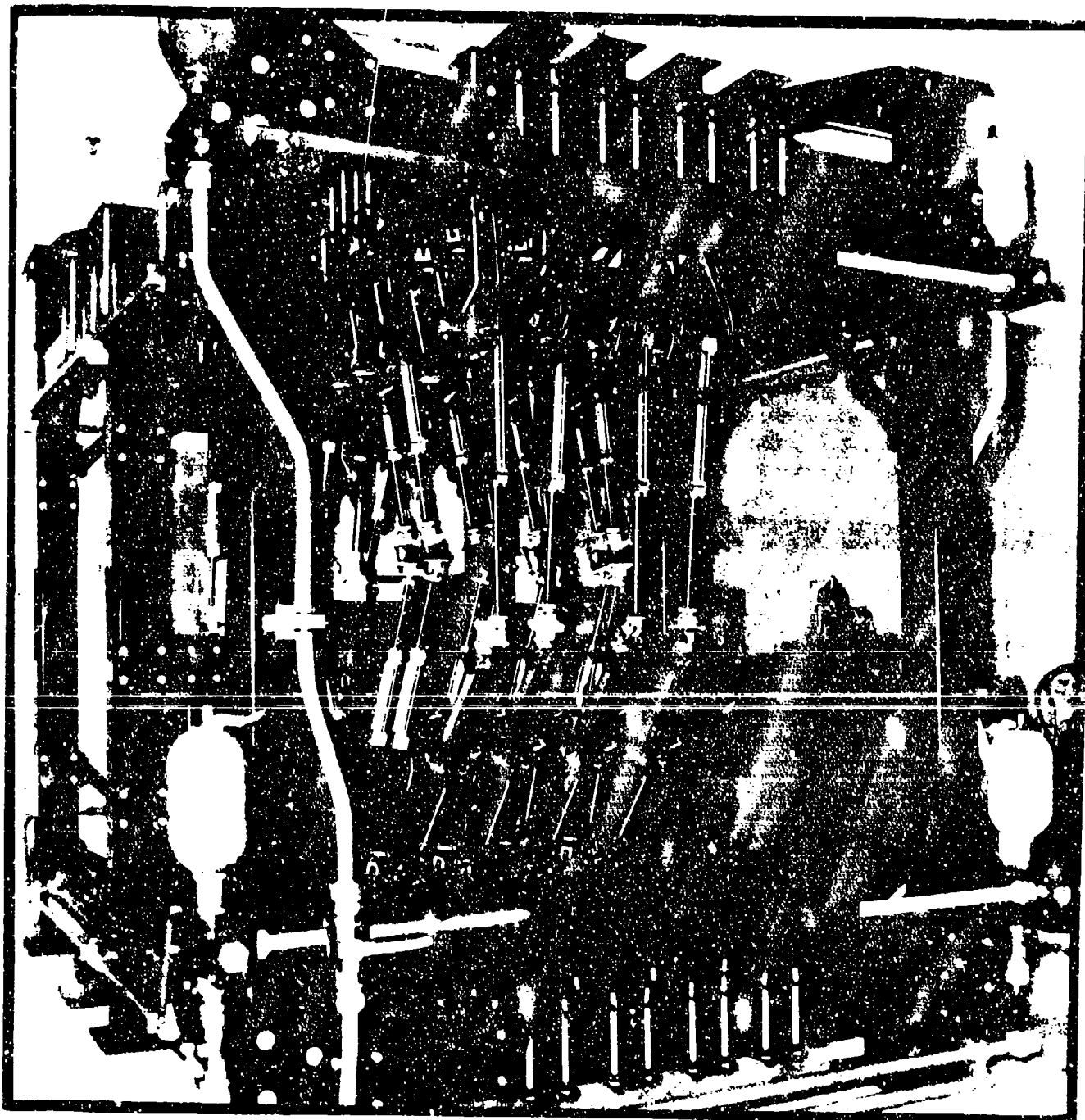
Figure 2 is a photograph of the MASTR's electronic control console. The console houses the electronics which provide closed loop control of each load channel. The console also provides automatic data logging, local or remote input signal selection, load gain control, force limit set points and outputs for performance measurement.

The control system of the MASTR includes failure protection hardware to protect the test specimen from excessive loads. The protection is both electronic and hydromechanical.

System Specifications

The 36 load channels are designed to operate independently. The general specifications for each channel are the following:

Output force	± 100 lbs to ± 2000 lbs
Actuator Velocity	20 in/sec
Dynamic Load Tracking	$< \pm 100$ lbs @ rated velocity
Load Hysteresis	± 50 lbs
Load Threshold	$< \pm 2.0\%$
Fail Safe Limits	± 100 lbs to ± 2000 lbs



© 2000 Blackwell Science Ltd *Journal of Internal Medicine* 247: 161–167

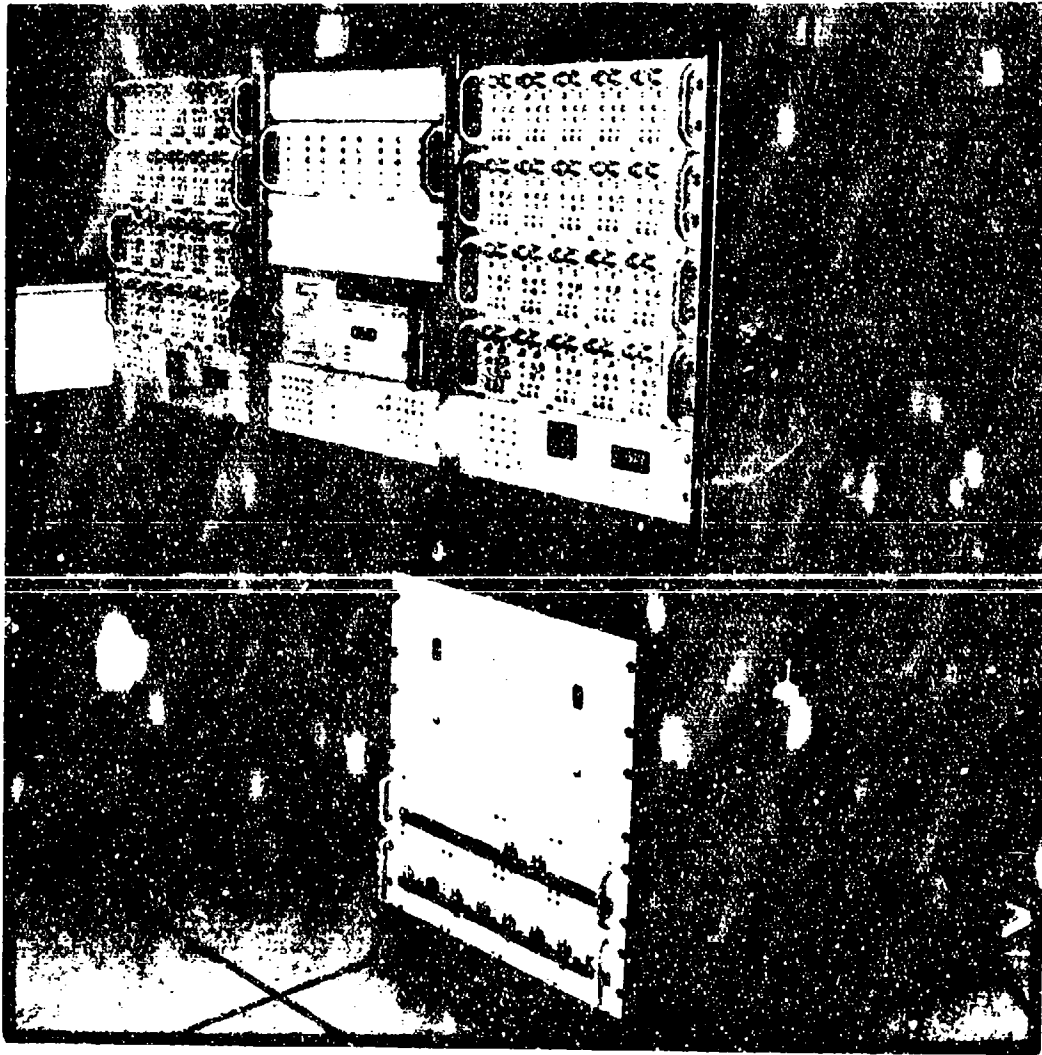


Figure 2. Electronic Control Console

The specifications for the structural framework providing the support for the test specimen and the reaction points for the loading actuators are the following:

Outside Dimensions	156" L x 115" W x 151" H
Maximum Test Specimen	120" L x 92" W x 30" H
Specimen Table	46" L x 92" W
Reaction Stiffness	$> 1 \times 10^6$ lbs/in
Structural Elements Resonant Freq.	> 45 Hz

The framework is constructed as a bolted together assembly of welded sections. The upper and lower cross beam members are bolted in, with corner braces for torsional stiffness. The structure can be expanded to accommodate larger test specimens by inserting extensions. The vertical columns incorporate cut-outs to allow filling the columns with dry sand if increased structural damping is required.

The specimen table is constructed with removeable clamping plates to clamp wing boxes to the table. Rotary actuators are mounted to an intermediate support structure designed for the particular actuator. The intermediate structure is then bolted directly to the MASTR specimen table.

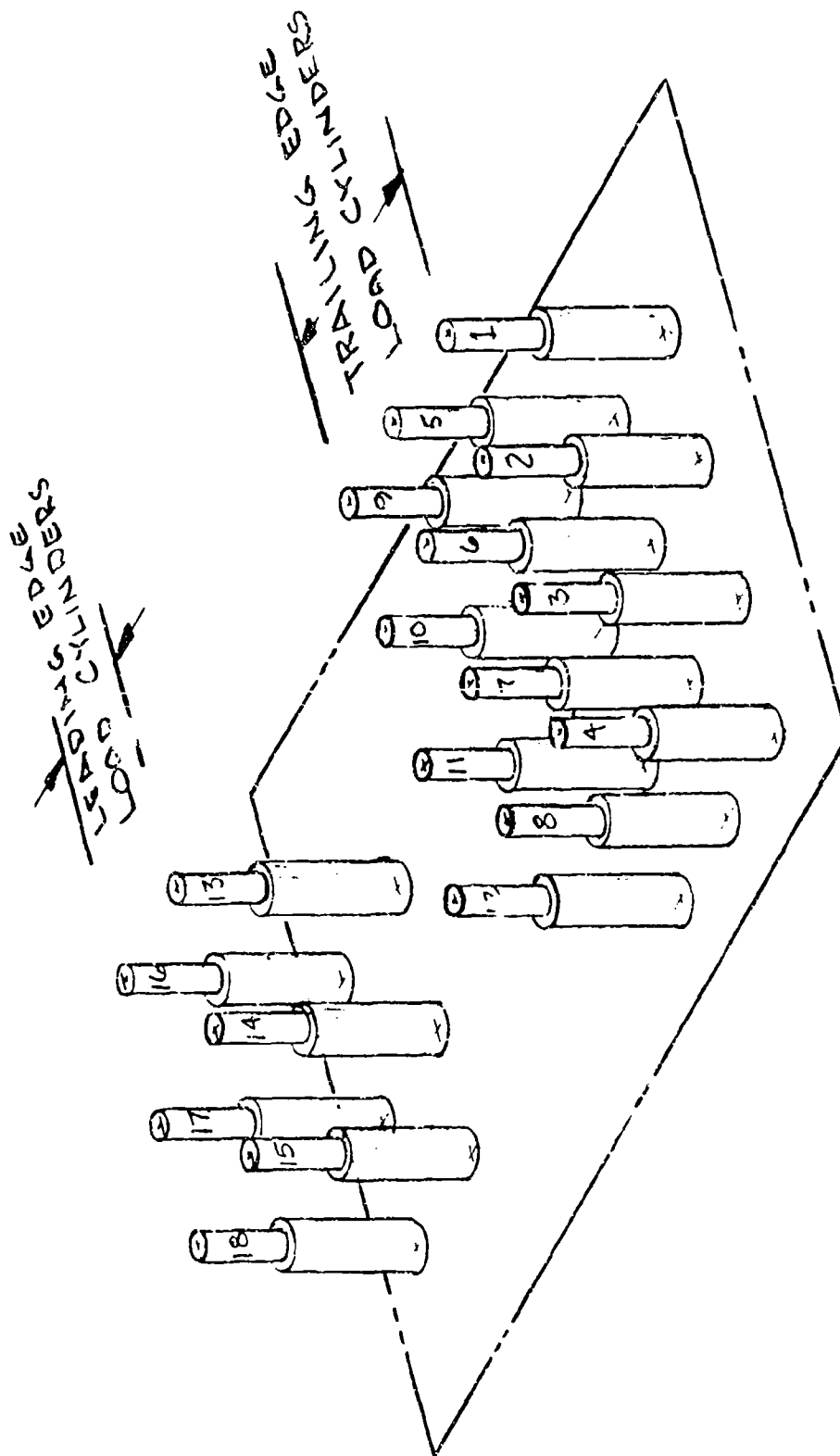
Hydraulic Load System Supply Description

The hydraulic load actuators with their manifolds and load transducers are designed as removeable units. Figure 3 illustrates the load actuator location numbering system used with the load system. The load actuators are powered by the 240 gpm, 3000 psi hydraulic system used in the laboratory area in which the MASTR is installed.

The hydraulic plumbing system for the MASTR is divided into two separate systems with shut-off valves in the pressure and return lines. One section supplies the upper load actuators and the other supplies the lower load actuators. Hydraulic distribution manifolds are provided as shown in Figure 4 for the upper trailing edge, upper leading edge, lower trailing edge and lower leading edge actuators. The flow demand of the actuators when operating at 10 Hz and 10% of full scale amplitude was used to size the hydraulic connection lines. A line flow velocity limit of 15 feet/second was used to determine the interconnecting tubing diameters. The hydraulic line sizing resulted in the following different hydraulic line sizes for connection to these MASTR components:

Trailing Edge Manifolds	2 inch diameter
Leading Edge Manifolds	1.25 inch diameter
Control Actuators	0.50 inch diameter

Four 2.5 gallon bladder type accumulators were used with the plumbing and were mounted on the structure. Two accumulators were used for each hydraulic



LOWER LOAD CYLINDERS ARE SHOWN, THE UPPER CYLINDERS ARE THE SAME. EXAMPLE: #1 LOWER IS OPPOSITE #1 UPPER

Figure 3. Load Actuator Location and Channel Number

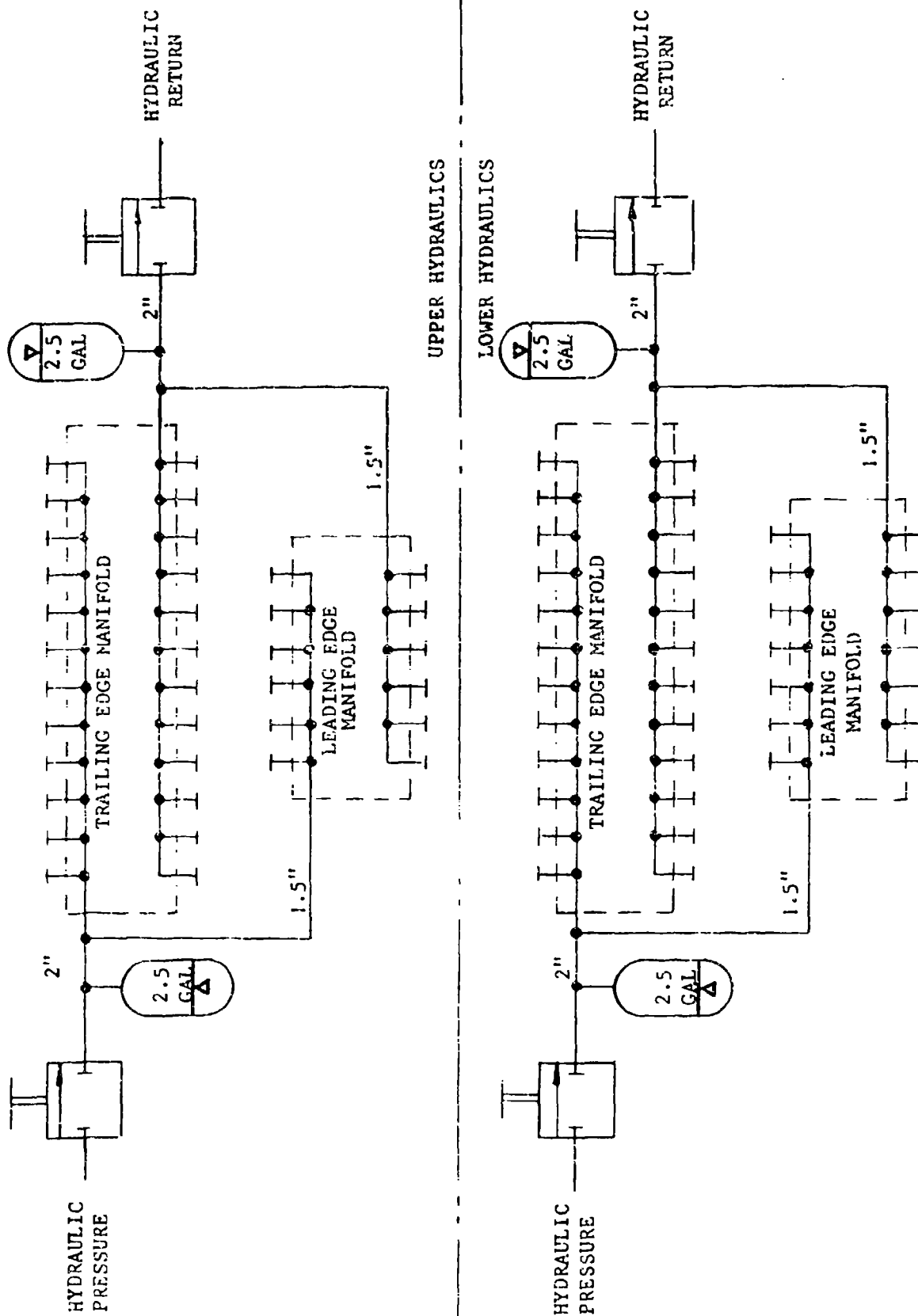


Figure 4. MASTR Hydraulic Distribution Schematic

section, one for the pressure line and one for the return line. Figure 4 is a schematic of the hydraulic distribution system.

Servo Valve Selection

Two types of servovalves were considered for the MASTR load control. These were the pressure control and flow control type valves. Pressure control valves incorporate pressure feedback internally in order to produce an output pressure proportional to input current. Typical blocked port frequency response for the load pressure is nominally 20 Hz for pressure control valves. The response degrades dramatically with increasing output flow demand.

Flow control valves are designed to provide an output flow proportional to input current. The output pressure gain is typically "supply pressure/1% input current" or higher. For a control valve supplied with 3000 psi and requiring 0.020 amperes for full flow, the pressure gain is nominally 15,000 psi/ma. This high pressure gain makes control of low output force levels difficult. The input control signal level required for changes of 50 to 100 psi output pressure are within the usual noise levels of the control system. By "breaking" the pressure gain of the flow control valve with either a bypass orifice or underlap on the control valve edges (or both), a flow control valve can be used for load control. The pressure response of the flow control valve with flow demand will generally be better when a flow control valve is used than when a pressure control valve is used.

Moog Model A-067 servovalves rated at 10 gpm flow with 1000 psi pressure drop across the valve and manufactured with 3% underlap on the control edges were used for the MASTR. The 3% underlap condition was recommended by the valve manufacturer. The 10 gpm flow specification was determined by the requirement to exceed the flow requirement for the load actuator (with a drive area of 0.98 square inches) operating at a rate of 20 inches/second. The 20 inch/second rate for the load actuator requires an input flow of 5.09 gpm. The 10 gpm valve was the nearest standard valve which would exceed the maximum rate requirement.

Each servovalve was used with a variable orifice connecting the cylinder ports. The orifices were used to trim the valves to a pressure gain of 500 psi/milliamp. The valves and orifices were installed as a matched set. The average leakage flow for the servovalves was measured at 1 gpm.

Hydraulic Manifold Description

Figure 5 is a schematic of the hydraulic manifold used for each of the load actuators. The manifold is the interfaces of the servovalve to the load actuator cylinder. Mounted on each manifold as plug-in units are the variable orifice connecting the servovalve cylinder ports together, two pressure relief valves and a solenoid operated bypass valve. The variable orifice is used to establish the pressure gain of the servovalve. The pressure relief valves are connected between the servovalve cylinder port lines and return. These relief valves are used for hydromechanical load limiting for each load actuator. The solenoid operated bypass valve is used for electronic load limiting. Output load forces greater than preset limits are electronically detected and used to bypass the load actuator.

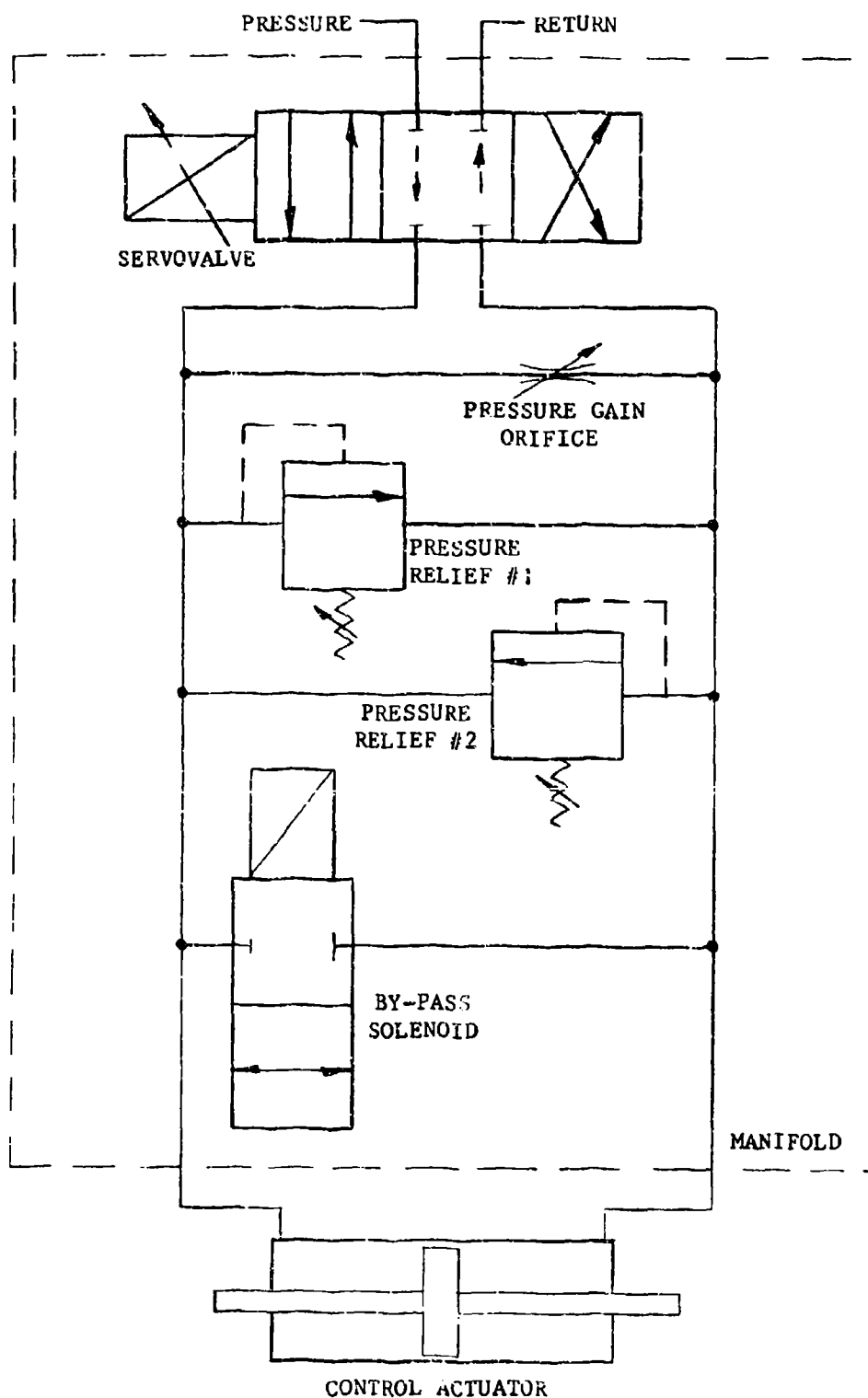


Figure 5. Manifold Hydraulic Schematic

The internal porting of the manifold was sized to have less than 100 psi pressure drop at a flow rate of 10 gpm. The following is a list of the components used as part of the manifold:

Servovalves:

Manufacturer Moog
Model A-076-10S
Flow 10 gpm @ 1000 psi differential pressure
Lap Condition 3% underlap
Coil resistance 400 ohms
Rated Current +0.008 amperes
Operating Pressure 3000 psi

Bypass Solenoids:

Manufacturer Fluid Power Systems
Model 107-115 (normally closed)
Operating Pressure 3000 psi
Flow 10 gpm @ 50 psi differential pressure
Operating Voltage 110 VAC @ 60 Hz
Holding Current 0.4 amperes

Adjustable Orifice:

Manufacturer Sun Hydraulics
Model NFBCLDN
Operating Pressure 3000 psi
Orifice Area Range 0.00 to 0.093 inch effective diameter

Relief Valves:

Manufacturer Racine Hydraulics
Model 1351-3
Flow 5 gpm @ 50 psi differential pressure
Operating Pressure 3000 psi maximum

Control Actuator Description

The control actuators used for the load system are double acting commercial cylinders with modified rod seals. A design output force of 2000 lbs while moving at a maximum rate of 20 inches/second was used for cylinder size selection. The cylinder selected has a 1.50 inch diameter bore and a 1 inch diameter rod giving a drive area of 0.98 square inches. The design output force is met with nominally 1000 psi drop across the control valve at the 20 inch/second actuator rate.

Standard commercial cylinders manufactured by Sheffer were selected as load actuators because of their basic low friction design. The actuators use a filled Teflon wear strip as a piston bearing and glass filled Teflon piston seals. The actuator rod seals used by Sheffer were a pressure energized "W" type seal. As illustrated in Figure 6, the "W" seals were replaced with lower friction slipper seals in order to minimize the load actuator's internal friction. The threshold of a load control actuator is a direct function of the

AFTER

BEFORE

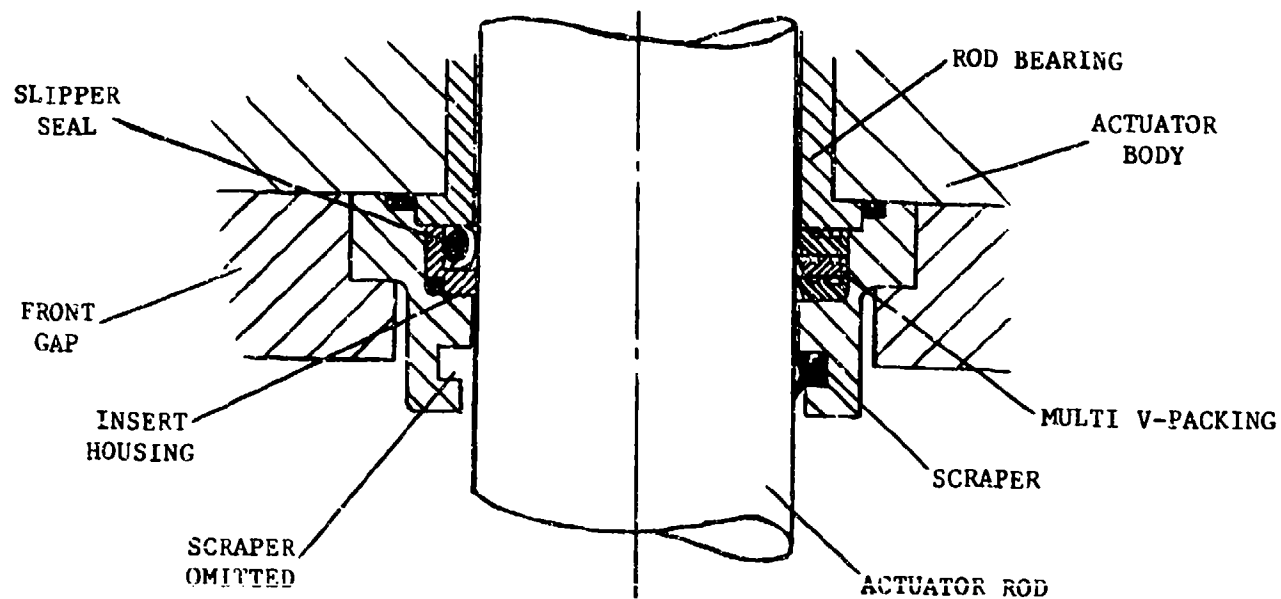


Figure 6. Actuator Rod Seal Modification

actuator's internal friction. The rod seal change reduced the internal friction force of the load actuator from a nominal 100 lbs to 40 lbs.

Two load actuator stroke ranges are used in the MASTR. Both 10 inch stroke and 17 inch stroke actuators are used. The two range of stroke actuators accommodate the expected output motion of test specimens.

Instrumentation Transducers

The output of each load control actuator is connected through a load cell to the reaction structure in order to provide a load measurement signal. The load cell output signal is used for load channel feedback, load measurement and for failure detection. The load cells used are a strain guage design manufactured by Lebow as part number 3132-5K. The rated maximum force for the load cell is 5,000 lbs in tension and compression.

Four position transducers are used for trailing edge position measurement. Three position transducers are used for leading edge position measurement. The trailing edge position transducers have a 24 inch stroke and a 6,500 ohm resistance element. The leading edge position transducers have a 12 inch stroke and a 3,200 ohm resistance element. Both position transducers have a rated linearity of 0.5% full scale. The transducers are produced by Waters Manufacturing Company as part numbers LF-S-12/300-E-B and LF-S-24/600-E-B for the 12 and 24 inch stroke, respectively.

Control Console Description

The control console shown in Figure 2 contains all of the control circuits used with the MASTR. In the lower right hand section, the console contains the power supplies and optically isolated relays for the bypass solenoids. The input-output wiring interface is installed in the left rear section. The switches which appear on the lower right panel in Figure 2 are used to apply 110 volt AC to the power supplies. The left and right switches provide power for the upper and lower load actuator bypass solenoids, respectively.

The upper three sections of the console contain the load channel control electronics. The right and left hand sections are dedicated to the upper and lower load actuator control. The top four chassis contain five self-contained load controllers each. Two modules in the fourth chassis from the top are used for spare module storage. The bottom chassis of the left and right sections are used for monitoring, status indication and the over-load alarm electronics.

The center of the console is shared by both the left and right load actuator control sections. This section contains the signal conditioners for surface position, an input panel and a data logger that can monitor up to 40 channels of data.

Figure 7 is a rear view of the control console showing the location of the control electronics for load actuators as identified previously in Figure 3. Figure 8 is a photograph of the control console rear, showing the construction.

The control console provides 36 channels of load loop control, signal conditioning, signal monitoring, input/output signal management, power supplies

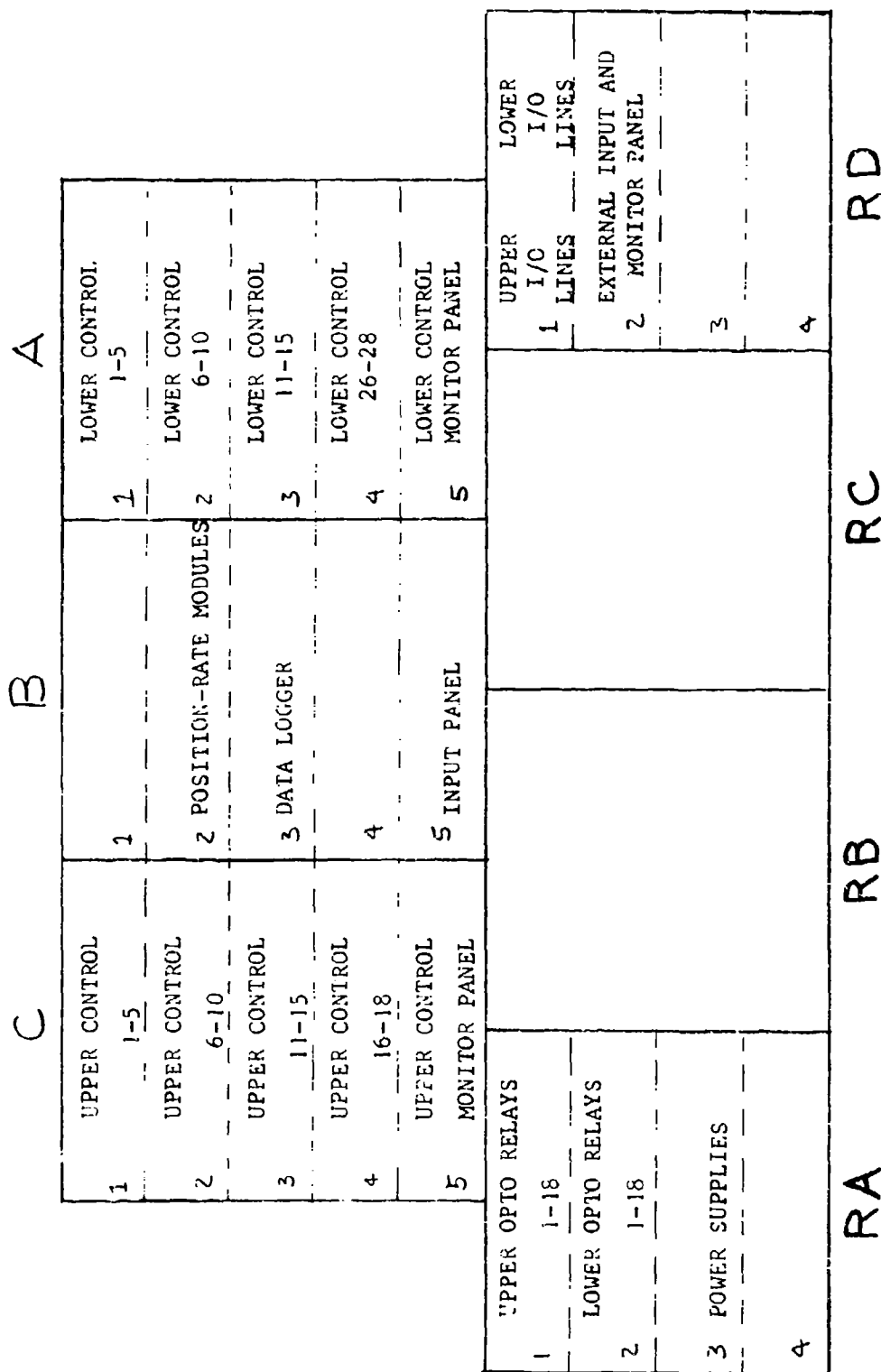


Figure 7. Rear View of Control Console

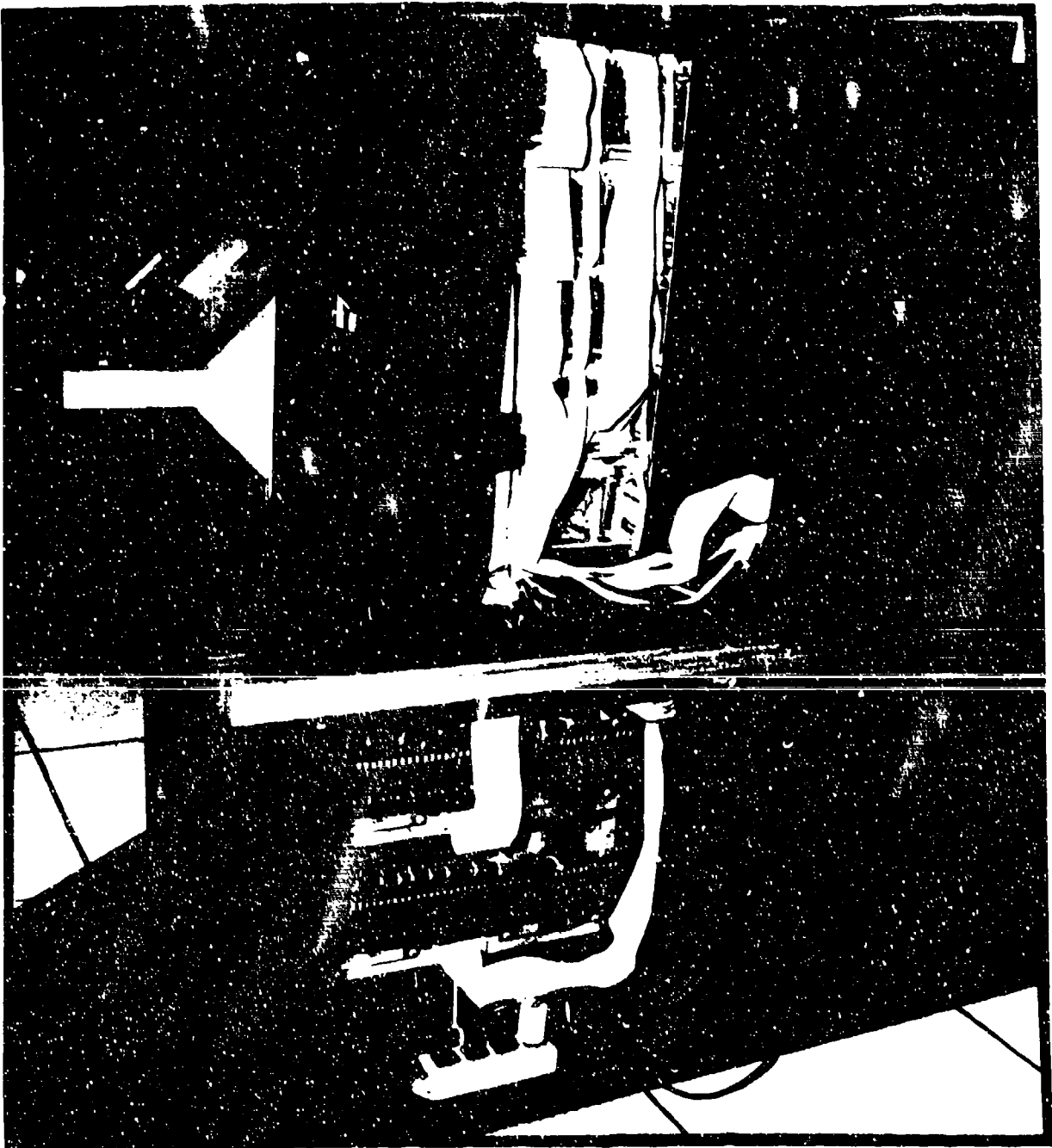


Figure S. Rear Console Construction

and isolated solenoid drivers. The location of the plug/jack or modules are identified by the following numbering system:

XX - X - XX - XX - XX
1 2 3 4 5

Where: 1 = Chassis section location

2 = Rack location within the section, numbered from top to bottom

3 = Plug or jack in rack, P & J for standard plugs and jacks
RJ & RP identifies flat cable connections

4 = Plug or jack number in a particular rack, numbered from right to left when viewed from the rear

5 = Pin number to the connector

For example, A-2-J-1-4 identifies Section A (lower load control), second rack from the top, first jack from the right (load control channel 5), Pin 4.

Load Control Module Description

Figure 9 is a photograph of the load control module's front panel. Figure 10 shows the internal construction of the module with its printed circuit board. The specifications for the module are as follows:

Input Voltage ± 10 VDC

Input Impedance > 1 meg-ohm

Gain Range 0.0 to ± 200 lb/volt

Load Limit Range 0.00 to ± 2000 lb

Output Current ± 0.02 amperes

The functions of the controls shown on the front panel of the load controller are as follows:

Panel Label	Schematic Label	Descriptive Function
IN	TP1	This test point allows the monitoring of the external input and/or the surface position input at the output of the gain potentiometer R14.
GAIN	R14	This ten turn potentiometer provided to adjust the external input and/or position input to the desired level from zero to 100% (100% = 200 lbs/volt). The potentiometer setting is also displayed in monitor section of the control by

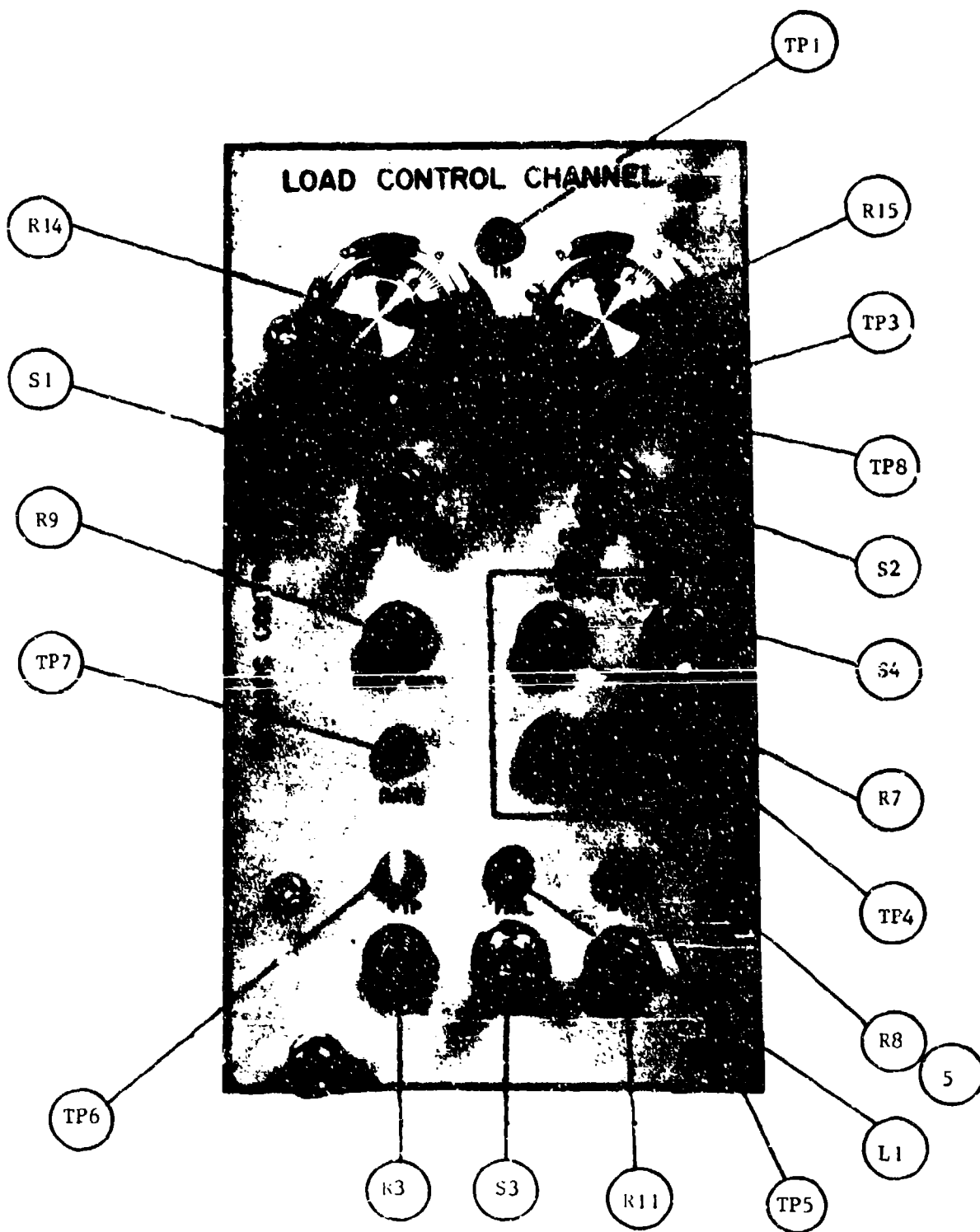


Figure 9. Load Control Module Front View

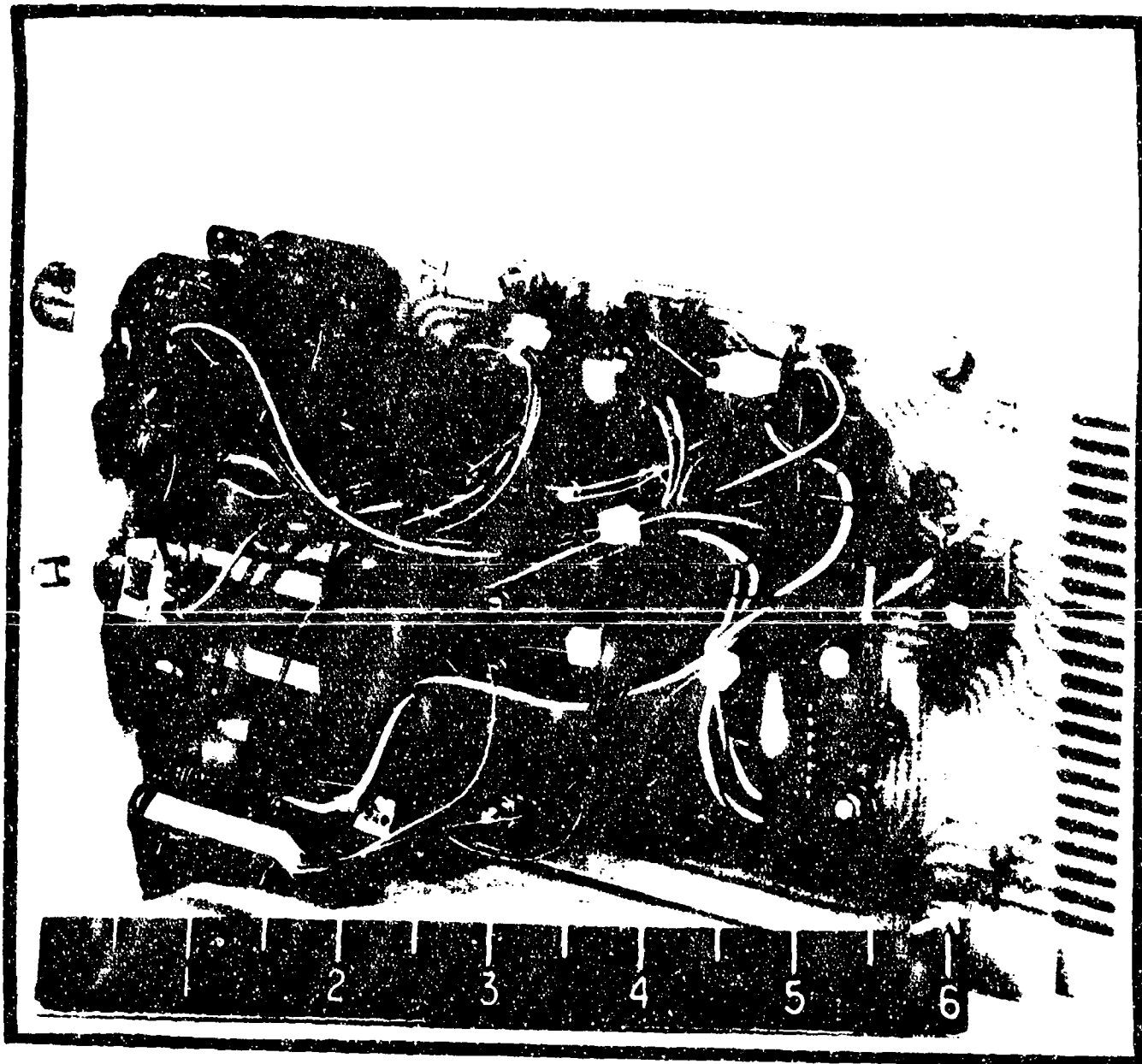


Figure 10. Load Control Module Rear View

Panel Label	Schematic Label	Descriptive Function
		addressing the desired channel. 100% = 200 lbs/volt.
BIAS	R15	This ten turn potentiometer is provided to adjust the force bias to be applied to the channel. The range is ± 10 volts. A pot setting of 0.50 equal to zero volts.
C _S	TP3	This test point monitors the sum of external input, position input, bias and rate feedback which is the command sum, C _S . The scaling at this point is 200 lbs/volt.
I _S	TP8	This test point provides a monitor for the current through the servovalve, I _S , with a scaling of 100 ma/volt.
EXT. INPUT	S1	This switch connects the applied external input signal to the load controller in the up position and zero volts in the down position.
FORCE POS.	S2	The load controller will provide a force proportional to the surface position when the switch is in the up position and zero volts input in the down position.
RATE GAIN	R9	The rate gain potentiometer provides a gain adjustment for rate feedback up to 20 volts/sec.
RATE	TP7	This test point provides a monitor for the rate feedback.
LOAD CELL	R7	This twenty turn panel mounted potentiometer is used for calibration, providing a $\pm 20\%$ adjustment of the nominal load cell gain of 200 lbs/volts.
LOAD CELL GAIN	S4	This detented switch must be pulled out to operate. The switch provides a calibration voltage for the load cell.
LOAD CELL GAIN	R8	This twenty turn potentiometer is provided to adjust the signal conditioner null voltage (with a range of ± 1.00 volt.)
LOAD CELL	TP4	This test point is provided to monitor the load output of the signal conditioner. The scale is 200 lbs/volt.

Panel Label	Schematic Label	Descriptive Function
+TP	TP6	This test point is provided to monitor the (extend) force limit set by the "+LIM" potentiometer. The scale factor is 200 lbs/volt.
FAIL	L1	This LED illuminates when either the + or - limits are exceeded.
-TP	TP5	This test point is provided to monitor the - (retract) force limit set by the "-LIM" potentiometer. Scale factor is 200 lbs/volt.
+LIM	R3	This twenty turn potentiometer is provided to adjust the + force limit from 0 to 10 volts with a scale factor of 200 lbs/volt.
RESET	S3	This momentary switch is provided to reset failures.
-LIM	R11	This twenty turn potentiometer is provided to adjust the - force limit from 0 to 10 volts with a scale factor of 200 lbs/volt.

Figure 11 is a schematic of the load controller circuitry. The external input is buffered by A1-A and then selectively chosen by the operator using switch S1. The position input for an operational mode where the force is proportional to surface position is selected through S2 and summed with the external input at A2-A (with a gain of 1.0). The summed input signal passes through the DPST electronic relay to the "GAIN" pot R14. The function of the electronic switch is to allow the operator to visually monitor the gain setting with the digital volt meter (DVM) on the monitor panel. The solid state relay is pulsed by a signal whose on state is 20×10^{-6} seconds, and off time is 2×10^{-3} seconds. While the relay is on, 10 VDC is applied to R14, and simultaneously the R14 output is captured with a sample and hold in the monitor then displayed on the DVM.

Once the gain pot is set, the external and/or position signal is summed with a rate input (from R9) and a force bias input (from R15) at A2-B at a gain of 1.0. This command sum, C_s , is connected to A2-A through the second half of the solid state relay AS-1. The function of AS-1 is to provide a zero command to the load servovalve when the preset force limits are exceeded. The command sum signal is summed out of phase with the force feedback signal to create the appropriate forward loop error which drives the current feedback amplifier. The current amplifier has a gain of 2 ma/volt with bias provisions to adjust any null errors within the servovalves.

The load cell signal conditioner is an instrumentation amplifier with an adjustable bias and gain. S4 and R42 allow the instrumentation amplifier to be locally calibrated by actuating S4 and trimming the gain to match calibration values. This feature eliminates the requirement to remove each entire load actuator assembly in order to calibrate the load cells. The calibration values include the mass of the actuator assemblies.

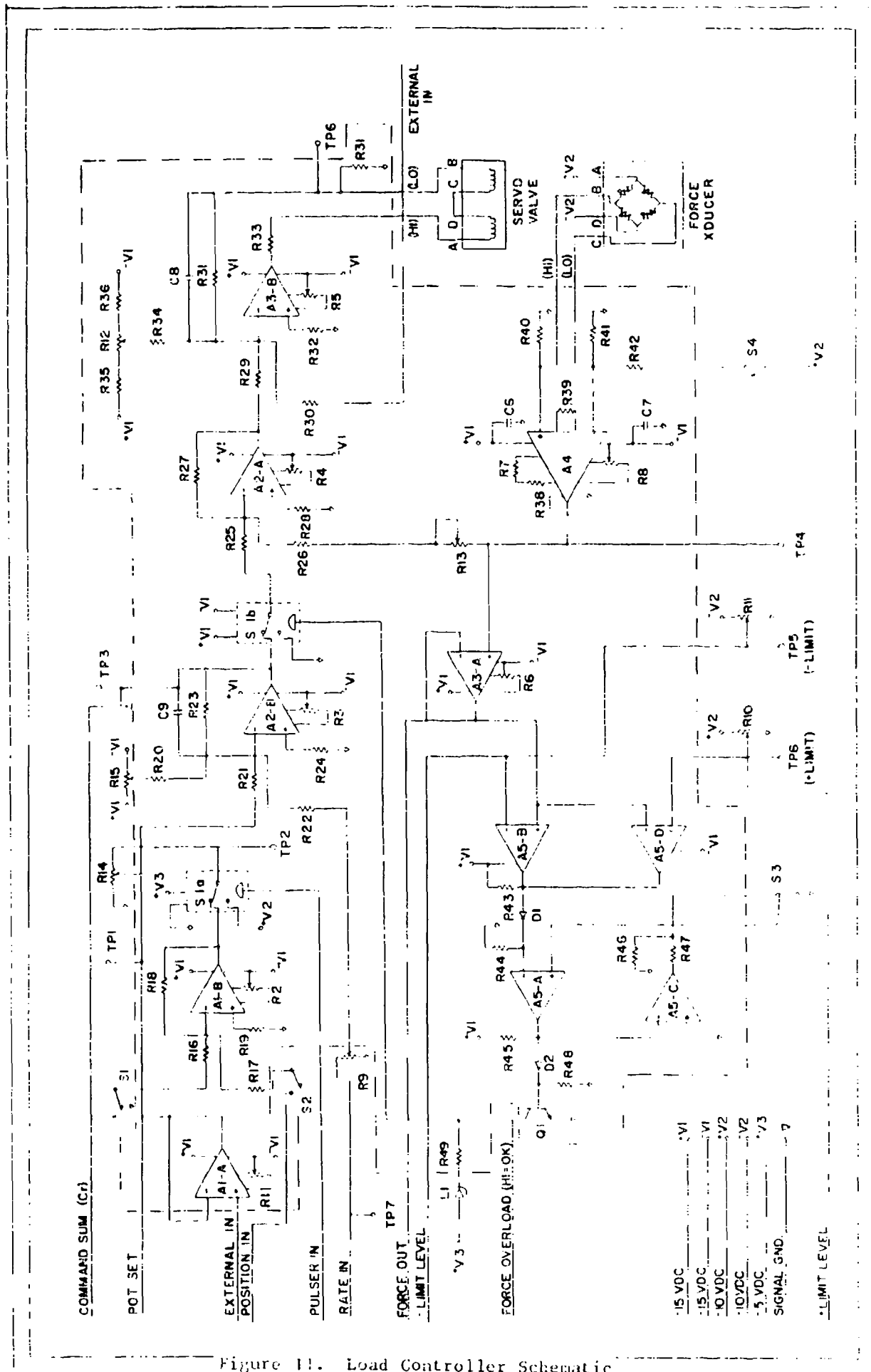


Figure 11. Load Controller Schematic

The load force signal is connected to A3-A for monitoring and to the force overload limit circuitry. The force limit circuit uses a quad comparator that first determines if the signal is within the adjustable limits set by R10 and R11. Each of these potentiometer outputs are monitored locally through panel test points and displayed on the DVM in the monitor panel. The scale factor is set at 200 lbs/volt. Once the limits are exceeded, the remaining comparators act as a latch to drive Q₁, which illuminates the LED (L1). The output of Q₁ is connected to the monitor panel to define the failure location and sound an audible alarm. The failure comparator is reset by switch S3. Each load control circuit board has bypass capacitors connected to the power input lines to reduce the effects of line noise and transients.

Surface Position Signal Conditioner

The surface position signal conditioners are contained in four dual channel modules located in the top chassis of the center console. A of the modules are interchangeable. Figure 12 is a front view of one surface position signal conditioner. Note that the controls and test points for two channels are mounted on the module's front panel. Figure 13 is a rear view of the module. This view shows the printed circuit board used in the construction of the unit. The specification for the module are as follows:

Input Impedance	> 1.0 meg-ohm
Gain	0.00 to 0.60 volts/volt
Position Bias Range	\pm 10.0 volts
Output with MASTR transducers:	
(+10 volt Position Transducer	
Excitation)	
12 Inch Stroke	1.66 volts/inch
24 Inch Stroke	0.83 volts/inch
Rate Signal Output	0.160 volts/volt/second
	(using position output)
Rate Signal Break Frequencies . .	62.8 radians/sec
(First Order Lag)	and 628 radians/sec

The function of the front panel controls for the position/rate module are as follows:

Panel Label	Schematic Label	Descriptive Function
POSITION GAIN	R7	The twenty turn panel potentiometer adjusts the position gain from zero volts per inch to \pm 0.6 volts/volt.
NULL OFFSET	R8	This twenty turn potentiometer adjusts the conditioner bias by \pm 10.0 volts.

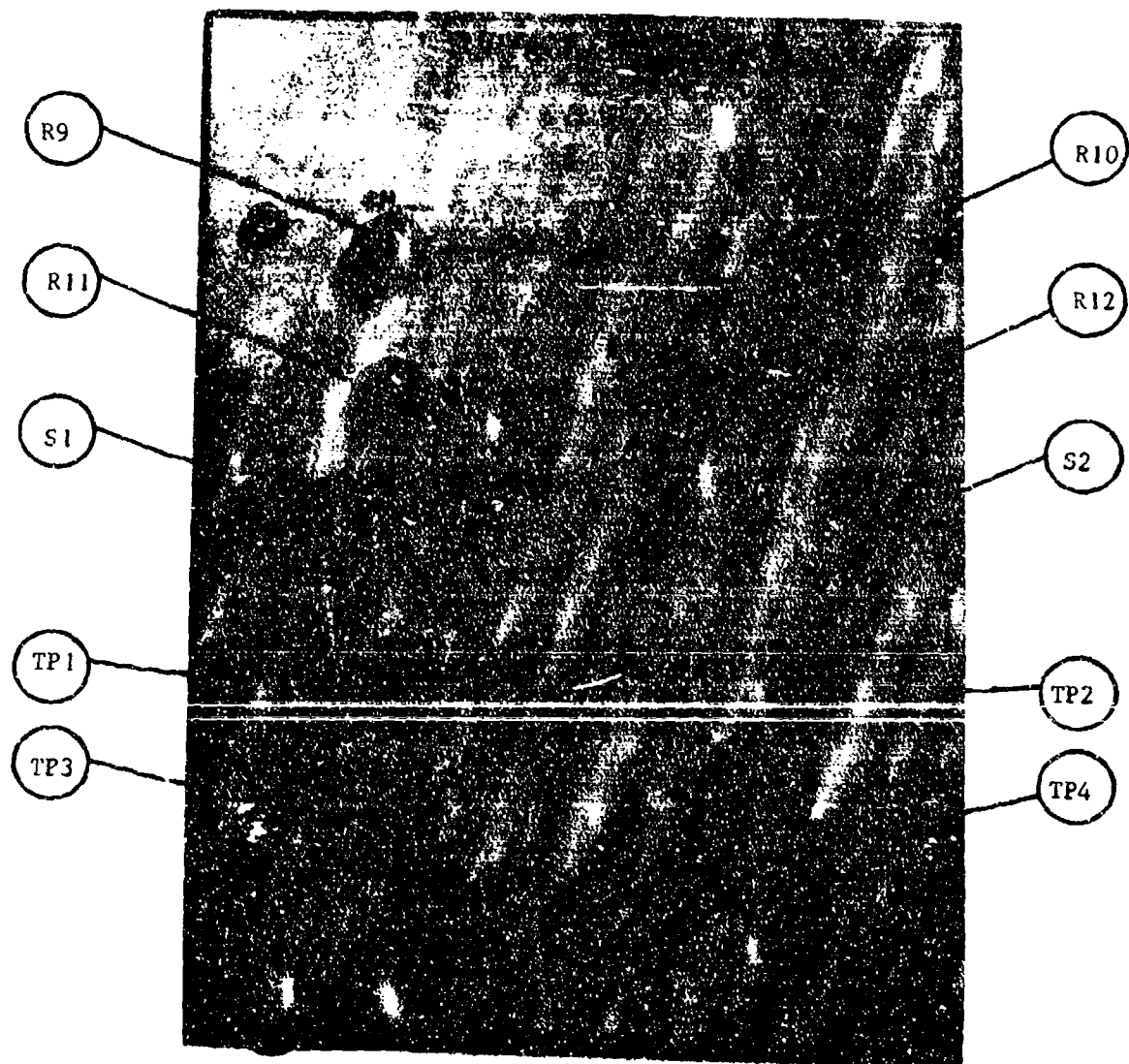


Figure 12. Position/Rate Module Front View

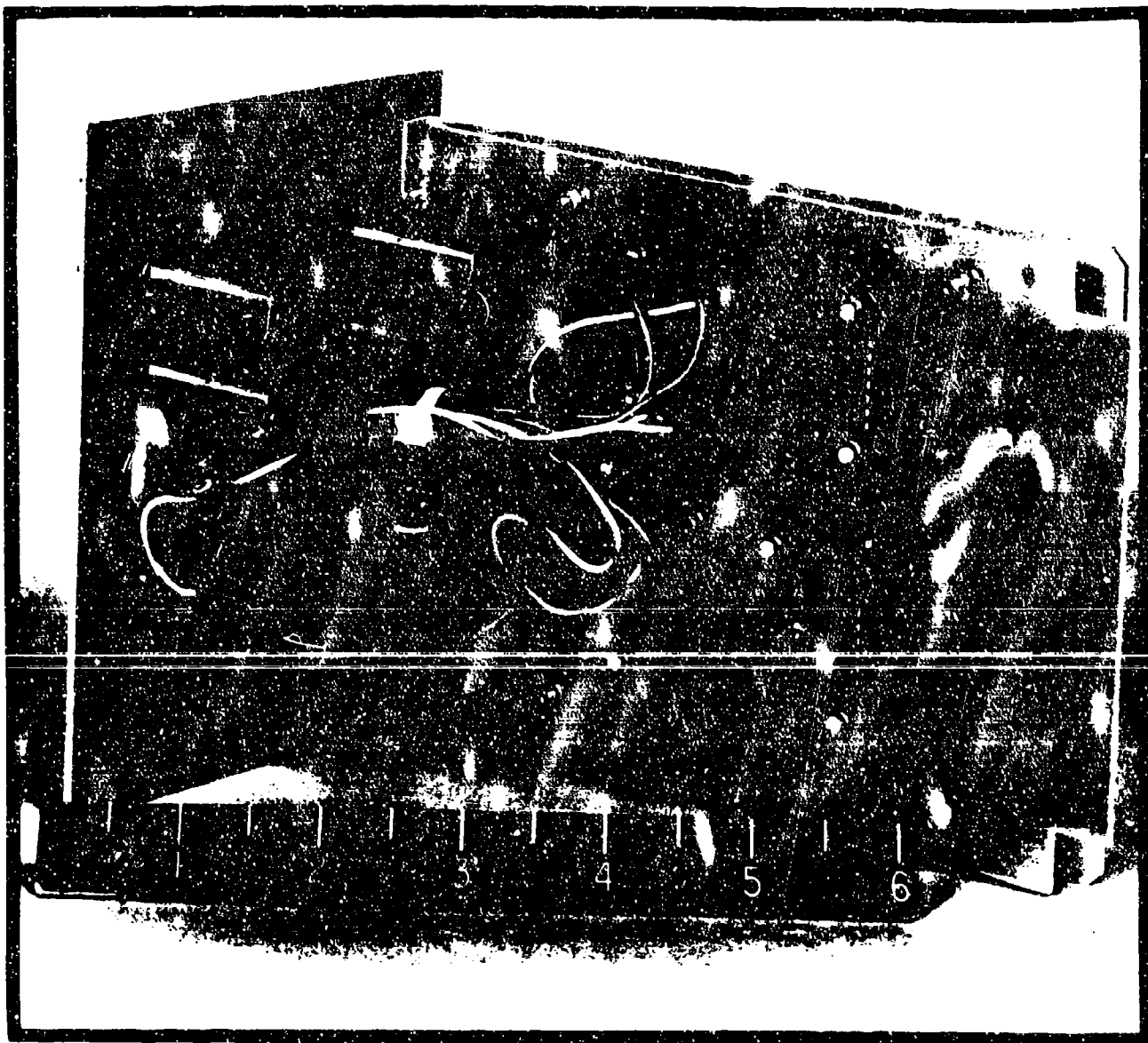


Figure 13. Position Rate Module Rear View

Panel Label	Schematic Label	Descriptive Function
OUTPUT DIRECTOR	S1	This three position switch directs the position output; UP = upper channels, CTR = upper and lower channels, DOWN = lower channels.
POSITION MONITOR	TP2	This is the monitor point for the conditioned position signal.
RATE MONITOR	TP1	This is the monitor point for the conditioned rate signal.

Figure 14 is a schematic of one section (of two identical sections) used in the position/rate module. The ± 10 VDC output of the linear position potentiometer is buffered by A1-A. R1 in series with R7 is used to scale the input signal range to ± 6 volts. The output of the gain potentiometer R7 is summed with the output of bias potentiometer R8. This signal is then routed to the proper output by switch S1.

The rate signal is generated by differentiating the position signal with operational amplifier A2-A. The gain of the differentiator is 0.16 volts/volt/second. The circuit has a first order lag break frequency at 10 Hz and 100 Hz. Amplifier A2-B is used as a high input impedance buffer between the differentiator and the rate output of the module.

Channel Failure and Signal Monitor

The Channel Failure and Signal Monitor panels located on the lower left and right of the control console top section provides a status indication for each load channel and an audible alarm upon failure of any channel. The panel also incorporates an addressable signal monitor made up of an address thumb wheel switch and a voltmeter.

The status of the 18 actuators monitored by each Channel Failure and Signal Monitor panel is displayed on the left side of the panel by 18 LEDs arranged in the same general configuration as the load actuators. The LEDs illuminate when the force limits are exceeded. The audible alarm and bypass solenoids are triggered simultaneously with the LEDs. A switch to disable the audible alarm is mounted to the right of the LEDs.

The center and the right portion of the panel contains a 2 digit plus sign thumb wheel switch. To the right of the thumb wheel switch is mounted a digital voltmeter (DVM) and two sets of test jacks. The thumb wheel switch is used to address the signal to be displayed on the DVM. The channels are numbered 1 through 18. The channel number is added to a suffix in order to display a particular signal within a channel. (Channel 1 has an address of 01, Channel 2 an address of 02, etc.) The addresses used for the different signals within a channel are the following:

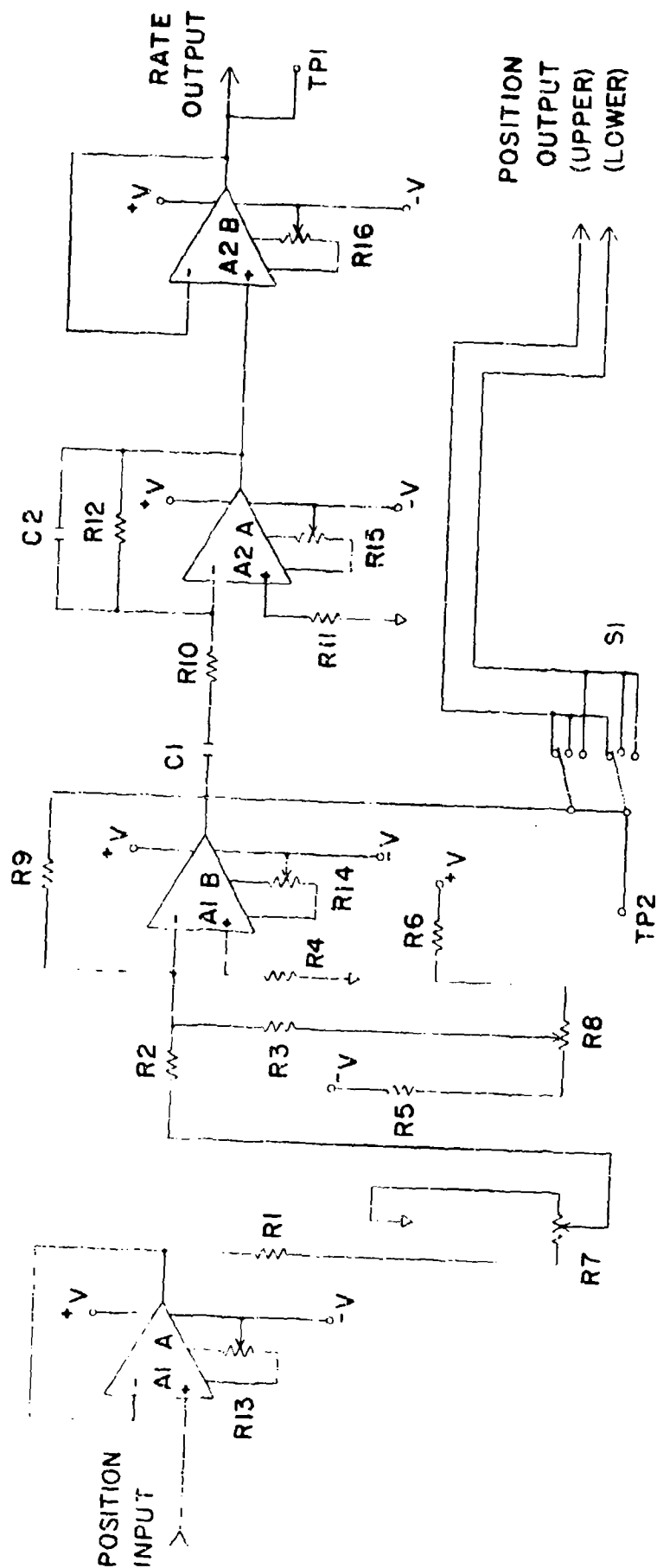


Figure 14. Position/Rate Module Schematic

Basic Address	Signal Addressed
+00 + Channel #	Positive force limit voltage
-00 + Channel #	Negative force limit voltage
+20 + Channel #	Servo current (100 ma/volt)
+40 + Channel #	Command voltage C_s
+60 + Channel #	The input gain potentiometer as a percentage of full scale (10% = 1.0 volt)

In addition, the thumb wheel switch is used to address the outputs of the position transducers and external inputs with the following addresses:

Basic Address	Signal Addressed
+81 to +84	The conditioned output of the four position transducers connected to the trailing edge of a test specimen
+85 to +87	The conditioned output of the three position transducers connected to the leading edge of the test specimen

Addressing is accomplished by selecting the desired prefix and adding the desired suffix. For example, if you want to view the servo current of channel 12, add 12 to +20 for a sum of +32. When the thumb wheel switch is set to +32, the current will be displayed on the DVM with a scale factor of 100 ma/volt.

The signals can also be displayed on a dynamic analyzer, such as an oscilloscope, by using the output jacks labeled "Monitor". There are no elements within the monitor circuitry that will effect the dynamics of the signal being monitored.

With an address of +00, the DVM will display any signal that is connected to "External Input" jacks. The DVM has a range switch on the front panel that will allow using either +2.000 volt or +20.00 volt full scale ranges.

Electronically the failure monitor is made up of 5 NAND gates (4 inputs each) that receive a status signal from each control module. The NAND outputs are summed by 4 NOR gates (2 inputs each) which drive another four input NAND gates whose output turns on the audible alarm and drive the optically isolated relay controlling the solenoid which bypasses the particular load channel.

The electronics of the monitor use the thumb wheel switch to address one line of the 15 Precision Monolithics MUX-08 eight input multiplex switches. The two position sign switch output is high or low (for the + or - selected). The "tens" switch is ten position with a decimal output and the "units" switch has ten positions with a binary coded decimal (BCD) output. The sample and hold circuitry and "pot set" pulses are also developed in this section of the

electronics. The use of the pulses were described previously in the load control module description.

Solenoid Driving Relay Description

The bypass solenoids are actuated with 110 VAC and require 0.3 amperes holding current. Optically isolated solid state relays (OPTO-22, P/N CAC-15) are energized by the failure or overload signal generated at the load control module. Both the lower and upper load actuator systems have 18 of the solid state relays mounted on a chassis. The relay chassis is located in the lower rear section of the desk console as shown previously in Figure 8. The optically isolated solid state relays offer a considerable reduction in the control signal transients resulting from energizing and de-energizing inductive relay coils.

Data Logger Description

A model 2200B Data Logger manufactured by the John Fluke Mfg. Co. was installed in the center electronic console. The data logger is programmable to sequentially select any of its 40 inputs at a rate of 3 to 15 channels per second. The data is printed in a 16 column format at 2.5 lines per second.

The Data Logger is connected to monitor and record the input (command sum) and output (force) of the upper or lower loading system. The third operating mode available is the recording the output force from both the upper and lower systems. The transfer between monitoring modes is accomplished through three separate input connectors at the rear of the data logger. Connector switching is required because each record mode requires 36 of the 40 recording channels.

Input Signal Panel

The input signal panel, located at the lowest location of the center console (reference Figure 2) provides an input point for operation of the MASTR from a local source. The panel is divided into two sections, with the right hand section dedicated to the upper load channels and the left section dedicated to the lower load channels. The inputs for each channel can be individually accessed or accessed from a common input point. The input jacks are arranged in the same order as the load actuators are mounted on the MASTR.

There are three rows of four inputs and two rows of three inputs. Each row has a switch that will connect its inputs with the common input or allow isolated operation. These inputs are connected electrically in parallel with the external input jacks located at the right rear of the lower console.

Power Supplies Description

The system power supplies are centrally located in the lower right section of the desk console below the relay chassis. The power supplies (the PX series) are manufactured by the Power/Mate Corporation and have better than 0.1% regulation (no load to full load) and less than 15 millivolt output ripple.

The power supplies provide ± 15 volts DC at 3.2 amps, ± 10 volts DC at 2.5 amps and 5 volts DC at 5.8 amps. Each power supply has a front panel meter, output level adjustment and monitor jacks in order to provide easy access and adjustment during initial setup.

Interface Wiring Description

The complexity of connecting the 36 control channels required the development of an overall scheme for routing the wires interconnecting the test rig and electronic control console. The reaction structure and loading actuators are located approximately 75 feet from the electronic console.

The general wiring scheme used was to connect the electronic signal lines from the control console to the test rig through a junction box physically located close to the test rig. The electronic power lines (110 VAC solenoid actuation power) are routed separately in an effort to reduce the possibility of transients being induced into the signal conductors. The wires are routed through existing laboratory wire ways previously dedicated to signal and power lines. The junction boxes contribute flexibility and a convenient maintenance access to the system electronics.

The wires used for the interface connections are shielded, twisted pairs for each control function with each pair being contained within a multipaired cable. The conductor sizes used are 22 gauge for the signal lines and 18 gauge for the power lines. The test rig wire labeling within the junction boxes is keyed to the control actuator position and upper or lower system.

Load Control Loop Description

The MASTR's 36 individual force control channels are identical except for the stroke of the control actuators. The trailing edge actuators have a 24 inch stroke range and the leading edge actuators have a 12 inch stroke range. Figure 15 is a block diagram of a single force control channel.

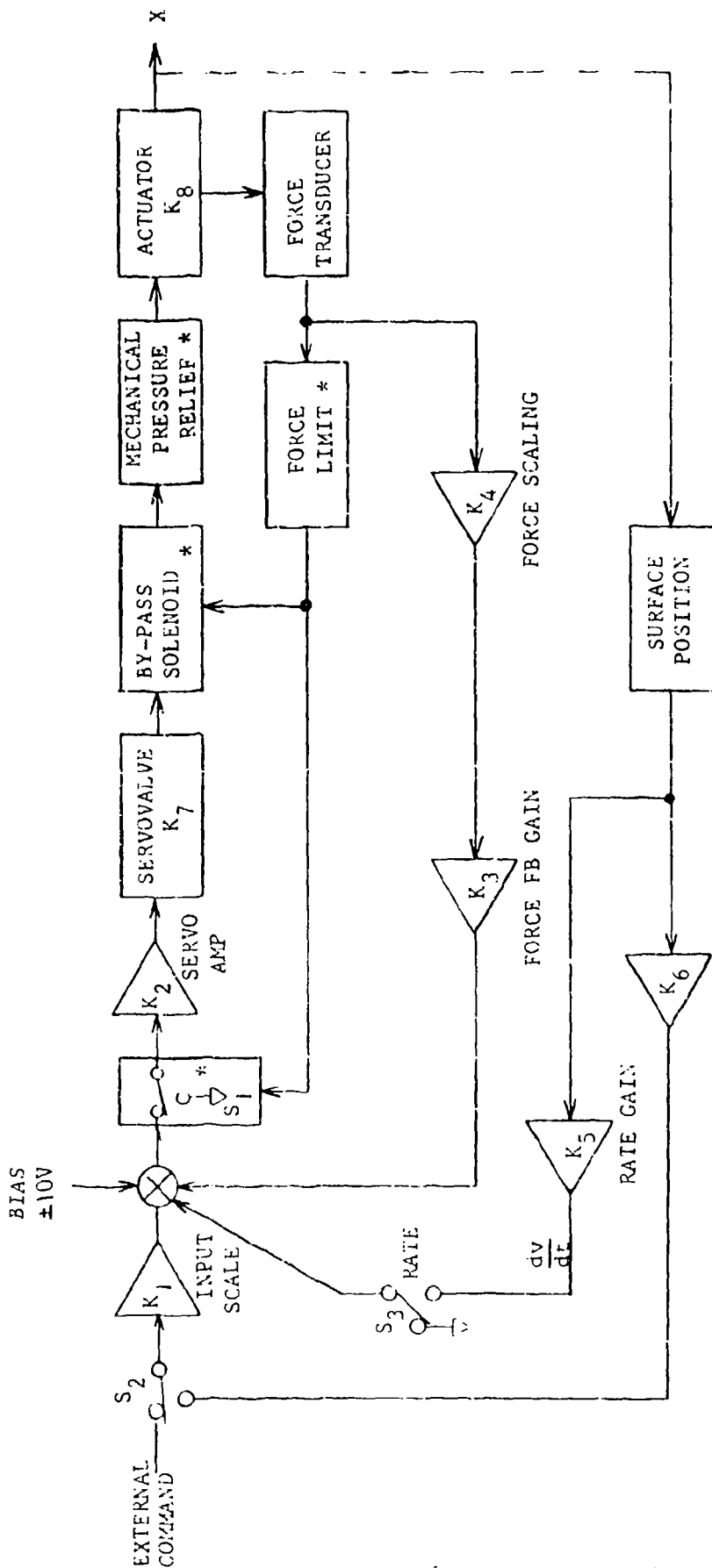
Referring to Figure 15, the static load control relationship can be derived using the closed loop feedback relationship "Output/Input = $G/(1 + GH)$ " where G on Figure 15 is the product $(K_2K_7K_8)$ which is equal to 9996 lbs/volt. The H term is the product (K_3K_4) which is equal to 0.0049 volts/lb. With these values for G and H , the force gain of the control loop is 200 lbs/volt.

MASTR Component Design Verification

A design with the amount of components of the MASTR required a step-by-step design verification. The MASTR is made up of 36 channels which are essentially identical. The design has sufficient trim or fine tuning capability that all hardware could be adjusted after assembly. The electrohydraulic component testing and adjustment was carried out for each individual channel.

To achieve low friction from the load actuators, the end cap of each load actuator was removed in order to place the original rod seals with the low friction seal cartridge. The reassembled, modified actuators were bench checked by lubricating the shaft with MIL-D-5606 hydraulic fluid and performing a breakout and running friction test. The maximum test limits were 15 pounds for breakout and 10 pounds for the running friction.

During testing, several actuators required 100 pounds for the breakout frictions and not more than 10 of the assemblies would meet the requirements. The problem was solved in 90% of the cases by using an assembly procedure to centralize the new seal cartridge. The technique used was to install the



K_5 - 0 to 0.5 volt/inch/second

K_6 - 0 to 0.5 volt/inch

K_7 - 500 psi/ma

K_8 - 0.98 pound/psi

K_1 - 0 to 1.0 volt/volt

K_2 - 20.4 ma/volt

K_3 - 0.98 volt/volt

K_4 - 0.005 volt/pound

*Indicates items that provide fail-safe operation

Figure 15. Control Channel Schematic

cartridge and "finger" tighten the actuator tie rods. The actuator was then cycled full stroke several times and the tie rod tightened equally in a cross corner sequence. The actuator was cycled after every 12 in/lbs of torque increase until the full value of 96 in/lbs was obtained.

The remaining 10% of the actuators required the seal cartridges to be hand fitted, and the actuator rod to be rotated to meet the requirement. The basic problem was found with the commercial actuator assembly tolerances. The double ended actuators have one of the rods threaded into the piston without a close tolerance pilot to preserve axial alignment.

The servovalves were mounted on a manifold to record the "as received" pressure and flow gain data. Figure 16 is a typical pressure gain plot indicating 2,800 psi/ma gain with some null deadband, also caused by the valve undercut. The addition of a bypass orifice tends to soften these effects. Figure 17 is a typical flow gain plot indicating a 1.0 gpm/ma flow gain with 1.1 gpm of null leakage flow. The high leakage value is due to the 3.0% underlap of the servovalve edges.

The reaction structure shown on Figure 18 was designed and fabricated for the initial setup and testing of each load actuator assembly. The structure was designed to be loaded to 2,000 lbs. The 2,000 lb load resulted in a 1.2 inch deflection of the actuator. The structure was designed as a spring load which allowed the actuator under test to move when a force output was commanded in order to verify the control system's dynamic load response. Loading systems that have no output motion requirement generally have a load response nearly equal to the flow response of the control valve. Once a system requires flow, the dynamic response degrades.

To evaluate each load actuator assembly, the actuator, load cell and manifold were mounted in the reaction structure. The pressure gain of the servovalves was first set using the adjustable bypass orifice to achieve a pressure gain of 200 psi/ma. Once the pressure gain was established, the servovalve and orifice were treated as a matched set. All of the pressure relief valves were adjusted to 2,000 psi for the initial setup. This setting was achieved using a special test manifold.

Each actuator's control manifold was assembled with its servovalve, bypass orifice, bypass solenoid and pressure relief valves for the preliminary testing. This consisted of measuring the control channel's static and dynamic threshold and the dynamic response in the reaction structure.

Figure 19 is a typical dynamic response with a 0.0 Db input of ± 1.00 volt corresponding to a ± 200 lb command. The bode plot shows a -6 Db and -90° phase at 10 Hz with no peaking. Figure 20 shows typical static and dynamic threshold time history plots. The static threshold corresponds to ± 20 lbs and is obtained using a 0.1 Hz ramp input with gradually increasing amplitude. The amplitude at which an the output responds to the input is the threshold value. The dynamic threshold is measured using a sinusoidal input at a frequency of 1/2 the bandpass of the control system. The amplitude at which the 5.0 Hz input causes the output to follow the input corresponds to a peak amplitude of 21 lbs.

The range of threshold data recorded for all the actuators was a low of 10 lbs and a high of 36 lbs. Additional tests with load bias inputs were recorded

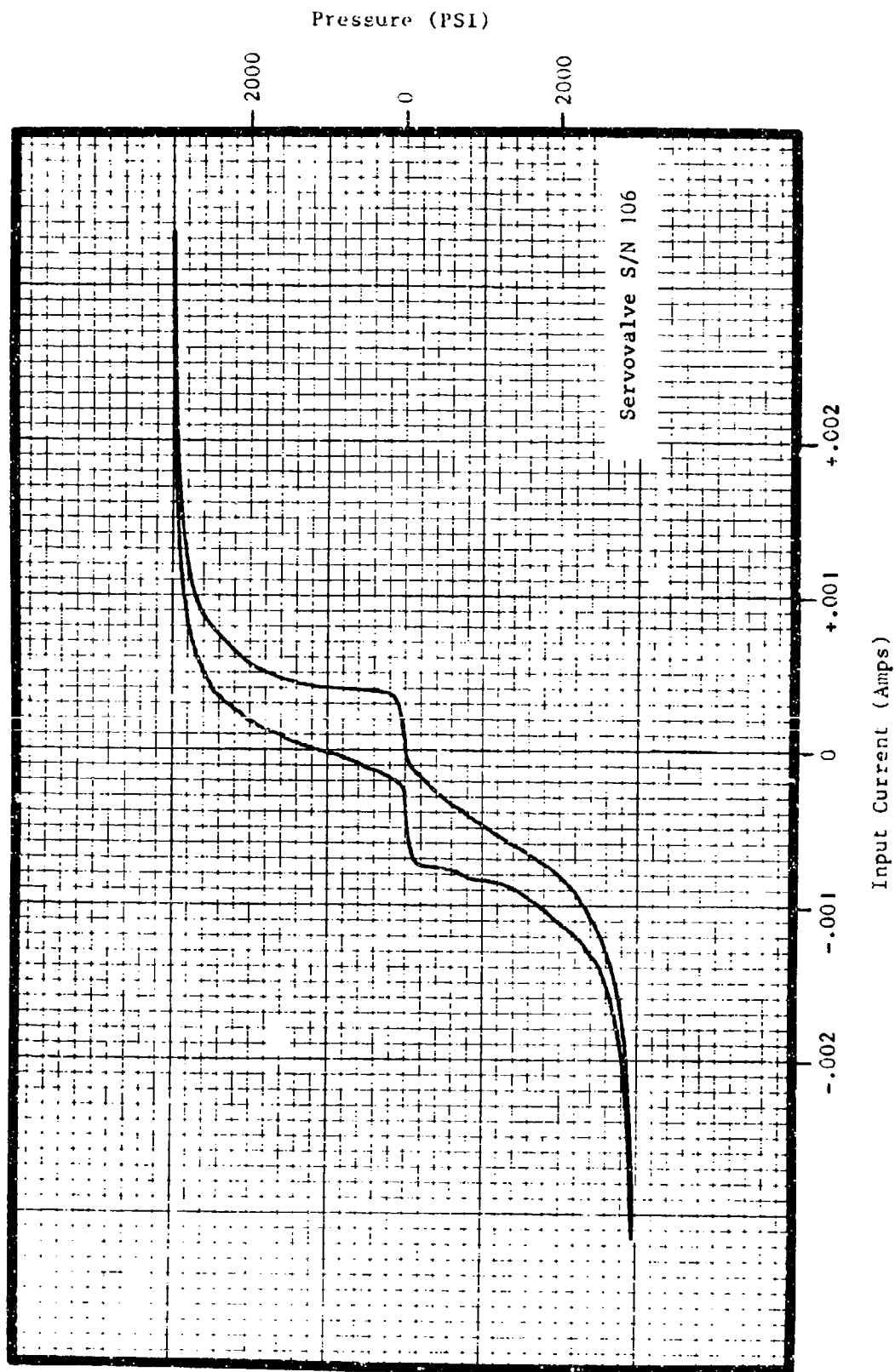


Figure 16. Servo Valve Pressure Gain - Typical

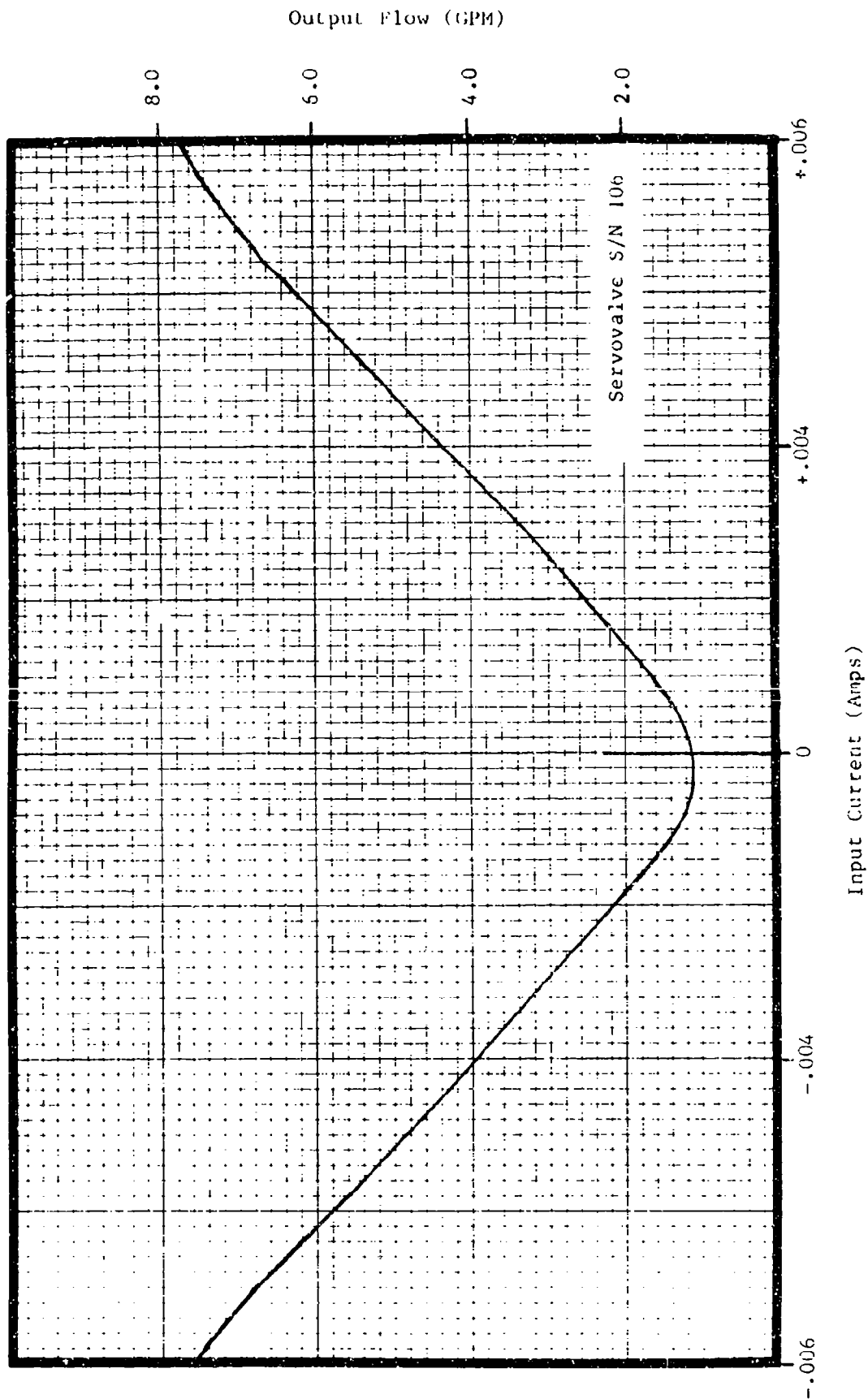


Figure 17. Servo Valve Flow Gain - Typical

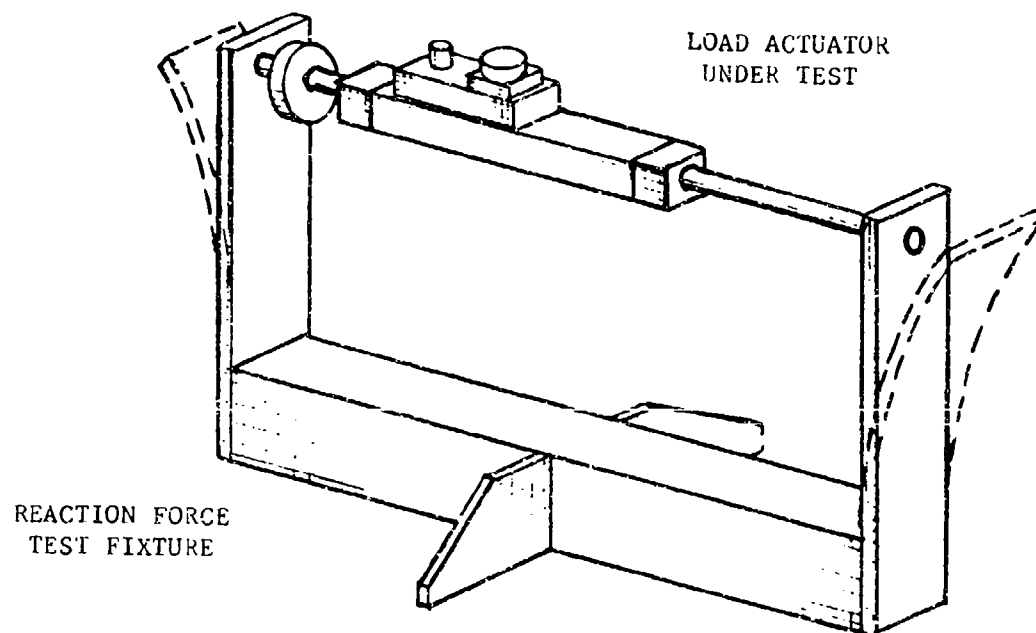


Figure 18. Reaction Structure

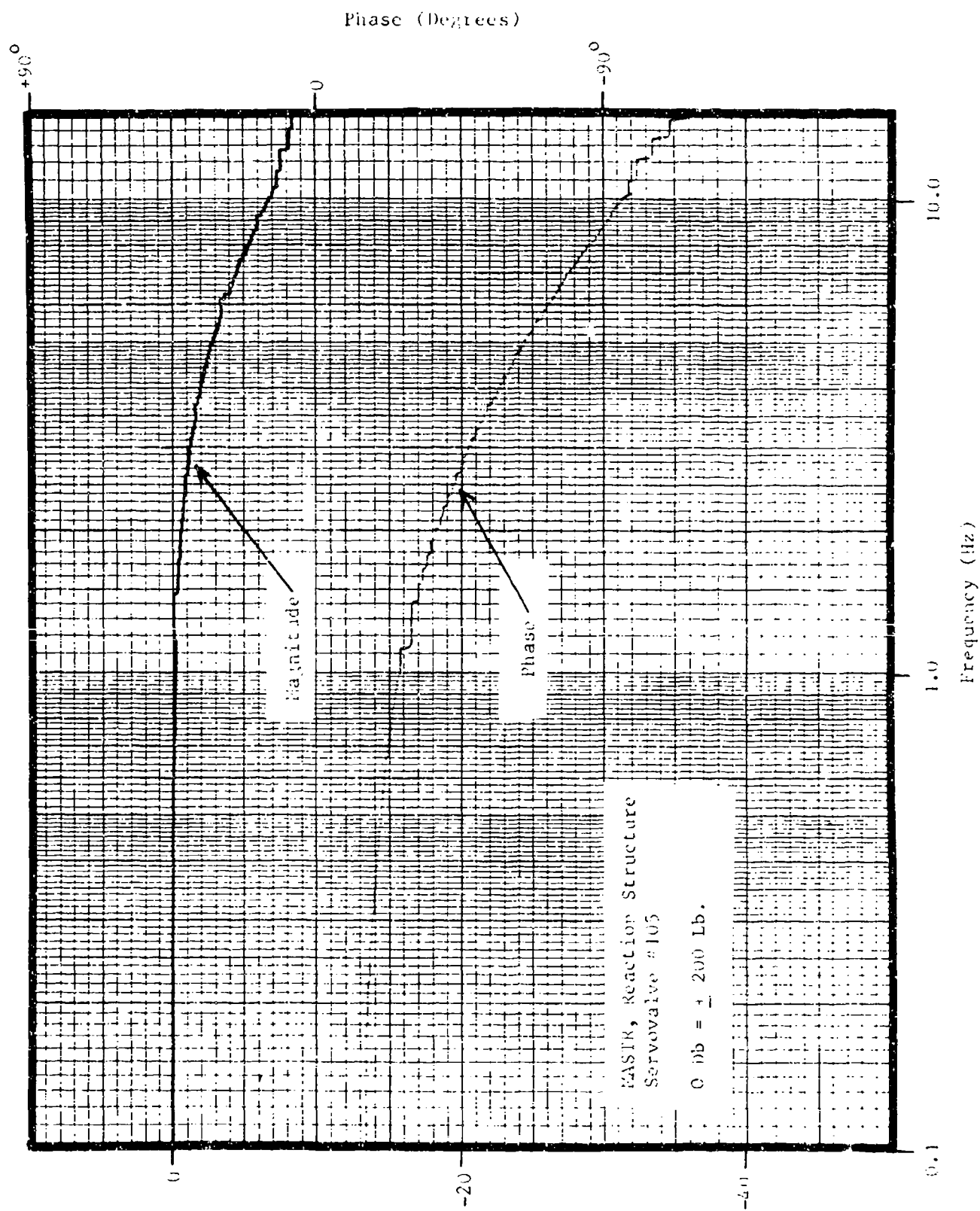


Figure 19. Load Actuator Dynamic Response

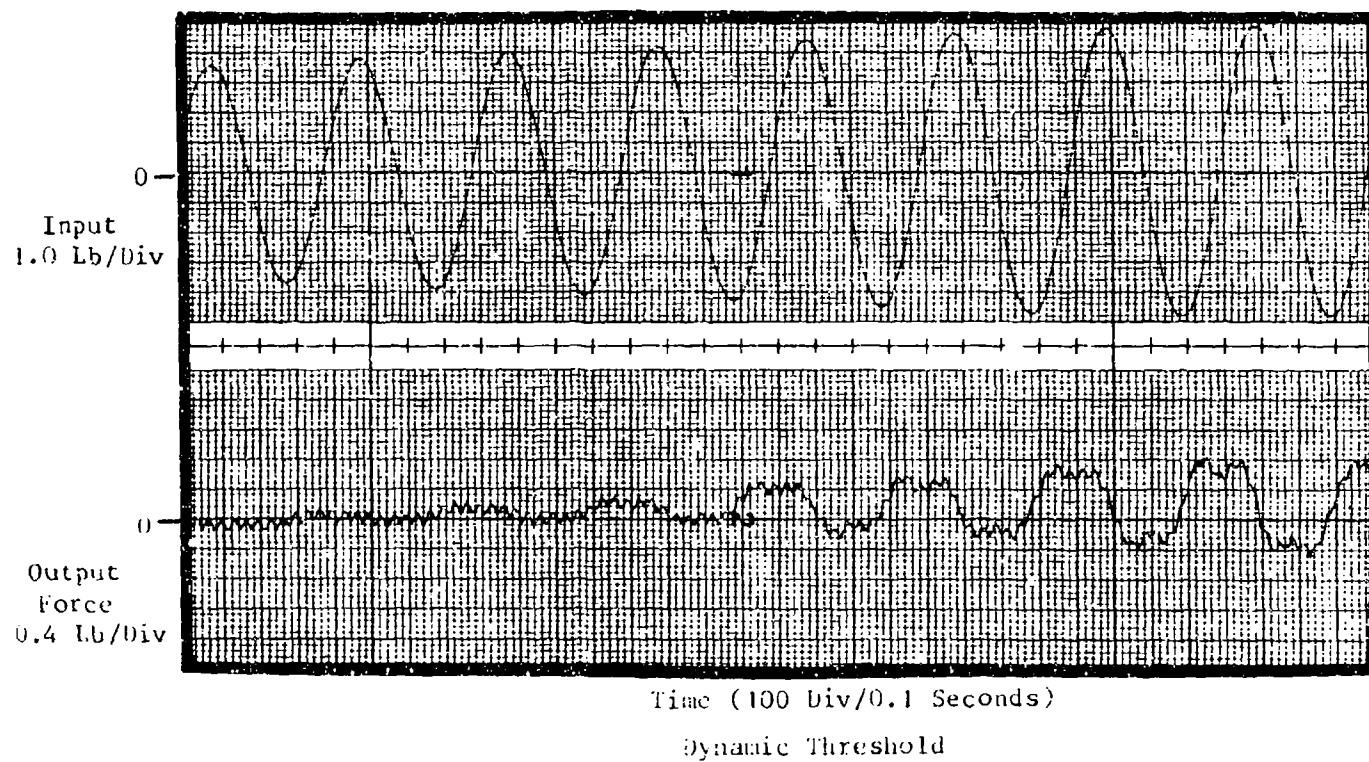
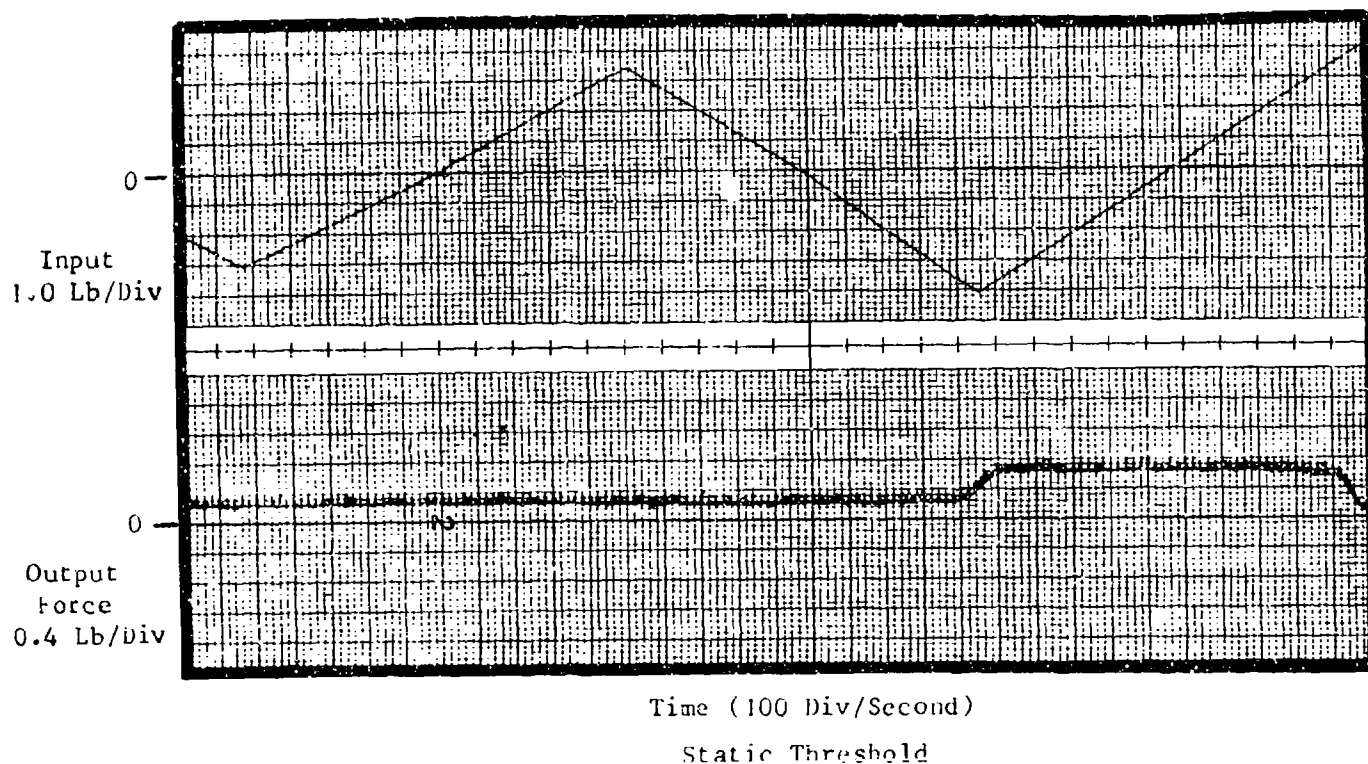


Figure 20. Load Actuator Static and Dynamic Threshold

without significant changes to the threshold data. All of the testing was recorded using a hydraulic supply pressure of 2,000 psi.

MASTR Final Assembly & Check-Out

A reaction plate was fabricated to provide a flexible test structure. The plate was mounted in the MASTR as shown in Figure 21 and the load actuators attached to the plate. The reaction plate was fabricated from 7075-T6 aluminum plate 3/4 inch thick and 42 inches wide. This provided a maximum load capability on the trailing edge of ± 4500 lbs (with a corresponding deflection of 6.8 inches) without yielding the plate. The analysis was based upon using 2/3 of the 72,000 psi allowable stress. The maximum load distributed over the 12 actuators is 700 pounds per actuator or load point. The section of the reaction plate for the leading edge provided a maximum total load of 10,000 lbs with a deflection of 0.84 inches and a 1,160 pounds allowable for each of the six load points.

All actuators were attached to the reaction plate for final performance evaluations. Figures 22 and 23 are typical linearity/hysteresis plots of a load channel. The plots represent a ± 2.5 volt input to command a ± 500 pound force output. Figure 22 (Channel 5 lower) is one of the best channels with 20 pound hysteresis and a linearity of better than 0.5%. Figure 23 (Channel 15 lower) represents one of the poorer performances with 40 lbs hysteresis and 1.0% linearity. However this worst performance is within the MASTR's performance goals.

Figures 24 and 25 are typical frequency response characteristics for the load actuators. The 0.0 Db input corresponds to a command of ± 500 lbs. Figure 24 shows the response of channel 4 lower section. Figure 25 shows the response of channel 14 lower section. The main difference between the two plots is that Channel 4 had the most compliant load attach point, being mounted at the extreme edge of the trailing edge position. Channel 14 had the least compliance load, being mounted at the point closest to the clamp point of the leading edge. Both channels have greater than a 10 Hz frequency response which meets the design goals.

The MASTR exhibited satisfactory performance with all upper control channels, all lower control channels, and both upper and lower control channels operating simultaneously.

Conclusion

The MASTR has met all its design goals. It should prove to be a useful test tool for evaluation of nonseparable control surfaces. Caution should be exercised during initial setup of the test rig in terms of insuring that all safety limits have been properly set to protect the test specimen from overload damage.

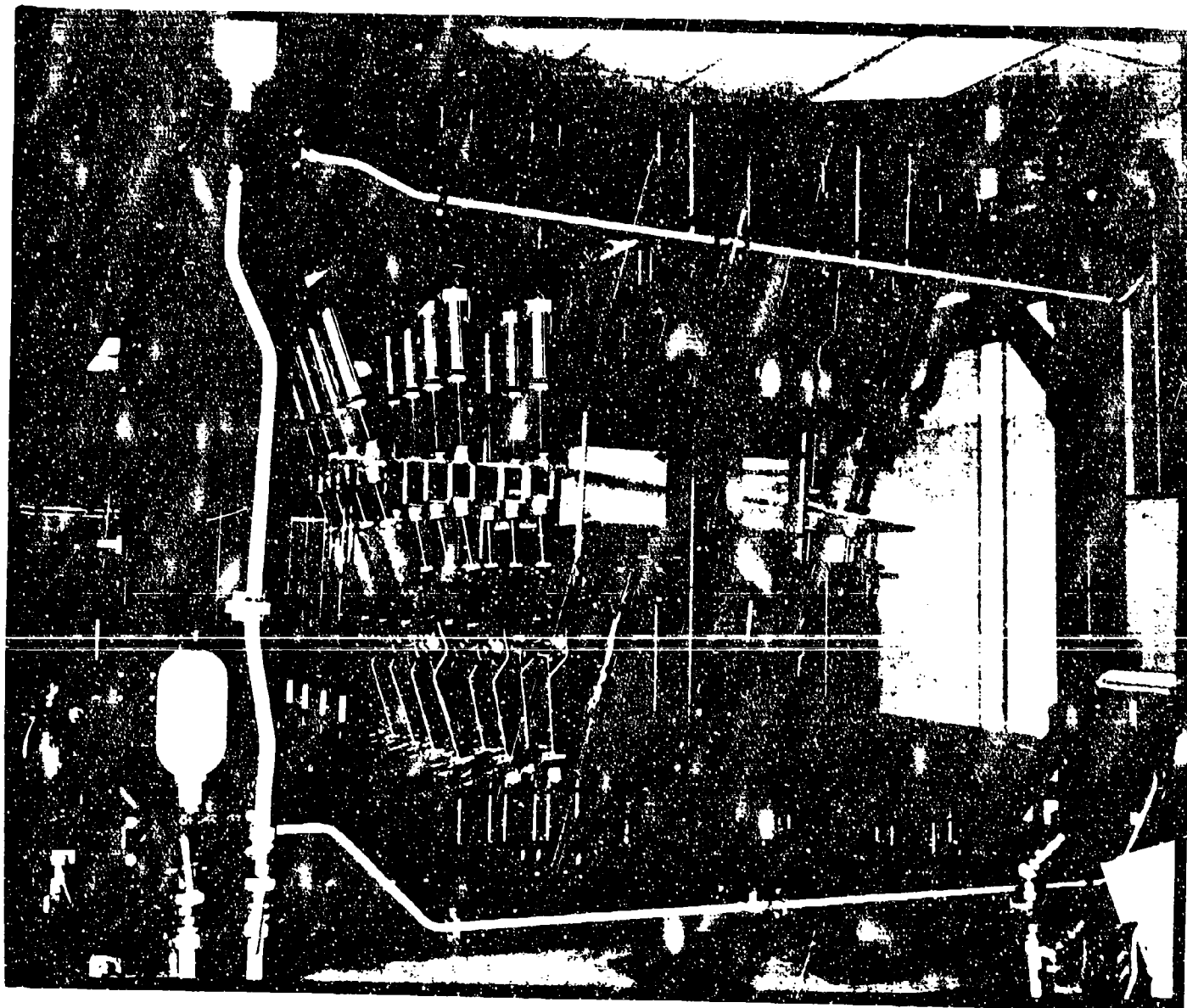


Figure 21. Test structure of TASI

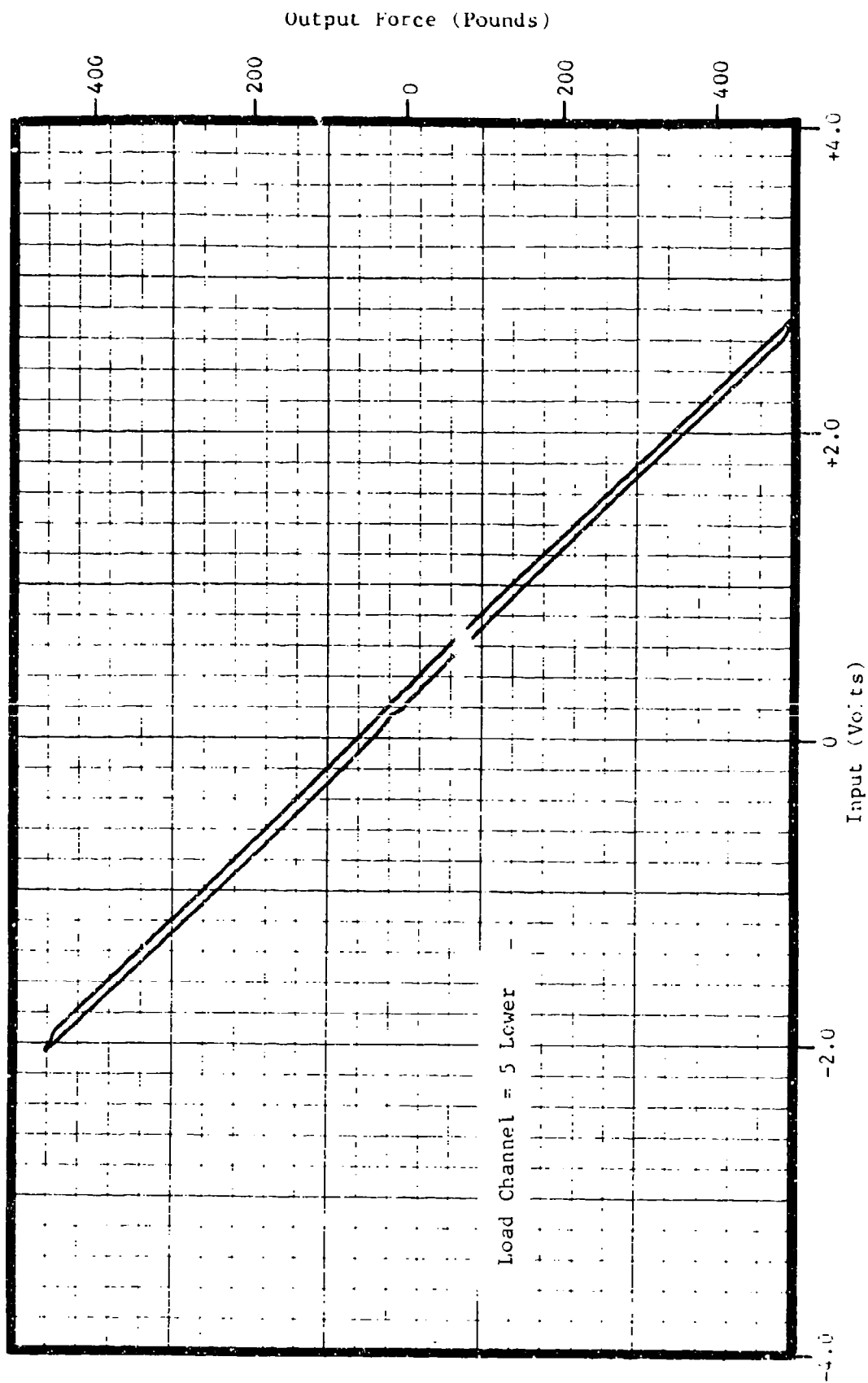


Figure 22. Load Channel #5L Linearity/Hysteresis Plot

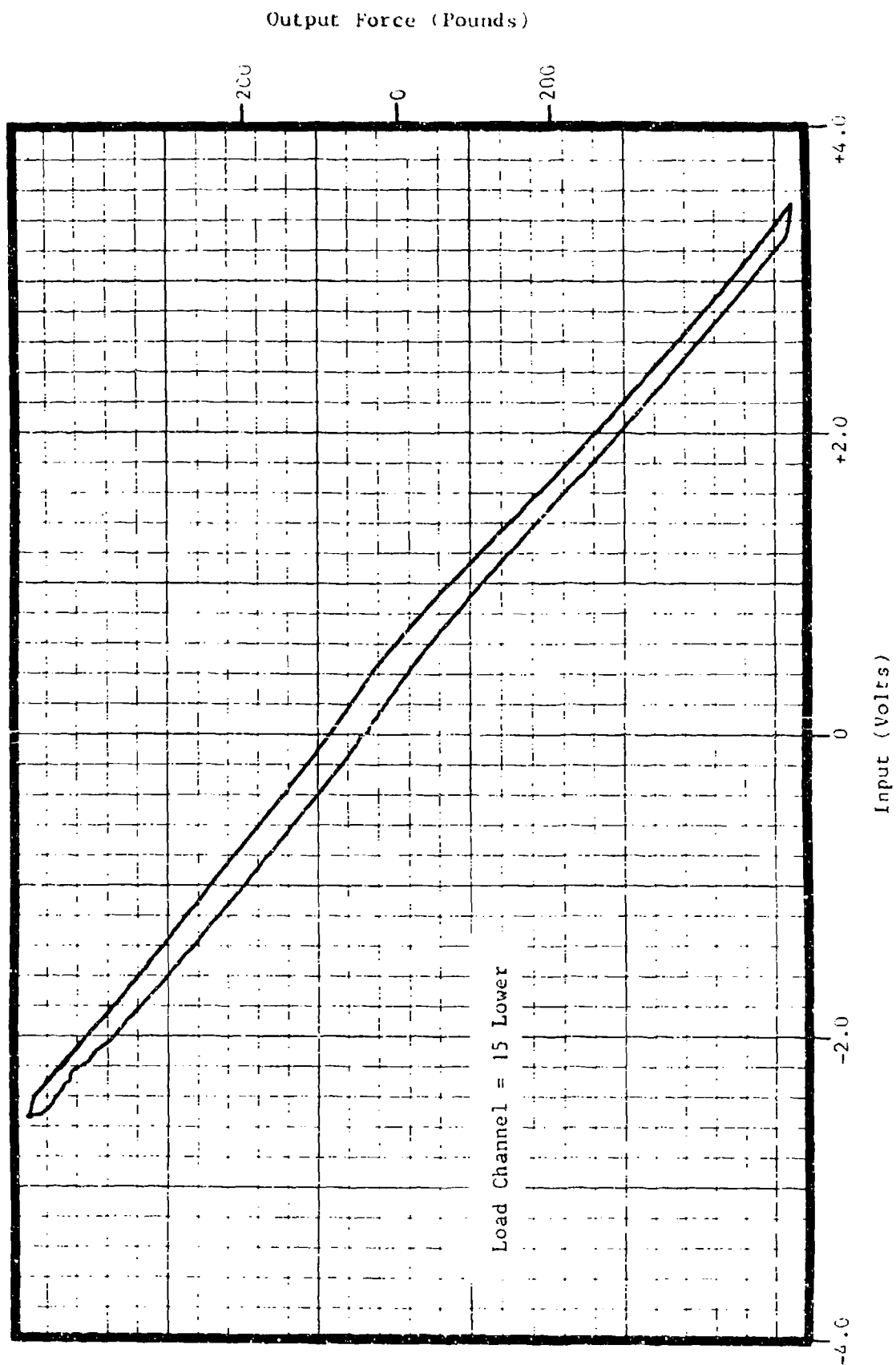
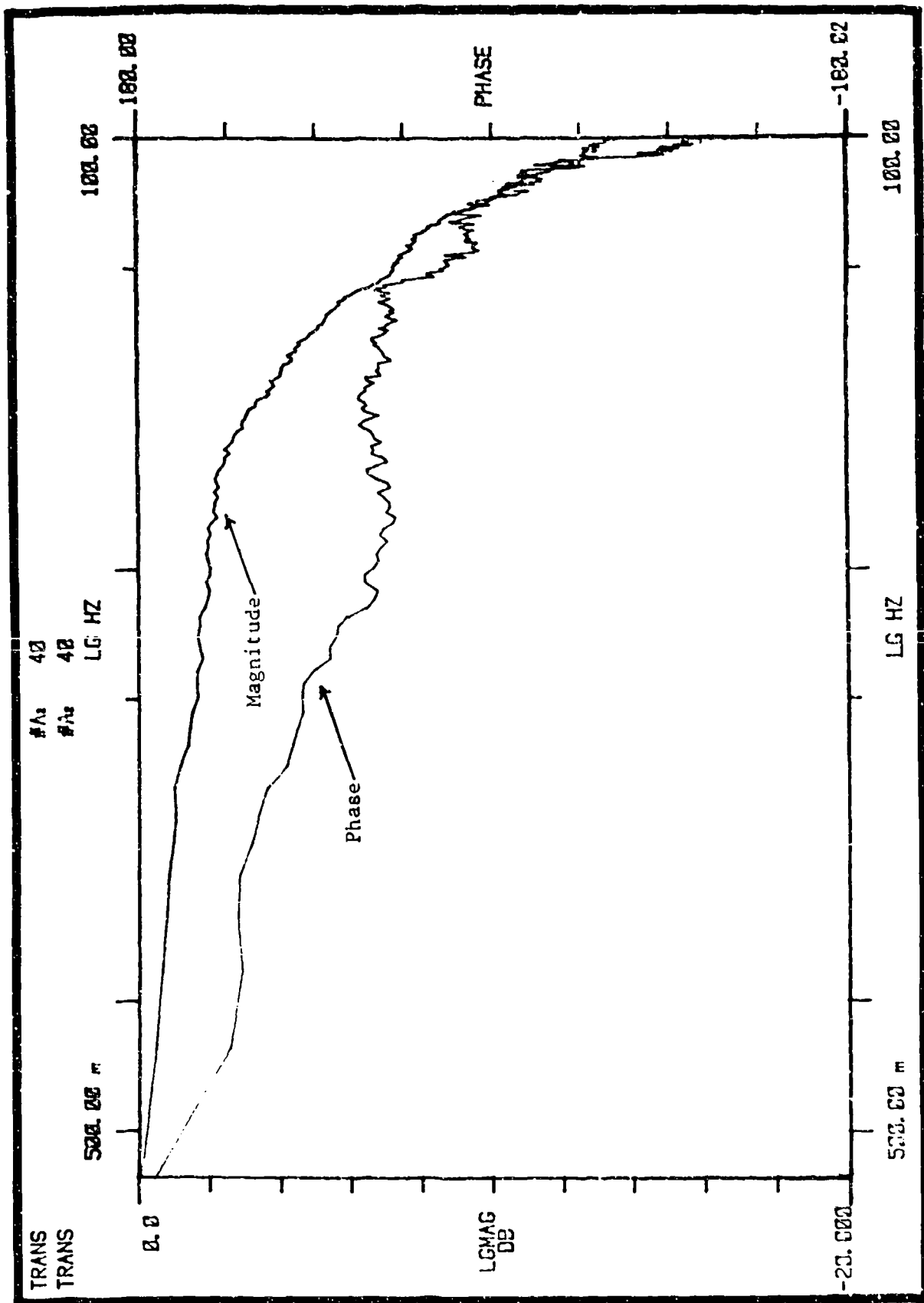
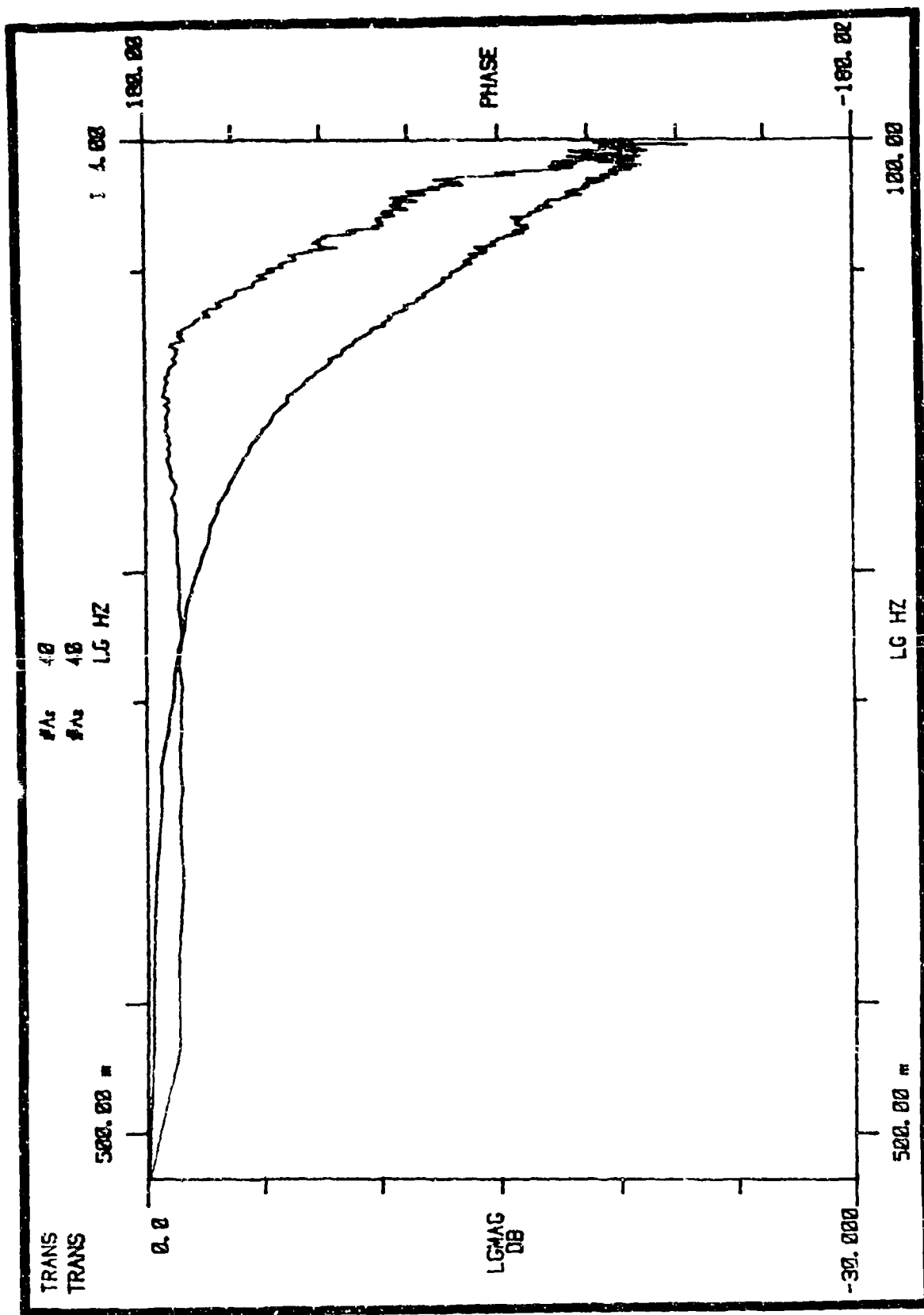


Figure 23. Load Channel #15L Linearity/Hysteresis Plot



Channel = 4 Lower
0 Db = + 500 Lb.

Figure 24. Channel #4L Frequency Response



Channel = 14 Lower
0 Db = + 500 Lb.

Figure 25. Channel #14L Frequency Response

SECTION II. FLUTTER SUPPRESSION ACTUATOR

General Investigation Description

The flutter suppression actuator investigation conducted under this contract was directed at fabrication and laboratory test of a flutter damping technique based upon using load pressure feedback. The technique uses load pressure sensing to change the impedance of the actuator controlling a slab type aerodynamic control surface. The investigation used an F-4 stabilator as a tool for application of the technique. This work is a continuation of a flutter investigation which is described in technical reports AFFDL-TR-75-29 and AFFDL-TR-79-3117 (Volume I). The activity described in this report is the integration and test verification of flutter damping hardware which incorporates improvements based upon previous test results.

The investigation is directed at the "classical flutter" problem of all moving control surfaces (such as canards and horizontal tails). Classical flutter involves both the torsional and bending motion of an aerodynamic surface. Flutter occurs because the speed of flow over the surface effects the amplitude and phase of the torsional motion in relation to the bending motion of the surface in such a way that energy is absorbed by the surface from the airstream. At the flutter frequency, the motions of the surface in bending and torsion are in a phased relationship where the potential energy that is stored when the surface bends is transferred to the torsional twisting of the surface. The flutter frequency of motion lies between the individual resonant frequencies of the bending and torsional vibration modes. The conventional method of increasing the flutter speed of a control surface is to increase the torsional stiffness of the surface. For slab type surfaces (like the F-4 and F-111 horizontal tails), the control surface itself is torsionally rigid and the torsional stiffness of the surface is primarily determined by the control actuator. Increasing the torsional resonant frequency of the control surface is accomplished by increasing the actuator stiffness. This is done by increasing the actuator size, particularly the drive area since the oil column stiffness generally dominates value for actuator stiffness. This stiffness increase (by increasing the size of the actuator) carries with it a weight and hydraulic power consumption penalty. The penalty for a given application increases with an increase in hydraulic system operating pressure. With increasing supply pressure, the drive area of an actuator for a given output force requirement decreases while the drive area required for a given actuator stiffness does not change. The difference between the greater actuator drive area required for stiffness and the drive area required for maneuvering the aircraft represents a weight and power consumption penalty for that method of solving the slab surface flutter problem.

The technique used for flutter suppression with the F-4 stabilator actuator is based upon using negative pressure feedback to cause the stabilator actuator to act as a damper at the torsional resonant frequency. The damper should absorb

energy in the torsional mode and eliminate the transfer of energy between the torsion and bending modes of the surface. The capability of adding torsional damping with little added weight allows sizing the control actuator for the force output required to maneuver the aircraft, rather than "over" sizing the actuator to increase the torsional resonant frequency. For the F-4 stabilator, the actuator drive required for maneuver loads is 3.44 square inches. The drive area of the normal F-4 stabilator is 6.00 square inches as sized for the flutter requirement.

The use of load pressure feedback to add damping or stability to flight control actuators connected to inertia loads has been used in several applications, particularly with European designed aircraft. The Jaguar uses load pressure feedback in the rudder control actuator. The Toronado aircraft uses load pressure feedback in the taileron actuator. The load pressure feedback mechanization in the Toronado actuator provides a damping response characteristic quite similar to that used in the flutter investigation with the F-4E stabilator actuator.

As described in technical report AFFDL-TR-79-3117, the wind tunnel test with one half of a stabilator surface and an actuator with a damping module did not produce the expected torsional damping results. In that test sequence, the indication was that the F-4 stabilator was decoupled from the actuator at the first torsional resonant mode. Engaging and disengaging the operation of the damping module had insufficient effect on the apparent damping of the torsional resonant mode. Subsequent tests of the stabilator surface in the laboratory indicated that the particular stabilator did not move as a rigid body in torsion at the torsional resonant frequency, but had a torsional twisting mode for part of the surface. This twisting mode was not indicated in a mode test report of the F-4E stabilator surface which was written when leading edge slats were first applied to the tail surface. The flutter damping technique being investigated requires that the slab surface move as a rigid body at the first torsional resonant mode.

The flutter suppression investigation activity in this section describes the integration of the damping circuit (with improvements based upon previous test data) into one control package for an F-4 stabilator actuator. The control package included the normal servovalve, solenoids, main control valve and secondary actuator components used in the normal F-4 mechanization. The control valve package was mounted on the reduced drive area stabilator actuator previously used for wind tunnel testing. The emphasis in this investigation activity was to optimize the performance of the damping circuit in a single package which would be representative of flight hardware. AFFDL/FGL-TM-78-73 "General Design Criteria for Hydraulic Power Operated Aircraft Flight Control Actuator", June 1978 was used in all phases of the design as a guide.

From the previous testing of the damper module operation (reported in AFFDL-TR-79-3117), there were two areas of design improvement which would benefit the operation of the damping circuit used with the F-4 stabilator actuator. These design areas involved a reduction of the threshold of the damping and isolation spools and an increase in the damping flow through the circuit.

Test evaluation of the integrated design was conducted in the laboratory. The testing was primarily response measurements of the damping circuit performance. The test data verified the design improvements incorporated into the integrated package and the correct operation of the module.

Hydromechanical Pressure Feedback Characteristics

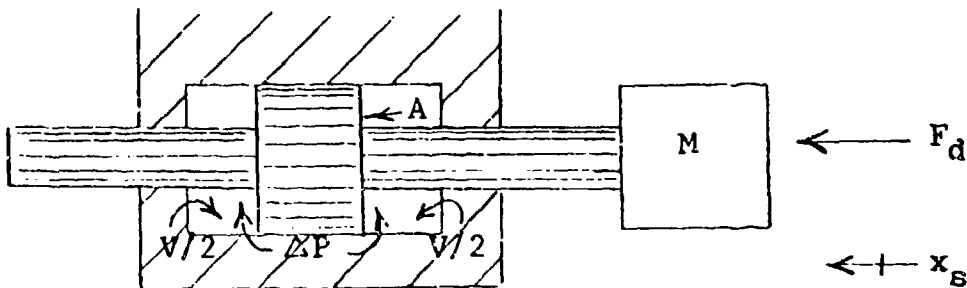
The following material is a summary of the analysis published in AFFDL-TR-75-29. The sizing calculations for the F-4 stabilator actuator are included by way of example. Values of the drive area, stiffness and surface resonance were taken from hardware drawings and test data. For calculation purposes, a resonant frequency of 23 Hz (first torsional mode) was used for the stabilator surface on the actuator and mounting compliance. In the following analysis, the effect of the control valve is not included. Omitting the control valve effect is reasonable since the normal actuator frequency response is well below the surface flutter frequency. By assuming that no structural feedback motion is introduced into the control valve and using a "washout" in the load pressure feedback loop, the operation of the control valve and the pressure feedback spool can be considered non-interacting.

This summary is divided into the following sub-sections:

1. Undamped Actuator and Surface Mass Response
2. Actuator and Surface Mass Response with Load Pressure Feedback
3. Actuator and Surface Mass Response with Load Pressure Feedback and Washout Circuit
4. Washout Transfer Function Description
5. F-4 Stabilator Sizing Calculations

Undamped Actuator and Surface Mass Response

Consider a control actuator with no damping. For simplicity, the control valve is assumed to remain centered and can be ignored. The actuator is assumed operating around its mid-stroke position. The equations of motion for the actuator and surface in response to an applied driving force are:



The motion equation for $\frac{x_s}{F_d}$ in Laplace Transform Form is

$$\frac{x_s}{F_d} = \frac{\left(\frac{V}{4\beta A^2} \right)}{\left(\frac{V M}{4\beta A^2} \right) (s^2) + 1} \quad (\text{Equation 1})$$

Where: F_d = the driving force

M = surface mass

x_s = surface motion

V = total volume of oil in actuator

β = bulk modulus of oil

A = actuator drive area

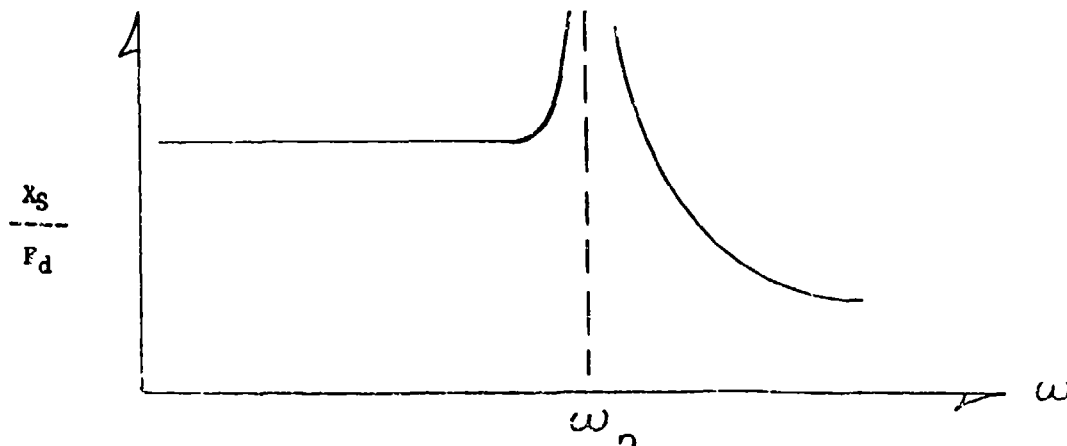
S = Laplace Operator

Comparing Equation 1 to the standard second order expression of Equation 2:

$$\frac{x_s}{F_d} = \frac{K}{\frac{s^2}{4\omega_n^2} + \frac{2\delta s}{\omega_n} + 1} \quad (\text{Equation 2})$$

$$\text{Implies that } K = \frac{V}{4\beta A^2}, \quad \omega_n^2 = \frac{4 A^2}{V M}, \quad \delta = 0$$

This transfer function implies an amplitude response to the driving force which resembles the following:



Actuator and Surface Mass Response with Load Pressure Feedback

For ΔP (Load Pressure) Feedback, the equation of motion is:

$$\frac{X_s}{F_d} = \frac{\left(\frac{C_1}{K_t} \right) (S + 1)}{S} \cdot \frac{\frac{K_f}{A^2}}{\left(\frac{MC_1}{A^2} \right) S^2 + \left(\frac{MK_f}{A^2} \right) S + 1} \quad (\text{Equation 3})$$

Where: F_d = the driving force

M = surface mass

X_s = surface motion

V = total volume of oil in actuator

$$C_1 = \frac{\beta V}{4}$$

K_f = pressure feedback gain in unit flow rate/unit pressure

β = bulk modulus of oil

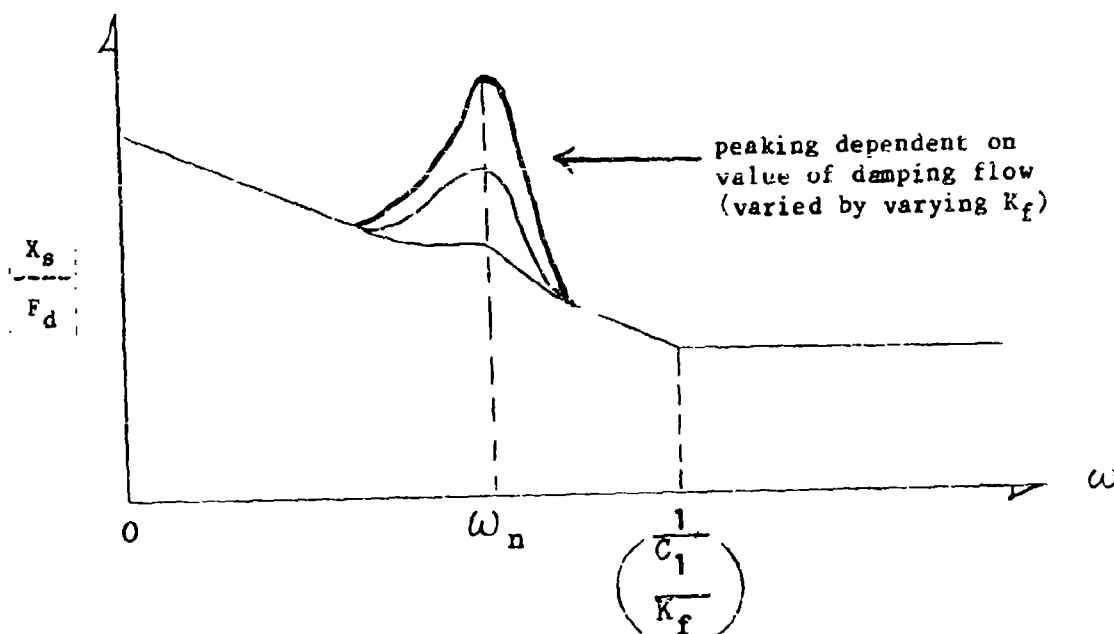
S = Laplace Operator

Note: The right hand term of Equation 3 is the normal second order transfer function with:

$$\omega_n = \sqrt{\frac{A^2}{MC_1}}, \quad \delta = \frac{K_f}{2A} \sqrt{\frac{M}{C_1}}$$

This shows that the damping is varied by changing the pressure feedback gain K_f .

Sketching the amplitude response indicated by the transfer function of Equation 3 for $\frac{X_s}{F_d}$ with load pressure feedback:



Note: the rising amplitude below $\omega = 1/(C_1/K_f)$ occurs because no washout circuit was included in the derivation. The section following shows that the washout circuit eliminates the rising low frequency characteristic.

Actuator and Surface Mass Response with Load Pressure Feedback Plus Washout Circuit

Consider a low frequency washout circuit in the AP feedback of the form:

Where: $\left(\frac{K_W S}{rS + 1} \right)$ = the washout circuit

(Equation 4)

r = washout rolloff time constant

K_W = washout circuit gain

Combining Equation 4 and 3, the equation of motion is:

$$\frac{X_s}{F_d} = \frac{(C_1 + K_f) \left(\frac{C_1 r}{C_1 + K_f} \frac{S + 1}{S + 1} \right)}{MC_1 r S^3 + M(C_1 + K_f) S^2 + A^2 r S + A^2} \quad \text{(Equation 5)}$$

Where: $K_f = K_f K_W$

F_d = the driving force

M = surface mass

x_s = surface motion

β = bulk modulus of oil

A = actuator drive area

S = Laplace Operator

r = washout time constant

K_W = washout gain

K_f = pressure feedback gain (flow rate/psi)

Note: This transfer function is of the form:

$$\frac{X_s}{F_d} = \frac{K (T_1 S + 1)}{(T_2 S + 1) \left(\frac{S^2}{\omega_n^2} + \frac{2\delta S}{\omega_n} \right) + 1} \quad \text{(Equation 6)}$$

which for $T_1 = T_2$ reduces to a simple second order function. This indicates that the washout circuit can be used to eliminate the rise in amplitude of X_g/F_d that occurs without the washout circuit at low frequencies.

Washout Transfer Function Description

In the analysis of the load pressure feedback transfer functions, the washout transfer function was not defined in terms of physical parameters. The operation of the washout circuit is apparent from the Flutter Damper Schematic, Figure 26. The isolation piston eliminates feeding steady differential load pressures to the damping spool. As the load pressure varies sinusoidally with increasing frequency, the isolation piston movement creates a flow. At low frequencies, the flow from the isolation piston goes primarily through the washout orifice R_2 . As the frequency of the load pressure variation continues to increase, the damping spool moves.

The equation of motion for the $X_{sp}/\Delta P$ is:

$$\frac{X_{sp}}{\Delta P} = \frac{\frac{A_1^2 R_2 A_2}{K_1 K_2} S}{\left(\frac{R_2 A_2^2 K_1 + K_2 A_1 R_2}{K_1 K_2} \right) S + 1} \quad (\text{Equation 7})$$

Which is of the form $\frac{K_\omega S}{r S + 1}$ as used in Equation 4.

Where: ΔP = load pressure drop across actuator piston

X_{sp} = damping spool position

A_1 = isolation piston drive area

A_2 = damping spool drive area

X_{ip} = position of isolation piston

R_2 = washout orifice resistance

K_1 = isolation piston spring rate

K_2 = damping spool spring rate

S = Laplace Operator

Note: The damping orifice in the hardware configuration will port the actuator piston alternately to pressure and return. The porting to pressure and return

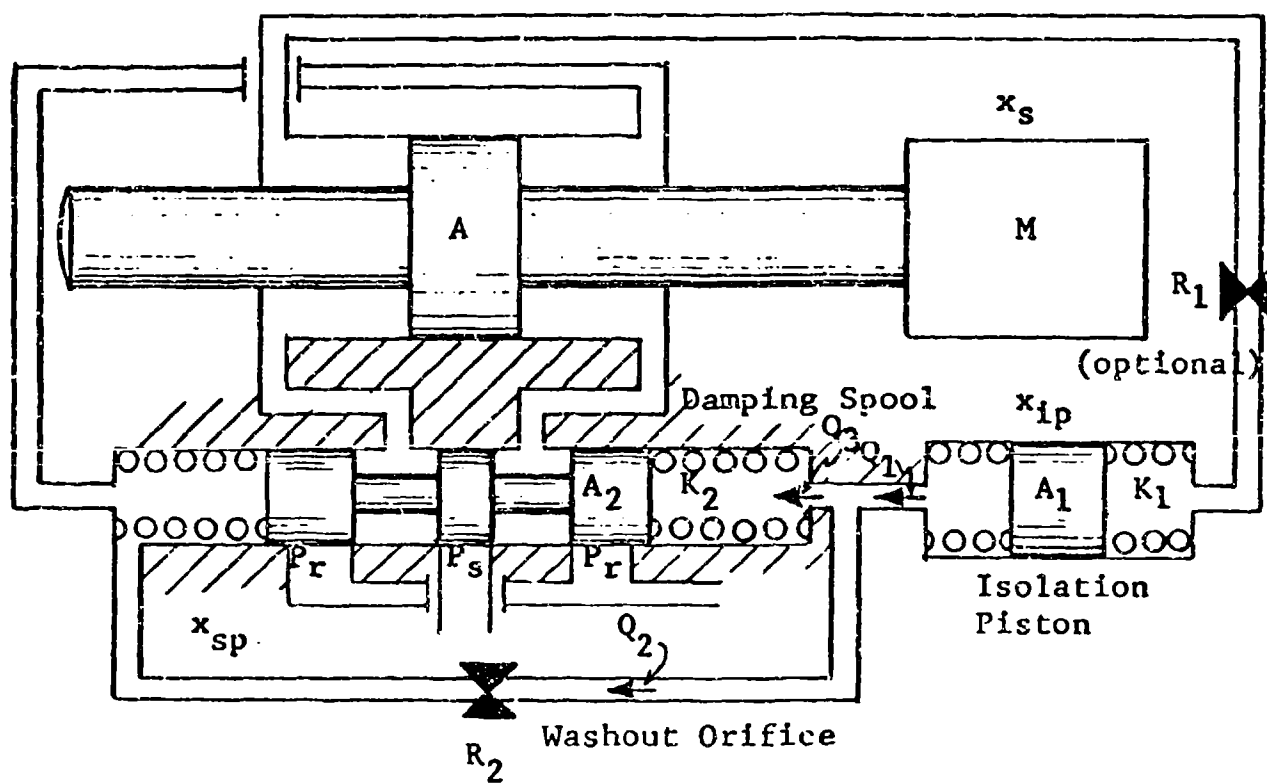


Figure 26. Hydromechanical Damping Circuit Schematic

piston alternately to pressure and return. The porting to pressure and return is required to maintain correct polarity of the pressure feedback when operating with a bias load applied to the actuator piston.

F-4 Stabilator Actuator Sizing Calculations

The following general data for the normal F-4E stabilator actuator and control surface is used in the example calculations:

a. The torsional resonant frequency of the stabilator surface on the stabilator actuator with both sections of the actuator pressurized is nominally 23 Hz. (The frequency varies from 21.65 to 23.55 Hz according to AFFDL-TR-71-20, Supplement 2, pages 217 and 218.)

b. The actuator drive area for each half of the F-4E actuator is approximately 6.0 in².

c. At frequencies above 1.5 Hz, the normal F-4E stabilator actuator stiffness is approximately 200,000 lbs/in (for one half of the actuator pressurized, according to measured data from AFFDL-TR-72-13, page 190).

d. The normal maximum hinge moment requirement for maneuvering of the F-4E is 8,600 lbs at the actuator at 6.9 in/sec rate (according to AFFDL-TR-71-20, Supplement 3, page 179).

The following calculations illustrate the procedure for determining the pressure feedback gain for damping the torsional resonance of the F-4E stabilator with a reduced area actuator. Additional calculations for the other parameters of the damping circuit are published in AFFDL-TR-75-29.

a. Calculation of the F-4E Stabilator Actuator Inertia Load

From the resonant frequency of 23 Hz and the stiffness of 400,000 lbs/in (both halves of the actuator pressurized), the surface mass as seen by the actuator is calculated as 19.14 lbs sec/in² (simple spring-mass resonance).

b. Calculation of the Actuator Drive Area

The worst case hinge moment requirement of the stabilator actuator is 8,600 lbs at 6.9 in/sec. Allowing 2,500 psi across the piston, 500 psi drop across the control valve, the maneuvering force can be generated with 3.44 in² drive area with only one hydraulic system operating. This is a considerable reduction from the 6.0 in² drive area normally used in the F-4E stabilator actuator.

c. Calculation of the New Torsional Resonance Frequency

Reducing the drive area of the actuator also reduces the stiffness and hence the torsional resonance frequency. For one half of the actuator pressurized, the surface resonance frequency with 3.44 in² drive area and one system operating will be 12.31 Hz and is calculated as follows:

Stiffness Reduction

$$\frac{\Delta F}{\Delta x} = 200,000 \left(\frac{3.44}{6.00} \right)$$

$$= 114,666 \text{ lbs/in}$$

New Torsional Resonant Frequency

$$F_n = 23 \sqrt{\frac{114,666}{400,000}}$$

$$F_n = 12.31 \text{ Hz}$$

d. Calculation of the Pressure Feedback Gain for a Specific Damping Ratio

For the pressure feedback gain K_f , consider equation 3 for the surface motion/driving force with pressure feedback (but without the washout circuit included):

$$\frac{X_s}{F_d} = \frac{\left(\frac{C_1}{K_f} s + 1 \right)}{s} \cdot \frac{\left(\frac{K_f}{A_2} \right)}{\left(\frac{MC_1}{A^2} \right) s^2 + \left(\frac{MK_f}{A^2} \right) s + 1}$$

The coefficient of the S term in the denominator of the above equation corresponds to the $2\delta/\omega_n$ term of a standard second order transfer function, where ω_n is the resonance frequency, δ is the damping ratio. Therefore, equating the coefficients and substituting in the following values allows solving for the pressure feedback gain:

$$\text{For: } A = 3.44 \text{ in}^2$$

$$\delta = 1.0 \text{ (critically damped)}$$

$$M = 19.15 \text{ lbs sec/in}^2$$

$$f_t = 12.31 \text{ Hz}$$

$$\frac{2\delta}{\omega_n} = \frac{MK_f}{A^2}$$

$$[K_f = 0.016 \text{ in}^3/\text{sec}/\text{lbs}/\text{in}^2]$$

F-4E Damping Circuit Summary

Figure 27 is a hardware photograph showing the incorporation of the damper circuits into an F-4E stabilator power actuator as add-on modules. The modified actuator is illustrated in comparison to the standard F-4E. Note that the damper package is composed of two identical damper circuits mounted immediately under the control valve package.

The damping circuit and actuator values used for the add-on module hardware are the following:

Actuator drive area	$A = 3.44 \text{ in}^2$
Damping spool diameter	$= 0.312 \text{ in}$
Isolation spool diameter	$= 0.312 \text{ in}$
Damping spool spring rate	$K_2 = 1050 \text{ lbs/in}$
Isolation spool spring rate	$K_1 = 1050 \text{ lbs/in}$
Washout orifice resistance	$R_1 = 1419 \text{ lbs/in}^2/\text{in}^3/\text{sec.}$
Rolloff orifice resistance	$R_2 = 567.6 \text{ lbs/in}^2/\text{in}^3/\text{sec.}$
Normal damping ratio	$= 1.0$
Rolloff break frequency	$= 100 \text{ Hz}$
Pressure feedback gain	$K_f = 0.016 \text{ in}^3/\text{sec}/\text{lbs/in}^2$

The above values, with two exceptions, were used for the integrated control valve package. The exceptions involved pod diameter and centering spring sizing.

Optimized Flutter Suppression Actuator Description

Figure 28 is a photograph of the optimized flutter damping package installed on the same reduced drive area actuator body as shown previously in Figure 27 with the add-on damping modules. In contrast to the add-on adapter plate and damping modules shown in Figure 27, the integrated control body incorporates the normal F-4E control components in the same body which holds the operating components of the damping circuit.

From the evaluation of the previous test results with the add-on damping modules, it was decided in the design of the integrated control package to:

- a. Increase the active drive area of the damping and isolation spools.
- b. Increase the damping flow porting to provide a higher damping flow gain.

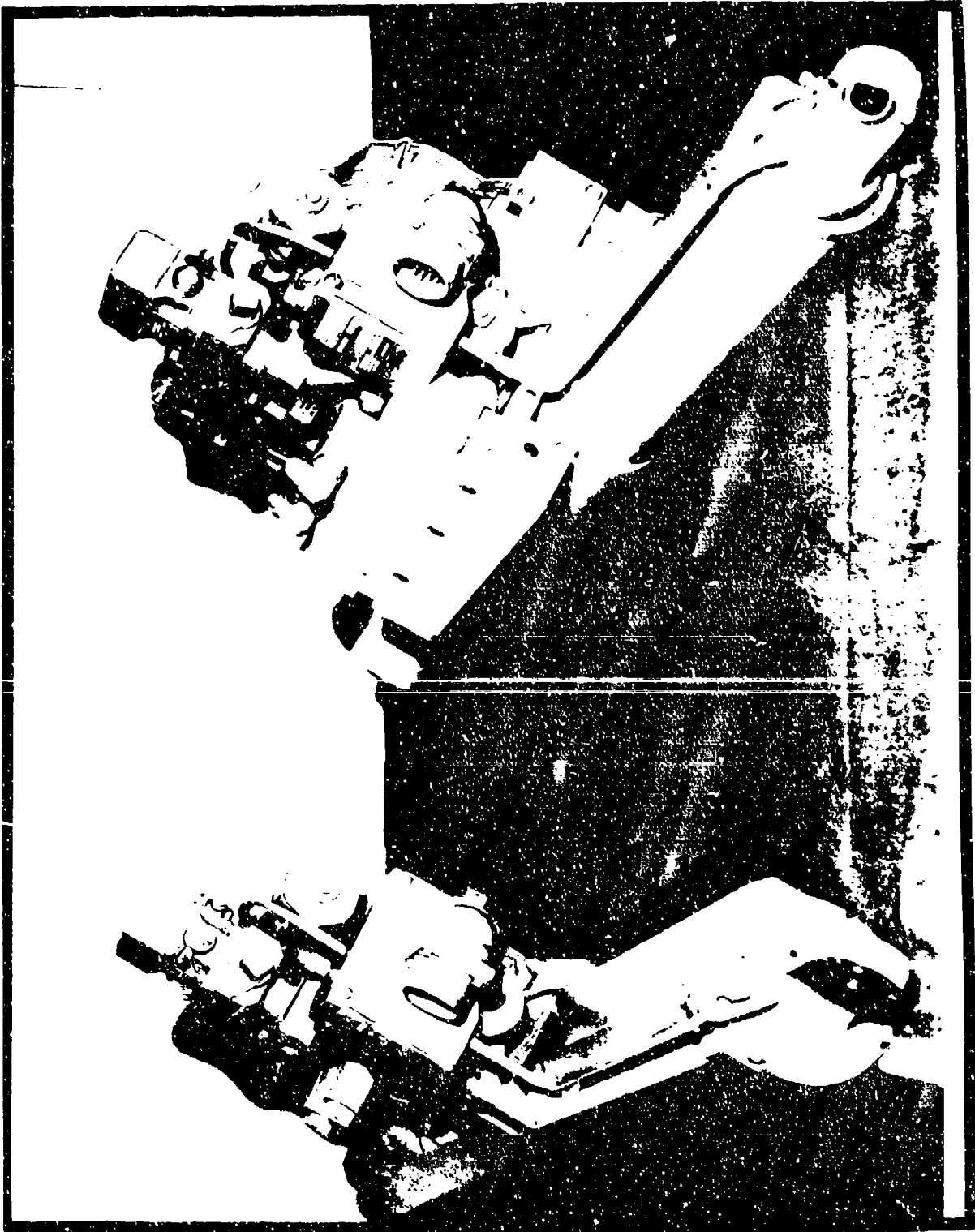


Figure 27. Modified F-4 Actuator With Add-on Damping Modules

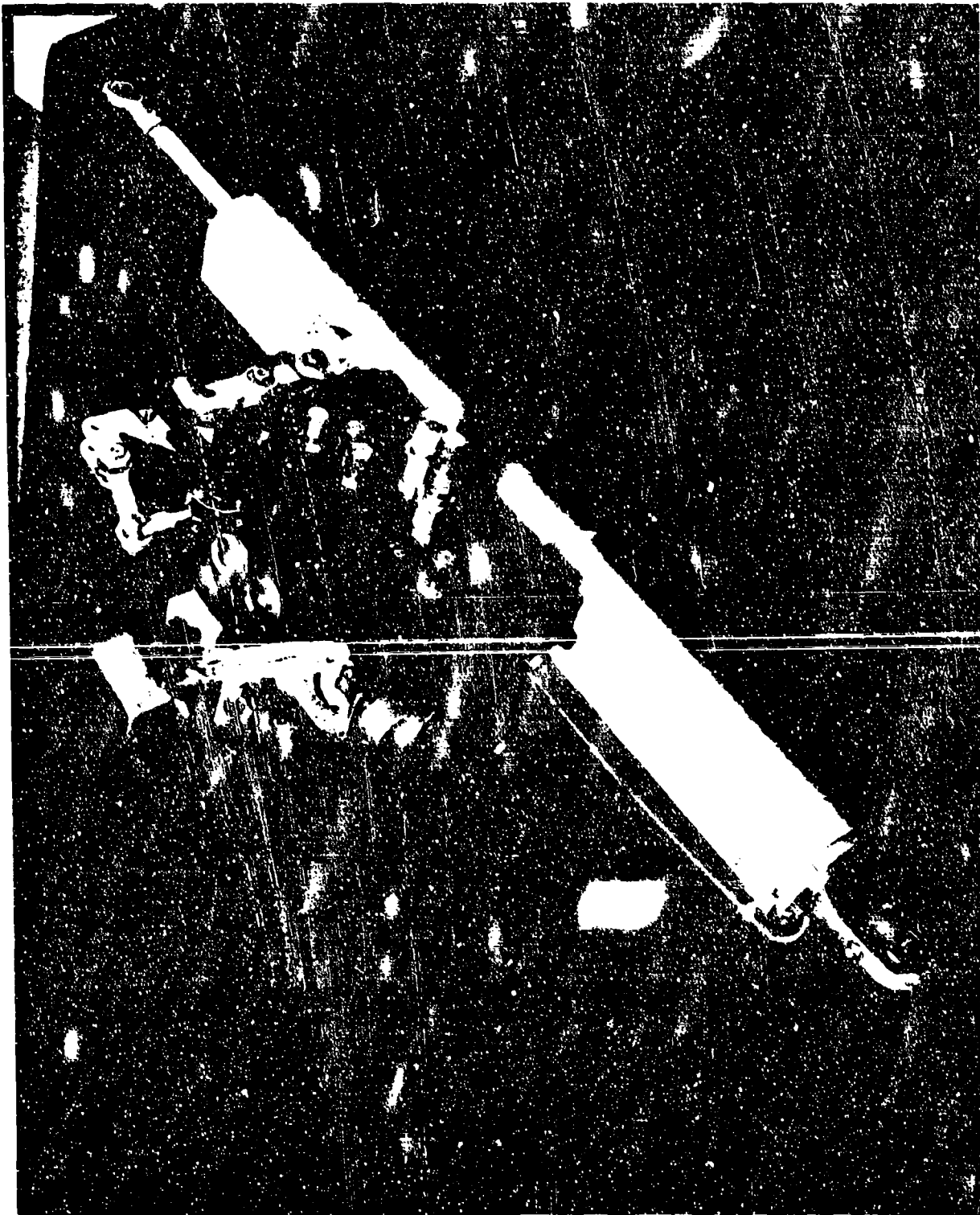


Figure 28. Modified F-4 Actuator With Integrated Control Package

In designing the control package, the porting passages through the damping module were kept as short and as large as practical. The following subassemblies from the standard F-4E stabilator were used without change:

1. Pilot input linkage assembly
2. Lock-out valve assembly
3. Auxiliary servo ram assembly
4. Servo and by-pass valve package

The basic requirement in designing the package was to duplicate the exact functions of the original control valve package with the addition of the damping modules as part of the valve body. This included providing the three different operational modes of:

1. Manual mode
2. Series servo mode
3. Parallel auto-pilot servo mode

Two solenoid operated hydraulic switching valves are incorporated to provide the above modes of operation on receiving the appropriate signals from the pilot.

The damping module design values for the damping module components were:

Damping Spool Diameter	0.438 in
Isolation Spool Diameter	0.438 in
Damping Spool Centering Spring Rate	2,250 lbs/in
Isolation Spool Centering Spring Rate	2,250 lbs/in
Nominal Damping Ratio	2
Washout Break Frequency	5 Hz
Rolloff Break Frequency	100 Hz
Pressure Feedback Gain (min)	0.032 in ³ /sec/psi

In comparing the design sizes for the integrated control damper with the add-on module values, it is apparent that the damping spool and isolation piston diameters have been increased to give a spool drive area approximately twice the add-on module valve. This was done to reduce the threshold on the operation of the damping circuit. The spring rate of the centering springs was correspondingly increased by a factor of two in order to keep the stroke of the isolation piston and damping spool strokes at the original value. In addition to the damping spool diameter change, the porting area of the flow slots were doubled compared to the original modules. This was to give a margin of safety

on the measured damping and provide theoretically a damping ratio of 2 with the F-4E surface inertia and nominal resonant frequency of 12 Hz.

Figure 29 shows the end view of the integrated control housing body. The center section (between the 5 and 7 inch marks on the scale in Figure 29) housed the normal F-4E stabilator control components. The position of the body to the right and left of the center section houses the damping circuit components. The general appearance of the internal damping components (damping spools, isolation pistons, centering springs and sleeve) were similar to those used in the non-integrated damping modules. (Reference page 7 and 8 of the AFFDL-TR-79-3317 report.)

Figure 30 shows the side view of the integrated control housing body. The P_1 and R_1 port connections are located as shown in this figure. The P_2 and R_2 ports are located on the opposite face of the body (the back face as shown in Figure 30). Note that smaller ports labeled P_1 , P_2 , P_3 , C_1 and C_2 are also provided on this face of the integrated body. These ports were used as instrumentation ports during testing and setup of the damping circuit powered by the P_1 hydraulic system. A similar set of ports was included on the opposite face for the damping circuit powered by the P_2 hydraulic system.

General Test Procedure

For the evaluation of the integrated control package performance, the package and reduced drive area actuator were mounted in the general purpose actuator test rig (GPATR). In measuring the damping module response, the GPATR was used as a simple holding fixture. For the measurement of the flow response of the damping circuit, the GPATR was used for providing dynamic loading of the stabilator actuator. The tests conducted on the stabilator actuator with the integrated control package were limited to verifying operation of the damping circuits. The tests were similar to those used to investigate the operation of the damping circuit of the module units (as reported in AFFDL-TR-79-3117). The performance of the normal F-4E stabilator actuator components used in the control package was not recorded as part of the test program.

Figure 33 shows the reduced drive area actuator and control package mounted in the GPATR for evaluation. The load actuator applies a load to the left end of the actuator as shown in the Figure 33. The F-4 stabilator actuator is a moving body actuator where the motion of the actuator follows the motion of the input linkage. As shown in Figure 33, the input linkage attach point was connected to the actuator rod which in turn was connected to the GPATR framework. Note that in Figure 33, there is a servovalve on a small manifold block located immediately below the modified F-4E actuator. The servovalve was connected to the damping module as a dynamic pressure source for setup of the damping circuit washout orifice. Note also that in Figure 33, the mechanical input summing linkage includes an additional motion summing linkage from a normal F-4E actuator. This linkage was added because in the initial operation of the control package and modified actuator, it was discovered that the flow porting from the normal F-4 control valve to the actuator cylinder ports had been reversed. The additional linkage corrected for the porting error. Although the internal control package modification to correct the porting error was straight forward, the input linkage reversal was the most efficient modification for the evaluation testing.

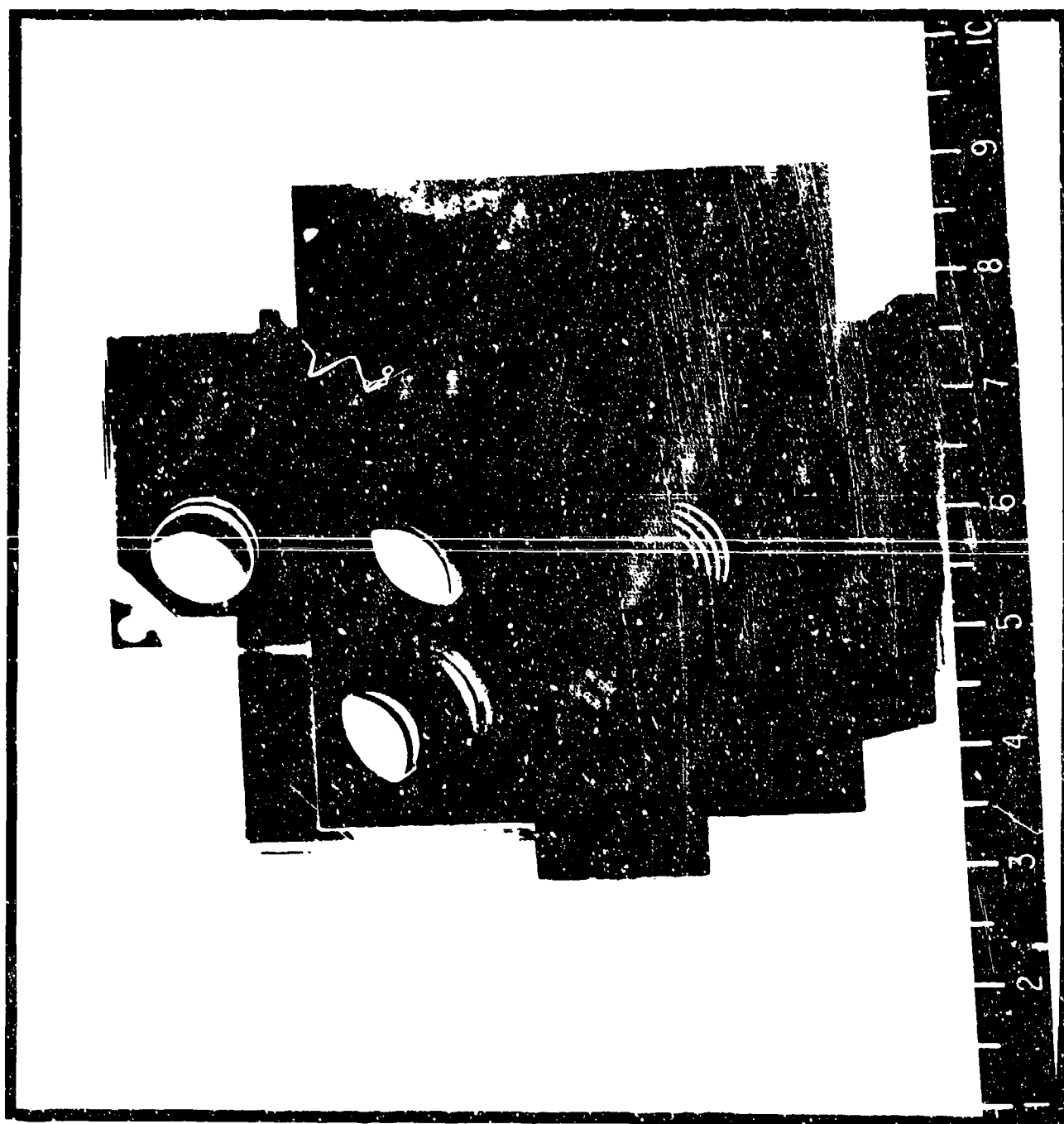


Figure 29. Integrated Control Package Housing (End View)

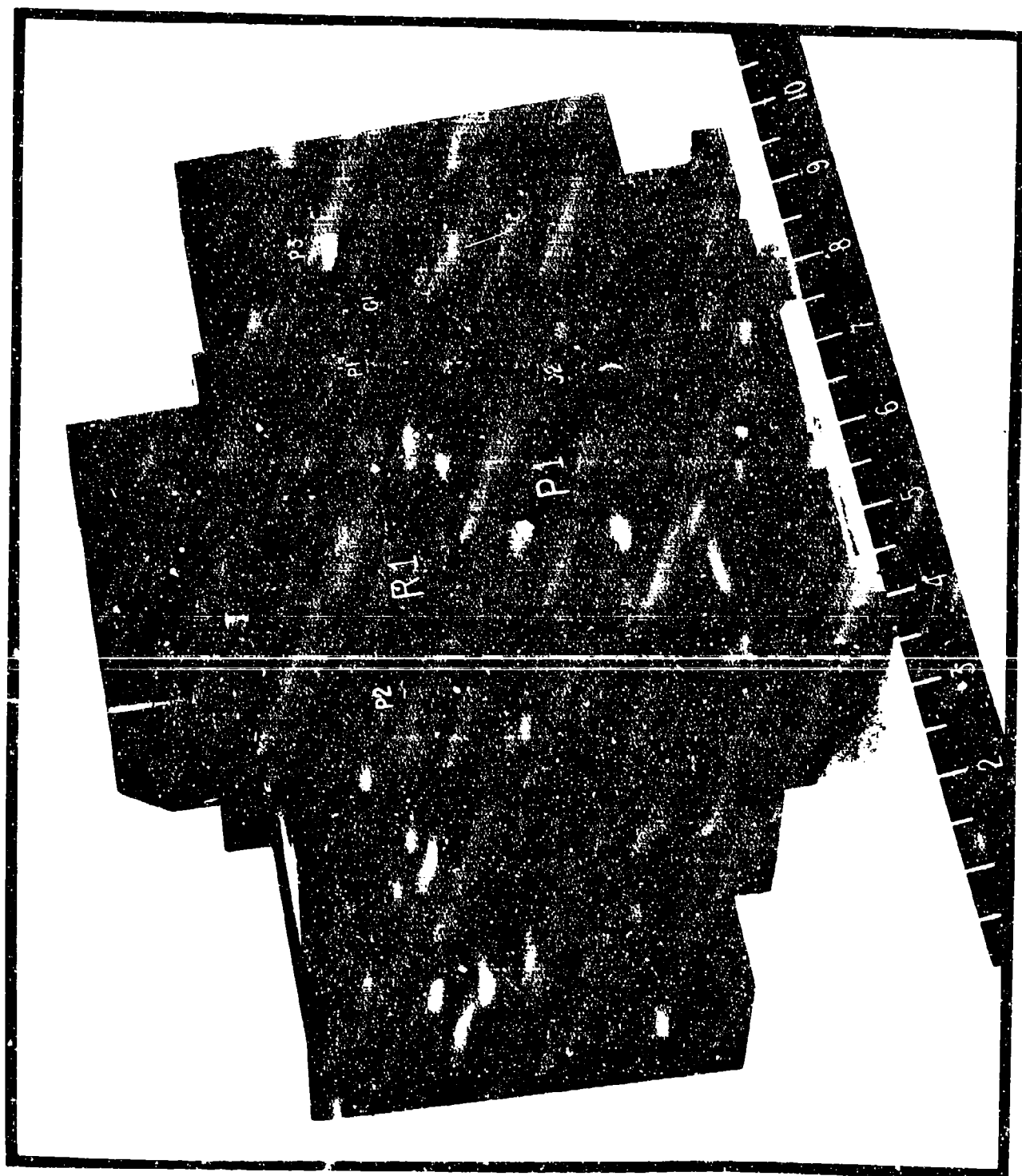
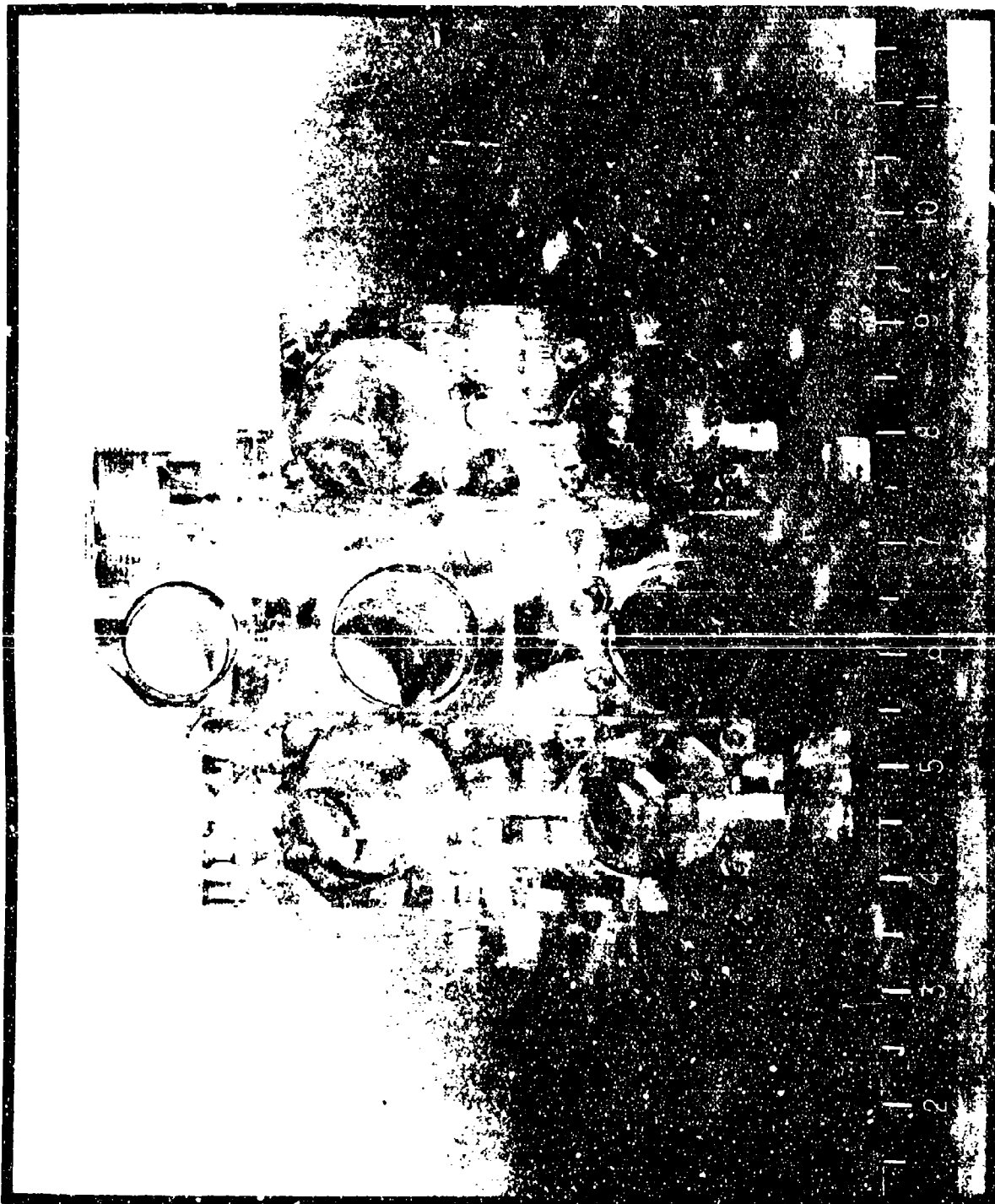


Figure 39. Integrated Control Package housing (side view)



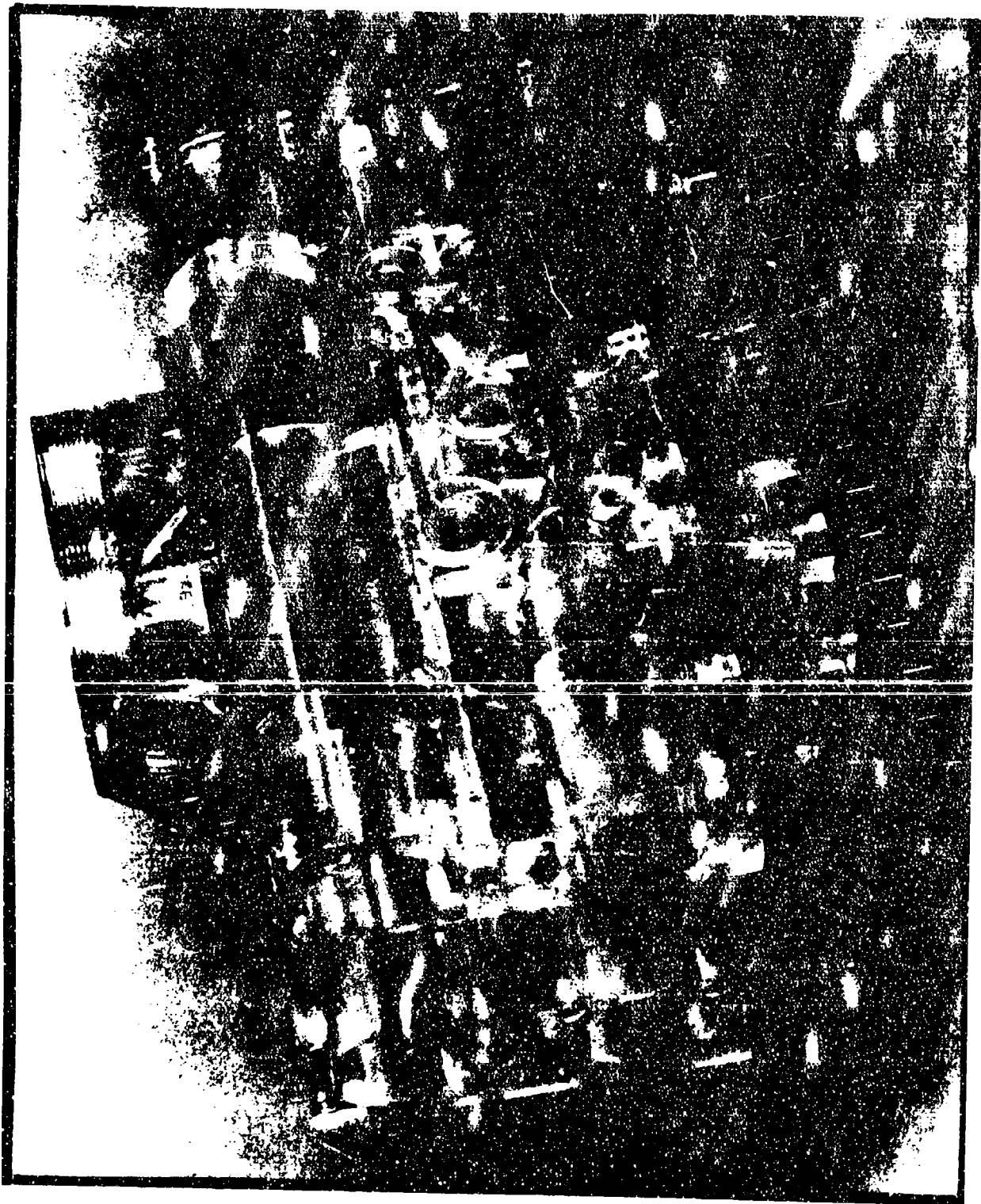
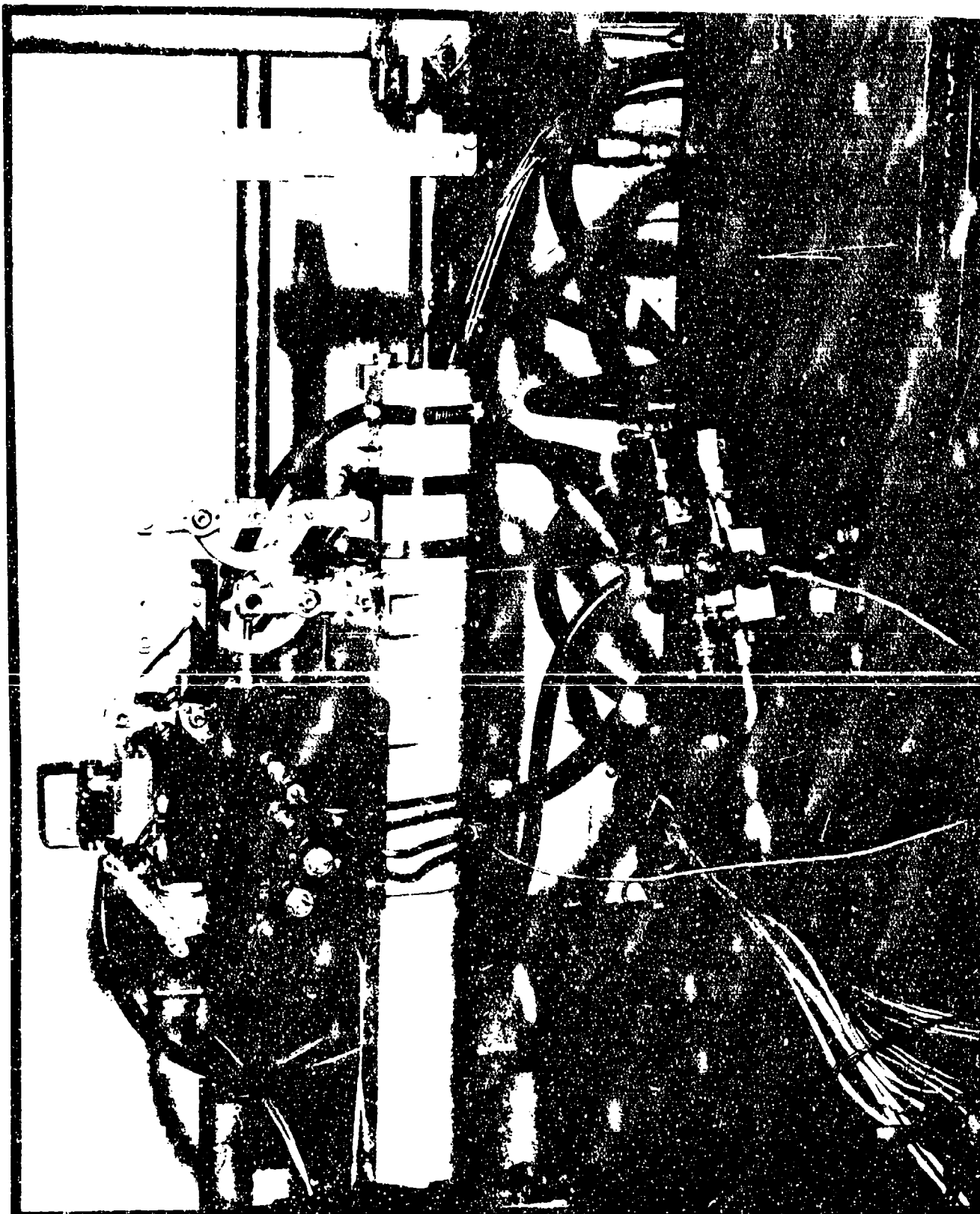


Figure 32. Plastic Machining Aid or Control
Package Housing (Side View)



Isolation and Damping Spool Differential Pressure Response

Figure 34 is a schematic of the test setup used to record the differential pressure response across the damping spool and isolation piston. Note that a servovalve with a pressure gain reducing orifice across its cylinder ports was used to create the excitation differential pressure across the isolation pistons-damping spool combination. For these tests, the roll-off orifices used in the cylinder port lines from the actuator drive area to damping circuit were shut off. The cylinder port output lines from the servovalve were connected to the C_1 , C_2 or C_3 , C_4 test ports in order to generate the test input differential pressures. Differential pressure transducers connected across the isolation piston and damping spool were used to measure the pressures across as a function of input frequency. Each damping circuit was evaluated independently. For the section of the actuator not being measured, the supply pressure was turned off and the cylinder ports connected to atmosphere. The BAFCO response analyzer and XYY' plotter were used to measure and record the amplitude and phase of the differential pressures compared to the total differential "cylinder port" pressure.

Figures 35 through Figure 40 show the isolation and damping differential response for the washout orifice setting adjusted to give the desired response. The response measurements of Figure 35 through Figure 37 are for the components in the damping section powered by the P_1 supply. Figure 38 through Figure 40 are measurements of the damping section powered by the P_2 supply. Each figure uses a different input excitation pressure in order to show the change in the response characteristics with a change in excitation level.

Figure 35 shows the response of the P_1 section with the applied differential pressure equivalent to an applied load to the actuator section of $\pm 1,720$ lbs. This load is 16.6% of the stall load on one half of the reduced drive area actuator with its drive area of 3.44 square inches. Note that 0 Db for the isolation piston is ± 500 psi. At low frequencies, the differential pressure across the damping spool is low and rises at a slope of 6 Db/octave with increasing frequency up to a frequency of 10 Hz. The differential pressure across the isolation piston decreases with increasing frequency. At frequencies above 10 Hz, the differential pressure across the isolation piston and the damping spool approach each other. Note that the phase angle of the damping spool starts out at a leading phase angle of greater than 40 degrees. The leading phase characteristic is consistent with the designed washout transfer function of $KS/(TS + 1)$. Note that the isolation piston differential pressure is nearly in phase with the applied pressure at 1 Hz. The damping spool differential pressure response is in phase within ± 10 degrees with the applied dynamic pressure from 10 to 18 Hz.

Figure 36 shows the response of the P_1 section with the applied load of $\pm 3,612$ lbs. This is nominally twice the excitation level used for Figure 35. The phase and amplitude characteristics of the damping spool differential pressures are similar to those shown on Figure 35. The phase angle of the damping spool pressure is a leading phase angle of 44 degrees at low frequencies (below 5 Hz). The amplitude of the damping spool pressure levels out above 10 Hz. The 2 to 1 input pressure excitation level change appears to have little effect on the response characteristics of damping spool and isolation piston.

Figure 37 shows the response characteristics of the P_1 damping section with an applied load of $\pm 6,192$ lbs. This is 60% of the stall load of the P_1 actuator

FLUTTER SUPPRESSION INVESTIGATION

Test: Isolation & Damping Δp Response
 Mode: P_1 Active - Orifice @ 3/4 Turns Open
 Load: +1,720 lbs.

Date: 16 November 1984

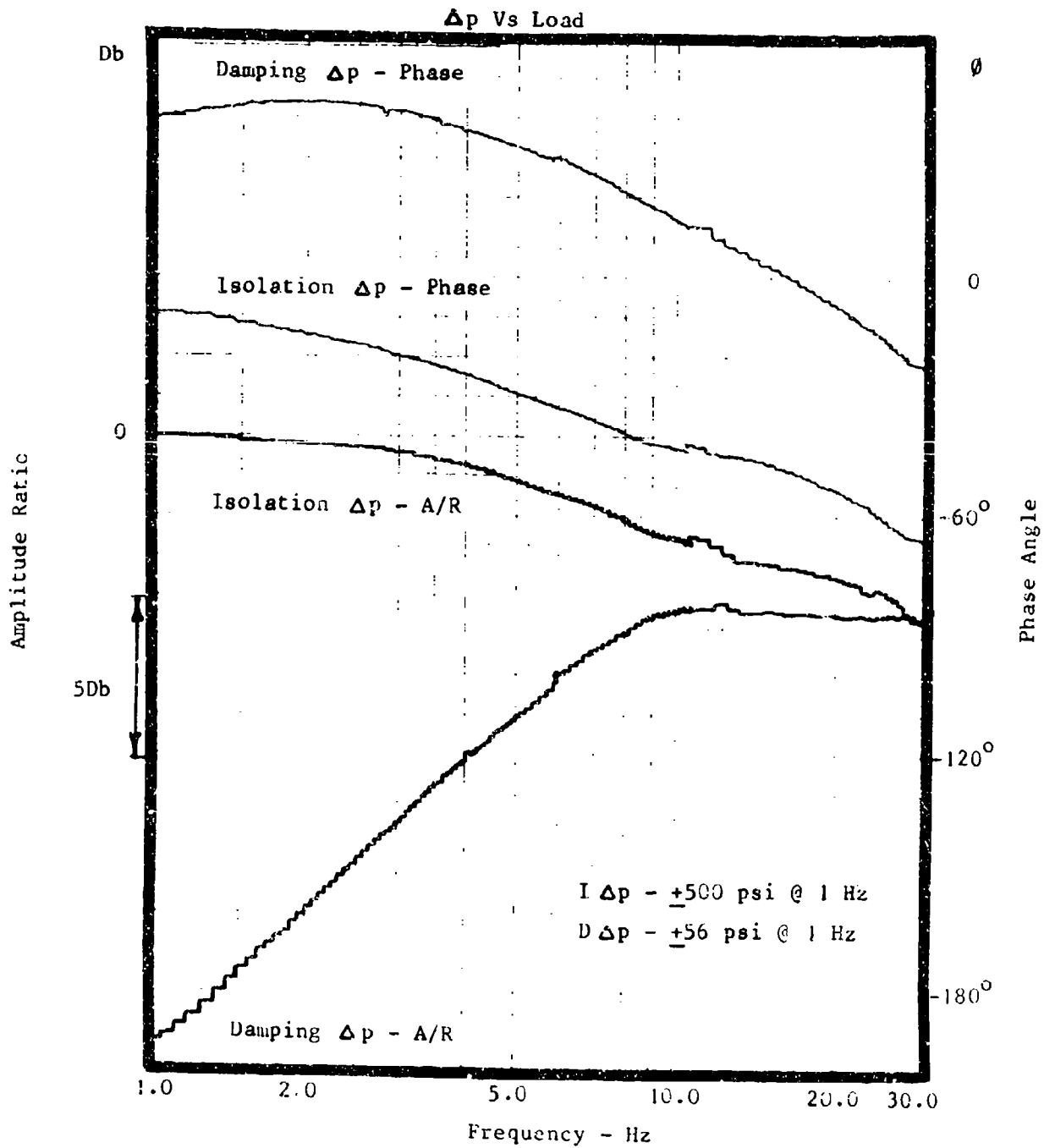


Figure 35. P_1 Isolation & Damping Δp Response at 1,720 Lb. Load

FLUTTER SUPPRESSION INVESTIGATION

Test: Isolation & Damping Δp Response
 Mode: P_1 Active - Orifice @ 3/4 Turns Open
 Load: +3,612 lbs

Date: 16 November 1984

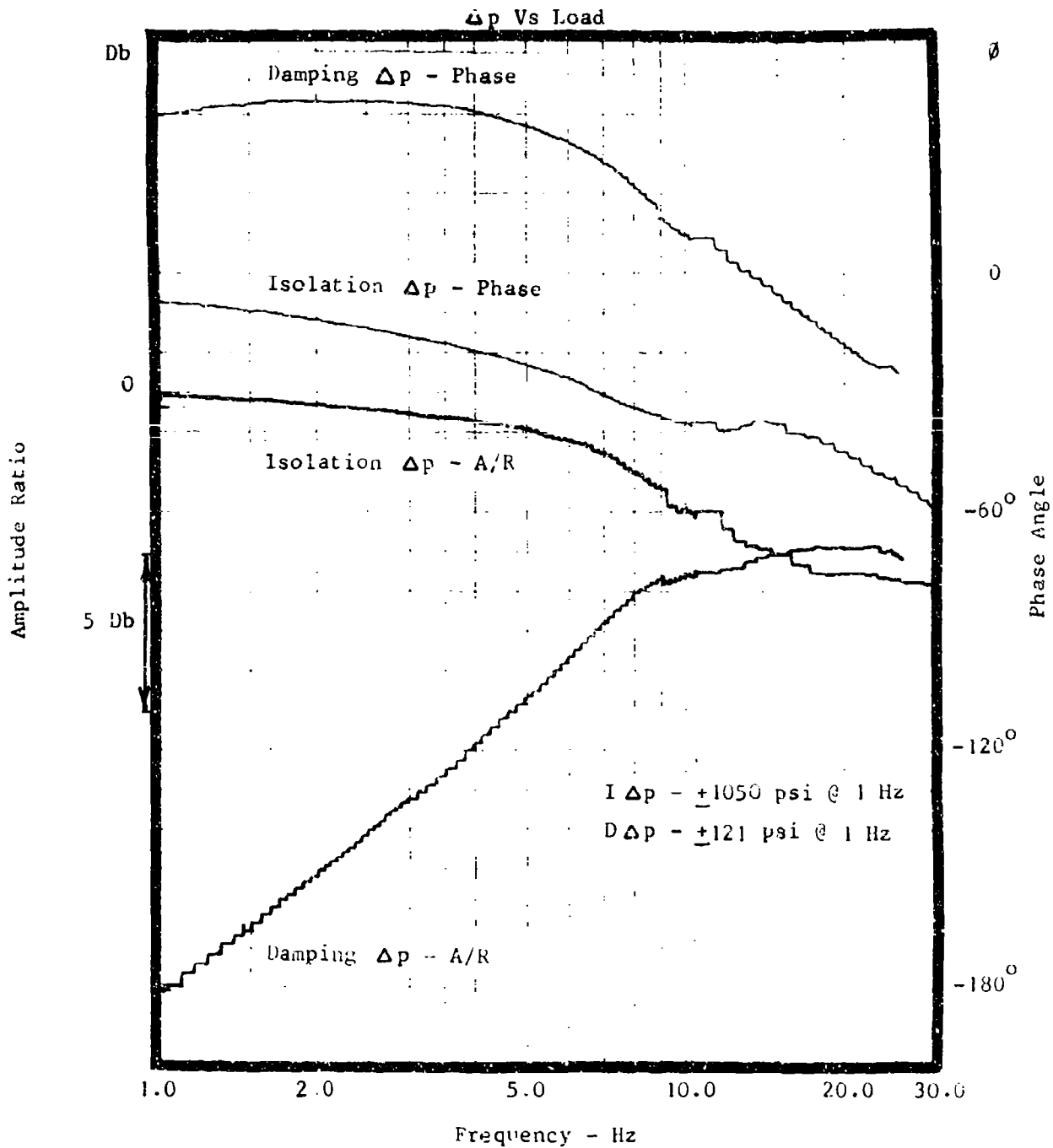


Figure 36. P_1 Isolation & Damping Δp Response at 3,612 Lb. Load

FLUTTER SUPPRESSION INVESTIGATION

Test: Isolation & Damping Δp Response
 Mode: P_1 Active -- Orifice @ 3/4 Turns Open
 Load: +6,192 lbs

Date: 16 November 1984

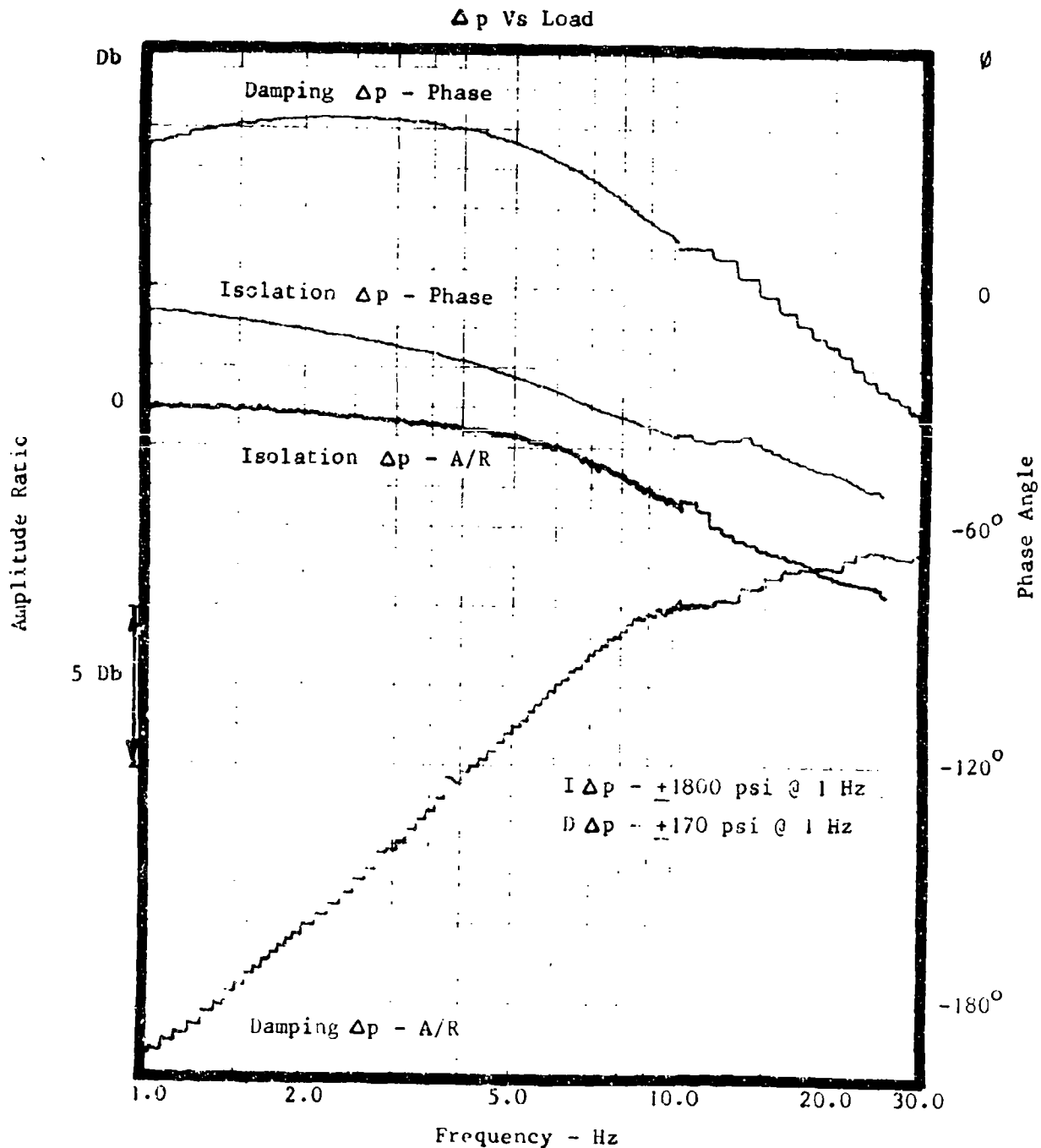


Figure 37. P_1 Isolation & Damping Δp Response at 6,192 Lb. Load

FLUTTER SUPPRESSION INVESTIGATION

Test: Isolation & Damping Δp Response
 Mode: P_2 Active - Orifice @ 3/4 Turns Open
 Load: +2,064 lbs.

Date: 16 November 1984

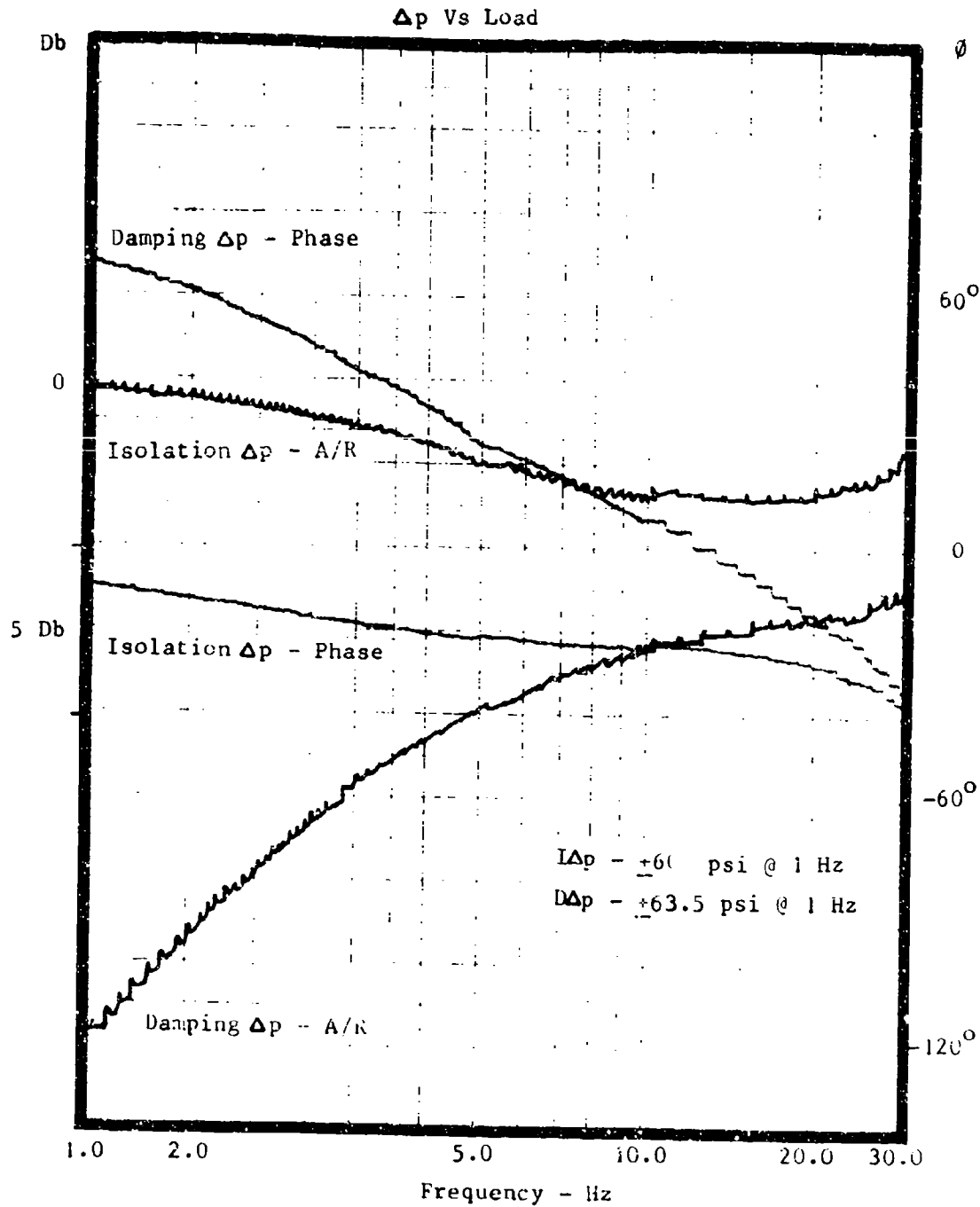


Figure 38. P_2 Isolation & Damping ΔP Response at 2,064 Lb. Load

FLUTTER SUPPRESSION INVESTIGATION

Test: Isolation & Damping Δp Response
 Mode: P₂ Active - Orifice @ 3/4 Turns Open
 Load: +3,784 lbs.

Date: 16 November 1984

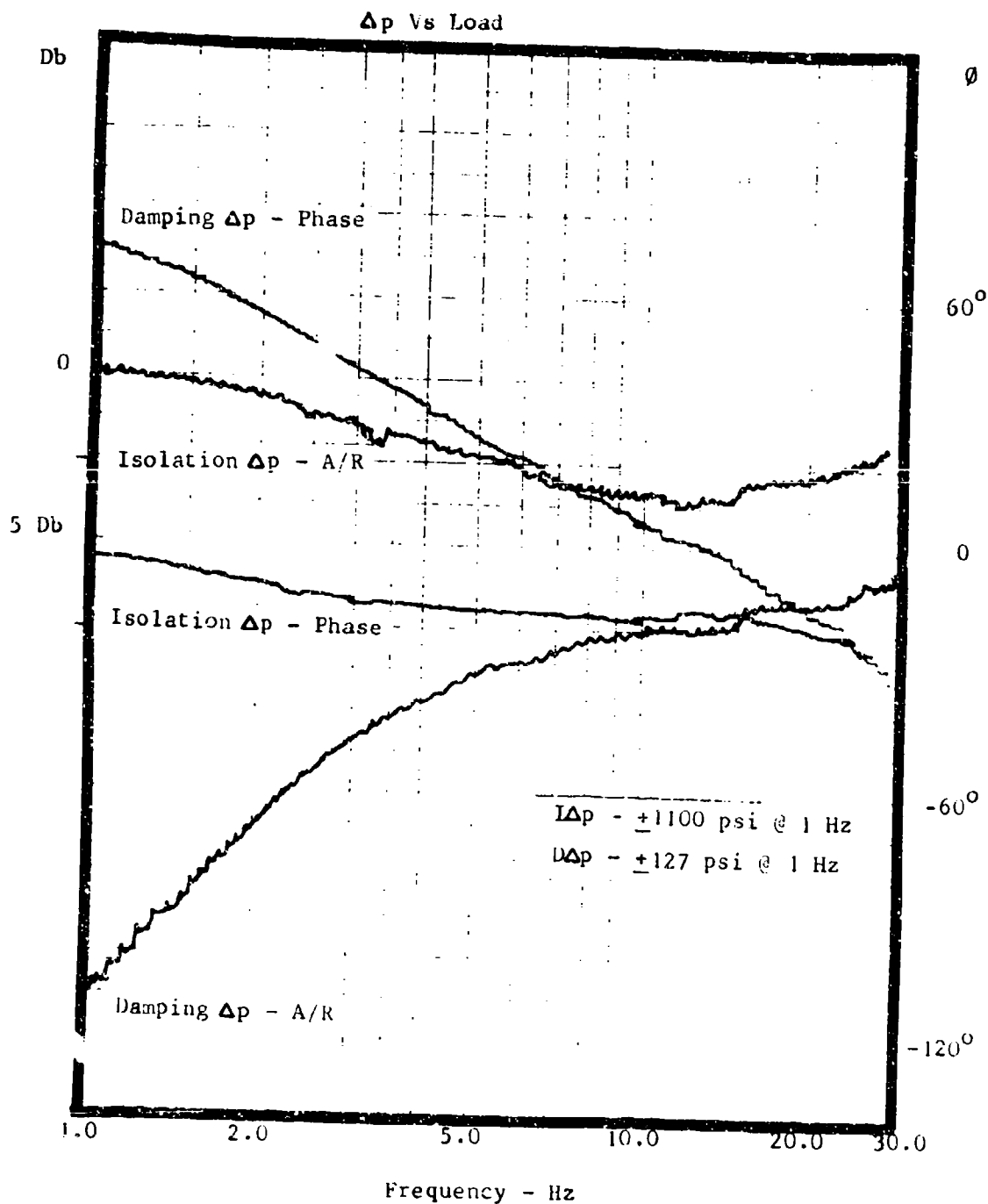


Figure 39. P₂ Isolation & Damping ΔP Response at 3,784 Lb. Load

FLUTTER SUPPRESSION INVESTIGATION

Test: Isolation & Damping Δp Response

Mode: P₂ Active - Orifice @ 3/4 Turns Open

Date: 16 November 1984

Load: +5,504 lbs.

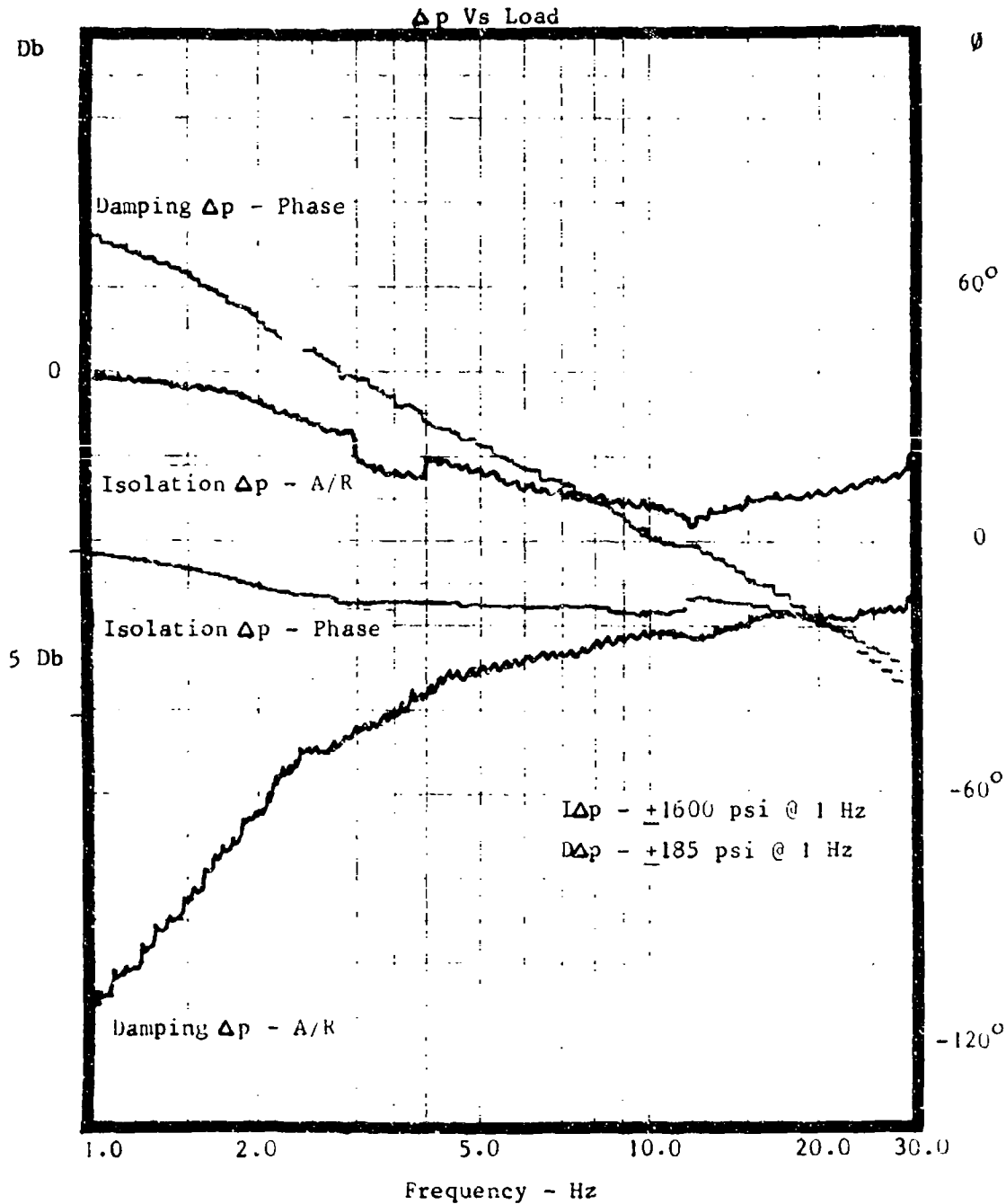


Figure 40. P₂ Isolation & Damping Δp Response at 5,504 Lb. Load

section. The response is quite similar to the other two P_1 response measurements at lower loads. The principal difference is the rise in the amplitude (1.5 Db) of the damping spool pressure over the frequency range of 10 to 30 Hz. At the lower excitation loads, the rise in amplitude over the same frequency range was from 0 to 1 Db.

Figures 38, 39 and 40 show the response curves of the P_2 damping section at different loads. The curves are similar to the P_1 section response curves with some minor differences.

Figure 38 shows the response of the P_2 damping section with excitation pressures equivalent to a P_2 actuator section load of $\pm 2,064$ lbs. Note that the damping phase leads the excitation phase by 68 degrees at 1 Hz. This phase lead is greater than that measured on the P_1 damping section at that frequency. However, over the frequency range of 10 to 16 Hz the phase angle of the damping spool pressure is within ± 10 degrees with the applied pressure. This is quite similar to the P_1 damping spool pressure phase characteristics of the P_1 section.

Figure 39 which shows the response of the P_2 damping section with an excitation load of $\pm 3,784$ lbs is similar to the response shown on Figure 38. The amplitude response of the damping spool pressure shows a break frequency of nominally 10 Hz. The amplitude response of the damping and isolation pressures of the P_2 section both show a slight amplitude rise above 20 Hz. This is different than that measured on the P_1 section where the amplitude either remained constant or attenuated slightly.

Figure 40 shows the response of the P_2 damping section with an excitation pressure corresponding to a P_2 actuator section load of $\pm 5,050$ lbs. The phase and amplitude response characteristics are similar to the other P_2 (and P_1) section pressure response measurements.

Individual Damping Section Dynamic Load Response

In order to verify the damping flow operation of the integrated control package installed on the modified stabilator actuator, both the GPATR load actuator as well as the servovalve pressure source were used. The GPATR load actuator was used to apply a dynamic load to the stabilator actuator. This allowed creating a differential pressure across the drive area of the stabilator actuator. This technique was used for several tests. In addition, the servovalve pressure source was used to drive the damping circuit with the circuit drive isolated from the cylinder ports. This allowed a comparison of the damping flow performance with both measurement techniques.

In making the damping flow gain measurements, the return line flow from the actuator section being evaluated was connected through a turbine flow meter. This allowed recording the flow from the integrated control package as the load system applied a dynamic load to the test actuator. In testing each of the damping sections, only the actuator half corresponding to the damping section being tested was pressurized. The other half of the actuator was bypassed and unpressurized. This allowed evaluating the performance characteristics of a single section of the control package without the interaction possible with two sections operating at the same time. The outputs of the turbine flow meter and the differential pressure transducer measuring the stabilator differential pressures were connected to a Brush chart recorder. The chart recorder data

(with correction for the dynamic characteristics of the turbine flowmeter) was used to generate the response plots of the damping flow gain (cis/psi) and phase as a function of frequency. The response plots obtained from the strip chart data are somewhat affected by waveform distortion and tend to be more irregular than those obtained from a response analyzer.

In evaluating the damping flow gain, the effect of the normal control valve on the damping flow response was evaluated. Under loaded conditions the motion of the actuator in response to loads causes the mechanical input control valve (which is connected to a ground point off the actuator) ports flow to oppose the actuator motion. The response of the control valve rolls off starting at a frequency of 2 Hz and would not be expected to affect the damping flow at 12 Hz and above. To verify this, for the servovalve pressure source tests the damping flow response measurements were made both with the input linkage attached to a ground point and the input linkage hand held at null.

Figure 41 is a plot of the strip chart data for damping section P_1 at a constant differential input pressure of $\pm 1,200$ psi across the damping spool and and isolation piston combination. This response measurement was conducted with the mechanical input linkage ungrounded and held at null in order to eliminate any dynamic flow contribution from the main control valve. Note that the flow response phase angle at low frequencies leads the phase angle at 10 Hz by nominally 60 degrees. The amplitude of the flow response increases up to a frequency of 10 Hz and then remains relatively constant from 10 to 30 Hz. The design amplitude ratio of 0.016 psi is met at 10 Hz and maintained from 10 to 30 Hz.

Figure 42 is a plot of the strip chart data for damping section P_1 at a constant differential input pressure of $\pm 1,200$ psi across the damping spool and and isolation piston combination. This is the same test as Figure 41 with the input linkage mechanically grounded to the GPATR frame. This attachment is similar to that when the actuator is mounted in the aircraft and allows any load induced actuator motion to create an opposing flow from the control valve (within its response capabilities). Note that except for the amplitude response of the damping flow in the response region from 0.5 to 2 Hz, Figure 42 resembles Figure 41. This verifies that the control valve interaction with the damping circuit is very slight.

Figure 43 is a plot of the P_2 section damping flow response strip chart data at the same input pressure differential of $\pm 1,200$ psi as Figure 42. The input linkage is grounded for the data used for Figure 43. The amplitude response characteristic is similar to that of Figure 42 with 0.016 cis/psi damping flow gain being obtained by 10 Hz and maintained to 30 Hz. The response below 10 Hz shows less roll off than the P_1 section, perhaps because of the particular setting of the washout orifice in this section.

Figure 44 is a plot of the damping flow response of section P_1 with the input linkage held at null. The applied damping circuit excitation pressure was $\pm 2,100$ psi (compared to the 3,000 psi supply pressure). The amplitude of the response remains nominally constant at the 0.016 cis/psi from 12 to 25 Hz.

Figure 45 is a plot of the damping flow response of section P_2 with the input linkage mechanically grounded to the GPATR frame. The applied damping circuit excitation pressure was $\pm 2,200$ psi, slightly greater than that used for Figure 44. The response of the P_2 section at frequencies above 8 Hz resembles that of

FLUTTER SUPPRESSION INVESTIGATION

Test: Flow Gain Response
 Mode: Damped - P₁ Active
 Load: +1200 psi (+4,128 lbs.)
 Input Linkage: Hand Held

Date: 9 October 1984

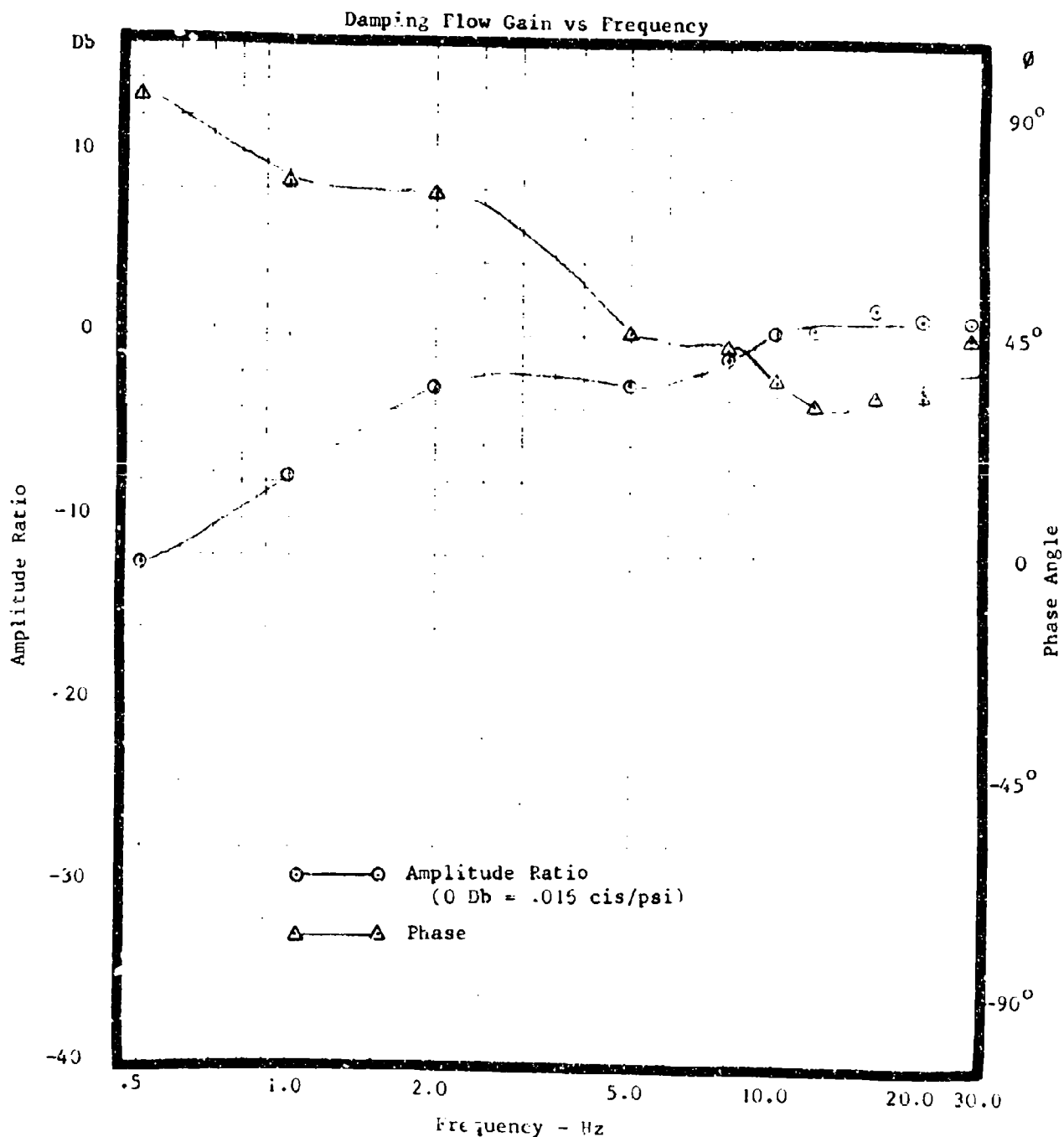


Figure 41. Damping Flow Response, P₁ Section, Hand Held Input.
 +1200 psi ΔP

FLUTTER SUPPRESSION INVESTIGATION

Test: Flow Gain Response
 Mode: Damped - P₁ Active
 Load: +1200 psi (+4,128 lbs.)
 Input Linkage: Mechanically Grounded

Date: 9 October 1984

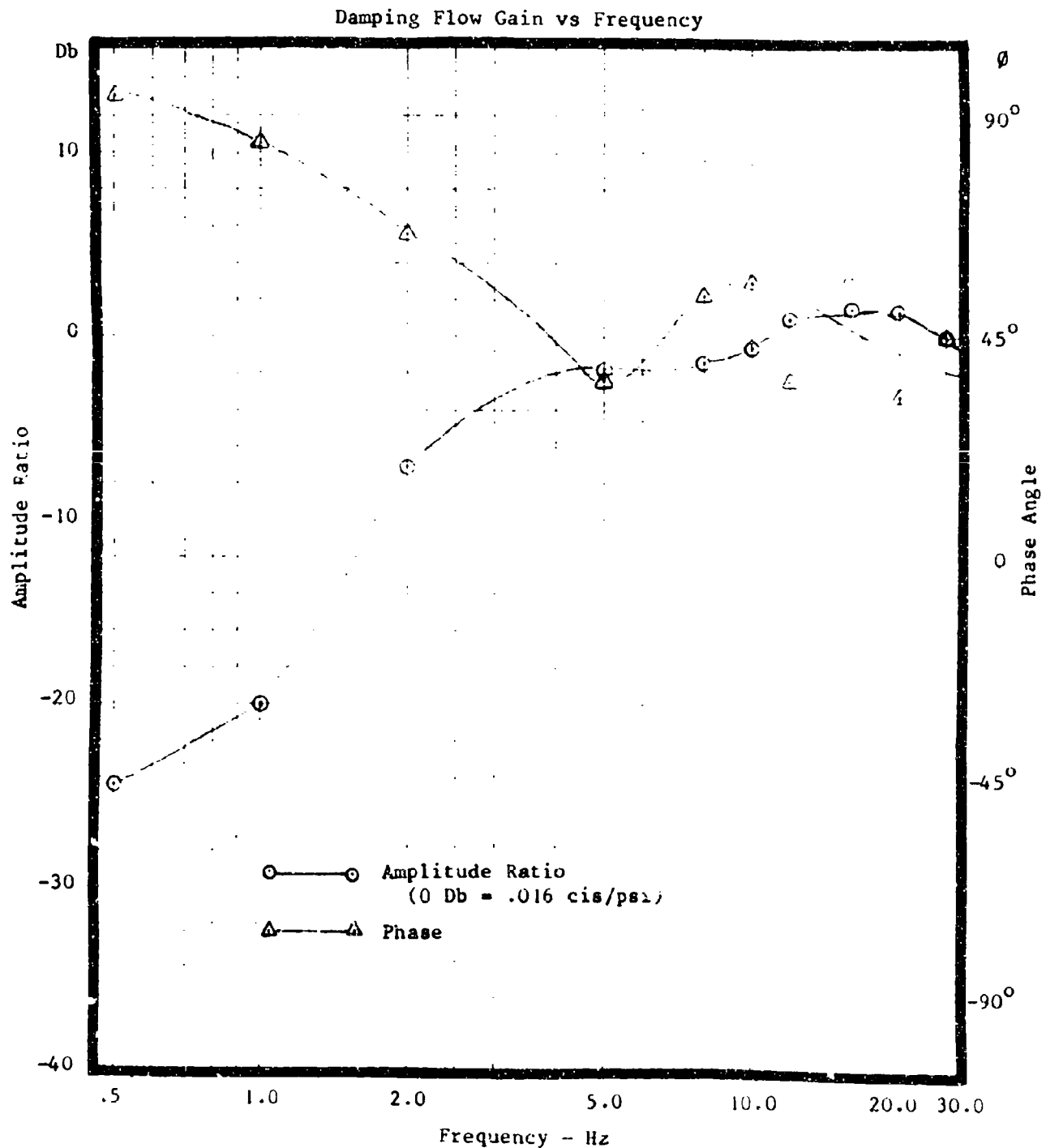


Figure 42. Damping Flow Response, P₁ Section,
 Mechanical Ground Input, +1200 psi ΔP

FLUTTER SUPPRESSION INVESTIGATION

Test: Flow Gain Response
 Mode: Damped - P_2 Active
 Load: +1200 psi (+4,128 lbs.)
 Input Linkage: Mechanically Grounded

Date: 9 October 1984

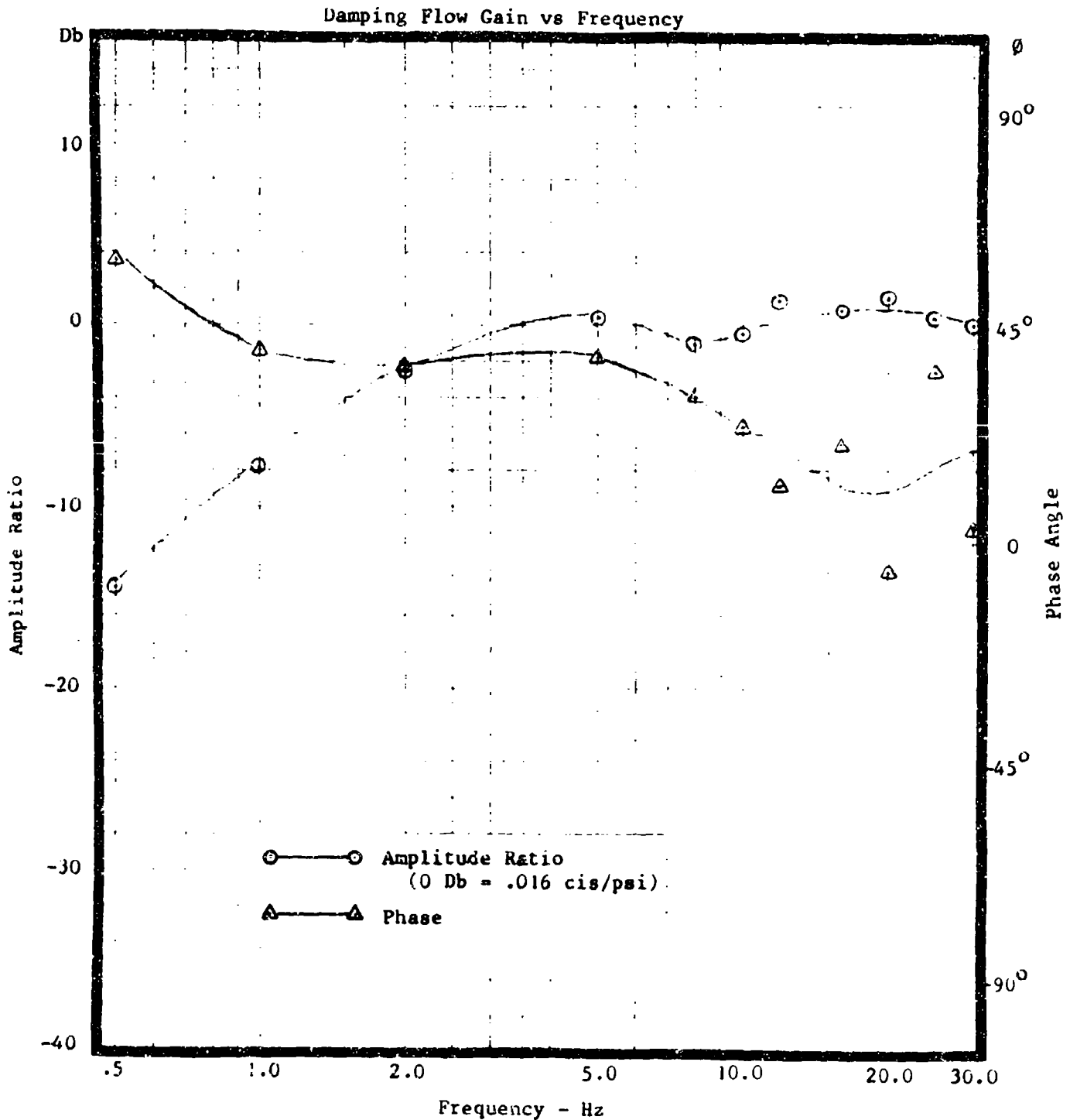


Figure 43. Damping Flow Response, P_2 Section, Mechanical Ground Input, +1200 psi ΔP

FLUTTER SUPPRESSION INVESTIGATION

Test: Flow Gain Response
 Mode: Damped - P_1 Active
 Load: +2100 psi (+7,224 lbs.)
 Input Linkage: Hand Held

Date: 9 October 1984

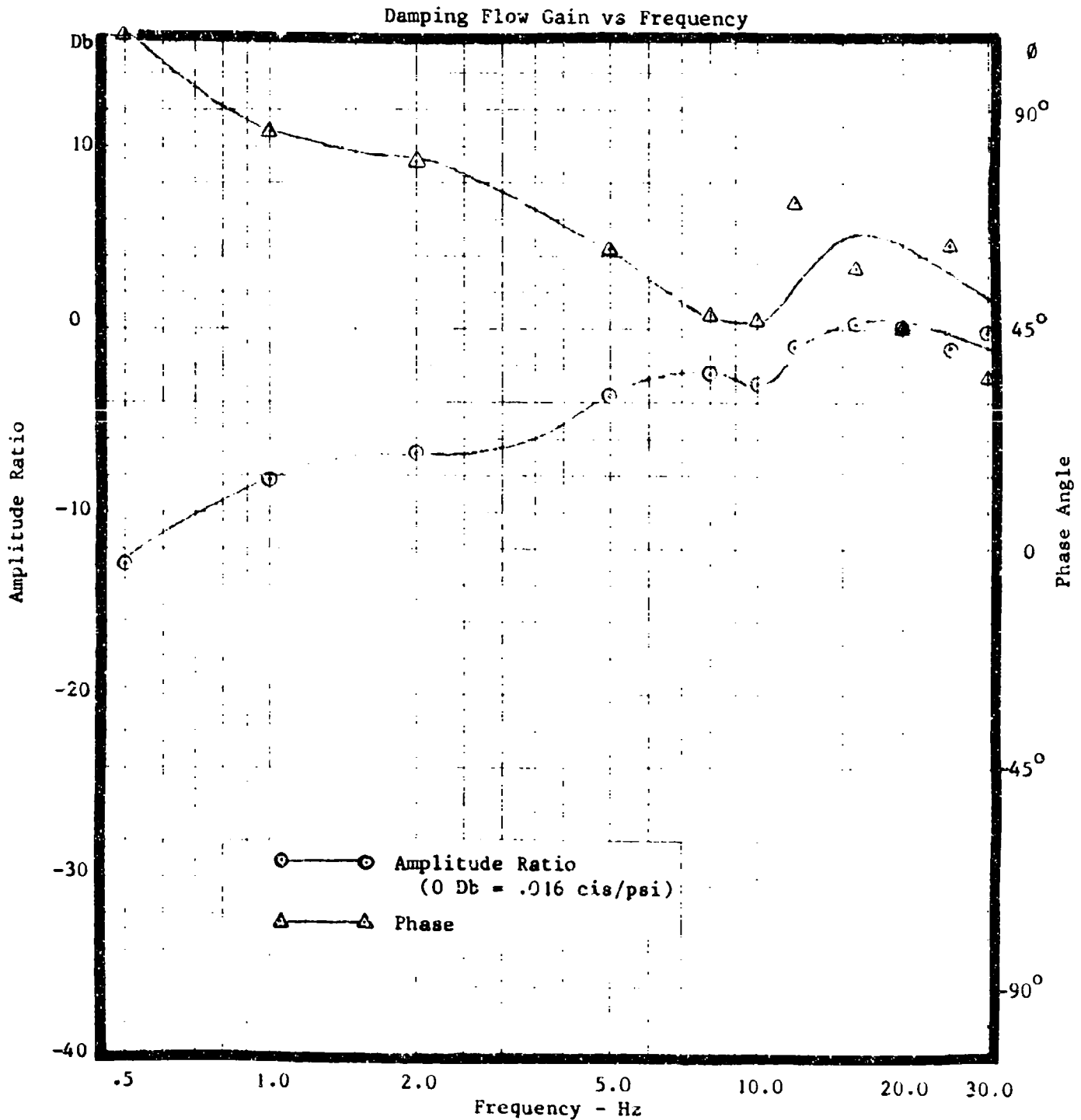


Figure 44. Damping Flow Response, P_1 Section, Hand Held Input, +2100 psi ΔP

FLUTTER SUPPRESSION INVESTIGATION

Test: Flow Gain Response
 Mode: Damped - P_2 Active
 Load: +2200 psi (7,568 lbs.)
 Input Linkage: Mechanically Grounded

Date: 9 October 1984

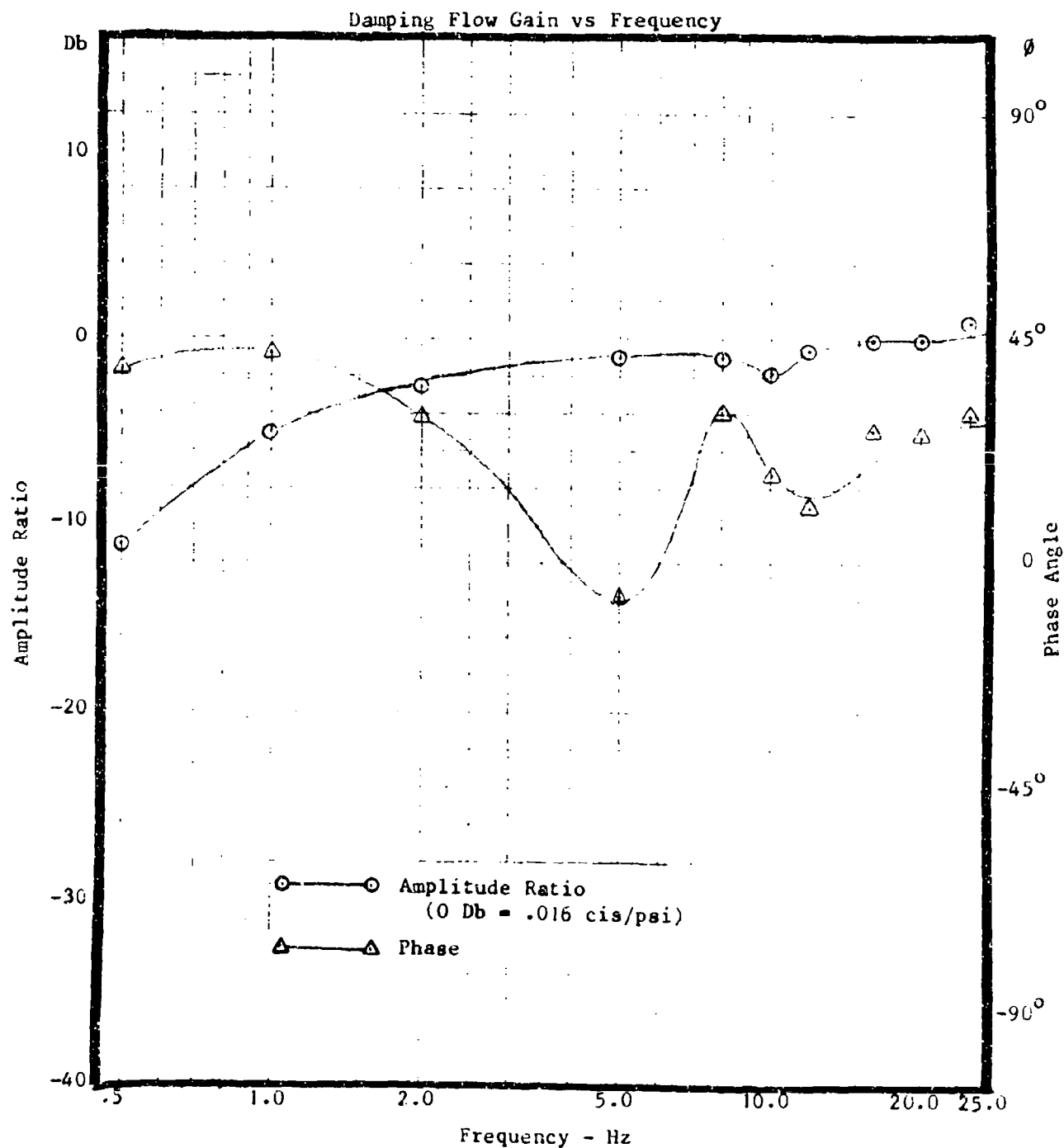


Figure 45. Damping Flow Response, P_2 Section, Mechanical Ground Input, +2200 psi ΔP

P₁ section at a similar excitation pressure. The amplitude response is almost identical. The phase response exhibits 15 degrees less phase lead than the P₁ section over the frequency range of 10 to 20 Hz. Below 8 Hz, the difference in response can be attributed to slightly different characteristics of the washout circuit operation and the difference in the input linkage grounding.

Figure 46 is a plot of the damping flow response with the load actuator generating the dynamic differential pressures in the stabilator actuator. This test includes the effect of the fluid transmission coupling from the actuator piston chambers to the damping circuit. The excitation force used creates a differential pressure of 581 psi across the damping circuit. For this test the input linkage was mechanically grounded. As shown in Figure 46, the damping circuit just meets the 0.016 cis/psi gain requirement at 12 Hz and is -4 Db from 15 to 30 Hz. The phase angle at 12 Hz is -15 degrees which is acceptable.

Figure 47 is a response plot of the damping flow for the P₂ section of the test actuator with the same test conditions as used to generate the data for Figure 46. The response of the P₂ section at the low load level of +2,000 lbs. is similar to that of the P₁ section. The amplitude of the damping flow gain is maintained out to 30 Hz which is slightly better than the P₁ section. However, the phase characteristics over the same frequency range are slightly worse (-20 degrees at 12 Hz vs -15 degrees).

Figure 48 is a response plot of the damping flow with the load actuator used to generate a dynamic load of +5,000 lbs over the test frequency range. The response of the P₁ section is shown. The amplitude response meets the 0.016 cis/psi design value from 5 to 20 Hz. The phase response is nominally 20 degrees leading over the 10 to 25 Hz frequency range. The response is similar to that measured at the +2,000 lb load level, indicating that the operation of the damping module is not greatly affected by the amplitude of the load pressure.

Figure 49 is a response plot of the damping flow for the P₂ section taken under the same test conditions as used for Figure 48. The P₂ section amplitude response is similar to the P₁ section at frequencies above 5 Hz. The P₂ section amplitude response attenuates less than the P₁ section at frequencies below 5 Hz. The phase response over the frequency range of interest (10 to 20 Hz) exhibits a little less lead (15 degrees) than the P₁ section.

The results of the flow gain response measurements showed that the design response gain of 0.016 cis/psi was maintained over the frequency range of 10 to 20 Hz by both damping settings and at load pressures from 581 psi to 2,200 psi. The input linkage coupling to the mechanical input control valve had minimal effect on the damping flow operation over the 10 to 30 Hz frequency range.

Dual Damping Sections Dynamic Load Response

In order to evaluate the damping response of both the P₁ and P₂ damping sections, the load actuator was used to apply a dynamic load to the modified F-4E stabilator actuator. The return line flows from the P₁ and P₂ actuator sections were connected together and passed through a turbine flowmeter. The output of the flowmeter and the load actuator force transducer were recorded on a strip chart recorder. The response of the return line flow to the load force was plotted from the strip chart data. For these tests, the input linkage was mechanically grounded to the GPATR framework.

FLUTTER SUPPRESSION INVESTIGATION

Test: Flow Gain Response
 Mode: Damped - P_1 Active
 Load: +2000 lbs. (+581 psi)
 Input Linkage: Mechanically Grounded

Date: 9 October 1984

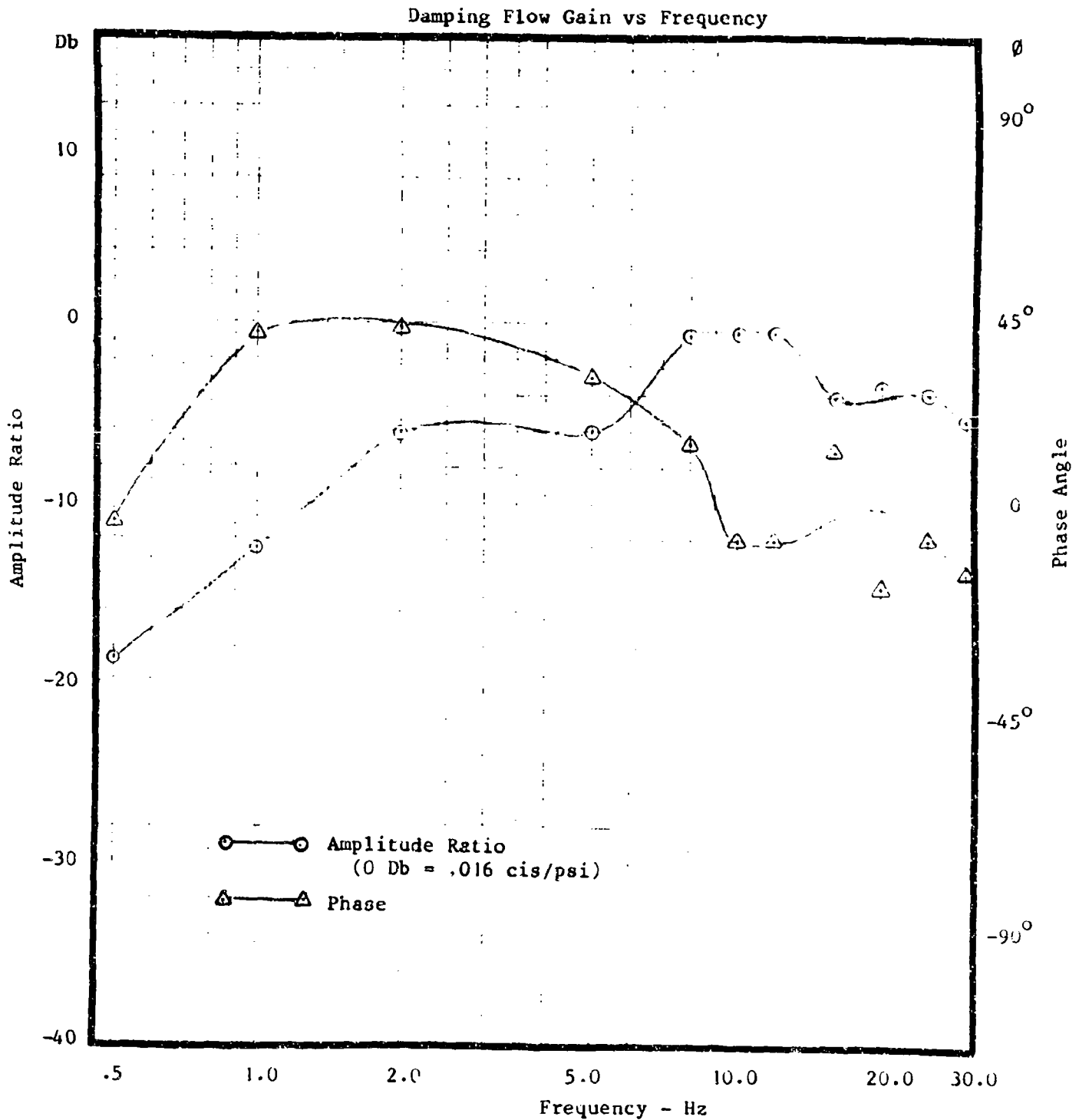


Figure 46. Damping Flow Response, P_1 Section, Mechanical Ground Input, +2000 lb. Load

FLUTT. . SUPPRESSION INVESTIGATION

Test: Flow Gain Response
 Mode: Damped - P_2 Active
 Load: +2000 lbs. (+581 psi)
 Input Linkage: Mechanically Grounded

Date: 9 October 1984

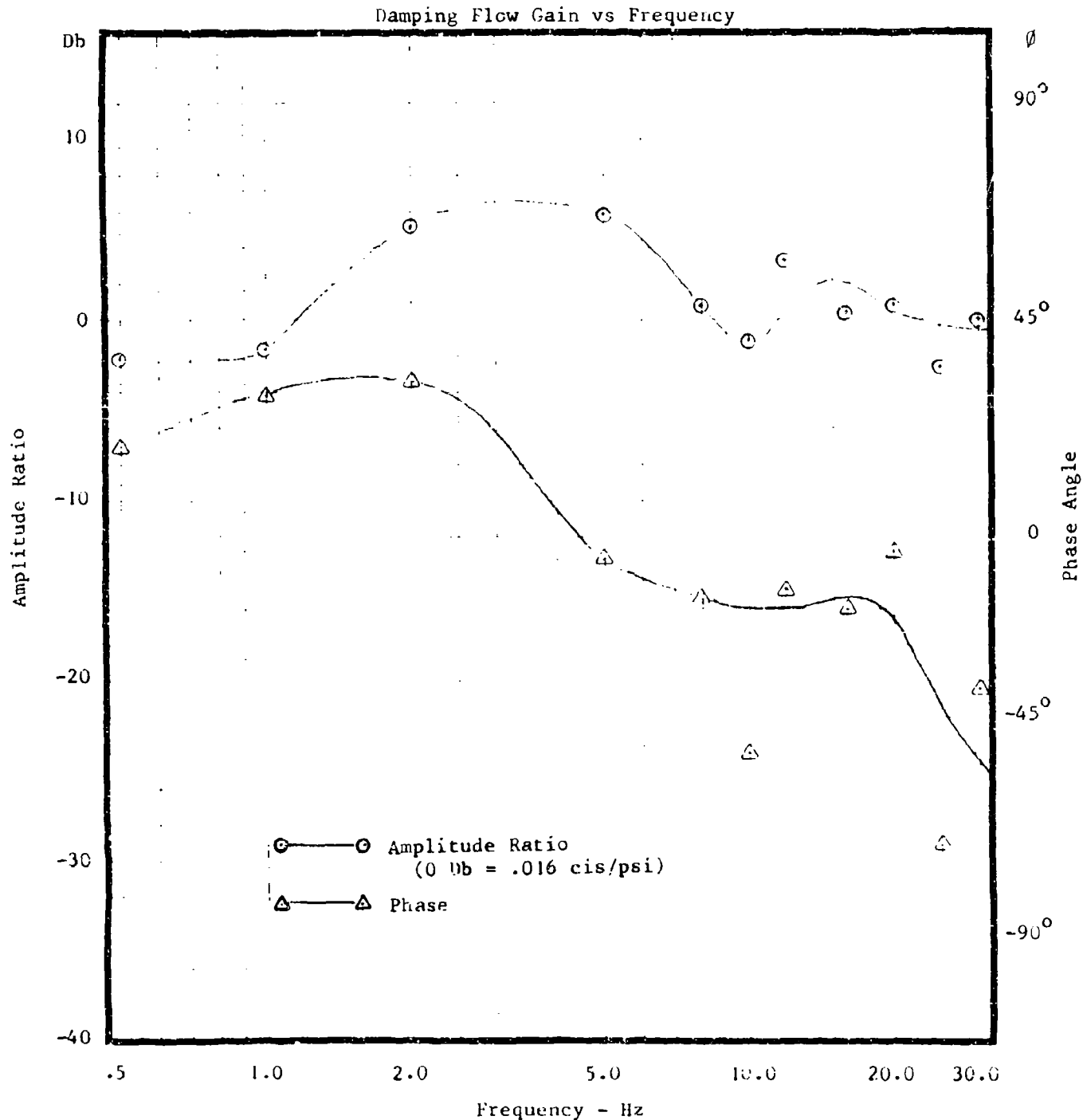


Figure 47. Damping Flow Response, P_2 Section, Mechanical Ground Input, +2000 lb. Load

FLUTTER SUPPRESSION INVESTIGATION

Test: Flow Gain Response
 Mode: Damped - P₁ Active
 Load: +5000 lbs. (+1,453 psi)
 Input Linkage: Mechanically Grounded

Date: 9 October 1984

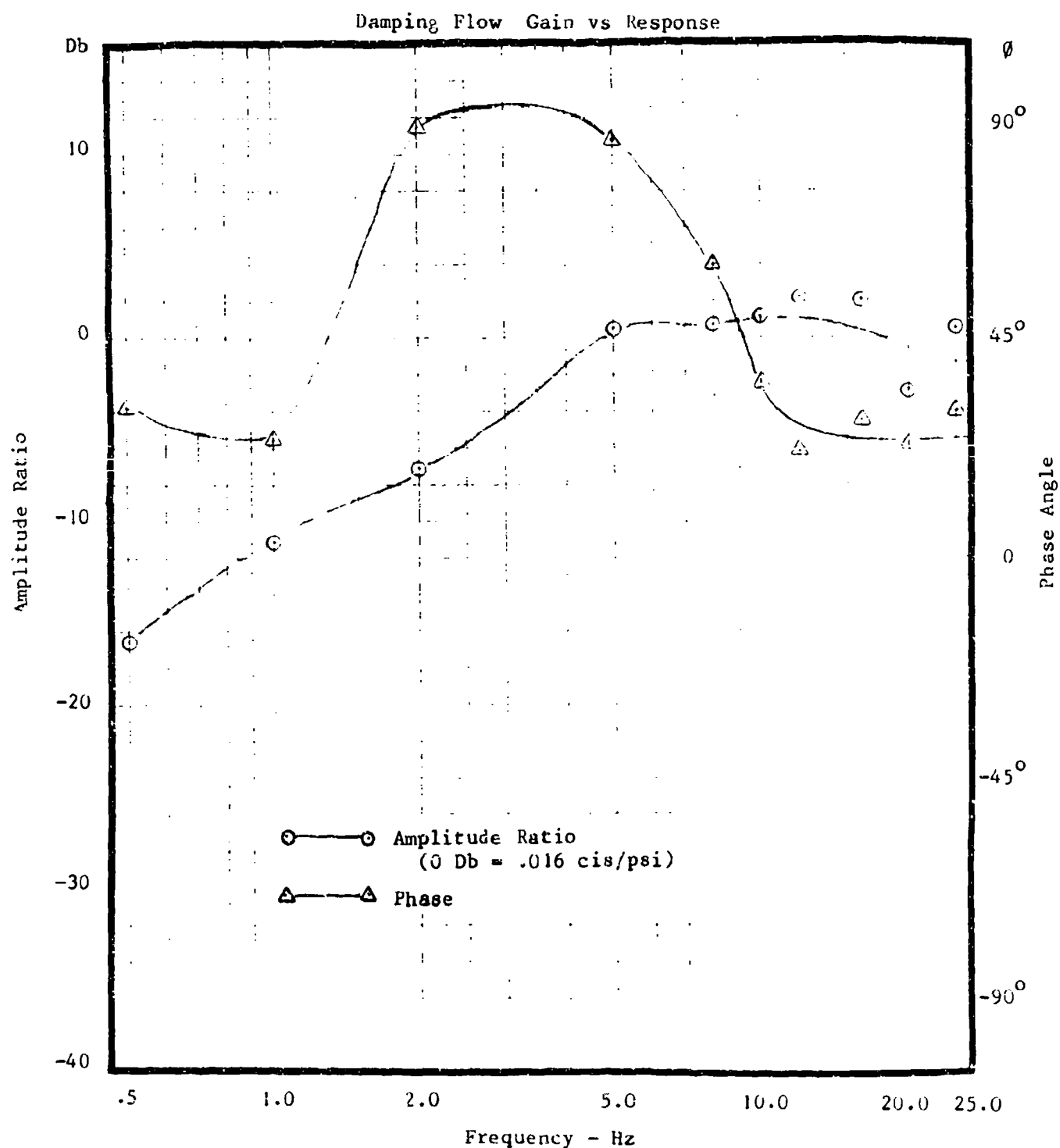


Figure 48. Damping Flow Response, P₁ Section, Mechanical Ground Input, +5000 lb. Load

FLUTTER SUPPRESSION INVESTIGATION

Test: Flow Gain Response
 Mode: Damped - P_2 Active
 Load: +5000 lbs. (+1,453 psi)
 Input Linkage: Mechanically Grounded

Date: 9 October 1984

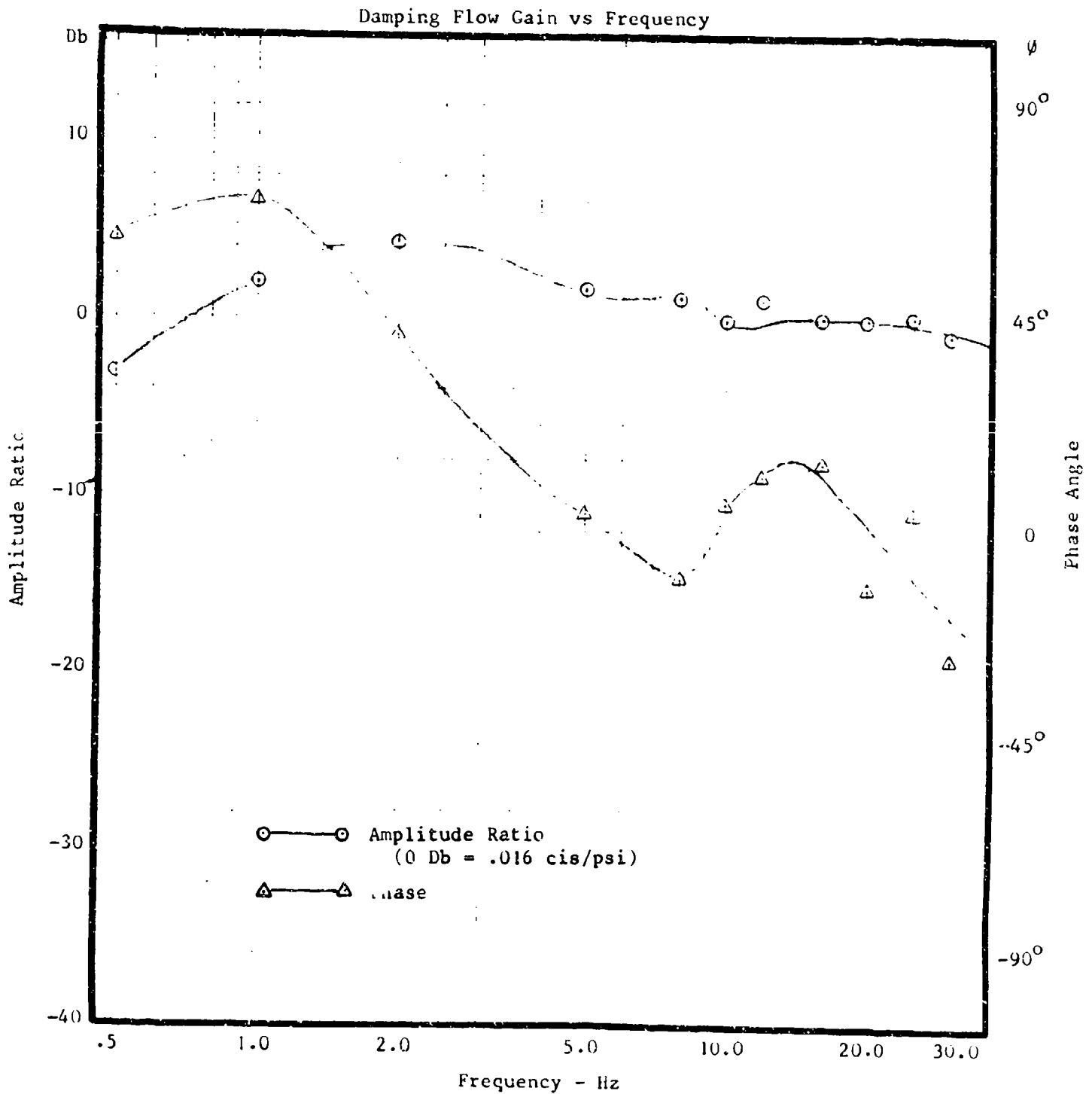


Figure 49. Damping Flow Response, P_2 Section, Mechanical Ground Input, +5000 lb. Load

Figure 50 shows a representative section of the strip chart data. In addition to the traces shown, the input command to the load system and the actuator position were recorded but not presented because of the page size constraint. The data shown is at 12 Hz at a load of ± 1200 lbs. The isolation piston and damping spool differential pressures resemble the load system force waveform and are in phase with the applied load. The waveform from the flow meter output measuring the return line flow is a "double" frequency waveform. The double frequency is created because the return line flow from a damping spool is lowest at the spool null and increases each side of null. As the damping spool strokes through its total deflection in response to a sinusoidal differential pressure, two flow peaks are created.

The return flow waveform is neither the best nor the worst recorded during the test measurements. At frequencies greater than the 12 Hz shown on Figure 50, the waveform is attenuated but appears sinusoidal with little distortion. The peak amplitude of the waveform and the time shift in relation to the input load were used to generate the damping flow gain response plots. Note that because of the flow waveform distortion, the amplitude and phase plots are not as regular as plots made using a response analyzer. A response analyzer using a Fourier transform technique looks only at the fundamental frequency component at each test frequency. Because of the frequency doubling characteristic of the return flow, using a response analyzer for the flow gain response measurements was not practical.

Figure 51 is a return line flow response plot of the modified F-4E actuator with the damping sections disabled and an applied load of $\pm 4,000$ lbs. This plot shows the return line flow contribution from the normal control valve with the actuator under load. Note that the contribution is more than 20 Db down at 12 Hz.

Figure 52 is a return line flow response plot of the F-4E actuator with the damping sections disabled and an applied load of $\pm 7,500$ lbs. The response resembles that of Figure 51, with the return line flow response attenuated more than 22 Db at 12 Hz from the 0.016 cis/psi design damping flow at that frequency. Since with the damping modules operating, the return line flow response is a combination of the control valve and damping spool flow. Figure 52 and Figure 51 indicate that the amplitude of the control valve flow above 10 Hz (even if in phase with the damping flow) has little effect on the total return line flow.

Figure 53 is a plot of the return line flow response to an applied load of ± 2000 lbs with both damping sections of the control package operating. This load creates a differential pressure across each drive area of the actuator of 291 psi. The response is 4 to 5 Db below the design nominal damping flow of 0.016 cis/psi over the frequency range of 10 to 18 Hz. The phase of the flow varies from -23 to -35 degrees over the same frequency range. The reduced amplitude response reflects the low differential pressure at this applied load. The threshold of the damping and isolation piston can reduce the effective flow gain at low differential driving pressures.

Figure 54 is a plot of the return line flow response to an applied load of ± 4000 lbs with both damping sections operating. The amplitude response from 10 to 20 Hz meets or exceeds the 0 Db design level of 0.016 cis/psi. The phase angle relative to the input load is -22 to -34 degrees over the same frequency range. The amplitude and phase response below 5 Hz is affected by the control

FLUTTER SUPPRESSION INVESTIGATION

Sample Chart Data

Date: 9 October 1984

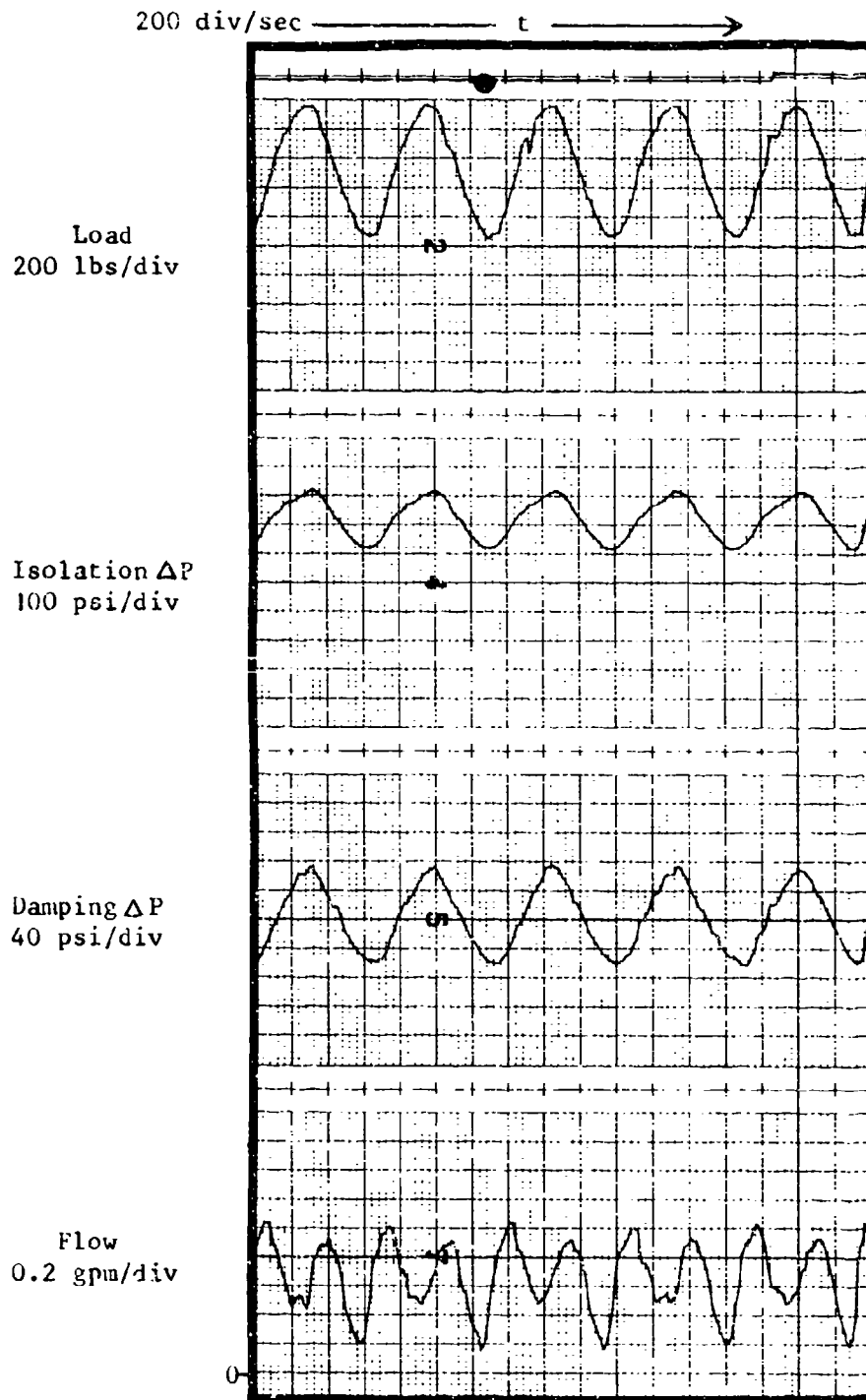


Figure 50. Chart Data, Dynamic Flow Response at 12 Hz

FLUTTER SUPPRESSION INVESTIGATION

Test: Flow Gain Response
 Mode: Undamped - P₁ & P₂ Active
 Load: +4000 lbs.

Date: 6 September 1984

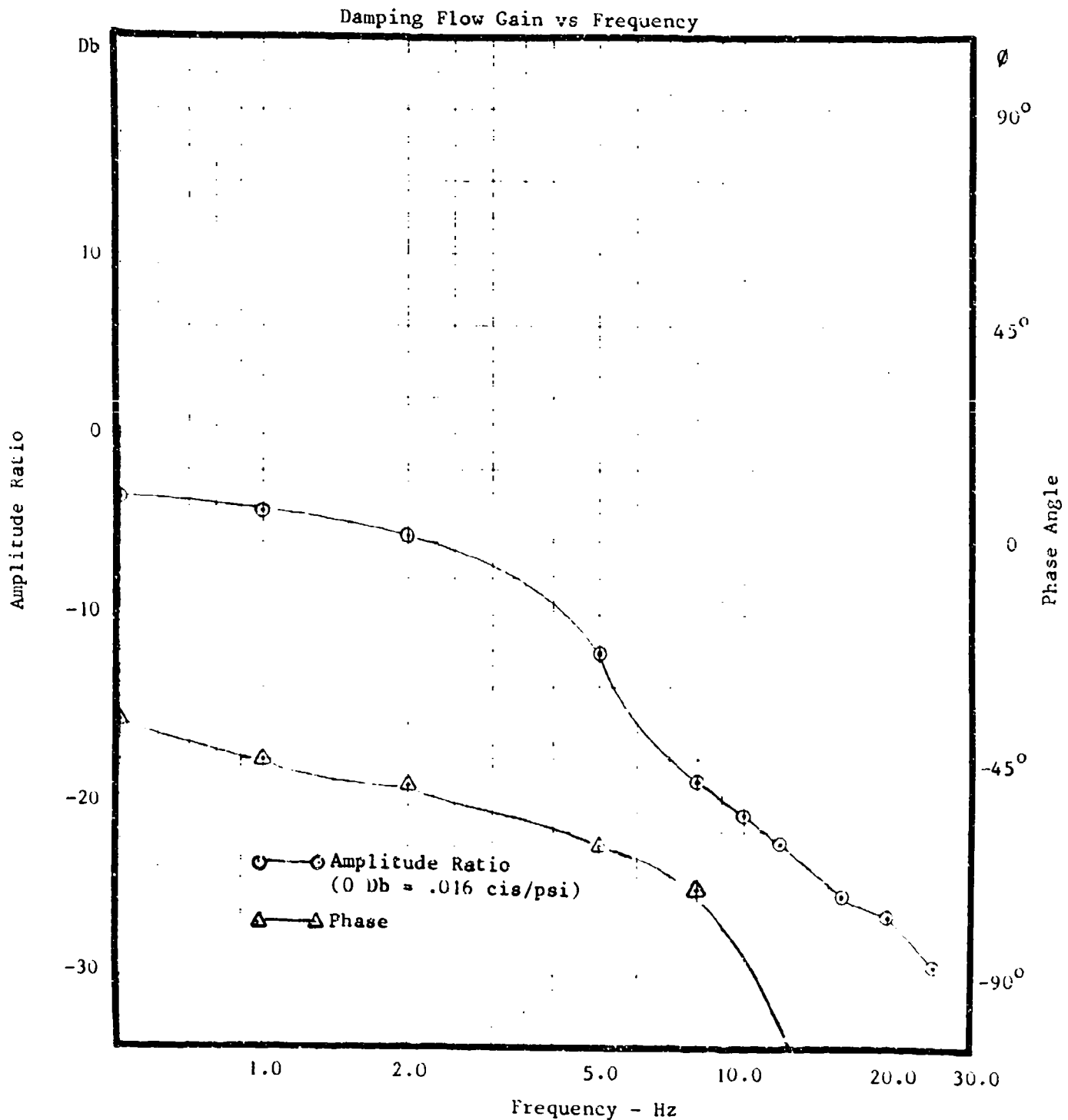


Figure 51. Flow Gain Response, Undamped, +4,000 Lbs.

FLUTTER SUPPRESSION INVESTIGATION

Test: Flow Gain Response
 Mode: Undamped - P_1 & P_2 Active
 Load: $\pm 7,500$ lbs.

Date: 6 September 1984

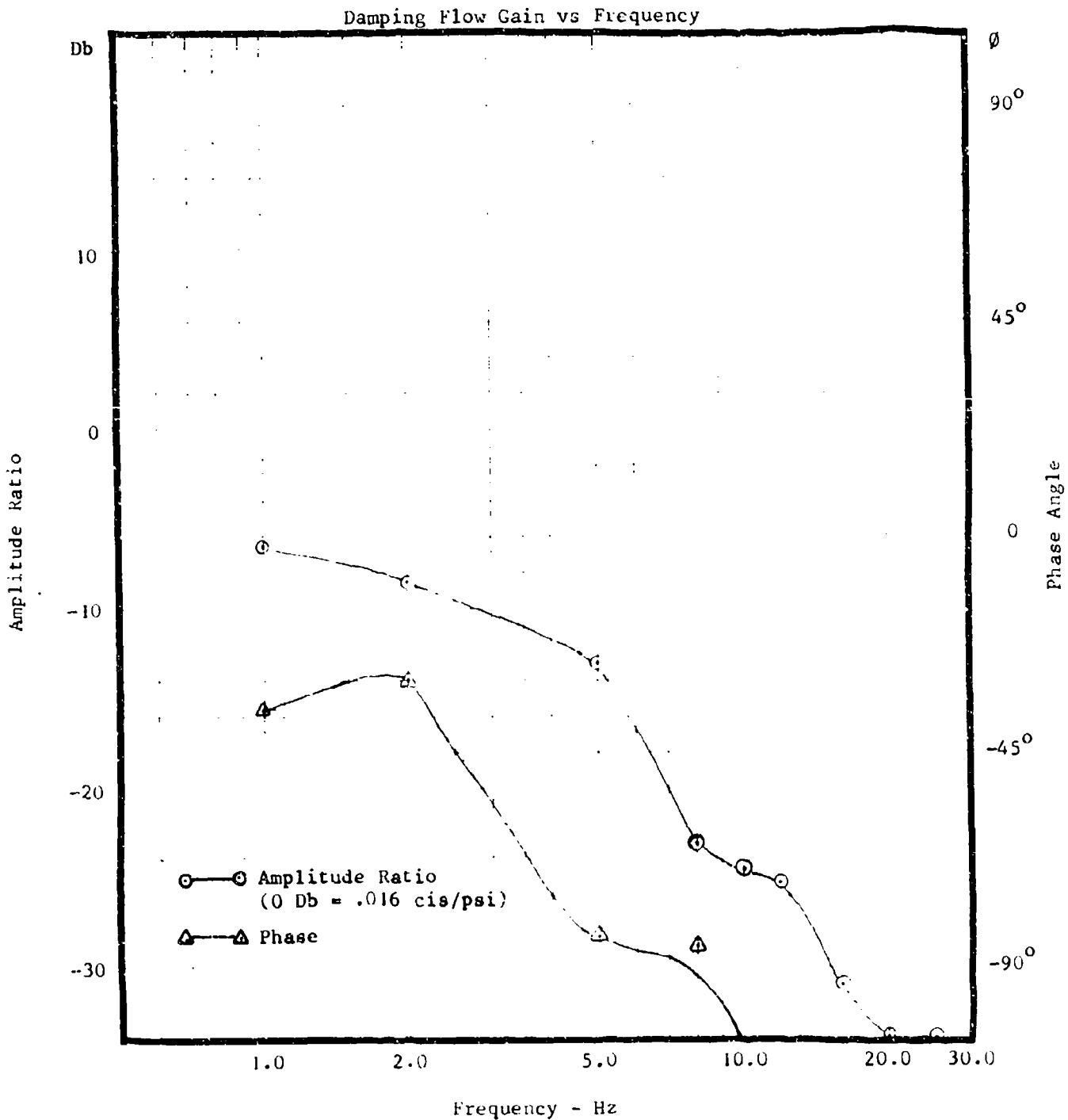


Figure 52. Flow Gain Response, Undamped, $\pm 7,500$ Lbs.

FLUTTER SUPPRESSION INVESTIGATION

Test: Flow Gain Response
 Mode: Damped - P_1 & P_2 Active
 Load: +2000 lbs.

Date: 6 September 1984

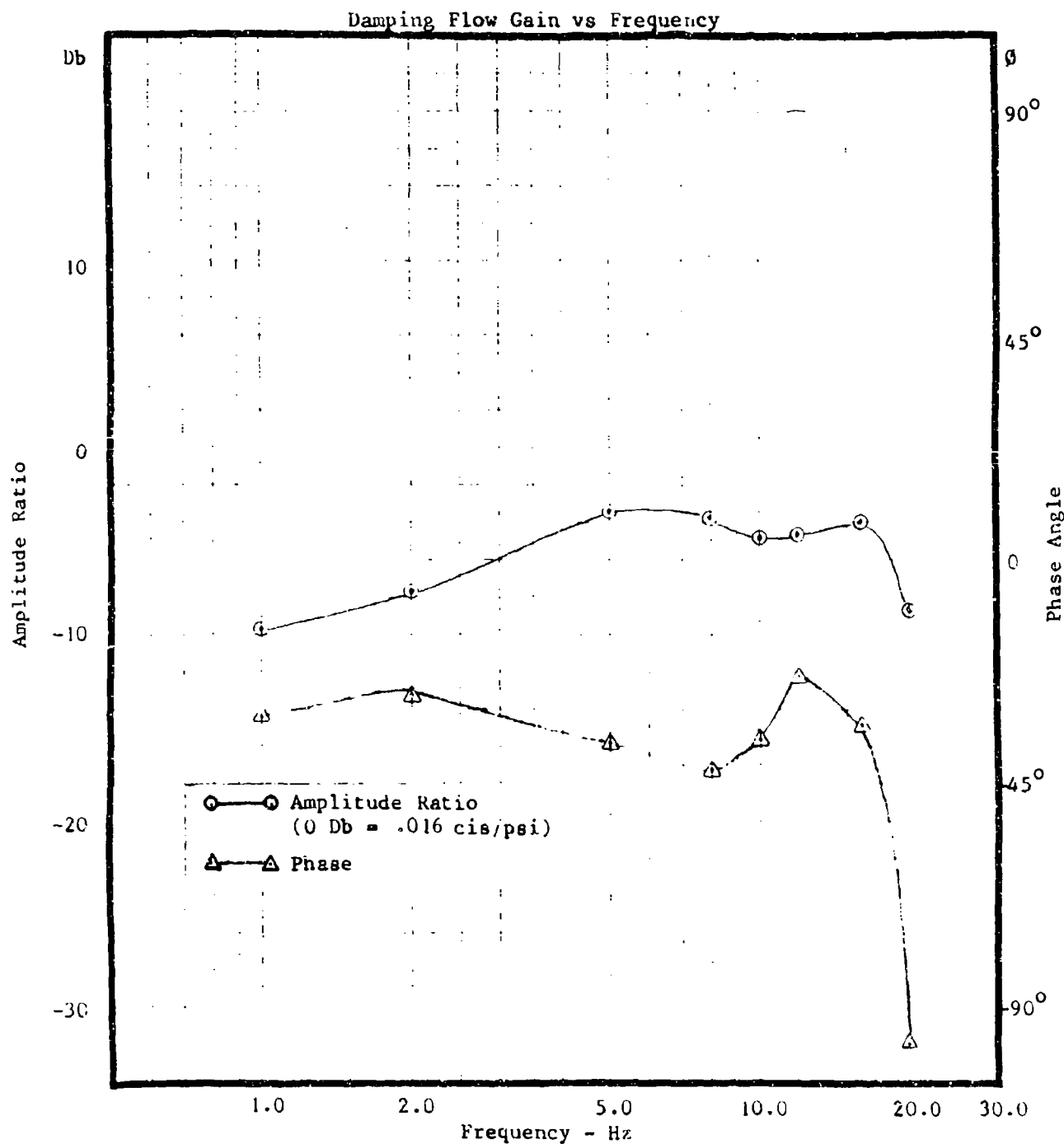


Figure 53. Flow Gain Response, Damped, +2,000 Lbs.

FLUTTER SUPPRESSION INVESTIGATION

Test: Flow Gain
 Mode: Damped - P₁ & P₂ Active
 Load: +4000 lbs.

Date: 6 September 1984

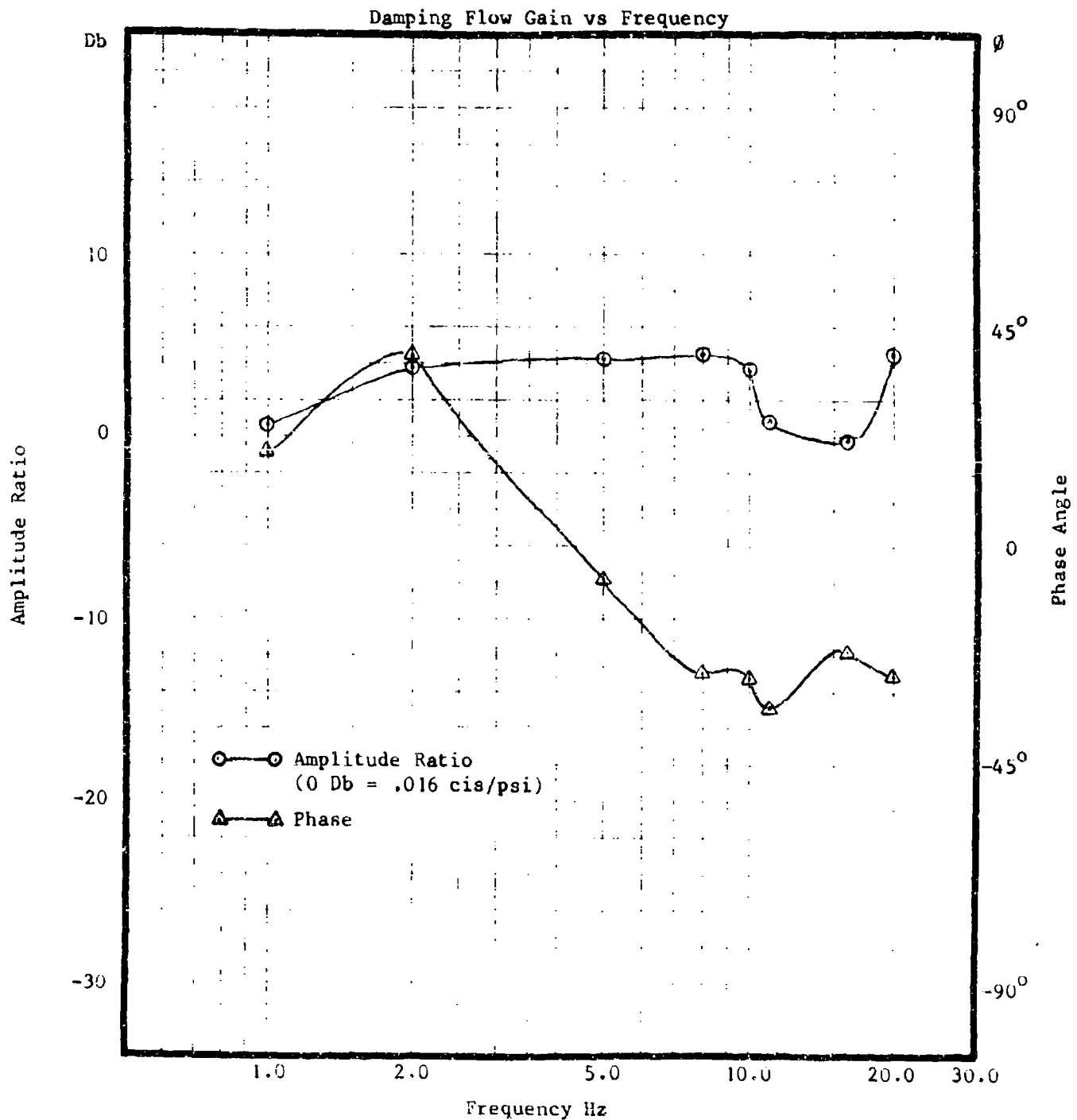


Figure 54. Flow Gain Response, Damped, +4,000 Lbs.

valve flow contribution as expected and remains above 0 Db from 5 to 1 Hz. This is consistent with the amplitude response of the control valve alone as shown previously on Figure 51.

Figure 55 is a plot of the return line flow response to an applied load of ± 7500 lbs. This load produces a differential pressure of 1,090 psi across each of the actuator drive areas. The flow gain amplitude response remains above the 0 Db (0.016 cis/psi) level from 10 to 19 Hz. The phase of the flow relative to the applied load is between -17 and -40 degrees over the same frequency range.

The operation of the control package with both the P_1 and P_2 damping sections was satisfactory. There is still threshold effect on the flow gain response at low excitation pressures. This is a direct function of the damping spool lap conditions, washout orifice characteristics and the damping spool and isolation piston friction levels. Modification of these characteristics within limits can be used to reduce the threshold level as required.

Flow Gain Excitation Sensitivity

Figure 56 shows the damping flow gain vs differential pressure at 12 Hz. Both P_1 and P_2 sections of the actuator were operational and the mechanical input connected to a ground point on the GPATR framework. The differential pressure scale on Figure 56 is for the differential pressure across each area of the actuator. Note that the lowest pressure data point corresponds to a ± 500 lb load applied to the test actuator. The largest differential pressure data point corresponds to a $\pm 10,000$ lb load applied to the test actuator. As shown on Figure 56, the flow gain of the damping sections continues to increase up to a differential pressure of 750 psi. The total increase from the lowest gain to the highest is 4.5 Db. The damping gain reaches the 0 Db (0.016 cis/psi) level at 150 psi differential pressure. In designing the control package, the porting area was increased by a factor of two for the damping spool. This would correspond to a +6 Db gain on Figure 56. The flow gain does not quite reach the +6 Db level, indicating that the integrated control package has some internal flow restrictions.

As previously stated, the threshold or low differential pressure characteristics of the damping circuit are affected by the washout orifice characteristics, the friction of the isolation piston and damping spool, and damping spool lap conditions. The washout orifice used in the integrated control package was a "short tube" design. The flow characteristics with applied differential pressure lie between that of a sharp edged orifice and a long pipe. The sharp edged orifice flow characteristics are proportional to the square root of the applied differential pressure and independent of the fluid viscosity. For pipe flow, the flow is directly proportional to the applied differential pressure and the viscosity of the fluid. The low differential pressure sensitivity could be increased by using a long tube or pipe at the expense of having a washout break frequency be a function of fluid temperature. The friction characteristics of the damping and isolation spool were improved in the integrated control package by increasing the drive area of those elements. Friction tends to increase with diameter while the driving force available for overcoming friction increases as the square of the diameter (for a given differential pressure). The limitation on the size increase of the drive area is one of volume and weight. The lap conditions of the damping spool are established when the spools are meter ground to the sleeve ports.

FLUTTER SUPPRESSION INVESTIGATION

Test: Flow Gain Response
 Mode: Damped - P₁ & P₂ Active
 Load: +7500 lbs

Date: 6 September 1984

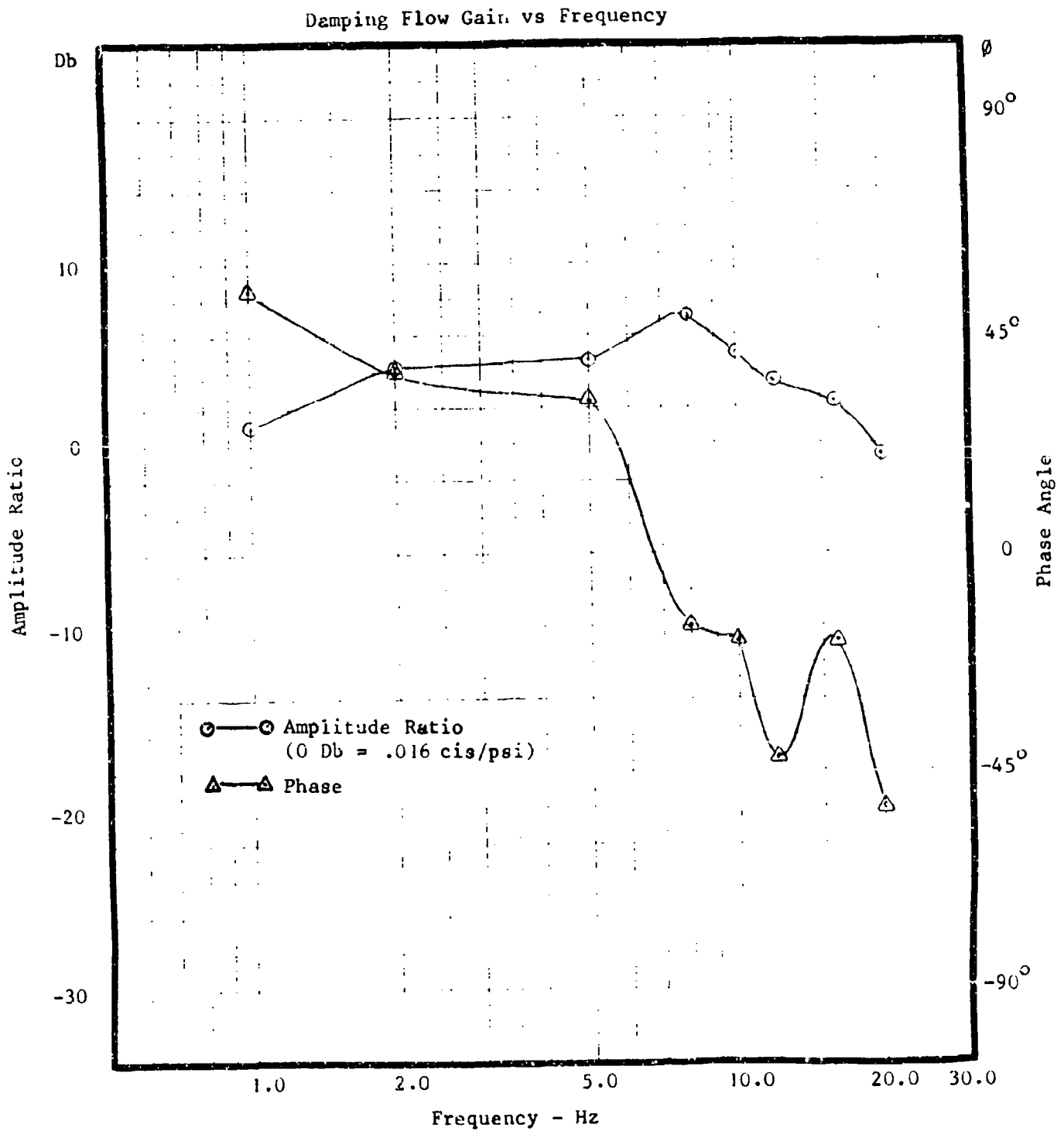


Figure 55. Flow Gain Response, Damped, +7,500 Lbs.

FLUTTER SUPPRESSION INVESTIGATION

Date: 6 September 1984

Test: Damping Flow Gain Vs Differential Pressure

Mode: Damped - P₁ & P₂ Active

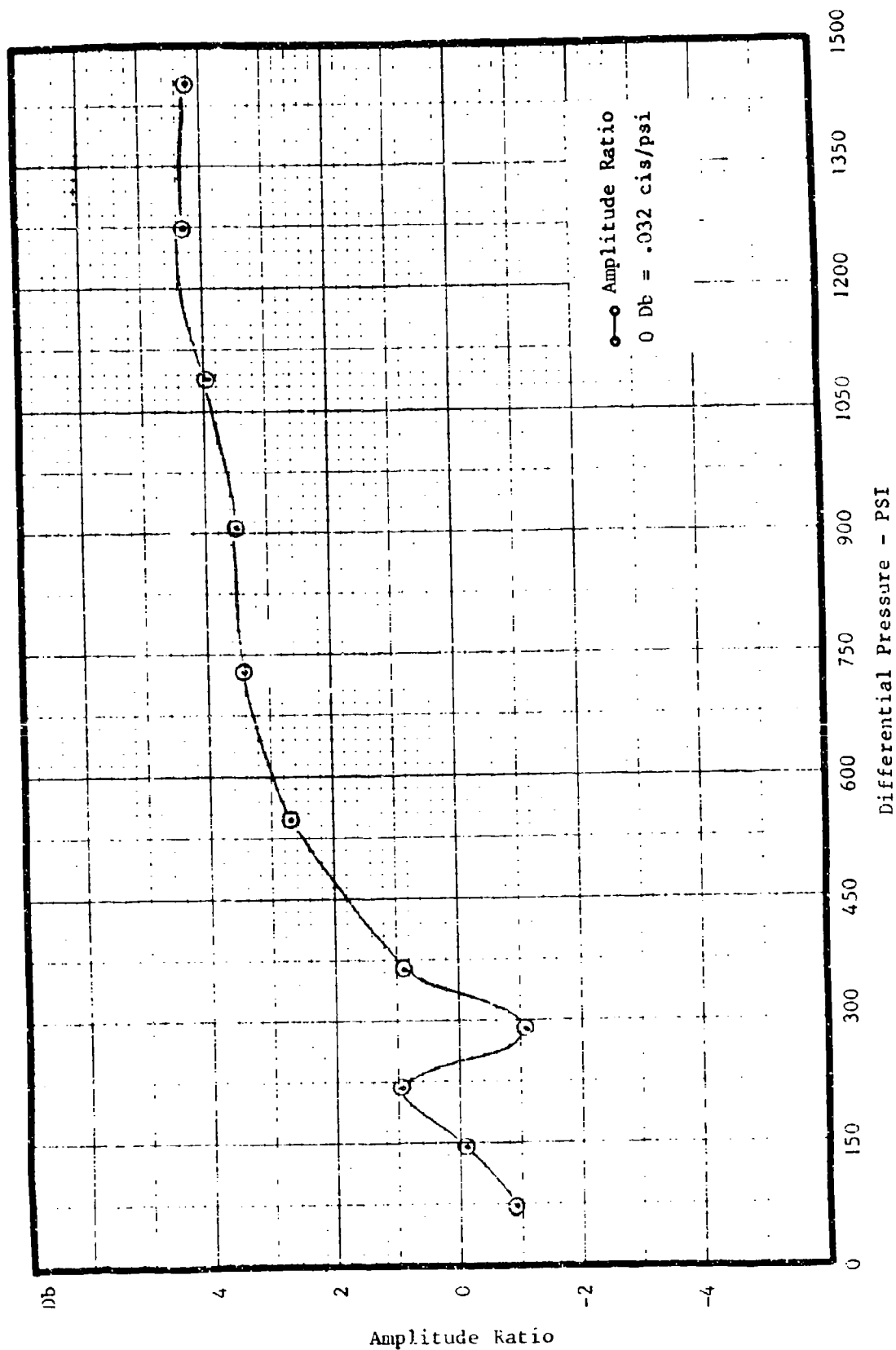


Figure 56. Damping Flow Gain Vs Differential Pressure at 12 Hz

Some small overlap is desirable in order to minimize the leakage through the damping spool when the spool is at null. The damping spools for the integrated package were made with a nominal 0 to 1% overlap.

Conclusions and Recommendations

1. The integrated control package operated nominally as expected from the design. The increase of the damping spool and isolation piston drive areas to a value twice that previously used for modular damping units did reduce the threshold and presented no packaging problem.
2. The flow gain characteristics as measured on the damping modules met the required minimum damping flow gain of 0.016 cis/psi at 12 Hz. The damping flow gain at excitation pressures across the actuator drive areas greater than 700 psi was 0.025 cis/psi, giving a theoretical damping ratio of 1.58. The damping should be sufficiently high enough to eliminate any amplitude peaking at the torsional resonant frequency at any differential pressure above 75 psi (corresponding to a load of ± 500 lbs with both actuator sections operating and ± 250 lbs with one section of the actuator operating).
3. The integrated control package with the hydromechanical damping sections incorporated into the unit along with the normal F-4 control hardware was successful. The control package was larger than the normal F-4E control package (as expected when adding additional hardware to an existing unit). However, the reduction of the actuator drive area to 3.44 square inches each section from 6.0 square inches provides a lighter, lower volume actuator body and a maximum rate flow requirement reduction of 43% from the normal F-4 actuator.
4. The potential of load pressure feedback for flutter suppression is good. The use of load pressure feedback on aircraft flight control actuators has been quite successful on modern European fighter-bomber aircraft. The technique is mechanized on a non-electric basis as part of the actuator's controls design. The current trend in hydraulic systems is towards higher system pressures than the 3000 psi supply pressure used on the F-4. With higher supply pressure, the actuator drive areas are reduced (for a given actuator output). The area reduction reduces actuator stiffness and for those surfaces that are stiffness critical (slab surfaces such as canards and horizontal tails) the airspeed at which flutter occurs is decreased. Without increasing the actuator drive area over that required for maneuver loads, some other technique of flutter suppression is required. Since load pressure feedback potentially is a solution to the flutter suppression problem for slab surfaces, it is recommended that the investigation to verify the technique be continued. Being able to mechanize the technique hydromechanically has been established. With the acceptance of Fly-By-Wire control systems, the use of electronic pressure sensors along with electronic gain and washout circuits in order to mechanize load pressure feedback is easily accomplished. It is recommended that this electro-hydraulic approach be investigated for mechanization feasibility and limitations.
5. It is also recommended that the energy absorption technique represented by the damping of the torsional resonant frequency be wind tunnel investigated. The F-4 tests run previously were inconclusive. A model approach to mechanizing a surface for testing could be used to verify or disprove the approach.

SECTION III. MOVING MAGNET FORCE MOTOR

General Discussion

With the development of high energy product rare earth magnet materials, many new magnetic circuits for force motors which can be used to drive hydraulic valves have become practical. The circuit options include moving coil, moving iron and moving magnet. Both moving coil and moving iron configurations have been developed and tested. The moving magnet configuration for rotary output has been developed in the form of permanent magnet motors. The moving magnet configuration for linear output (with a general arrangement of a solenoid) has not been extensively investigated, although the configuration can be easily used for hydraulic valve drivers.

The moving magnet force motor operates much like a solenoid with a magnetically saturated armature in that the force tends to be directly proportional to the input current. Magnetic materials made from Cobalt and rare earth material have the characteristic of high resistance to demagnetization in the presence of opposing fields. These materials are therefore quite suitable for the moving magnet application.

The investigation conducted on the moving magnet force motor was primarily experimental, using available samples of rare earth magnet material.

Technical Approach

Figure 57 is a cross section of the force motor configuration used for the investigation. The magnet material used was RAECO 16, a Samarium Cobalt magnet material developed by the Raytheon Company in Waltham, Mass. Three different lengths of 0.500 diameter magnet were evaluated. The lengths of magnets used were 0.187 inches, 0.25 inches and 0.300 inches. The magnets were polarized axially.

As shown in Figure 57, the center of the magnetic circuit surrounding the field coil was designed to allow changing the width of the air gap and the location of the gap relative to the position of the moving magnet.

The field coil used for the evaluation was constructed of 1000 turns of AWG 24 aluminum wire. The coil wires were held in place by EA 929 aerospace adhesive (manufactured by the Dysol Division of the Dexter Corporation). The measured coil resistance was 14.5 ohms. The magnetic circuit surrounding the coil was constructed of 416 stainless steel. This stainless steel has a saturation flux level similar to carbon magnet steel and a lower magnetizing force requirement than carbon magnet steel (for a given induced flux level).

The operation of the force motor configuration shown is based upon an attraction and repulsion of the cylindrical magnet by the flux induced in the gap of the magnetic circuit surrounding the coil. If the magnetic circuit is not saturated, the flux in the gap of the circuit is proportional to the coil current, and the flux polarity is dependent on the coil current direction. The magnitude of the force output of the configuration is therefore proportional to

current in the coil, and the force direction is determined by the current direction. This force tends to be independent of the particular position of the magnet location in the gap.

In addition to the control force which is dependent on the coil current, there is a force of attraction which is dependent on the position of the magnet in the gap. This is simply the force of attraction of a magnetic pole for the 416 stainless steel defining the air gap. This attraction tends to attract the magnet towards one end of the air gap. Spring centering is therefore necessary to maintain the magnet in a particular operating position.

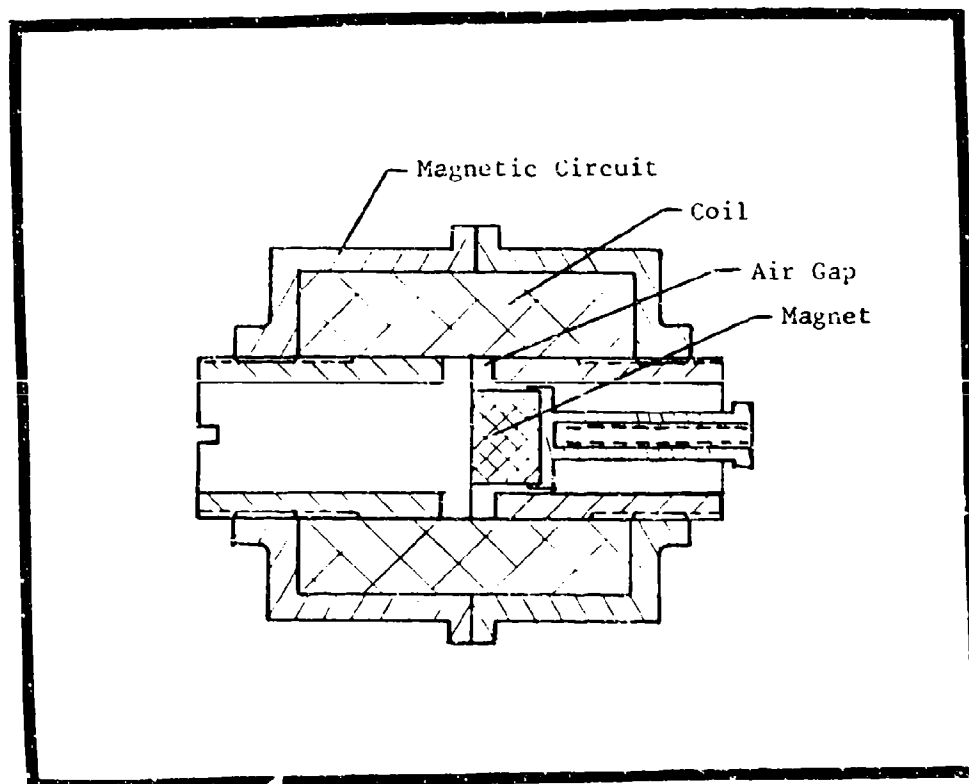


Figure 57. Force Motor Crossection

Magnetic Circuit Calculation

The total flux induced in a magnetic circuit by a coil having N turns and carrying a current I is given by the expression¹:

$$\Phi = \frac{0.4\pi NI}{\sum_{i=1}^m l_i / A_i U_i} \quad (\text{Equation 8})$$

Where: Φ = Total Flux in maxwells

l_i = path length in cm

A_i = path area in cm^2

U_i = relative permeability of path material
(relative to air)

N = Number of turns in the coil

I = Current in the coil in amperes

$\sum_{i=1}^m l_i / A_i U_i$ = reluctance of the magnetic path

For the configuration of Figure 57, the reluctance of the iron portion of the circuit is:

$$R_I = 5.26 / u_g \quad (\text{Equation 9})$$

Where for u_g = 900 for 416 Stainless Steel at an induced flux level of 2000 to 10,000 gauss

$$R_I = 5.26 / 900 = 0.0058$$

The permeability of the air gap (U of air = 1) is the quantity (length of the gap)/(area of the gap). The area of the air gap in Figure 57 is 2.11 cm^2 . For a gap length of 0.475 cm (0.187 in), the air gap reluctance is:

$$R_g = 0.475 / 2.11 = 0.225$$

Note that the reluctance of the iron portion of the circuit R_I is much smaller than that of the air gap R_g , indicating that changes of the iron permeability with circuit flux level can be ignored.

¹Baumeister, T. B. & Marks, L. S., "Standard Handbook for Mechanical Engineers", McGraw-Hill Book Company, 1967, p. 15-21.

For the circuit of Figure 57, and an air gap length of 0.475 cm. (0.187 in.), the total flux in the magnetic circuit is:

$$\Phi = 0.4 \text{ NI} / (0.275 + 0.0058) \quad (\text{Equation 10})$$

$$\Phi = 5.515 \text{ NI maxwells}$$

and the flux density in the gap (ignoring leakage) equation is:

$$B = \Phi / a_g \quad (\text{Equation 11})$$

$$B = 5.515 \text{ NI} / 2.11 \text{ cm}^2$$

$$B = 2.613 \text{ NI gauss}$$

Permanent Magnet Size

The permanent magnet pole flux directly effects the force output of the moving magnet force motor (the force output being proportional to the product of the gap flux field times the magnet flux field). The constraint on the selection of the length of the moving magnet is to operate a B/H ratio which gives the greatest pole flux density without deviating very far from the highest constant energy product curve. The B/H ratio is the ratio of the flux in the magnet to the magnetizing force of the magnet corresponding to the operating point on the

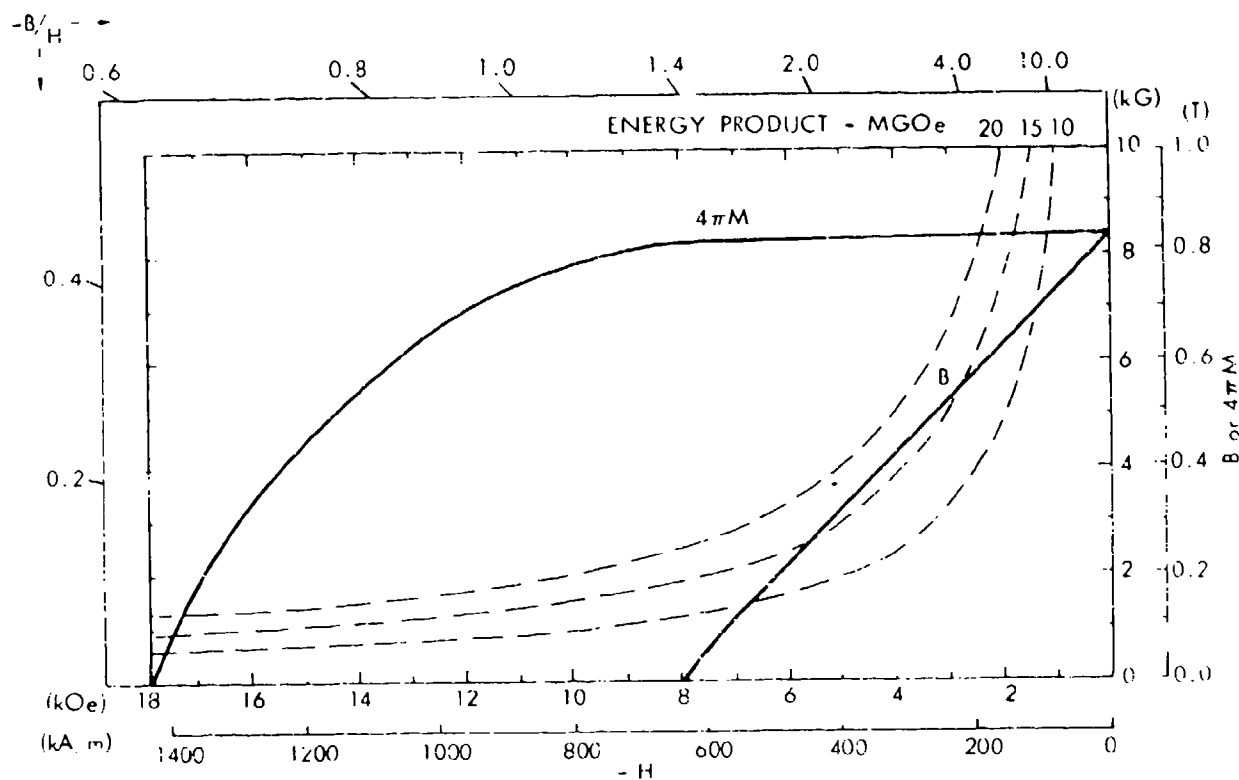


Figure 58. Typical Demagnetization Curve RAECO-16

demagnetization curve. Figure 58 shows a typical magnetization curve for RAECO 16, obtained from the manufacturer's product data. Note that at $B/H = 1$, the magnet is operating at its highest energy product point ($BH = 16$). For $B/H = 2$, the induction curve B intersects the $BH = 15$ energy product line at about $B = 5600$ kilogauss. For B/H greater than 2, the induction curve B departs significantly from its tangential relationship to the BH energy product curves and the magnet operates at lower energy product conditions. Since the minimum magnet volume in a given circuit occurs when the magnet is operated at its maximum energy product point, operating the RAECO 16 moving magnet at B/H much greater than 2 (or $B > 5600$ gauss) is inefficient.

As a starting point for sizing the moving magnet, the following general relationship for the B/H value can be analyzed:

$$B/H = L_m(P_g + P_l)/A_m \quad (\text{Equation 12})$$

Where: B = magnet flux in kilogauss

H = coercive force in oersteds

L_m = magnet length in cm

A_m = magnet area normal to magnetization direction
in cm^2

P_g = air gap permeance

P_l = leakage permeance

For an open-circuit magnet with no defined air gap, all the permeance is leakage permeance. This leakage permeance is a function of the exposed surface or limb. A convenient approximation of the permeance as a function of area is²:

$$P_l = 1.77 S^{1/2} \quad (\text{Equation 13})$$

Where: $S = 1/2$ the total exposed area of the magnet
(the area of a limb)

This equation is based upon the concept that each limb of a magnet can be considered as a spherical pole whose surface area is the same as the surface area of the limb. For rare earth magnets, the effective pole spacing is essentially the length of the magnet.

For an axially polarized rod magnet, the surface area S is:

$$S = (\pi/4) D^2 + \pi D L_m / 2 \quad (\text{Equation 14})$$

Where D = diameter of magnet in cm^2

L_m = length of magnet cm.

²Hitachi Magnetics Corp., "Permanent Magnet Manual", p. 16.

Combining Equations 12, 13, and 14 gives an expression for B/H in terms of the diameter and length for an open circuit rare earth magnet:

$$B/H = 2 L_m (D^2 + 2DL_m)^{1/2} / D^2 \quad (\text{Equation 15})$$

Where: D = diameter of magnet

L_m = length of magnet

For Raeco 16 (reference Figure 58), the maximum energy product occurs at B/H = 1. For 0.5 inch diameter magnets, the corresponding theoretical magnet length is found (by using Equation 15) to be 0.210 inches.

For magnet lengths greater than 0.210 inches, the B/H ratio increases with increasing magnet length. As B/H increases, the pole flux B increases (reference Figure 57). For Raeco 16, increasing B/H from 1 to 2 increases the magnet flux density from 4.2 kilogauss to 5.5 kilogauss (a 31% increase). For this change, the energy product decreases from 16 to 15 Mega-Gauss-Orstedts (a 6.2% decrease). For the moving magnet force motor, the output force increases more rapidly than the magnet volume as B/H is increased above the maximum energy product operating point. The limit for this characteristic is the B/H at which the energy product curves and the induction curve diverge. This occurs for B/H > 2 for Raeco 16 as shown in Figure 58.

The preceding discussion considers the magnet in an open circuit condition. For the moving magnet force motor, the magnet is not operated in an open circuit. As shown in Figure 57 for the force motor investigated, there is a soft iron path from one pole of the magnet to the other over greater than 50% of the magnet length. For a given force motor air gap length, the percentage of the magnetic path which is soft iron increases with increasing magnet length. The effect of the iron is to decrease the reluctance of the magnetic path between poles and to increase the B/H operating point of the magnet. This is apparent when Equation 12 is examined. Therefore, the effect of soft iron in the magnetic circuit is to increase the B/H value for the permanent magnet and the pole flux density, allowing a shorter magnet for a given pole flux density.

Evaluation Procedure

To evaluate the characteristics of a moving magnet force motor configuration, sample quantities of 0.500 inch diameter RAECO 16 magnets were purchased in lengths of 0.187, 0.250 and 0.300 inches. A 1000 turn coil of #24 aluminum wire was fabricated and the 416 SST iron circuit of Figure 57 constructed with an adjustable air gap. The force motor was mounted in a holding fixture and connected to a force transducer. The force output of the motor as a function of coil current and magnet position in the gap was measured for three different gap lengths. In addition, the force of attraction of the magnet for the gap pole faces without coil current was measured as a function of the magnet's position in the air gap. Also measured was the flux change in the air gap as a function of coil current.

Figure 59 shows the test assembly used to measure the force output characteristics of the moving magnet force motor. A Daytronic Model 152A-100T transducer was used to measure force output of the force motor. This transducer has a force measurement range of ± 100 lbs and a linearity of better than $\pm 0.1\%$



Figure 59. Photo of Assembled Force Motor

of full scale. A variable DC power supply was used to supply current to the force motor coil. A Bell Model 610 Gaussmeter was used to measure the pole strength of the test magnets and the flux change in the air gap of the force motor.

Figure 60 shows the force motor partially disassembled. Note the threaded inner sleeves of the force motor housing which allowed changing the length of the air gap.

Test Results

Open Circuit Magnet Strength

The measured open circuit pole flux density for the three lengths of Raeco 16 magnet was the following:

<u>Magnet Length in Inches</u>	<u>Measured Flux Density in Gauss</u>	<u>Calculated B/H</u>	<u>Theoretical Flux Density in Gauss*</u>
0.188	2200	0.995	4000
0.250	3080	1.414	4800
0.300	2600	1.780	5300

*The theoretical flux density is obtained from Figure 58 using the B/H value calculated by Equation 15.

From the above data, the following two observations can be made:

1. The 0.300 inch length magnet was apparently a poor sample. Normally an increase in open circuit magnet length (for the same cross section magnet size) will result in an increase in pole flux density. However, the 0.300 inch length magnet exhibited a lower pole flux density than the 0.250 inch long magnet.

2. The B/H value calculated from Equation 11 does not give pole flux values which agree well with the measured results (for the two magnet lengths of 0.188 and 0.25 inches). However, a correction factor* of 0.4 for Equation 15 would give good agreement between the measured and theoretical flux density values for both the 0.188 inch and 0.25 inch long magnets.

*Subsequent to this force motor evaluation testing, three other open circuit magnets (axially polarized) were tested for pole flux with the following results:

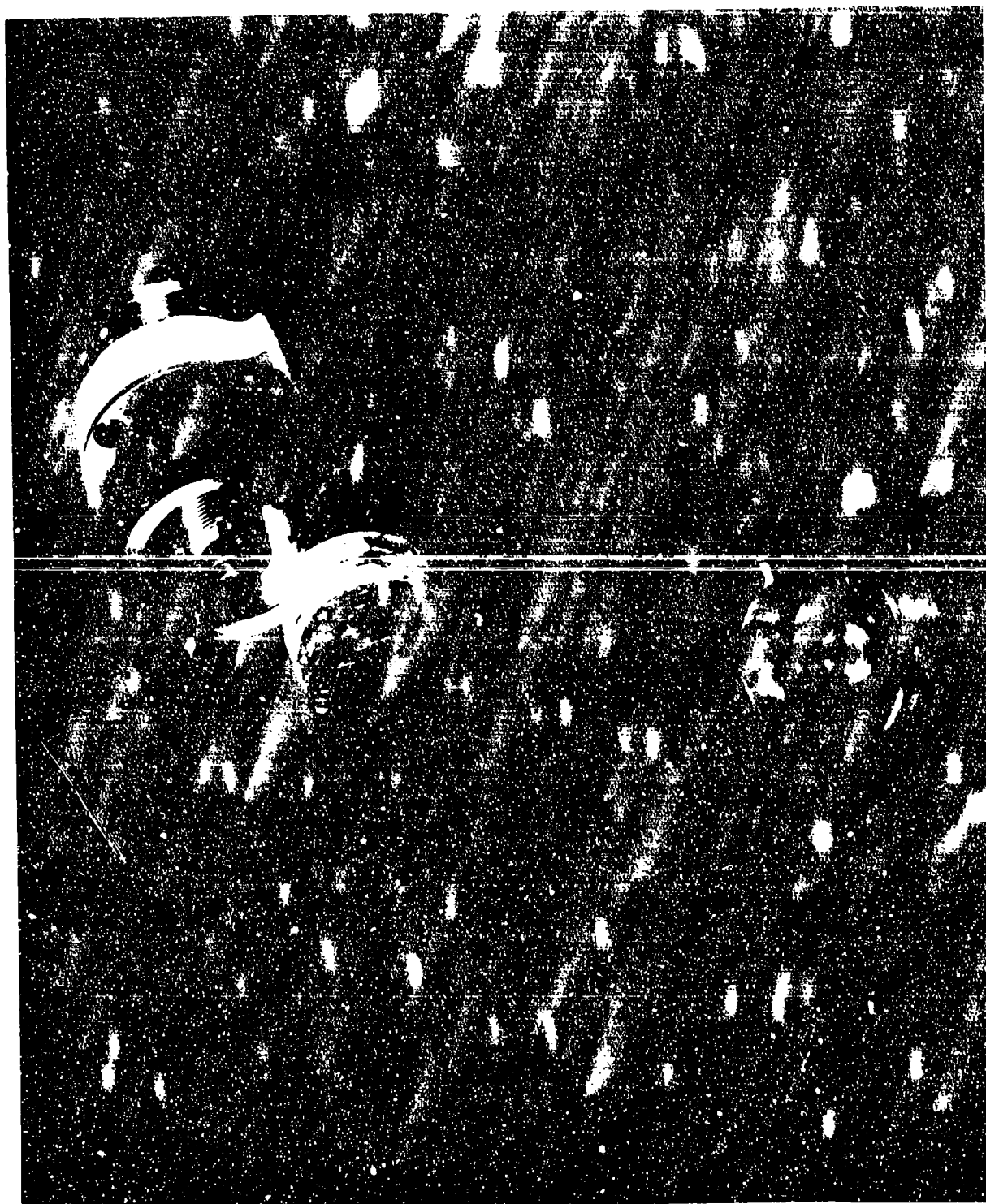


Figure 60. Photo of Force Motor Partially Disassembled

<u>Magnet Dimensions</u> <u>(inches)</u>	<u>Material</u>	<u>Correction Factor Required</u> <u>for Equation 15</u>
0.500 Diameter x 0.500 long	Tascore 21	0.231
2.00 Diameter x 0.500 long	Raeco 16	0.690
2.75 Diameter x 1.000 long	Tascore 21	0.567

This indicates that Equation 15 did not yield consistent prediction of the open circuit pole flux for the rare earth magnets tested (since the correction factor required varies between 0.231 to 0.690) and should be used with caution.

Air Gap Control Flux Density

Figure 61 is a plot of the flux density induced in the air gap of the force motor by the 1000 turn coil. The flux was measured with a gaussmeter with the probe inserted in the gap as the coil current was varied. The moving magnet was not installed in the force motor during the measurements.

Notethat Figure 61 shows the flux density-vs-coil current for three different air gaps. The relationship is fairly linear for all three gaps, indicating that the permeability of the circuit is primarily determined by the air gap and that no significant saturation of the iron in the magnetic circuit occurred for the coil currents used. The 0.116 inch air gap (which creates the highest gap flux density for a given coil current) exhibits the worst linearity, showing a slight rolloff of the flux density/current gain with currents above 0.75 amperes.

The measured flux density of 1700 gauss for the 0.187 inch gap and 1000 ampere turns excitation is less than the 2615 gauss predicted by Equation 11. This indicates that the magnetic circuit of Figure 57 has a nominal leakage factor of 1.5.

Test Setup - Force Output Measurement

Figure 62 is a schematic of the test setup used to measure force output of the force motor. The same setup was used for measuring the output force as a function of input current and the output force which is a function of the magnet position in the air gap at zero input current.

Figure 63 illustrates how the magnet's location relative to the air gap poles was defined for the force measurements.

Test Results - Bias Force Output

Figure 64 is a plot of the test results for the zero input current force as a function of magnet length. Note that data for gap lengths longer and shorter than the magnet length are presented for both the 0.188 and 0.250 inch length magnets. The direction of the bias force is indicated on the figure.

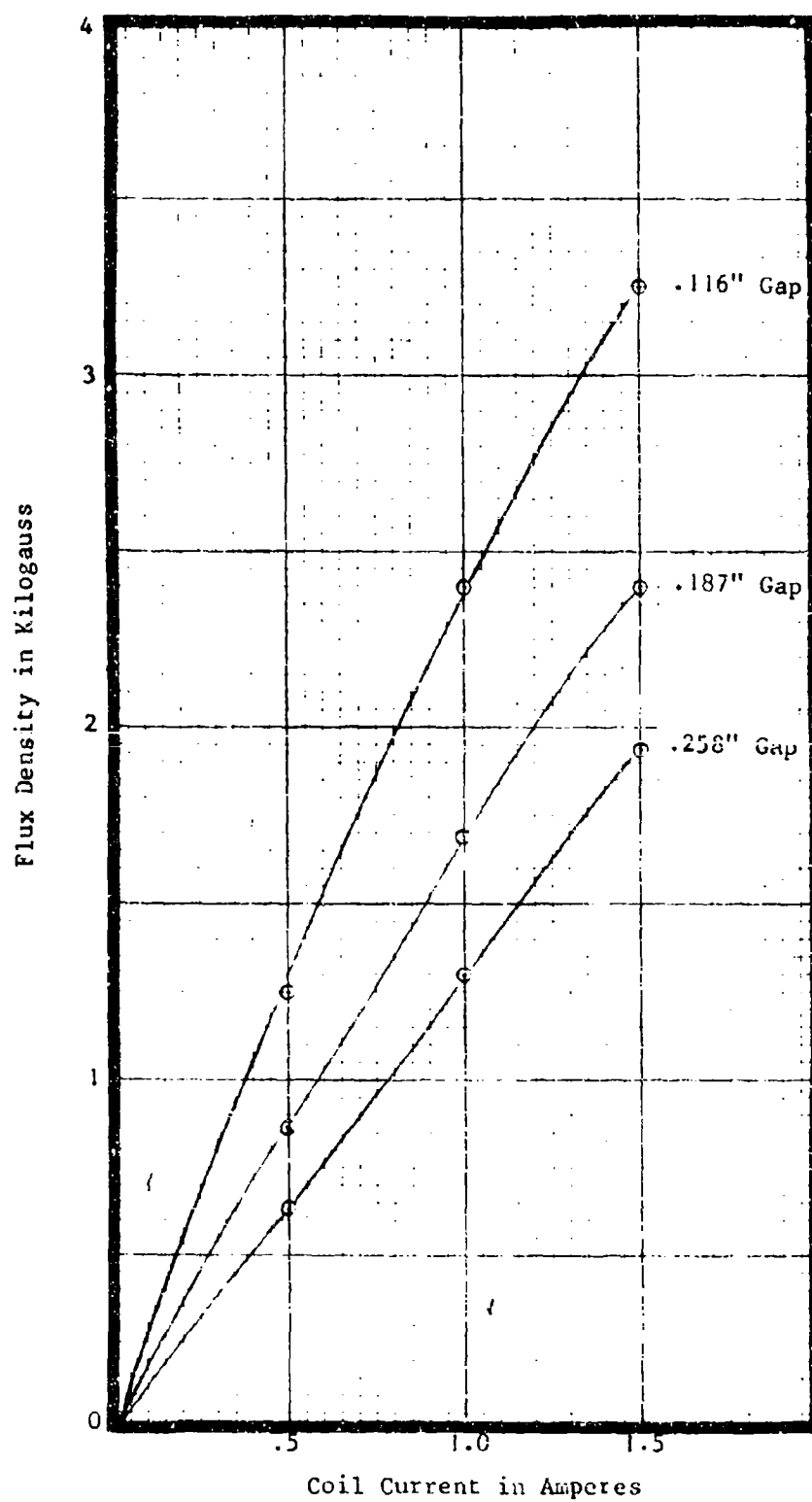


Figure 61. Air Gap Control Flux Density

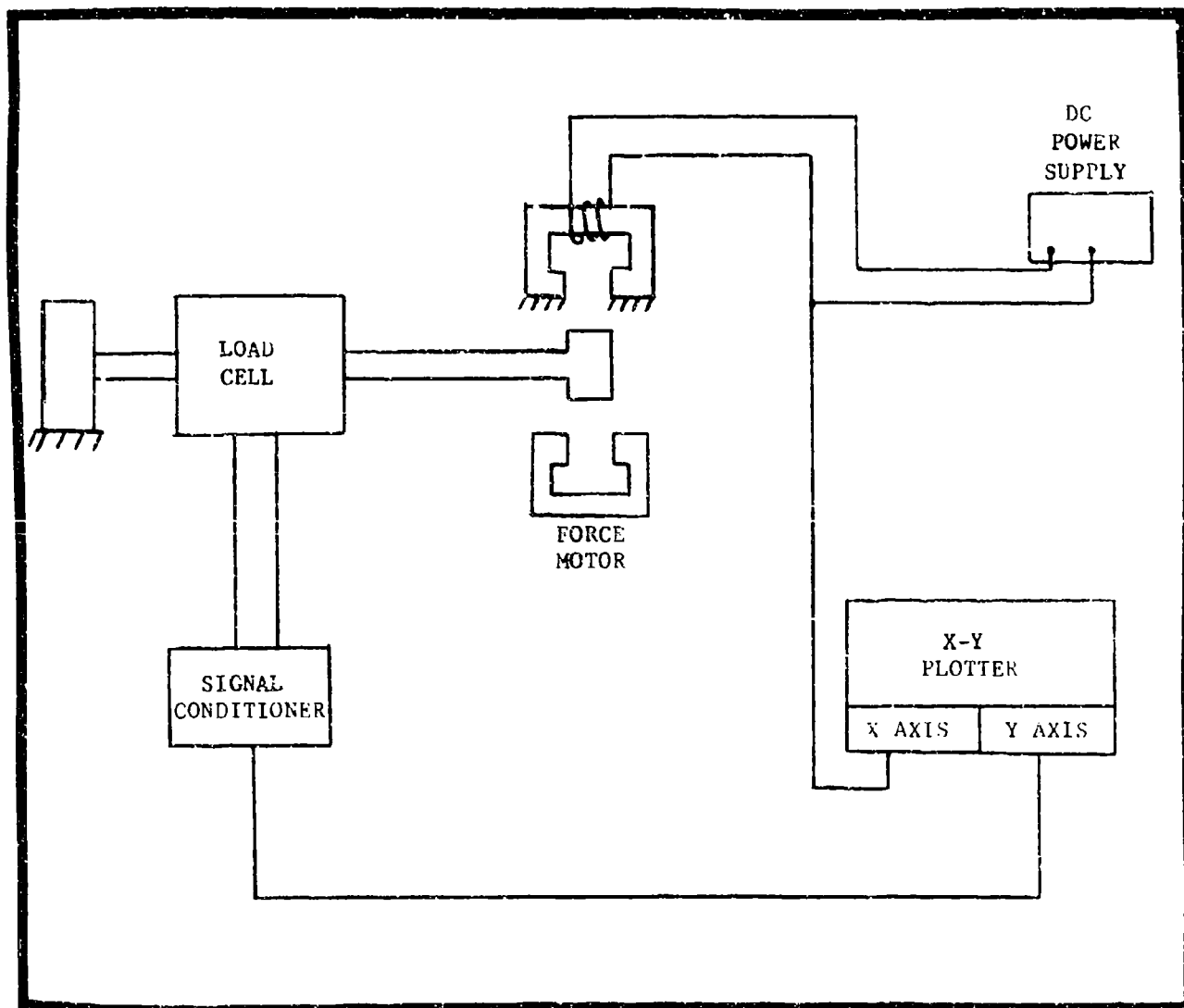
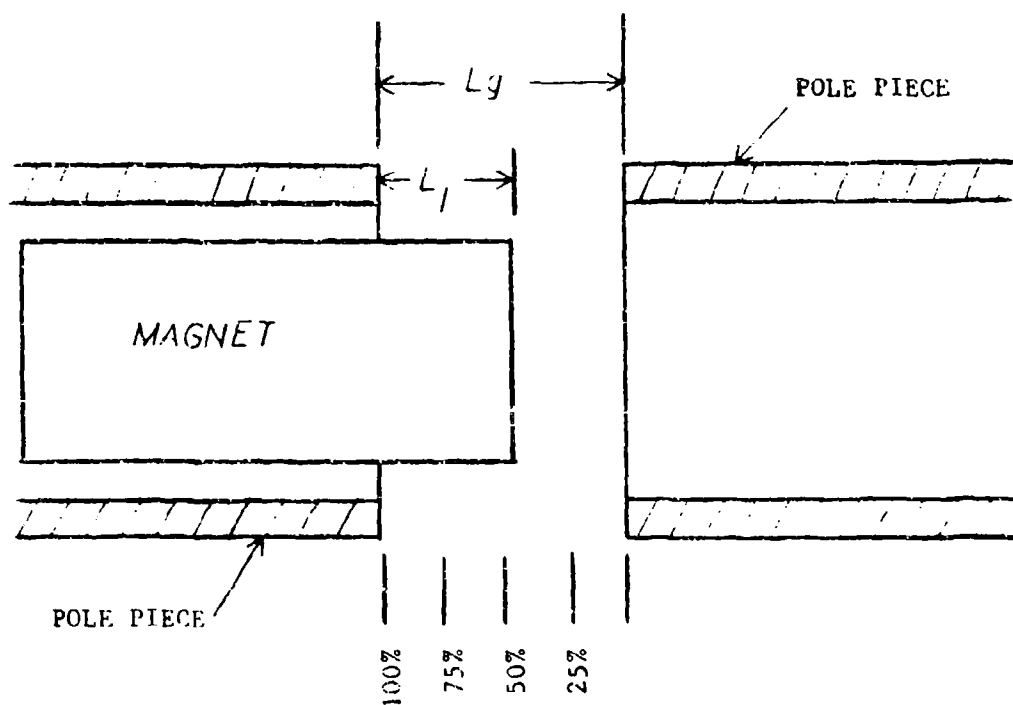


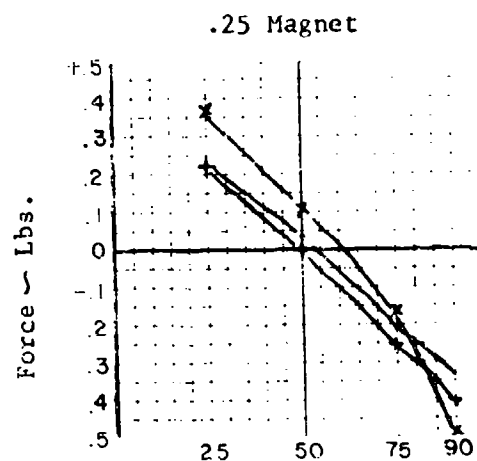
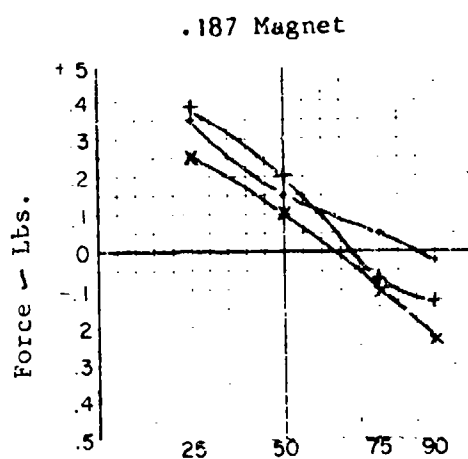
Figure 62. Schematic for Test Setup



$$\% \text{ of Gap} = \frac{L_g - L_1}{L_g} \times 100$$

where: L_g is the length of the air gap
 L_1 is the length of magnet in the air gap

Figure 63. Magnet Location Definition



• • .116" Gap
 + + .187" Gap
 x x .258" Gap

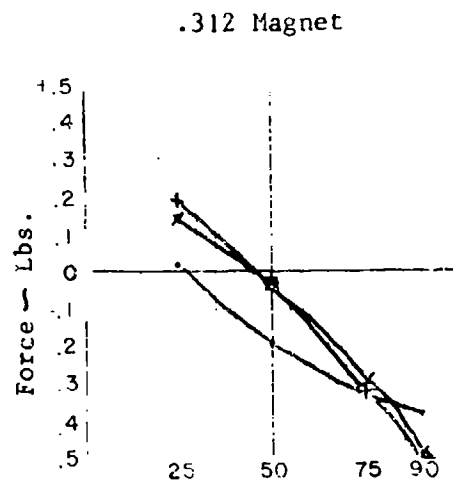
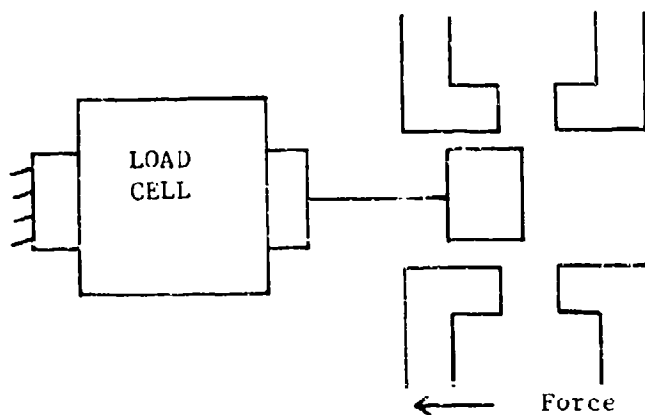


Figure 64. Bias Force Output Test Results

Note that as shown in Figure 64, the bias force change with magnet position for all air gap and magnet length combinations is monotonic, and centering stability can easily be accomplished by using linear centering springs. For a linear bias force gradient (such as measured with the 0.250 inch length magnet and a gap length less than the magnet length) the linear centering spring can be sized to almost cancel the bias force gradient, and there will be very little bias force effect on the force output available from control coil current. For a non-linear bias force gradient (such as measured with the 0.250 inch length magnet and the 0.258 inch length air gap), the linear centering spring must be sized to provide a force greater than the bias force over the entire movement range of the magnet. Therefore, with the non-linear bias force characteristic, part of the force produced by the coil current will be used to overcome excess centering spring force (over some portion of the movement range of the magnet).

For all three sample magnets, the maximum bias force was less than 0.52 lbs. The non-linearity of the bias force appears to be independent of whether the air gap is greater or less than the length of the magnet. From the shape of the bias force gradient curves, cancellation of at least 75% of the centering spring force by the bias force would occur. Therefore, for the worst case shown in Figure 64, an uncanceled force of 0.15 lbs would have to be overcome by the coil current at some particular magnet operating position.

Test Results - Current Controlled Output Force

Figures 65, 66 and 67 present the results of the output force measurements for output force as a function of coil current, magnet length, magnet position and air gap length. For each of the figures, the bias force is not included in the presented data. The bias force was "zeroed" out for each magnet position as the data was recorded. Both "negative" and "positive" force measurements are presented and correspond to the change in current flow direction through the coil.

Figure 65 shows the force characteristics for an air gap of 0.116 inches. Note that for the 0.187 and 0.250 inch length magnet, the output force at a given current level drops off for magnet positions from 0 to 25% of the air gap (note that as shown in Figure 63, 0% is with the face of the magnet in line with one pole piece and the body of the magnet extending across the entire air gap. For magnet positions from 50 to 100% of the air gap, the force output for given current level remains relatively constant. Note that the drop off in force between the 25 and 0% positions of the magnet is reduced as the magnet length is increased (although all magnets are longer than the air gap used with Figure 65). From the data on the figure, it appears that the best operating stroke for the moving magnet occurs between 25 and 75% of the air gap. The output force for 1 ampere coil current is over 2 lbs for all three magnets. The linearity for the output force to input current relationship is indicated by the spacing between the force curves for different current levels at a particular magnet position. Some saturation non-linearity is apparent at some magnet positions. However, for coil current below 1 ampere, the output change appears linearly related to input current for a given magnet position.

Figure 66 shows the test results for an air gap of 0.187 inches. For the magnet length of 0.187 inches, the output force drops off when the magnet is more than 50% extended into the air gap. For the 0.250 and 0.300 inch length magnet, the force curves resemble those obtained with an air gap of 0.116 inches. For

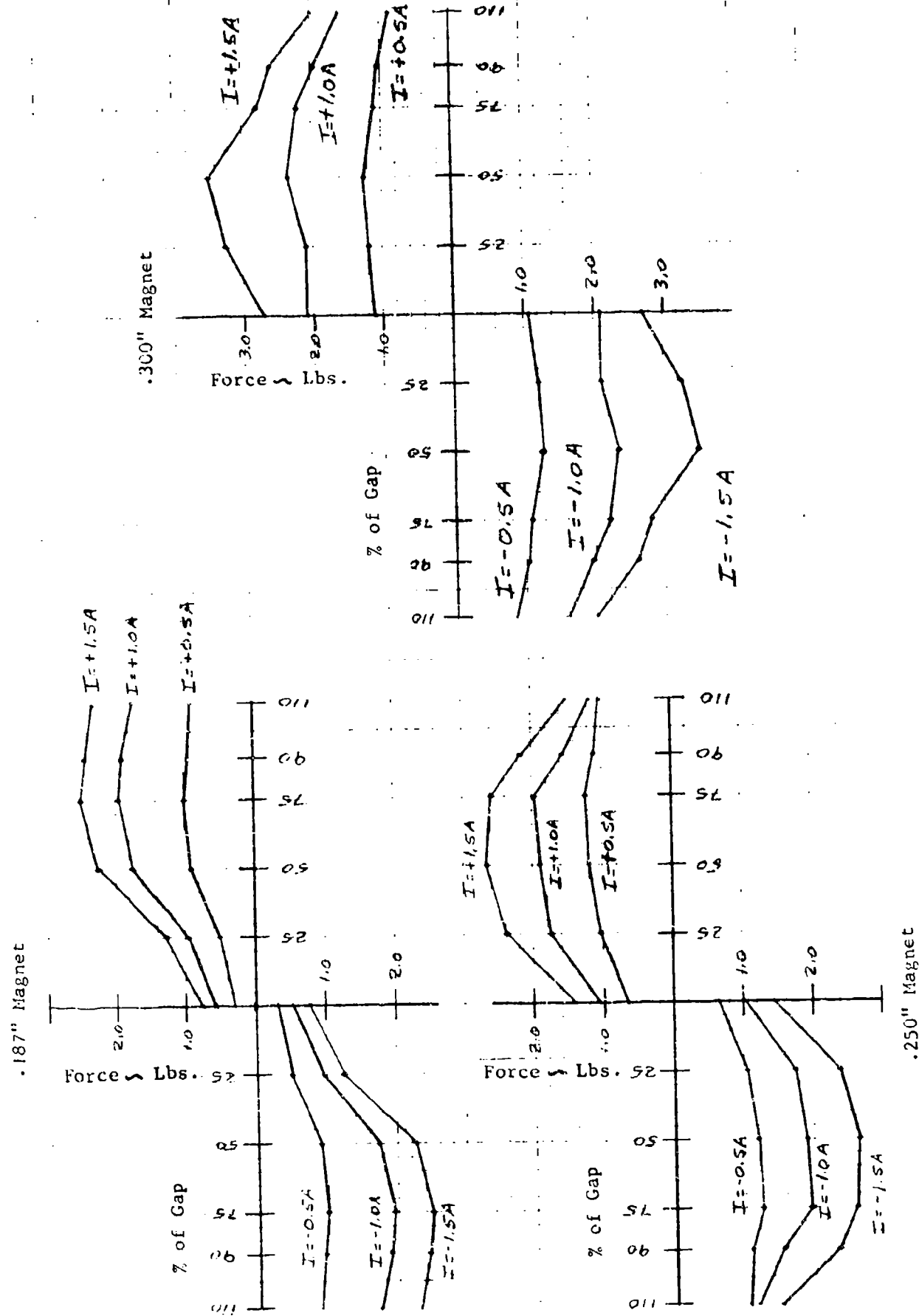


Figure 65. Output Force Measurements - 0.116" Gap

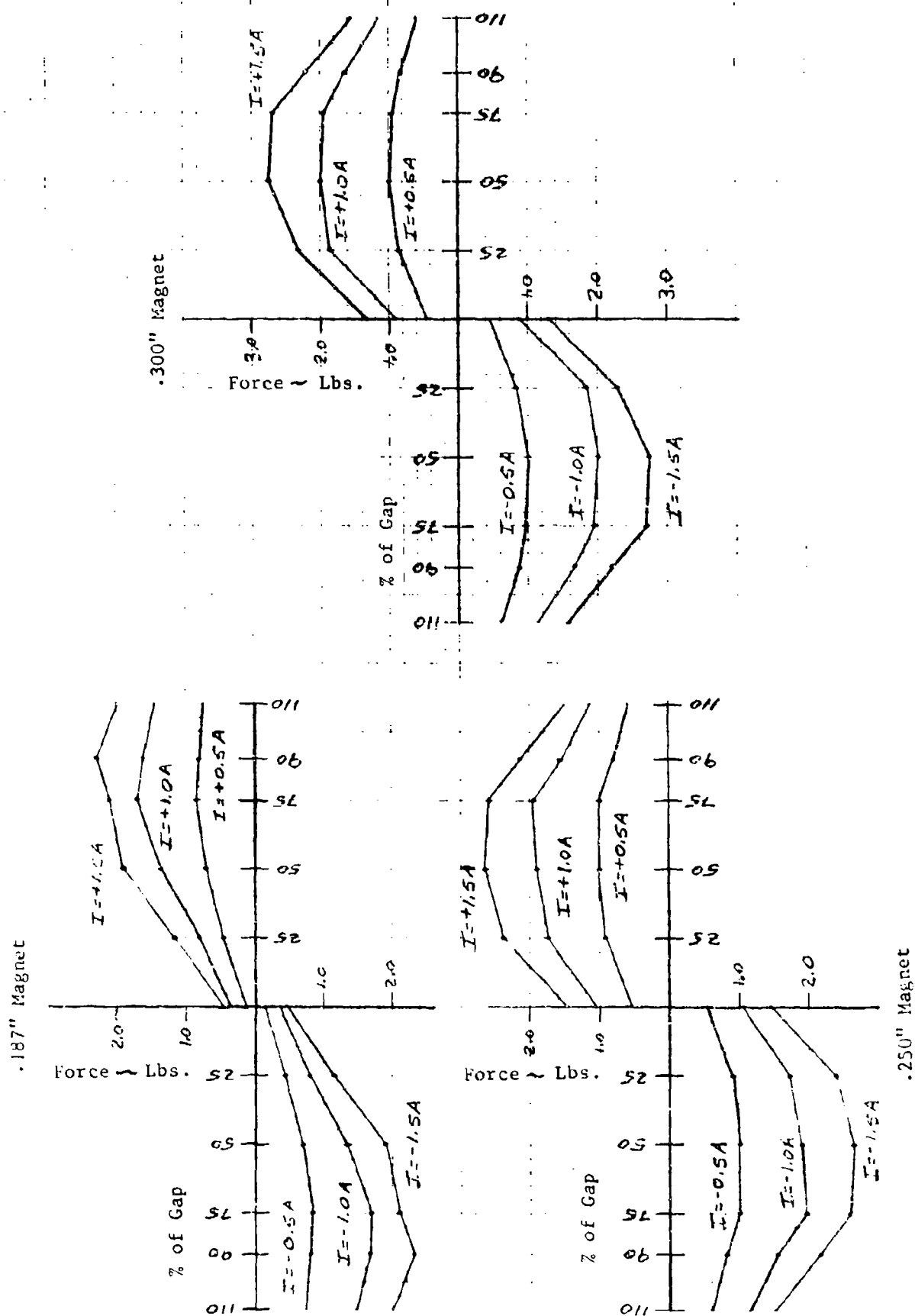


Figure 66. Output Force Measurements - 0.187" Gap

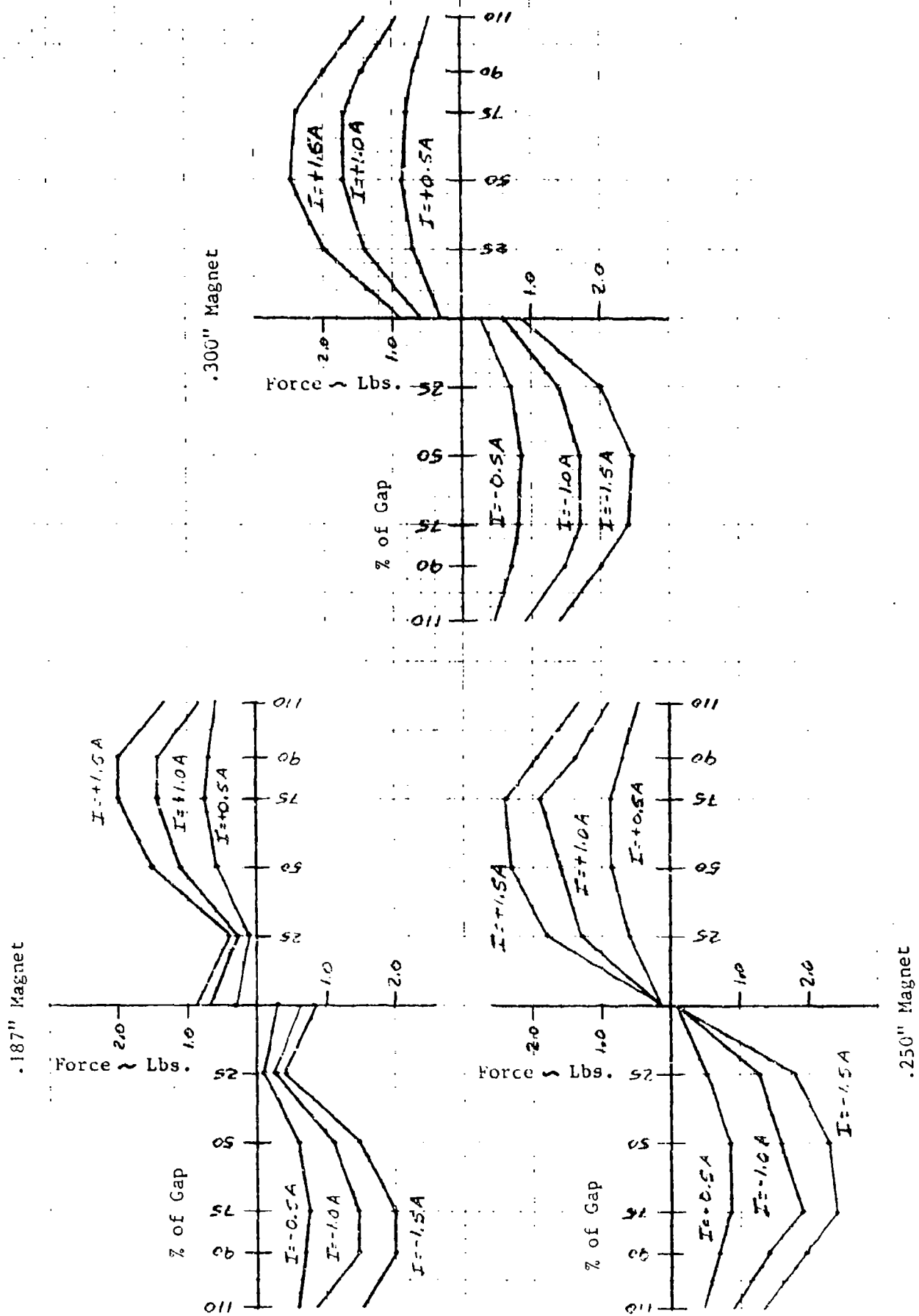


Figure 67. Output Force Measurements - 0.258" Gap

these longer magnets, the best operating range appears to be with the face of the magnet positioned between 25 and 75% of the gap. Note that the maximum force obtained from each of the magnets is lower for a given current level than with the shorter air gap of Figure 65. This is due to the lower current controlled flux change associated with increasing length of the air gap.

Figure 67 shows the test results for an air gap of 0.258 inches. This air gap is longer than both the 0.187 and 0.250 inch magnet lengths. The effect of the magnet length being less than the gap is apparent in the force curve characteristic for the 0 to 25% magnet position range. The operating range of 25 to 75% is valid for the 0.300 inch length and 0.250 inch length magnet. The maximum force for a given current level is lower than with the shorter air gaps shown on the data of Figures 65 and 66. The characteristic of the force curves for \pm coil current directions are identical.

Summary and Recommendations

The force motor configuration operated as expected. The force output with the particular magnet material and magnetic circuit measured nominally 2 lbs/1000 ampere turns. The force output drops off with increasing air gap for a given magnet size and the same coil current. However, the percent force drop off is not proportional to the percent gap increase, as illustrated by the following data from Figures 65, 66 and 67 for the 0.300 inch length magnet:

<u>Air Gap</u> <u>Inches</u>	<u>Force</u> <u>lbs.</u>	<u>Magnet Location</u> <u>%</u>	<u>Coil Current</u> <u>Amperes</u>
0.116	2.35	50	1.00
0.187	2.00	50	1.00
0.250	1.70	50	1.00

Using the force of 2.35 lbs and the air gap length of 0.116 inches as a base, the relative percent changes of force and air gap for the above data are:

<u>Air Gap</u>	<u>% Change of Air Gap</u>	<u>% Change of Force</u>
0.116	0	0
0.187	+60	-14.9
0.258	+222	-27.7

The work done by the force motor is proportional to the product of the output force and the distance moved. The useable motion range is 25 to 75% of the gap for all three gap lengths tested (for cases where the magnet is longer than the gap length). From the results listed above, it appears that the efficiency of the force motor is still increasing with increasing air gap (over the range of air gap evaluated).

The long stroke capability of the force motor potentially makes it useable as a positioning driver for control devices. The long stroke capability also provides the potential for creating a higher force output over a short stroke by mechanical gearing.

The force motor configuration has significant potential as a driver for control devices, and it is recommended that the technique be investigated further specifically, the effect of using higher energy product magnets (which are now readily available) and longer magnets and air gaps should be pursued.

SECTION IV. DIRECT DRIVE FORCE MOTOR ENHANCEMENT

General Discussion

Direct drive servovalves have been developed for flight control system use under several Air Force funded development programs. Included in these are contracts F-33615-75-C-3608 and F33615-77-C-3077 with Dynamic Controls, Inc. and contract F33615-76-C-3037 with General Electric. In a direct drive valve design the main control spool is driven directly electromechanically. The two stage control valve with its hydraulic amplification is eliminated. When used in a redundant Fly-By-Wire system, the secondary actuator used to mix the output of the parallel channels used for redundancy is eliminated. The direct drive approach to mechanizing a control valve has resulted in reducing the total parts count of the valve. Several of the parts eliminated, such as the components making up the flapper-nozzle or jet pipe first stages require precision manufacturing techniques. Because the hydraulic amplification stages are eliminated, the direct drive approach is less sensitive to contamination and more energy efficient (the quiescent leakage flow of the first stage is eliminated).

A parameter in which the direct drive servovalve falls short of the conventional two stage valve is the force that can be applied to the spool in order to break it free from a jammed condition. For example, a two stage servovalve with a 0.375 inch diameter main spool can exert slightly over 300 lbs of force on the spool when the valve is supplied with 3000 psi. The direct drive servovalve developed by DCI under the above contracts will generate 80 lbs of force with two channels operating. The 80 lb design force is based upon using two valve drivers with each having an output force capability of 40 lbs. The design force is the force required to shear a 0.015 inch diameter safety wire with the control spool edges.

There is some contention that a 40 lb force level may be inadequate to overcome a spool jam, although specific design values have not currently been established. Therefore, DCI investigated a technique which will, upon demand, double the force out of a linear force motor. The technique can be used with either a moving coil force motor or a moving magnet force motor where magnetic saturation with input current does not occur. If applied to a moving iron force motor, the magnetic circuit would have to be designed to remain relatively unsaturated for both the normal input and enhanced control input. For the investigation, DCI modified hardware previously developed for a direct drive control valve flight test program.

Technical Approach

The direct drive servovalve designed by Dynamic Controls, Inc. is based upon using a moving coil in a permanent magnet structure. The suspension used to guide the coil and provide spring centering is a folded design which accommodates packaging. Since it is a moving coil design, the force motor exhibits no output force saturation with increasing coil current.

For the normal (flight test version) DCI force motor, the 40 lb output force used as a design output for the force motor is generated with a total input

current of 1.7 amperes each coil section. The force motor coil uses two sections, each coil section electrically isolated. The output force capability of the DCI force motor design is dependent on the load capability of the flexure pivots used in the folding suspension. The flexure pivots are selected for a particular output force capability, based upon a minimum of 1×10^7 full scale cycles of design load and output deflection.

In order to accept the higher loads associated with the force enhancement technique, the suspension of the flight test direct drive control valve was modified to use larger pivot flexures which had a higher bearing load rating. Using larger bearings required reducing the force multiplication ratio of the linkage relative to that of the flight test force motor. Figure 68 is a plot of the available force from the modified force motor for inputs of up to ± 10 amperes into one coil. Note that the generation of 20 lbs output from one coil requires 2 amperes into a single coil section. This is higher current (2 amps vs. 1.7 amps) than the flight test force motor at the same force output. This difference between the input levels reflects the change of the linkage ratios.

To increase the force output of the force motor requires increasing the input current. Because of the good linearity characteristics of the moving coil force motor, doubling the force output requires increasing the current applied to the moving coil by a factor of two. To provide the increased force capability on a full time basis requires doubling the driving voltage to the coil and doubling the current output of the driving amplifier. For example, for the DCI direct drive coils with a 10 ohm resistance for each coil section (including the external connecting wire and coil current feedback resistor), the driving voltage must increase from 17 to 34 volts. The power supply for the driving amplifier would have to increase in size and weight. For example, the DC to DC inverters used with the DCI direct drive F-4 aileron actuator flight tested at Edwards Air Force Base (reference AFWAL-TR-82-3035) were Abbott Transistor Laboratories Model CC 16D2.0 (providing 2 amperes at 16 volts). These supplies weighed 3.9 lbs and had a volume of 71 cubic inches. The nearest Abbott supply towards meeting the double voltage and current requirement is Model CC 30D3.5 (3.5 amperes at 30 volts). This supply has a volume of 145 cubic inches and weighs 7.9 lbs, a nominal weight and volume increase a factor of 2. In addition to the power supply size increase associated with the force output capability doubling, the servoamplifier used to drive each coil would also become physically larger in order to dissipate the increased heat associated with the increased output power level.

The penalty in terms of weight and volume is considerable for a capability that may never be used. If the increased force requirement is viewed as an emergency mode, there is available another approach to the valve jam problem. The contaminate which causes a spool jam can be considered a temporary problem that requires additional energy from the force motor for a very short period of time. To provide this additional energy, a low cost energy storage system could be applied.

The approach in providing an energy storage system for the force motor was to store the energy in a capacitor. The energy is then discharged into the force motor coils as required. Discharge of the capacitor into the direct drive valve coil would occur when the electronics of the control system determine that a spool jam has occurred. In order to determine when a spool jam has occurred, the following is worthwhile considering:

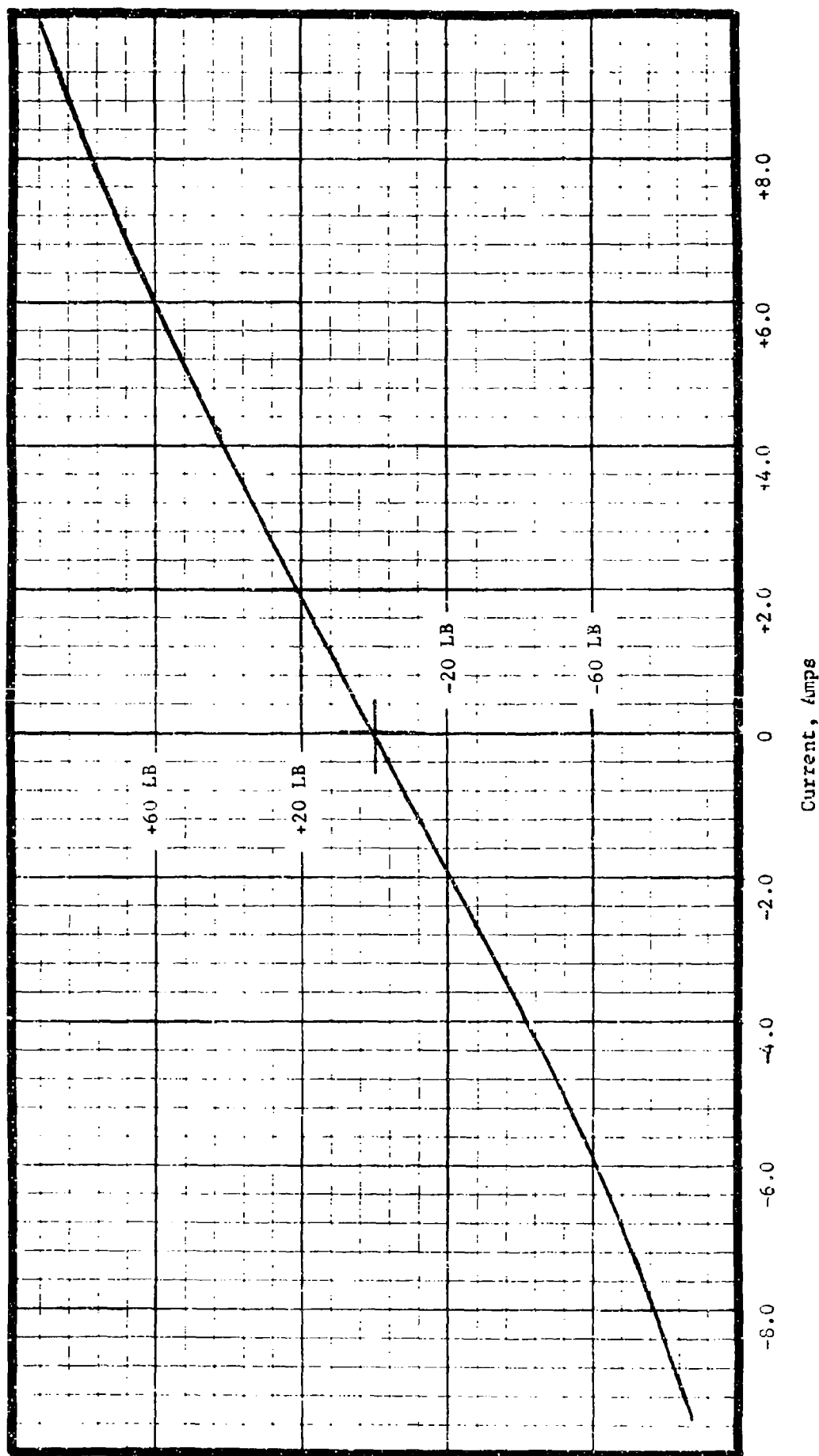


Figure 68. Force vs Current, + 10.0 Amp Input

1. **Forward Path Error Voltage** - The forward path error voltage can be monitored. When the amplitude exceeds that required to produce the maximum normal current input into the direct drive valve, the energy storage system can be activated. The polarity of the error voltage being monitored can be used to determine the polarity of the current enhancement applied to the system. Note that there are two conditions which normally would cause the energy storage system to activate when not needed. These are when velocity saturation or position saturation of the actuator occurs.

2. **Actuator Position** - For position systems where the actuator position reaches its mechanical limits before the input command amplitude saturates, the forward path error can build to a value greater than that necessary to create the maximum normal input current into the valve.

3. **Command Input Characteristics** - For step inputs and sinusoidal inputs of large amplitude, the actuator cannot respond rapidly enough so that the error voltage (input command minus the actuator feedback voltage) remains below the level for maximum normal input current to the servovalve.

4. **Error Voltage Polarity** - For a normal operating control valve, the direction of the actuator motion and the error signal polarity have a constant relationship. When a control valve is held open by contaminant carried into the flow porting of the control valve sleeve, the relationship between the actuator motion and the error signal reverses from normal. This is because the system in which the actuator is used will command the actuator to stop and return as it continues to move in response to the jammed open control valve.

There are several techniques for determining when a control valve jam occurs. The following use forward path error voltage monitoring as part of the technique:

a. A math model of the actuator control loop can be used to generate a prediction of the forward loop error voltage. The math model includes the velocity and position saturation characteristics and uses the actuator load instrumentation to modify actuator rate prediction. This model technique does involve using the actuator position, actuator command and actuator load signals as inputs to the model. Deviations of the actual forward loop error from the predicted error can be used to initiate the force enhancement operation.

b. If the flow control ports in the valve-sleeve combination are of a shape where the length of the port is greater than the width (as in an F-16 ISA main control valve), the contaminant (such as a piece of lock wire) would hold the control valve open at a position which is less than maximum valve stroke. The actuator would then move at some velocity less than maximum rate. At the same time, because the actuator was not tracking the input commands, the forward path error voltage would increase to greater than that for maximum rate of the actuator. The condition of the actuator rate being less than maximum rate and the forward path error voltage being greater than that for maximum rate can be used to initiate the force enhancement operation.

c. If the forward path error polarity and the polarity of the actuator rate disagree from the normal relationship, a jam can be declared and the force enhancement operation initiated. An amplitude threshold for the polarity comparison should be used to prevent "nuisance" force enhancement operation with low amplitude signals and noise.

Although any of the preceding techniques can be used to identify a jam condition and initiate the action for applying additional force to the control spool in order to free the jam, the same energy storage force enhancement mechanization would be used for all jam identification methods. For the force enhancement investigation, the jam determination technique used was technique "b" preceding, with the "jam identification" criteria being the actuator velocity below some percentage of maximum rate and the forward path error being above the level to generate maximum actuator rate.

Figure 69 is a logic diagram for the particular technique used for the investigation to identify a jam. Note that the criteria of the actuator velocity being less than 25% of maximum rate and the forward path error minimum level criteria of 200% of maximum velocity was used. The additional logic decisions shown on Figure 69 relate to whether the charging system has stored the charge necessary and whether the actuator velocity and forward path error criteria being met are caused by the actuator being "bottomed out". Note that the polarity sign of the error corresponds to applying a force to the spool which would cause the spool to move in a direction to drive the actuator towards a particular end stop. This relationship is the same force to actuator direction relationship of the normal operating system.

Upon force enhancement activation by the logic diagram of Figure 69, a charged capacitor is connected to the supply voltage of the servoamplifier driving the servovalve coil. This momentarily boosts the output voltage applied to the servovalve coils in the proper polarity. The servoamplifiers used in the flight test hardware designed and fabricated by DCI used Burr Brown Model 3572 operational power amplifiers. These amplifiers are capable of a continuous 60 watt output (up to ± 30 volts at ± 2 amperes). The amplifier specifications allow up to ± 5 amperes for a duration of 5 milliseconds. For this particular amplifier, the supply voltage to one side of the supply could be increased to 43 volts (maintaining the total differential supply voltage at or below the 60 volt manufacturer's limit) without exceeding the short term current limits.

In selecting the force enhancement pulse duration, some criteria needs to be applied. The criteria used for the research activity was that the pulse length be long enough to allow the valve to move through its full peak stroke as a minimum. For the direct drive valve used with force enhancement investigation, the response of the valve was -3 Db at 60 Hz (referenced to a stroke of ± 0.014 inches at 1 Hz. This corresponds to a first order response with a time constant of 2.6 milliseconds. For the application of a pulse amplitude sufficient to drive the spool to twice its normal stroke or 0.028 inches, the spool motion in 5 milliseconds can be estimated from the step response expression for a first order lag system with a time constant of 2.6 milliseconds as follows:

$$X_{out} = X_{in} (1 - e^{-T/\tau})$$

Where: T = the pulse duration in milliseconds
 τ = the system time constant in milliseconds
 X_{in} = the steady state input displacement

$$X_{out} = 0.028 (1 - e^{-5/2.6})$$

$$X_{out} = 0.024 \text{ inches}$$

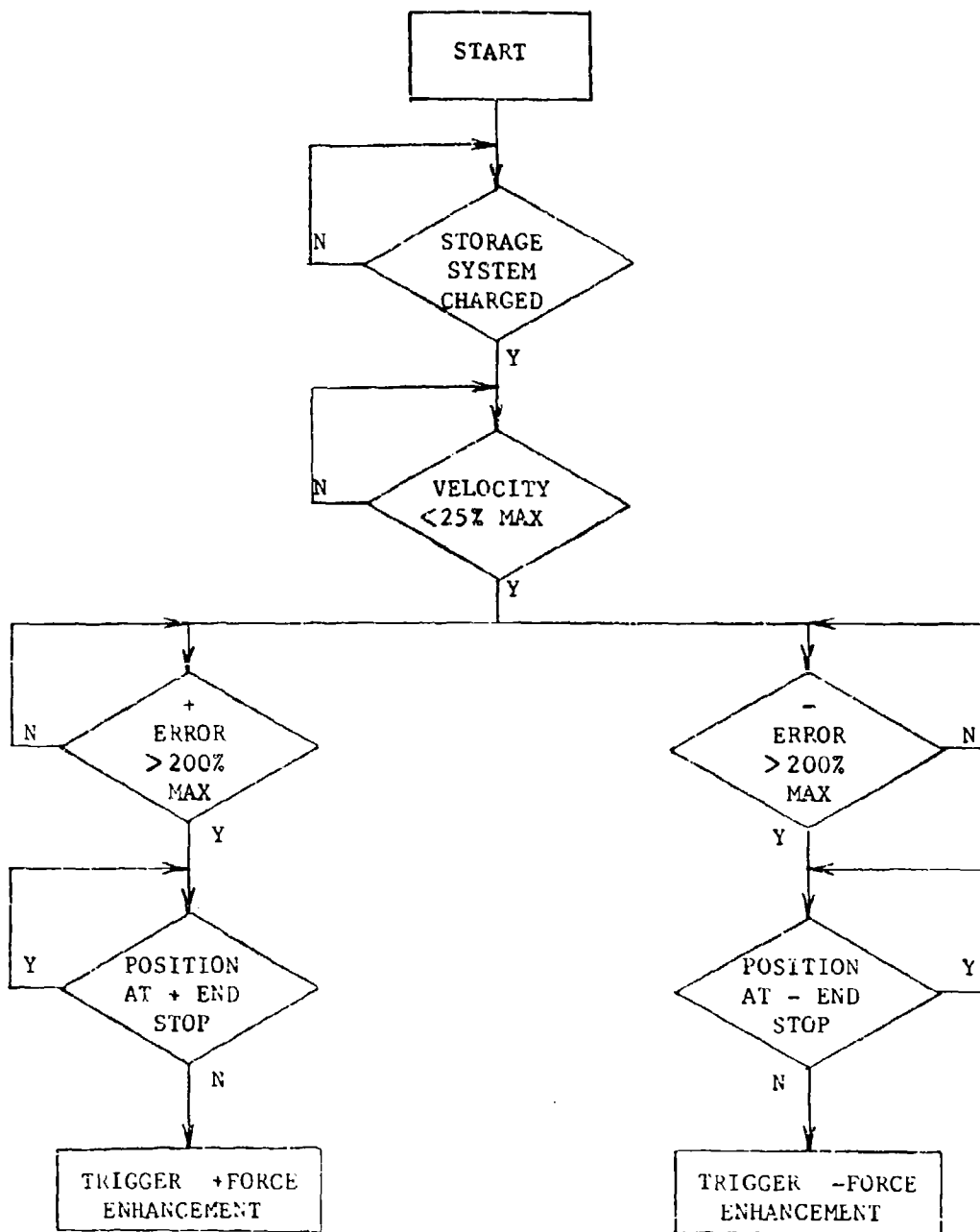


Figure 69. Enhancement Logic Tree

From this calculation, it is apparent that a 5 millisecond force enhancement pulse is more than adequate to move the control valve through more than its normal peak stroke of 0.014 inches.

With some servovalves, the L/R time constant can be a significant portion of the response time constant. For the moving coil force motor used for the force enhancement investigation, the 10 ohm coil had a measured inductance of 0.001 henrys. This gave an L/R time constant of 1×10^{-4} seconds which is less than 4% of the valve response time constant and 2% of the pulse duration. The L/R time constant of the valve would therefore not affect the operation of the pulse force enhancement circuit.

Figure 70 is a photograph of the force enhancement test setup. As shown in this figure, the failure detection electronics were breadboarded on a separate chassis. The solid state relays used to connect the storage capacitor to the supply of the servoamplifier were also mounted in the chassis. The demodulator shown in this figure was used with the load cell to measure the force output of the servovalve driver. The force motor and the control valve of the flight test hardware were mounted in the fixture. One force motor was removed from the direct drive control valve assembly in order to couple the force motor output through the control spool to the load cell. The force motor test assembly is shown mounted in the vertical position. This position was selected in order to retain the fluid in the magnet structure of the force motor for heat transfer from the direct drive coil.

Mechanical Design

As stated previously, the direct drive valve used for the force enhancement evaluation was developed for a flight test program and had a design force capability of 80 lbs minimum at null. In order to accept the higher force output capability of the coil with the force enhancement electronics, the suspension system required modification. The original suspension system had a design maximum load capability of 120 lbs. The redesigned suspension provided for an allowable output force of 240 lbs. This provided an indefinite suspension life while operating at the normal 40 lb maximum output. Operating at 106 lbs output would provide an estimated life of 25,000 cycles. Since force enhancement should normally be required very infrequently in the life of a control valve, the 25,000 cycle life appeared adequate.

The larger load capacity suspension required that the linkage ratio be reduced from 6.9:1 to 5.11 in order to fit into the original force motor package envelope. Since the linkage ratio is the force multiplying of the force of the coil to the output force, the modified force motor had a slightly lower force gain in lbs/ampere than the original design. However, the force enhancement electronics provided higher peak levels of output force without causing damage to the suspension system.

Electronic Design

The normal direct drive control electronic specifications before modification with the force enhancement design were as follows:

Servoamplifier Gain: 0.38 amperes/volt

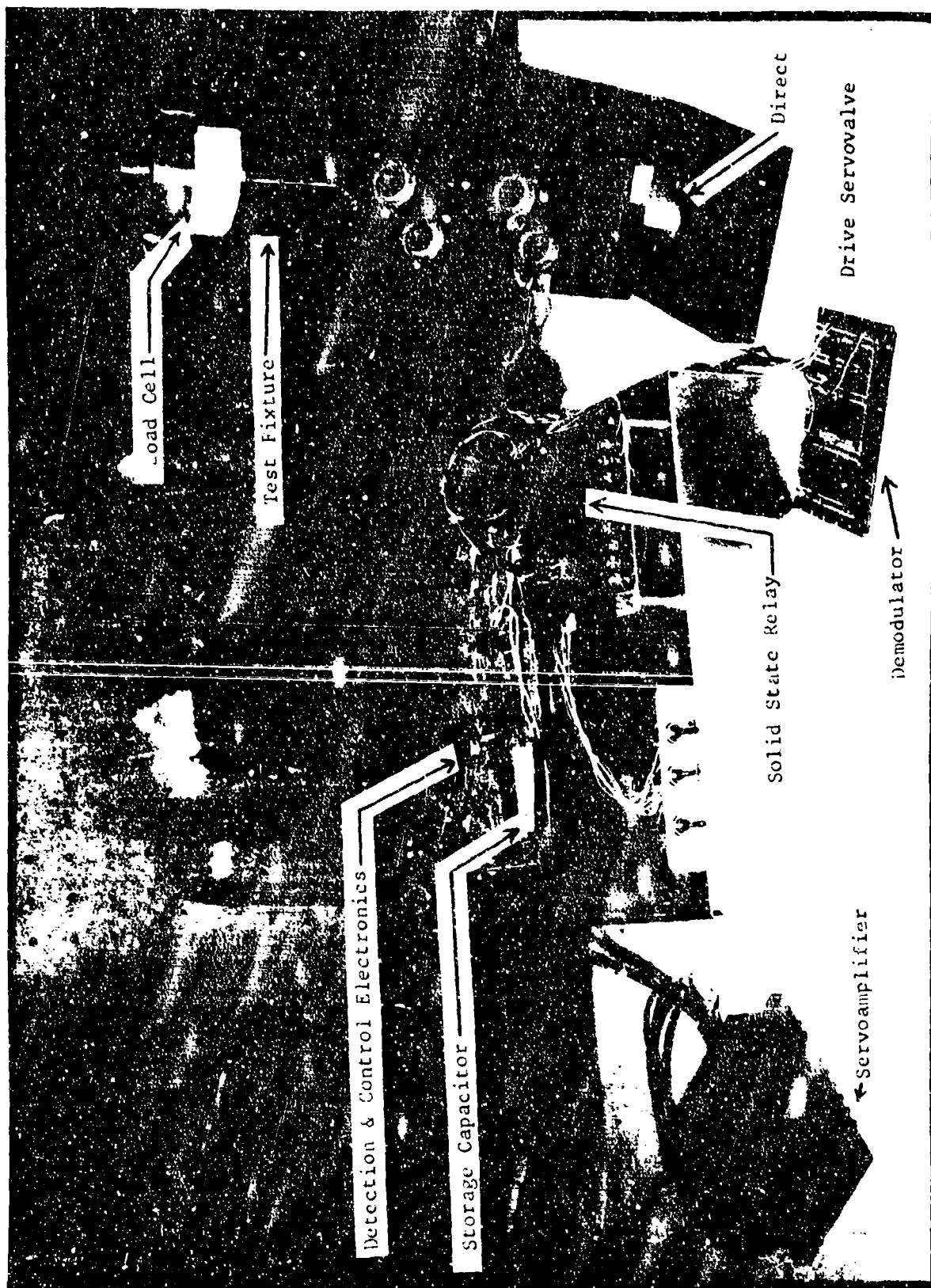


Figure 70. Force Enhancement Test Setup

Supply Voltage: ± 17 volts

Coil Resistance: 9.5 ohms

The normal driving current to the force motor coil was limited to ± 1.6 amps by the supply voltage of ± 17 volts. In addition, the amplifiers incorporated external current sensing resistors which were sized to limit the current to ± 1.7 amperes for amplifier protection. As part of the force enhancement modifications of the control electronics, the current sensing resistors were changed to allow a current output of ± 5 amperes. In addition, the 0.05 microfarad capacitors originally connected between the amplifier's supply voltage input and ground were removed. This prevented the supply line filter capacitors from absorbing part of the force enhancement pulse. To prevent the normal power supply from suppressing the enhancement pulse, diodes were installed in the supply lines. These diodes prevented current flow back into the ± 17 volts supply lines.

Figure 71 is the schematic of the electronics for the force enhancement circuit. Only the servoamplifier enclosed in dotted lines is part of the normal force motor or control loop electronics. All other electronic components shown on the schematic are associated with providing the force enhancement capability.

Comparators U_1 , U_2 and U_3 are quad comparators used to make the logic decisions for the jam determination. Comparators U_{1-1} and U_{1-2} are set for trip levels which are double the normal ± 4.2 volt servoamplifier input voltage for maximum valve position. These comparators identify when the forward path error voltage is at least 200% of the forward path error voltage for peak control valve stroke. Comparators U_{1-3} and U_{1-4} identify when the actuator is at the mechanical extend or retract end stop positions. Note that the "pullup" resistor for the extend command and extend endstop comparator outputs is shared. The "pullup" resistor for the retract command and retract endstop comparator is also shared. This technique prevents force enhancement when the actuator is commanded hardover and reaches the end of its stroke. U_{2-1} and U_{2-2} are used to identify actuator velocities greater than 25% of the full slew rate velocities. The actuator velocity is derived from the actuator's position transducer output signal. For the test setup, the integration of the actuator was modeled electronically. With this test setup, the onset of actuator rate changes has no time delay relative to the forward path error signal. With the actuator in hardware form, a passive time delay filter would have to be inserted in the forward path error signal to the comparator. This filter is required to compensate for the dynamic response characteristics of the servovalve causing a phase shift between the error voltage and the actuator rate signal.

Test switches S_1 , S_2 and S_3 are provided to simulate conditions causing the enhancement logic to operate. U_{2-3} and U_{2-4} determine the charge status of the storage capacitor. U_{3-1} and U_{3-2} are used as AND gates to provide the monostable multivibrators U_{4-1} and U_{4-2} with a pulse when the enhance conditions are met. The pulse duration from U_{4-1} and U_{4-2} had an adjustment range of 3 to 8 milliseconds. The pulse duration for the evaluation testing was set at 5 milliseconds.

The output transistors Q_1 and Q_2 drive, $K_1 + K_2$ and $K_3 + K_4$ optically isolated solid state relays respectively. Two relays are required for connection of the

capacitor to the + supply line and two relays for connection to the - supply line. The increased voltage is isolated from the supply lines from the normal ± 17 volt power supply.

The charging voltage for the energy storage capacitor is generated from the transformer coupled rectified output of the wein bridge type oscillator using amplifier A_1 . The design oscillator frequency was 10 KHz. The output amplitude of the oscillator was adjustable in order to establish the charging voltage level.

Test Procedure

The modified direct drive force motor was mounted in the test fixture and connected to the Daytronic 520-100 load cell. The load cell signal conditioner gain was verified at 10 lbs per volt. The rate frequency response of the load cell and its electronics was rated at less than -3 Db at 1,000 Hz. The operation of the enhance electronics and force motor output was verified by recording the following:

1. The resonance frequency of the suspension (by recording the velocity generated open circuit voltage of one of the force motor coils while driving the other).
2. The force output of the valve drive with up to a ± 3 ampere input (by recording with an x-y plotter the output of the force transducer vs the input current from a separate DC amplifier).
3. The time history of input, current output, force output and enhancement pulse while holding the position input at zero volts. (The input was varied at a rate of 0.4 volts per millisecond from zero to positive full scale and from zero to negative full scale. The time history was recorded with an FM instrumentation tape recorder in order to record the response correctly and then transcribed to a Brush chart recorder at a slower tape speed in order make a strip chart record.)

Test Results

During the initial checkout, it was found necessary to modify the force enhancement electronics. The first modification was a reduction of the U_4 supply voltage to 5 volts. This was necessary because when 17 volts DC (near the rated maximum of 18 volts DC) was used as the supply voltage, the positive and negative enhance pulses would both be applied when only one was commanded. The second modification involved the solid state relays. Because of transient suppression diodes built into the relays, the relays drew excessive current. The circuit modification to solve this problem involved adding D_6 and D_7 isolation diodes to prevent a power supply shorting mode. No other modifications were required for satisfactory operation of the electronics for the force enhancement operation.

Figure 72 is a plot of the velocity motion of the valve and modified force motor assembly. Since the coil of the force motor was wound with two coil sections, the output motion was measured by driving one coil with a servomplifier and monitoring the voltage generated by the second coil moving in the magnetic field of the force motor's air gap. For this plot, an input current of ± 1.0 ampere was used. At 1 Hz, a stroke of ± 0.024 inches produced an

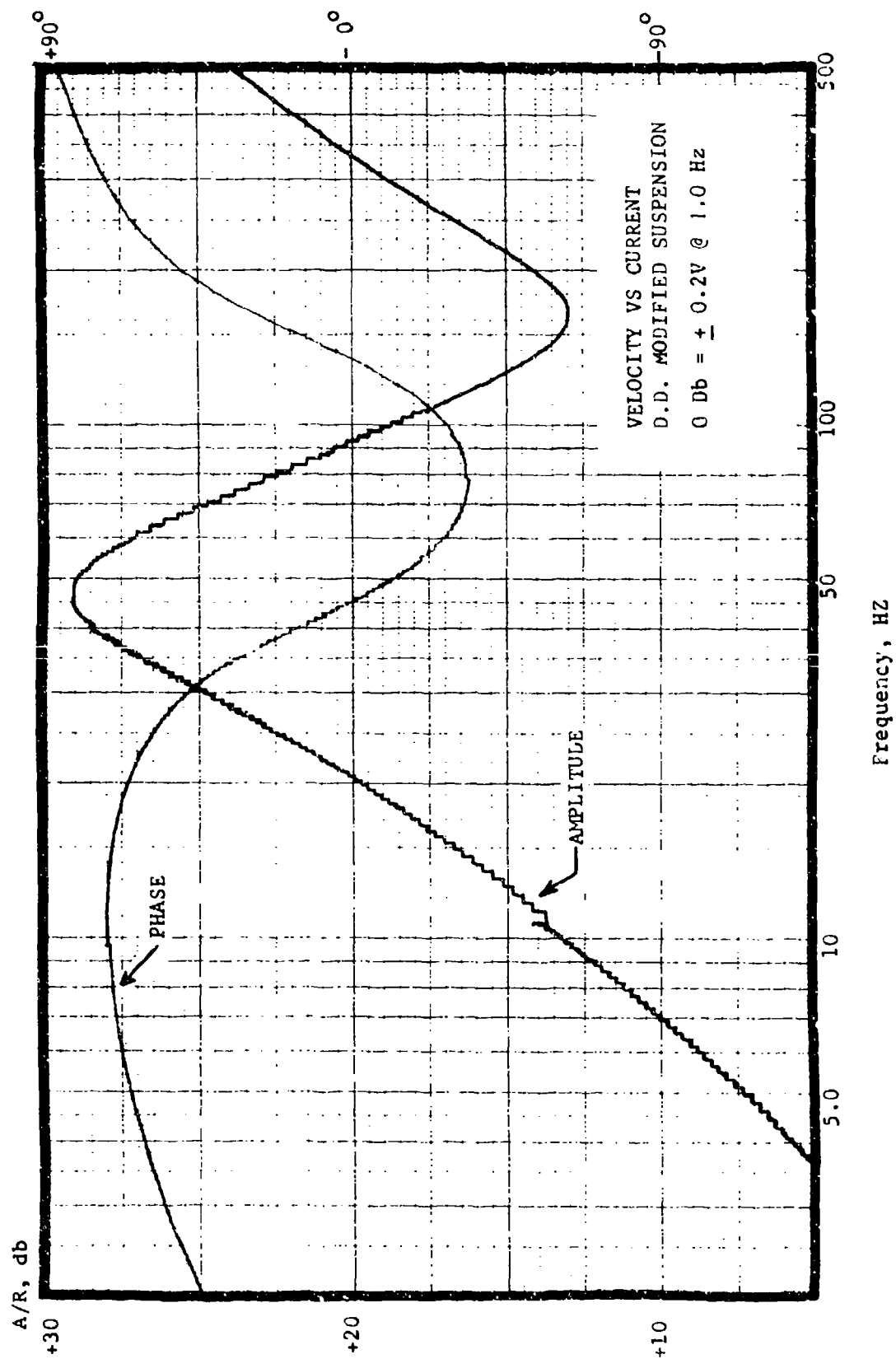


Figure 72. Suspension Resonant Frequency

output voltage from the monitor coil of ± 0.2 volts. From Figure 72, the frequency at which the phase angle has undergone a change of -90 degrees from the low frequency phase angle is nominally 50 Hz. This frequency is the natural frequency of the control valve with the stiffness of just one suspension. With both force motors connected to the control spool, the resonance frequency of the assembly will be near 65 Hz since the stiffness of the assembly is doubled while the moving mass is increased by a factor less than 2 (the spool mass dominates the moving mass of the assembly). The resonance peak of the velocity (deviation from a straight line rise of 6 Db/octave) is +2.5 Db. This corresponds to a second order system damping ratio of 0.45. The damping of the resonance peak is created by a combination of viscous damping of the coil in the oil filled force motor and the eddy current damping of the coil in the magnetic field.

Figure 73 is a plot of the force output of the modified force motor with an input current variation of ± 3 amperes. This plot was made using a Crown 300A amplifier rather than the normal servoamplifier used with the direct drive valve (since the normal servoamplifier is limited to 2 amperes output steady state). This plot verifies the linearity of the force motor operation over the current limits of the force enhancement. Note that the linearity is within 2% full scale over the ± 3.0 ampere range of the input current.

Figure 74 is a plot of the force output of the modified force motor with the normal servoamplifier providing the excitation current. The linearity is similar to that shown on Figure 73. Because of the expansion of the input current scale, some hysteresis appears at the ends of the plot. The hysteresis as shown on Figure 74 is a reflection of the friction in the suspension and spool.

In order to produce a hard copy of the force enhancement input-output time history characteristics, the data was first recorded on a Hewlett-Packard Model 3960 4 channel FM magnetic tape recorder at a recording speed of 15 inches/second. The data was then played back at 15/16 inches/second into a Gould-Brush Model 200 strip chart recorder at a chart speed of 100 millimeters/second. This conversion produced a time scale of 6.25×10^{-4} seconds/division for the strip chart data presented in Figure 75 and Figure 76.

Figure 75 shows the force enhancement operation in response to a negative ramp input for the forward path error signal. When the ramp amplitude reaches -8.5 volts (200% of the normal forward path error voltage level for maximum actuator rate), the force enhancement circuit is activated. Note that as the error voltage ramp builds up, the input current to the coil increases to 1.5 amperes and the output force increases to 14 lbs. These levels are the normal saturation levels for the servoamplifier and modified force motor. The normal saturation levels are achieved when the forward path error voltage reaches -4.3 volts. When the force enhancement is activated, the input current into the coil increases to 3.1 amperes for 0.005 seconds. The output force rises for the same time period to a peak value of 36 lbs. The 36 lbs is greater than the value of 31 lbs expected from the steady state force gain of 10 lbs/ampere measured. The 5 lbs difference is the overshoot associated with the step response of a system with a damping ratio less than 1.0. The slight force drop off before the current pulse is removed is associated with the overshoot of the step response of the system. The force build up takes nominally 4 milliseconds to reach the peak value. Note that the enhance pulse of 4 volts as shown on the lower trace of Figure 75 defines the time limits of the force enhancement.

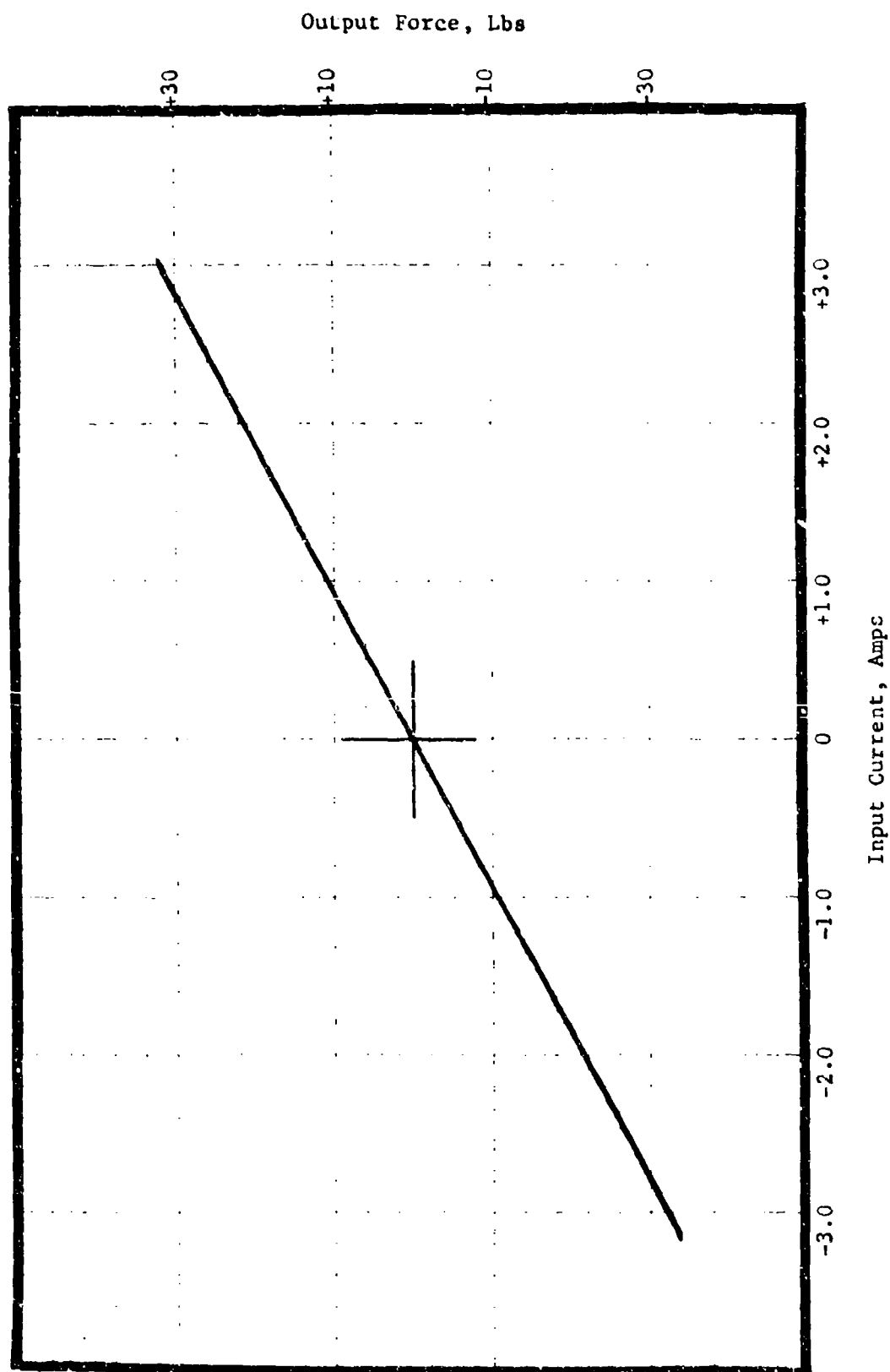


Figure 73. Force vs Current, +3.0 Amps
D.D. Modified Suspension

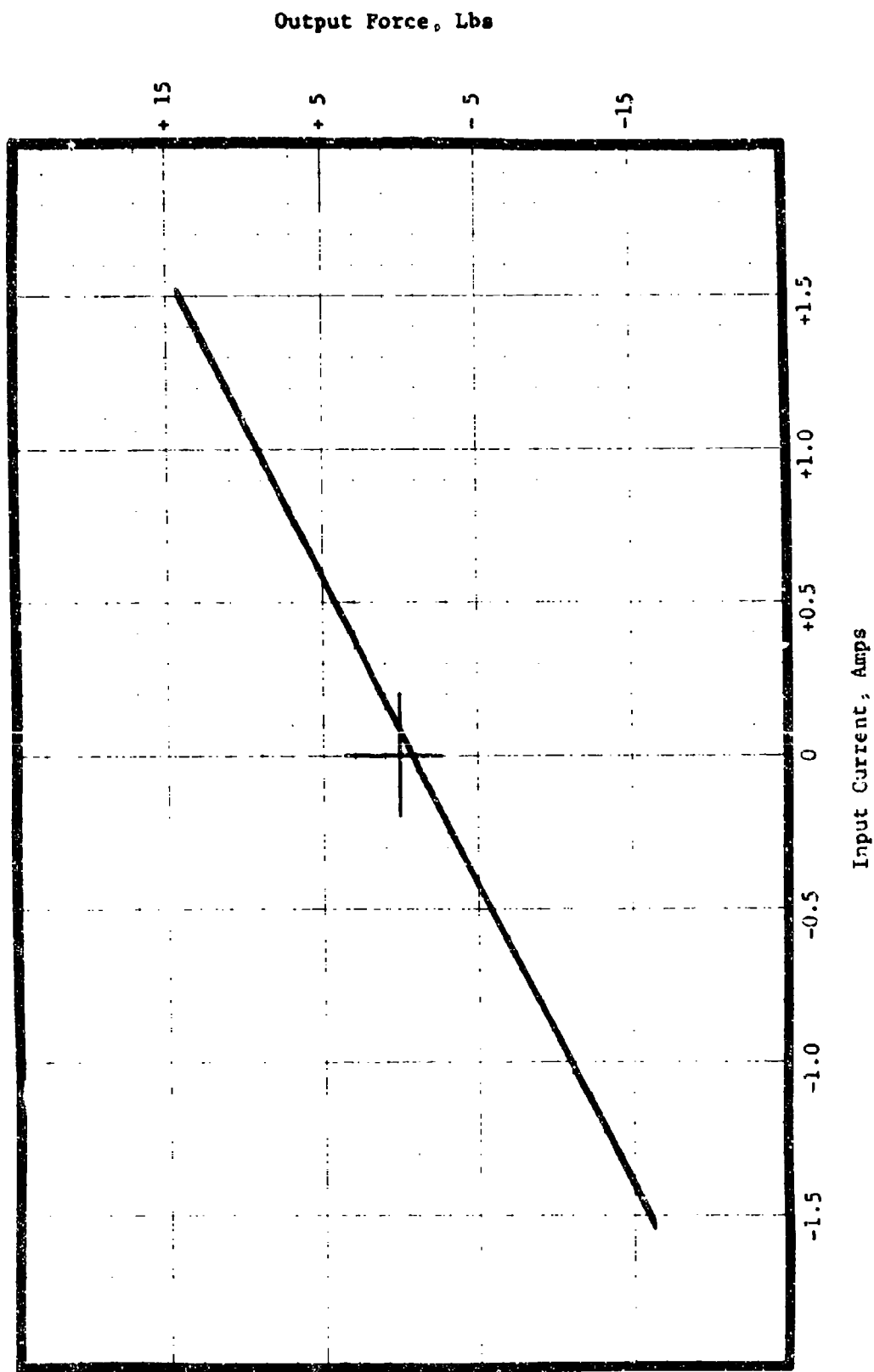
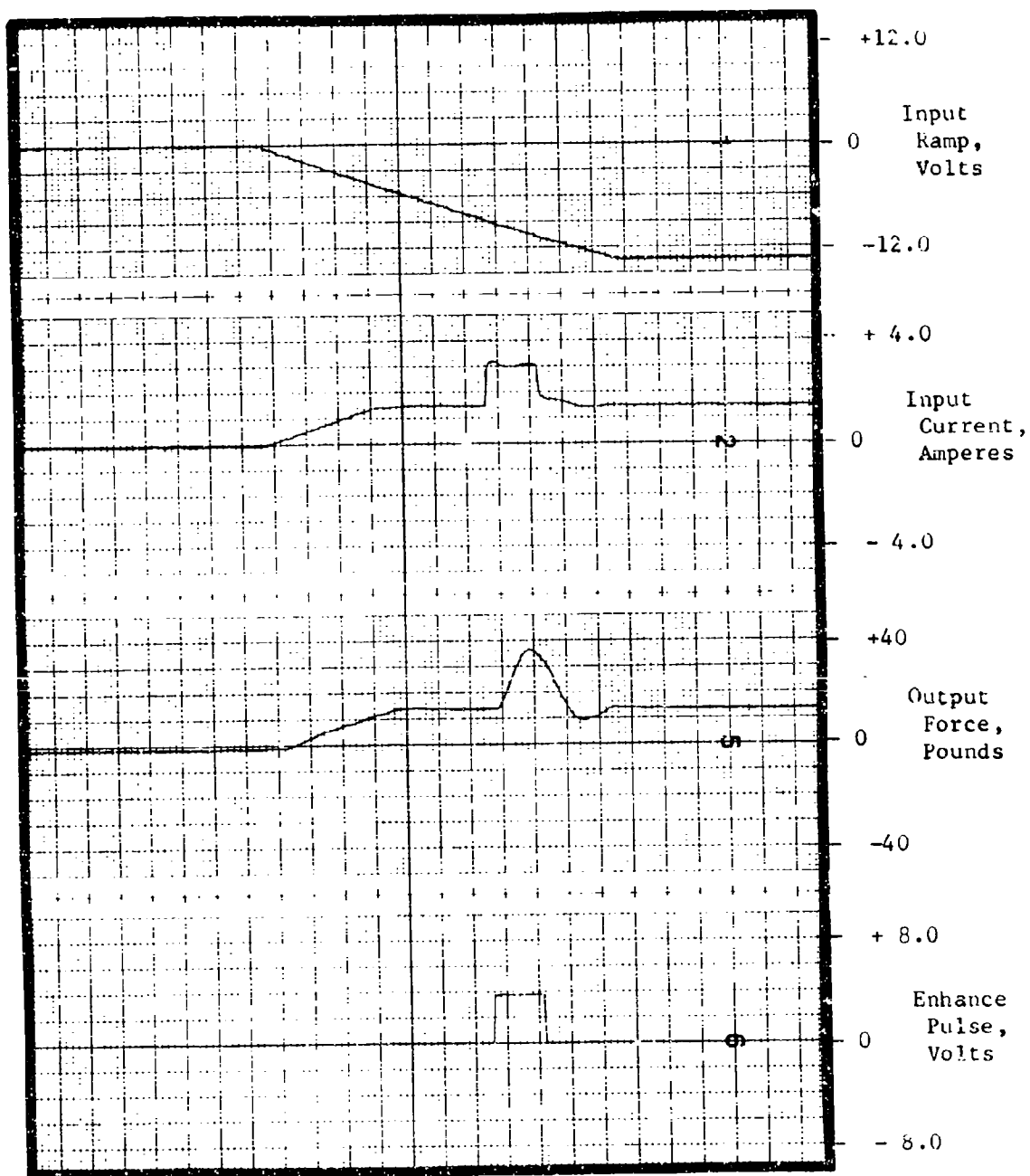


Figure 74. Force vs Current, +1.5 Amps
D.D. Modified Suspension



Time Scale Factor = 6.25×10^{-4} sec/division

Figure 75. Negative Current-Force Enhancement

Figure 76 shows the force enhancement operation in response to a positive ramp input for the forward path error. The operation is very similar to negative ramp input. The second order response characteristics of the output force is evident in the force response trace after the removal of the enhance pulse. The peak output force level obtained is -36 lbs, corresponding to a current level -3.1 amperes.

Conclusions and Recommendations

The investigation verified that the output force of a moving coil force motor can be doubled on an "as required" basis to provide short term chip shearing capability. The energy storage technique used in this investigation minimizes the weight and volume penalties of providing additional force capability for a moving magnet or coil force motor. The technique can also be applied to a moving iron force motor as long as the soft iron circuit remains relatively unsaturated.

The force enhancement technique used for this investigation was applied to only one of the four driving coils of the direct drive control valve. If applied to the original flight test configuration with the normal linkage gains, the available force for driving the spool would increase from 80 lbs to 160 lbs.

The breadboard hardware configuration is a good application for a dedicated microprocessor, since the force enhancement electronics involve only logic functions and timing circuits.

It is recommended that the energy storage force enhancement be considered in the design of a flight control system using direct drive. The technique allows meeting chip shear force requirements while designing the normal electronic driver for the force required to position the spool against the normal flow forces and suspension spring rates.

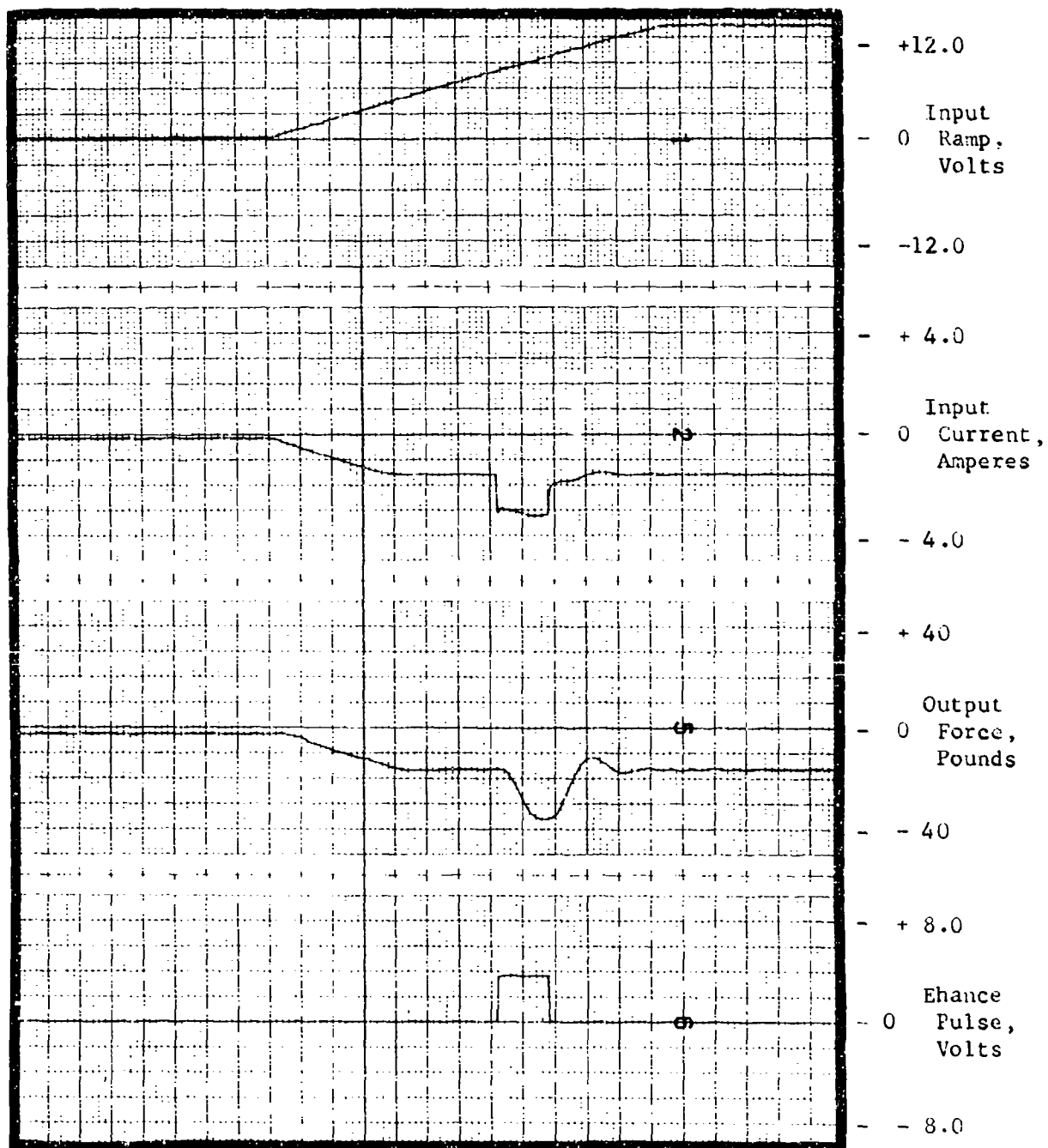


Figure 76. Positive Current-Force Enhancement

SECTION V. DIGITAL INTERFACE STUDY FOR HYDRAULIC CONTROL SYSTEMS

General Discussion

Applying a digital computer as a controller for a hydraulically powered control system requires special consideration at the points of interface. The digital controller operates from a time base with information processed in a binary format made up of discrete signals. The hydraulic portion of the control system is analog and operates in real time. The study described in the following material was an evaluation of the effect of a pulse width modulation interface on the life of the analog electrohydraulic hardware.

Interface Overview

Figure 77 illustrates the interface areas typical with using a digital controller with an analog electrohydraulic control system. As shown in this figure, the interface both in and out of the digital controller is a conversion. An analog to digital converter is used for the inputs to the controller and a digital to analog converter for outputs to the electrohydraulic portion of the control system. The inputs to the system and the feedback signals can be either analog or digital. The input command can be from another computer or an analog signal. The feedback signal from the output of the electrohydraulic control system can be created by a digital encoder or an analog output transducer. Although direct conversion of the digital output of the controller to valve flow commands have been accomplished within the servovalve in research programs, the generally accepted interface between the digital controller and the electrohydraulic servovalve use one of the following two techniques:

- a. A digital to analog converter (D/A) (as shown in Figure 77)
- b. Pulse Width Modulation (PWM)

The use of a D/A converter provides an analog signal to the servovalve which is much like that which would exist if the control system used an analog controller. The pulse width modulation signal is created by the controller and is a form of binary output suitable for driving the electrohydraulic control valve. The advantages of the PWM technique over using an A/D converter and analog amplifier are simplicity and size. The size advantage comes from both the elimination of the converter module and heat sink necessary for half power cooling of an analog amplifier. Because the PWM output is a two state output (on or off), the power dissipation in the output switching devices is a minimum for any output power required to drive the electrohydraulic servovalve.

Using a digital controller for an analog system operating in real time requires attention to be given to the following three basic parameters:

1. Update rate (sample rate)
2. Throughput time

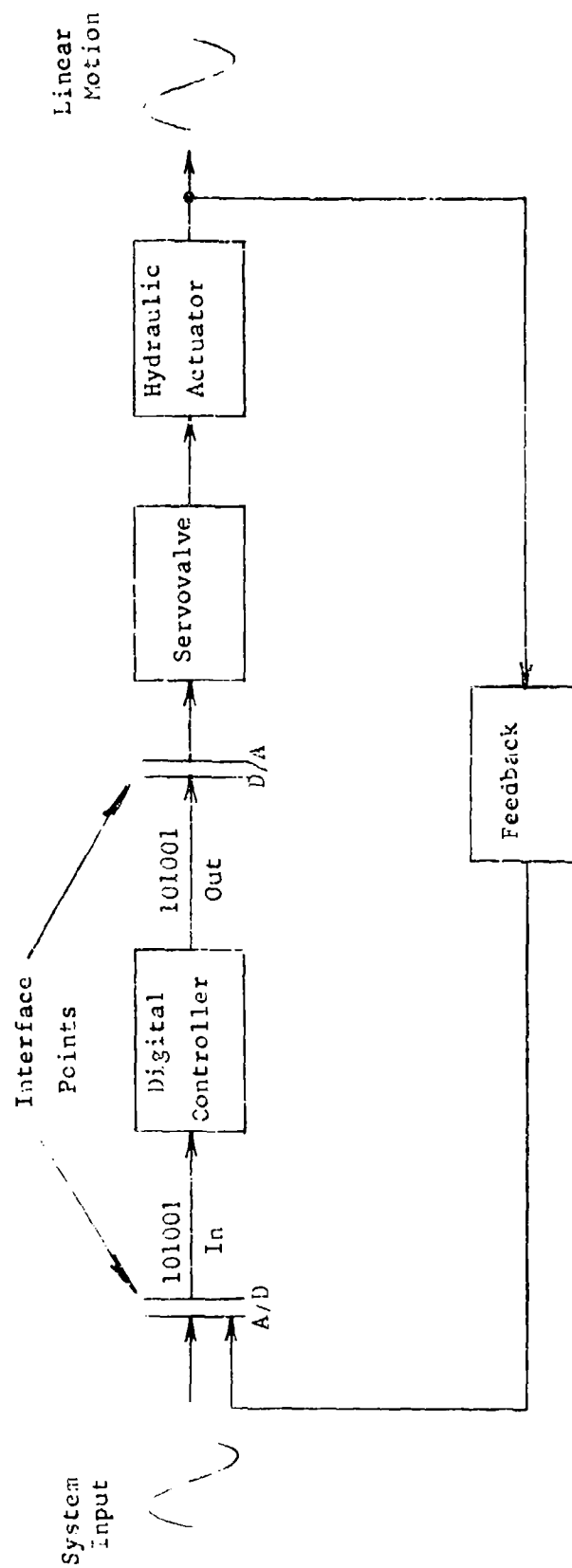


Figure 77. Analog - Digital System Interface

3. Signal resolution

Update Rate

The update or sample rate used by the digital controller is determined by the dynamic performance requirements of the total system. Based upon test results of using a digital controller with an electrohydraulic system (reference report AFFDL-TR-77-30), sampling at a frequency 8 times or higher than the bandpass frequency of the control system is recommended. The bandpass frequency is defined as the frequency at which the amplitude ratio of output to input is attenuated by 3 Db or the output lags the input by a phase angle of 90 degrees, whichever frequency is lower.

This criteria for the sampling frequency is consistent with sampling at a minimum of 2 times the highest frequency of interest in order to prevent aliasing (the Shannon sampling theorem). Consider that the typical rolloff rate of the amplitude ratio for an electrohydraulic actuator system is 20 Db/octave for a first order system (one in which the servovalve response is at least 10 times higher than the control loop response) or 40 Db/octave for a second order system (where the servovalve frequency response is 2 to 4 times the control loop frequency response). In choosing the sampling frequency, the selection of the "highest frequency of interest" determines the sampling frequency. The frequency at which the output amplitude is attenuated by 40 Db is a conservative choice for the "highest frequency of interest". The frequency response of a control system is normally measured at an input amplitude of from 2% to 5% of the maximum command input (corresponding to the same percentage of output deflection). Attenuation of 40 Db from a 5% output would be where the output amplitude decreases to 0.05% of the maximum output. This frequency for a second order system would be nominally a decade (10 times) higher than the system break frequency. This would require sampling at a frequency 20 times the break frequency to ensure that the amplitude of any aliasing of the output signal was below 0.05% of the maximum output amplitude. For the minimum 8 times criteria for the sampling frequency, assuming a second order roll off of 40 Db/decade and a 5% input command, the output amplitude at the frequency at which aliasing would occur is 0.315% of the maximum output amplitude, a level which may be acceptable for most systems.

Throughput Time

The throughput time associated with the digital controller appears as a time delay in the control loop. The throughput time is the time period between when an input is sampled and the appearance of the controller output corresponding to the sampled input. The time delay causes a phase lag which is directly proportional to the frequency of the input signal. This phase lag affects the closed loop stability. Decreasing the computational time and the time between samples decreases the time delay and the associated phase lag at each frequency.

Resolution

The accuracy of the controller output can be predicted by scaling the digital input/output value to the full scale analog signal value. The digital word used with electrohydraulic control systems is normally 8, 12, or 16 bits. Each digital word converted by an A/D converter will have 1 or 2 bits of

uncertainty due to the signal to noise ratio of the input signal. The loss of resolution associated with a two "least significant" bits loss is as follows:

- a. 8 bit word $3/2^8 \times 100 = 1.172\%$ full scale
- b. 12 bit word $3/2^{12} \times 100 = 0.073\%$ full scale
- c. 16 bit word $3/2^{16} \times 100 = 0.005\%$ full scale

If the analog signal is not scaled to the maximum digital word value, the resolution loss as a percent of full scale will increase proportionately.

PWM Interface

For a conventional two stage electrohydraulic servovalve, a bipolar input of less than 20 millamperes at 15 volts is required. The output flow from the valve is proportional to the input current. Figure 78 shows a typical PWM signal, generated by producing a pulse within a constant time frame "T". The on time is proportionately commanded by the digital word of the controller. In the case of the 12 bit word with a total count of 4,096 (representing T), a 50% pulse width would be represented by a count of 2,048. The resolution of the pulse width is much the same as that of the digital to analog converter since each count represents a portion $1/2^n$ of the pulse on time.

Technical Approach

The investigation conducted for the interface research activity was directed at evaluating the effect of operating conventional servovalves for extended periods of time with a pulse width modulated signal. Since the pulse width driving signal has a large amount of high frequency energy, the potential for increased wear and/or shortened service life of the servovalve was considered to be a possibility. The approach used for the evaluation was to use two electrohydraulic servovalves operating with the same hydraulic pressure and fluid under the same load conditions. One valve was driven with a PWM signal and the other with an analog signal. Performance measurements and visual inspections were used to evaluate both the absolute and relative degradation of the valves with operating time.

Two new Moog Model 76 servovalves were used for the evaluation. Both servovalves were operated for 300 hours with an input of 50% full scale at a frequency of 10 Hz. One valve was commanded with a pure analog sine wave. The other valve was driven with a PWM signal with an update frequency 4 times the rated frequency response of the valve.

In order to evaluate the effect of PWM on control valve edge erosion, the cylinder ports of the servovalves were interconnected with a restricting orifice set to flow 1 gallon per minute at 3000 psi differential pressure.

To evaluate the trend of wear, four data sets were used. The baseline set of data was taken prior to start of the test cycling and documented the performance of the valves as received. The same set of measurements were made on the valves after 100 hours, 200 hours and 300 hours of operation. The data taken included flow and pressure gain plots. The visual wear trends were recorded using examination under a microscope and macro photographic techniques.

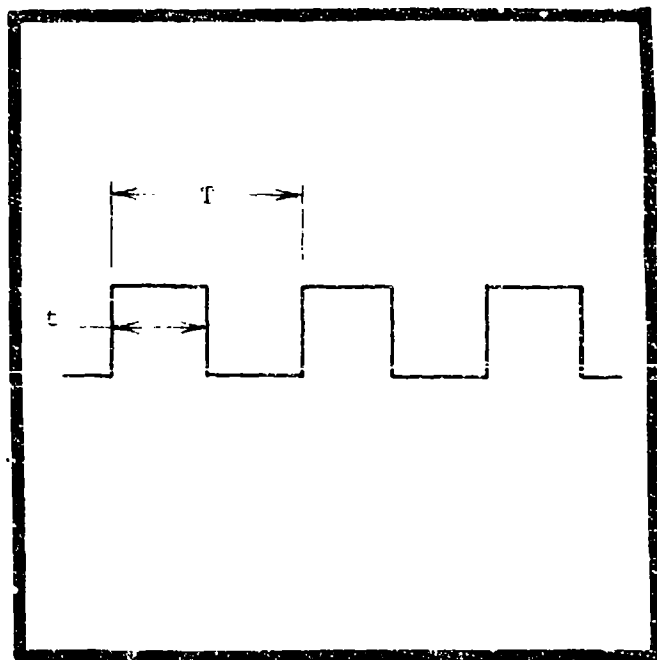


Figure 78. PWM Signal

Interface Evaluation Test System

Figure 79 is a schematic representation of the test system. The test setup consisted of two parts, the electronic control section and the hydraulic supply and load system. Note that the same signal source was used for driving both the analog and PWM electronic driving sections for the servovalves. Figure 80 is a photograph of the test hardware. During the 300 hour test, the system was instrumented full time with a digital thermometer, hour meter, hydraulic pressure transducer and flow meter. The two test units at the left center of Figure 80 are the units which generated the PWM signal from the analog input signal.

Electronic Control Description

An electronic control card was fabricated in order to provide a sinusoidal signal at 10 Hz as an input to the PWM and analog driving sections. Included on the card were the analog and PWM drivers for the servovalves. Figure 80 is the schematic of the control card's circuit. A Wein Bridge Oscillator was used to generate the 10 Hz sinusoidal signal. The output amplitude of the oscillator was adjusted to ± 6.2 volts peak to peak. The output of the oscillator is connected to the servovalve driver through potentiometer R_5 . For the cycling tests, R_5 was adjusted to provide ± 2.0 volts peak to peak from the servovalve driver to the analog driven servovalve. This corresponded to an input current of 0.010 amps which was 50% of the 0.020 amps required to produce maximum output flow from the valve.

As shown on Figure 80, the PWM signal was generated from two units, a Digital Hardware Voter Monitor Tester (DHVMT) and a Digital Hardware Voter Monitor (DHVM) originally produced as part of an AFWAL DAIS program. A description and test evaluation of the DHVM is described in report AFFDL-TR-77-30. The DHVMT is an A/D converter with a variable sample rate capability. The output is a 16 bit word transmitted in parallel to the DHVM. The DHVM converts the 16 bit input into a PWM signal with variable pulse width. For the test evaluation of the servovalve, the DHVMT was set for 1,000 samples/second and the DHVM was set for 244 updates/second.

Hardware driven with a PWM signal normally has high frequency response roll off frequency above which the amplitude to which the hardware responds attenuates at a minimum rate of 20 Db per decade of frequency increase. The roll off characteristic is used as a low pass filter to "decode" the PWM input. The PWM signal with $t = T$ on Figure 78 represents 100% modulation and maximum amplitude of the low pass filtered output of the hardware being driven by the PWM signal. Correspondingly, when $t = 0$, 0% modulation occurs and the minimum amplitude output occurs. The waveshape of the pulsewidth driving signal is a series of square wave pulses. The frequency content of these square waves is determined by the time duration of each pulse. The time duration is a direct function of the update frequency of the PWM signal and the percent modulation. For example, for a square wave of time duration T , the frequency content of the pulse has no attenuation up to a frequency of $0.1/T$ Hz. The amplitude of the frequency content attenuates over the frequency range of $0.1/T$ to $1.0/T$ Hz. The attenuation is from an amplitude ratio of 1 at $0.1/T$ Hz to zero amplitude at a frequency of $1.0/T$ Hz. For example, with $T = 0.00205$ seconds (which is one half the period corresponding to 244 update/seconds), the frequency content has no

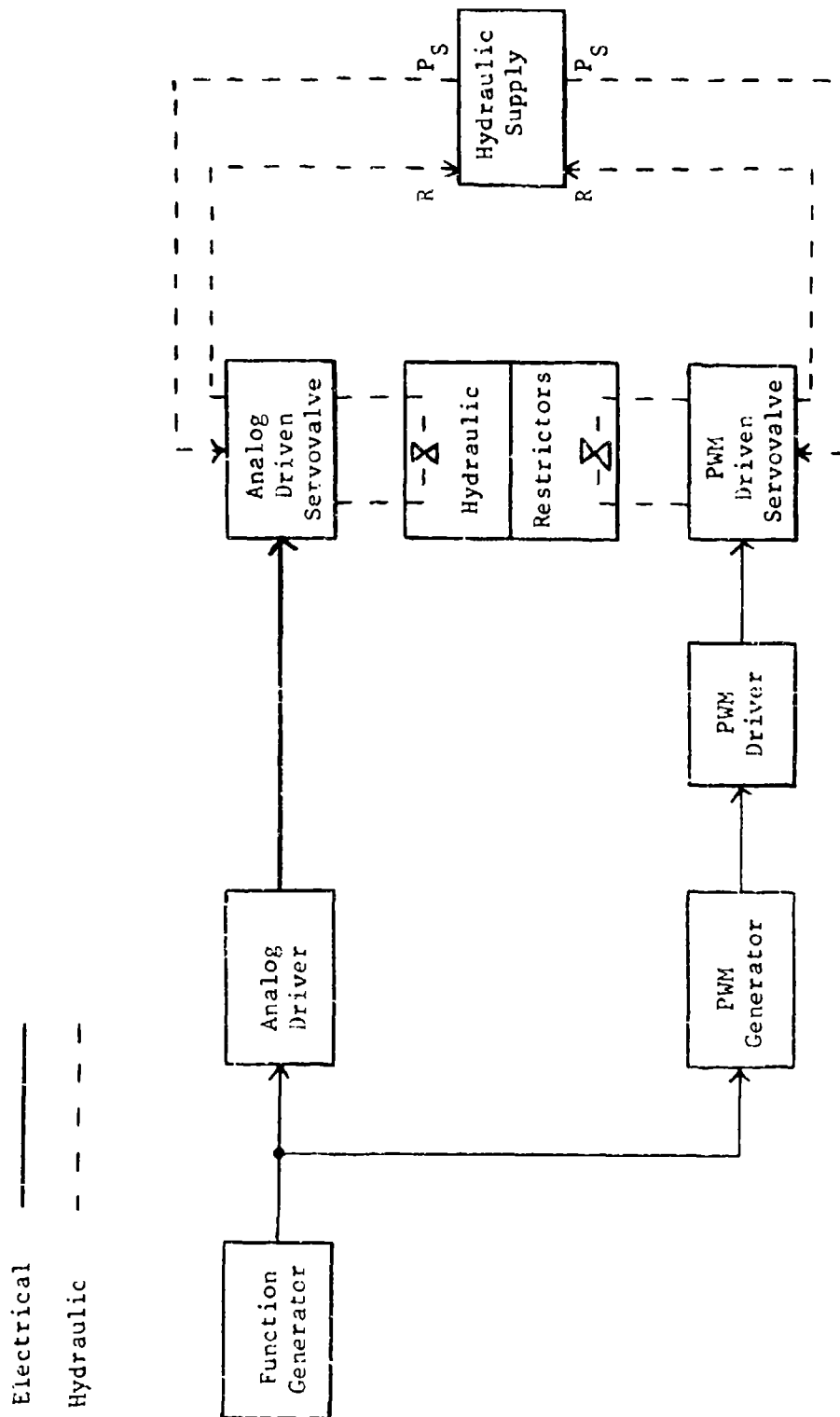


Figure 79. Interface Test System

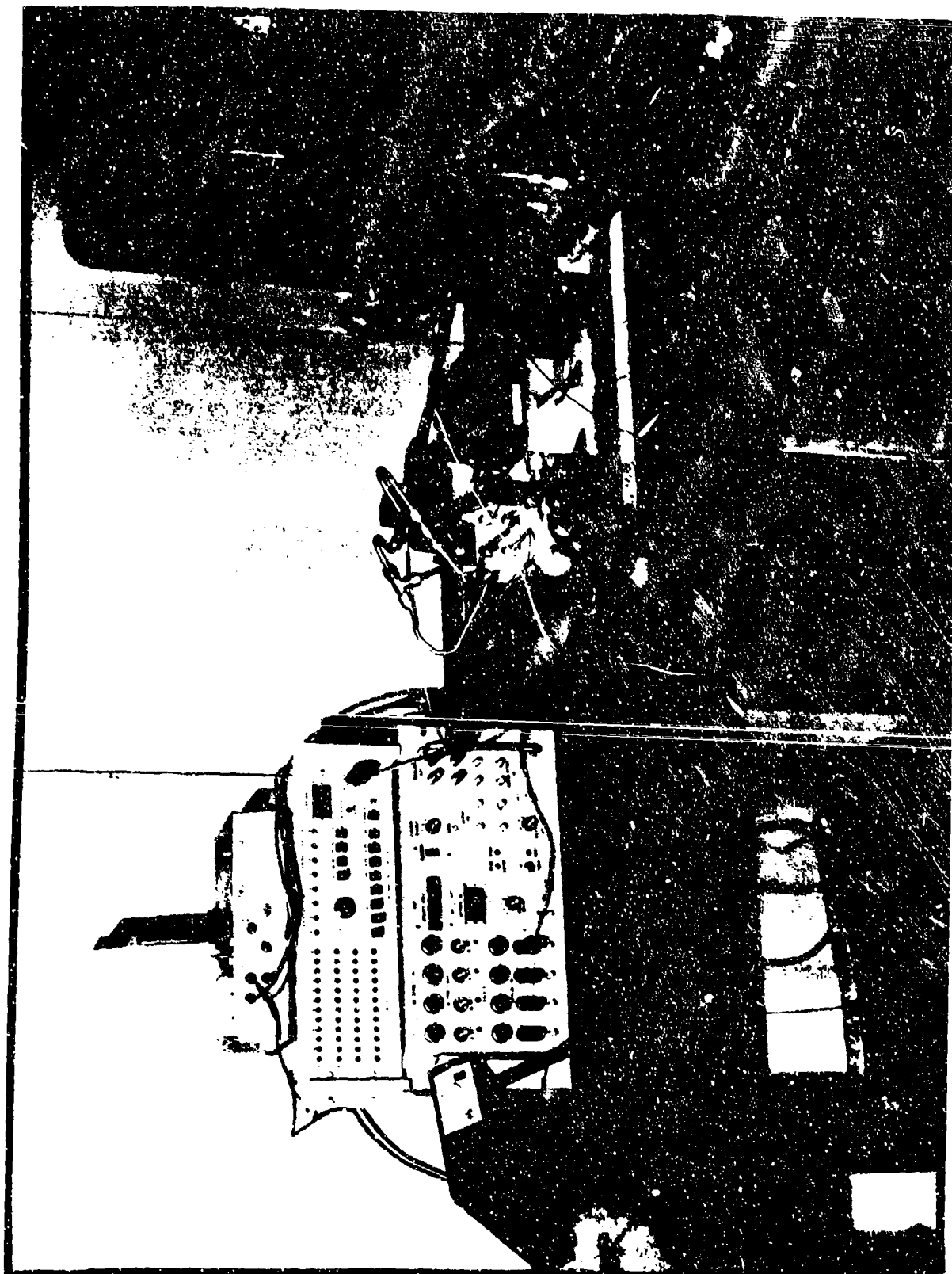


Figure 80. Interface System Test Setup

attenuation up to a frequency of 48 Hz and is attenuated less than 3 Db at 289 Hz. The frequency content is zero amplitude at 482 Hz.

Note as shown on Figure 78, both positive and negative amplitude square waves make up each pulse period, with the time for each square wave being equal at zero commanded flow. Since the control valve sees alternating positive and negative square wave inputs at "0" flow command, the flow control spool will alternately move in one direction and then the other from the null position. If the update frequency is higher than the frequency at which the valve can respond well, the valve spool does not respond at a large amplitude and there is very little increase in quiescent flow due to the use of the pulse width drive. However, the input stage (the torque motor plus flapper nozzle or jet pipe) normally has a higher frequency response capability than the total valve and can be driven to large excursions by a low update rate. The pulse width update rate is an independent parameter and can be set at an arbitrary value. To prevent problems with exciting resonant modes and/or fatiguing components, a safe approach to selecting update rate is to use a rate well above the highest frequency which the components of the valve can respond with significant amplitude.

The amplitude of ripple on the system output depends on the amount of attenuation of the amplitude of the frequency content of the PWM driving signal by the roll off of the system response. For a second order system with a roll off slope of 40 Db/decade, the natural frequency defines the corner frequency for the start of the roll off. Because of the more rapid attenuation with increasing frequency compared to the first order system (with its 20 Db/decade), for a given ripple level the frequency ratio between the PWM update frequency and the natural frequency of the second order system (above which the roll off starts) will be smaller than with the first order system. A typical aerospace two stage servovalve has a response is that of a second order system with a natural frequency of 100 to 150 Hz. The ripple frequency can have positive effect on the control system by acting as a dither signal which will reduce the effect of static friction and/or silting on threshold.

Since the output of the DHVM was two stage (0.5 volts "lo" and 3.5 volts "hi"), a servo driving circuit was required to convert the DHVM output to a ± 10 volt square wave. The PWM driver shown in Figure 81 used an offset input into the driving operational amplifier. The driver output also incorporated a dummy valve RC circuit as a switch selected load in order to set up the duty cycle for the test servovalve at 50% of the full scale current.

Test Valve Description

The valves used for the evaluation are valves manufactured by the Industrial Division of Moog. The valve specifications are:

1. Model A076-771
2. Rated Supply Pressure 3000 psi
3. Rated Flow @ 1000 psi ΔP 10 gpm
4. Coil Resistance 200 ohm (dual coils)
5. Rated Current (max flow) 0.020 amperes (single coil)

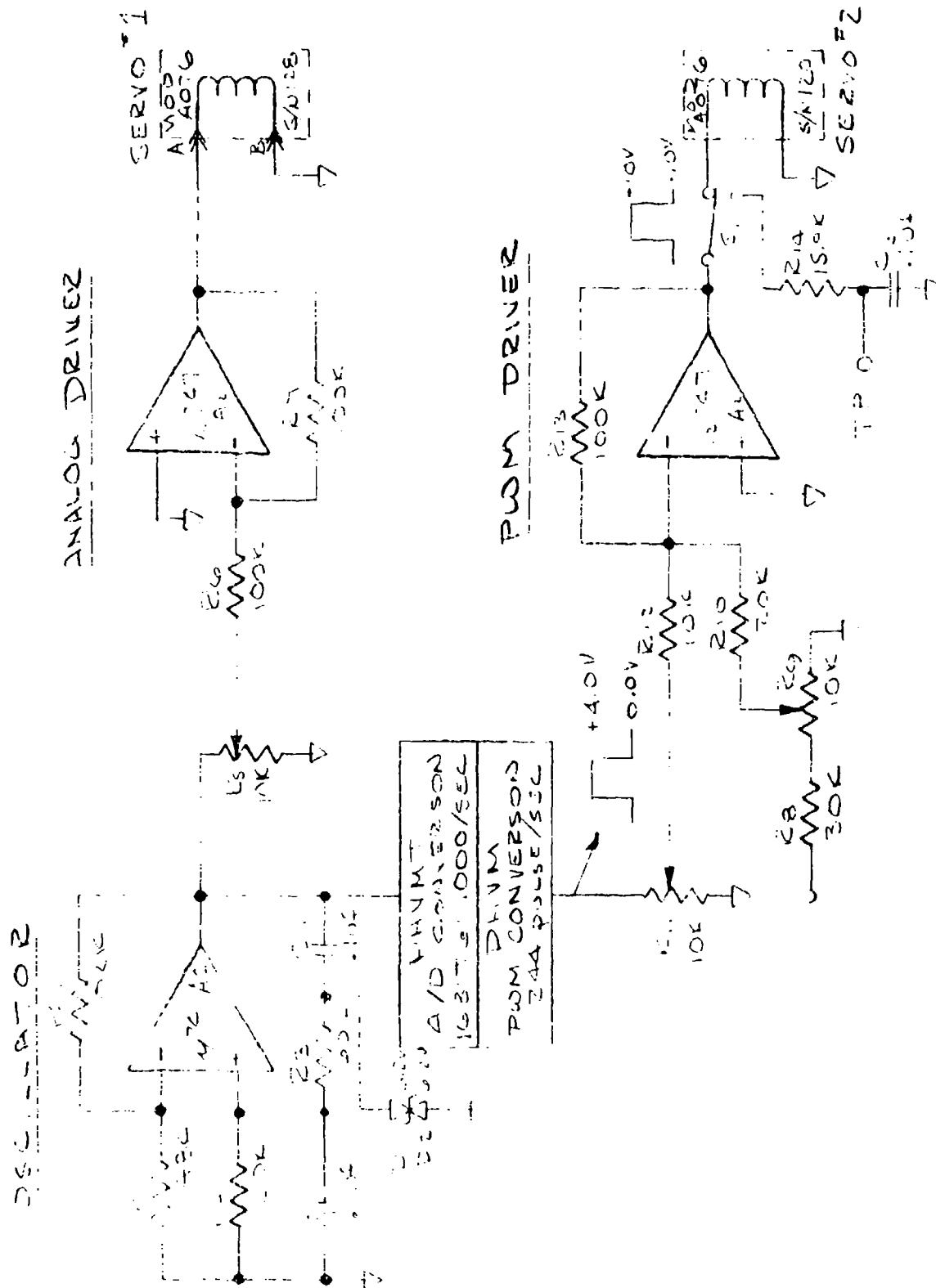


Figure 81. Electronic Schematic

6. Frequency Response (90° phase lag) . . . 75 Hz @ 40% rated current
7. Lap Specification 3% underlap
8. Serial Number 120 (analog driven valve)
128 (PWM driven valve)

The model A076-771 valve was manufactured with the underlap condition specified above in order to lower the valve pressure gain for a load control application. Figure 82 is a representative cutaway view of the valve. The areas that were expected to show the most significant wear were the ball at the end of the feedback wire and the groove in which it operated. The ball and groove are normally a lapped fit at original assembly. Any clearance in this area will be indicated by nonlinear flow and pressure gain around 0 input. The spool and sleeve are normally also a lapped fit to a diametral clearance of 50×10^{-6} inches. Excessive clearance and control edge erosion will show as increased leakage, lower pressure gain and a decrease in null flow gain.

Hydraulic Circuit

Figure 33 shows the hydraulic test circuit used for the evaluation. A 15 gpm at 3000 psi hydraulic supply using MIL-H-5606 hydraulic oil and 10 micron filtration was connected to the servovalves. Note that the C_1 and C_2 servovalve ports were connected to system return through orifices sized to flow 1.0 gpm at 1000 psi differential pressure. The orifices were initially installed to connect C_1 and C_2 together for each servovalve. However, at the start of testing, it was apparent that considerable heat was generated within the test block and retained in the block. The heat generation resulting from passing flow through the orifices was expected. However, with the 10 Hz driving frequency of the valve and the several feet of hydraulic lines between the orifice test block and the servovalves manifolds, there was very little steady state hydraulic flow through the orifice block to return. The oil in connecting lines tended to be pumped back and forth through the orifices rather than circulating into the test block and out to the pumping stand return. By porting the fluid from one side of each orifice directly to return, the temperature rise of the orifice block was minimized. The disadvantage of this loading method was that servovalve cylinder-port-to-return valve spool edges were metering less fluid and would show less erosion effects.

Test Results

Base line data was recorded prior to the start of the cycle testing. Examination of the feedback balls and the control spools did not reveal any distinctive patterns or imperfections. Figure 84 and 85 are sample photographs of the hardware's initial status.

Figure 86 and 87 are the base line pressure gain plots for the test valves serial numbers 120 and 128. Note the deadband in the pressure gain plots. This characteristic was undesirable for the original intended use of the valves in the control of a loading system. The characteristic caused the valves to be rejected for the load system application, making them available for the interface test program. Since only changes of the pressure gain during the evaluation testing was important for the interface testing, the valves were satisfactory for the interface evaluation.

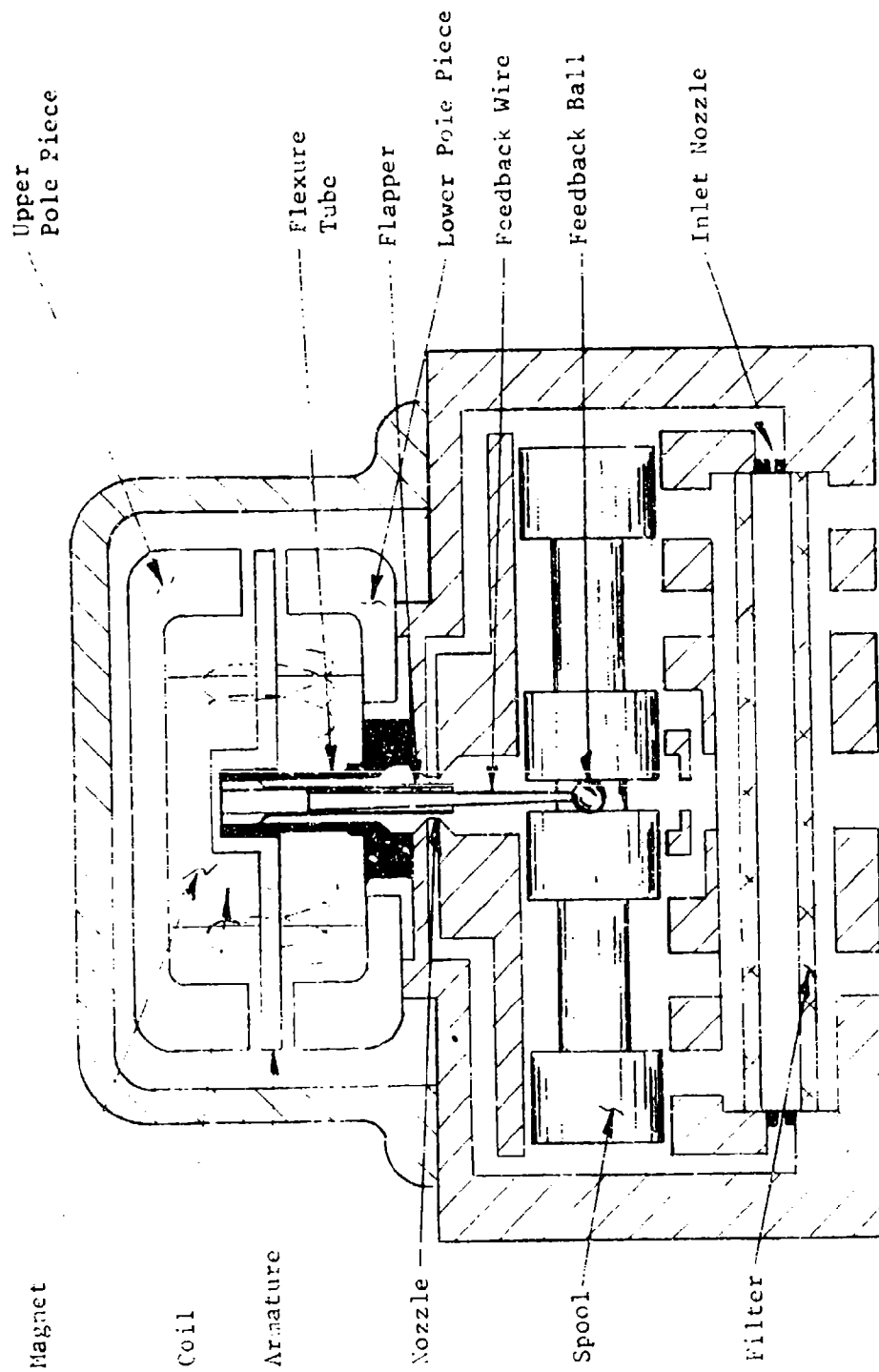


Figure 82. Servovalve Cross Section

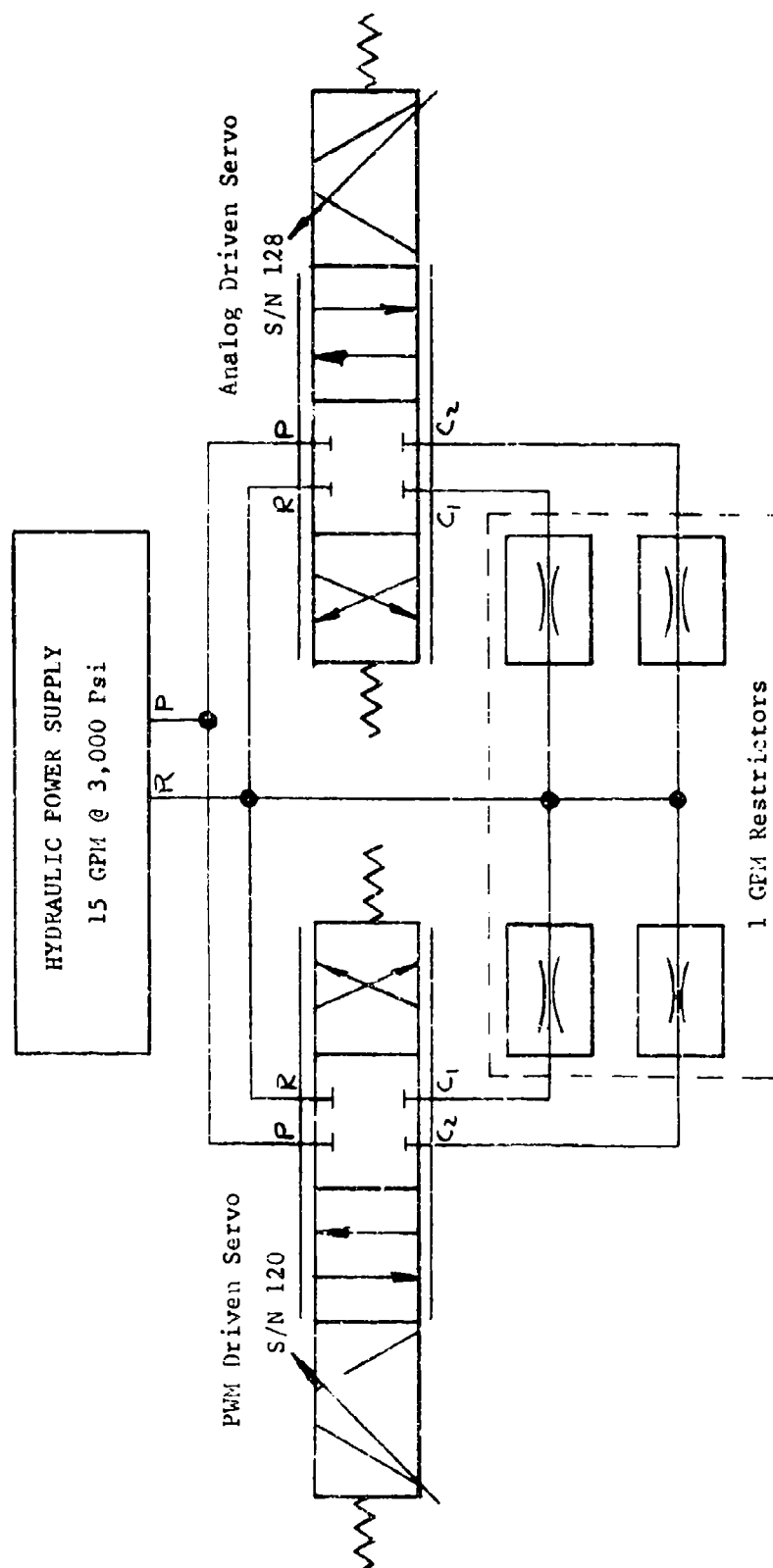


Figure 83. Hydraulic Schematic

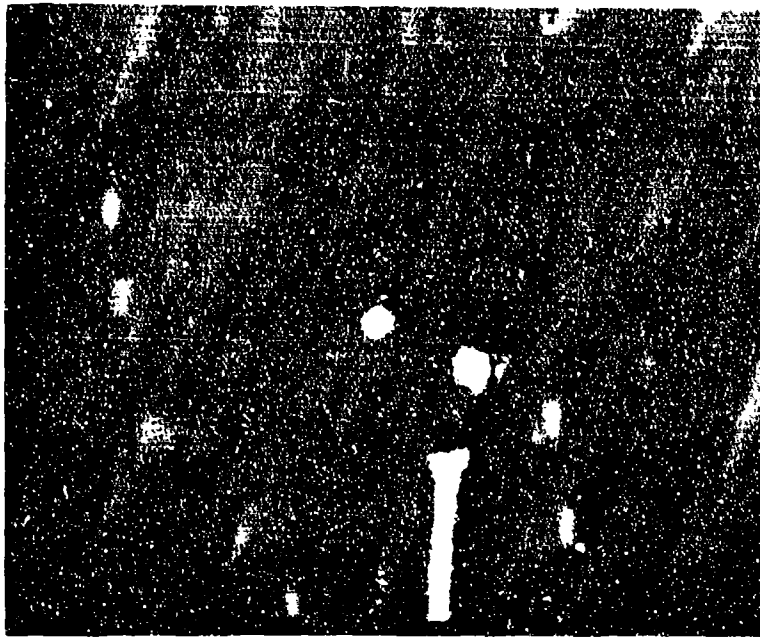


Figure 84. Base Line No. 120 Feedback Ball Photo 35X Actual

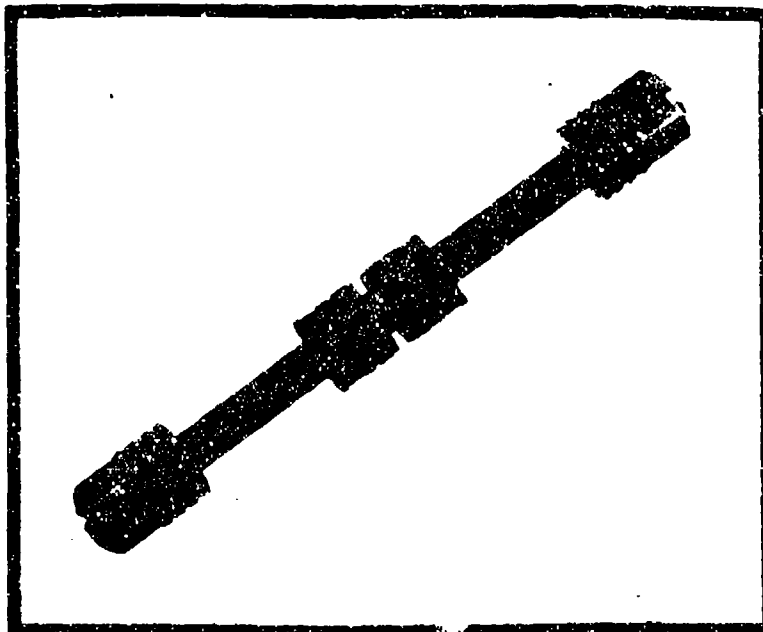


Figure 85. Base Line No. 120 Control Spool Photo 2X Actual

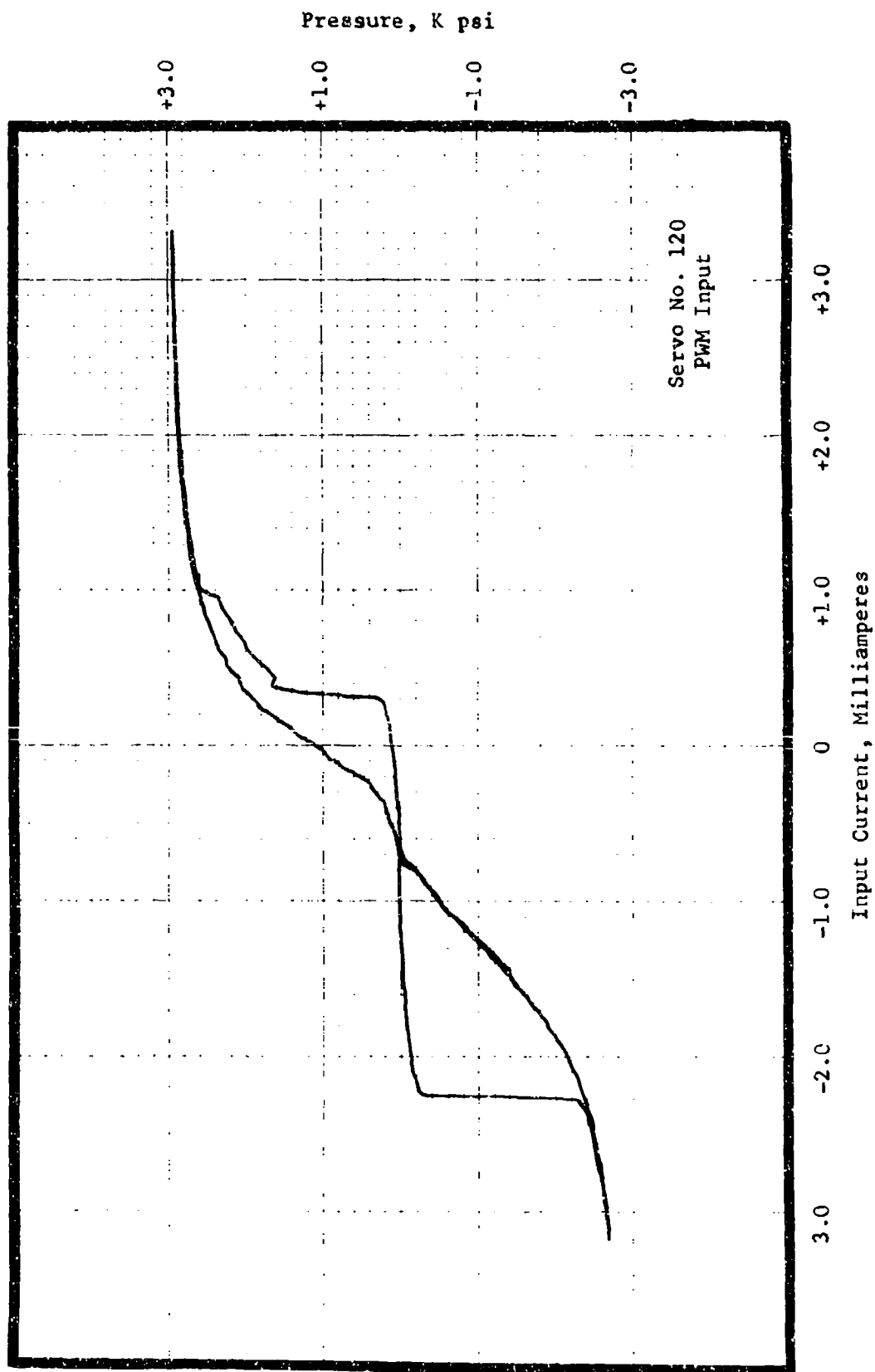


Figure 86. Base Line Pressure Gain, S/N 120

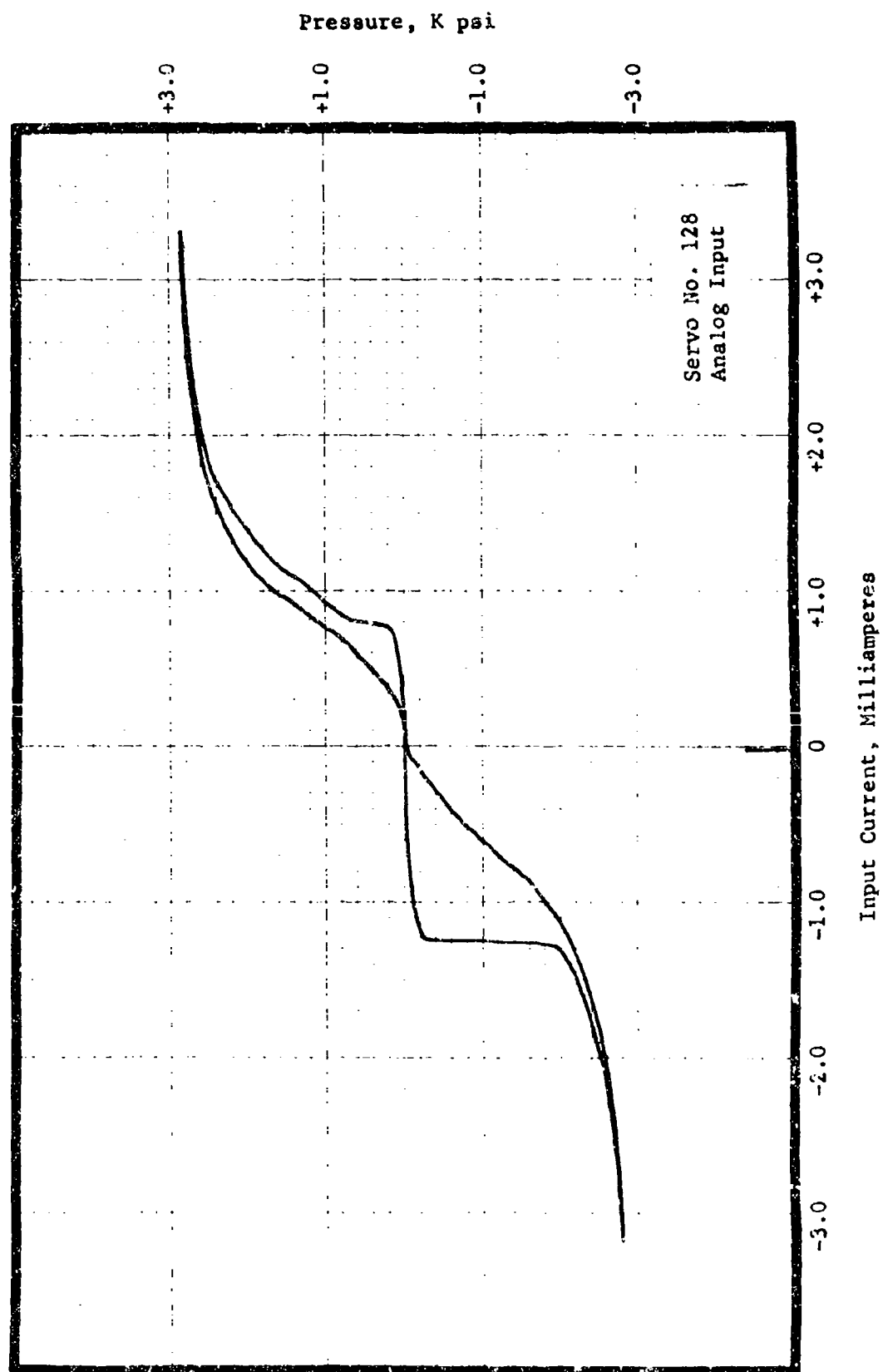


Figure 87. Base Line Pressure Gain, S/N 128

Figure 88 and 89 are the base line flow gain plots for the test valves. The PWM drive servovalve serial number 120 shows a flow gain of 0.87 gpm/milliamp for positive current inputs and 0.95 gpm/milliamp for negative current inputs. The analog driven valve's flow gain as shown on Figure 89 is 1.00 gpm/milliamp for both positive and negative current inputs. The null leakage of nominally 1 gpm for both valves is due in a large part to the 3% underlap specification to which the valve was manufactured. The flow was measured by a flow meter placed in the return line from the valve. The flow therefore includes both the first stage quiescent flow and the second stage leakage flow.

Table 1 is a tabulation of the recorded flow and pressure gains measured during the test program. Note that the servovalves were tested before cycling and after each 100 hours of operation. Note that the flow gain increases slightly on both valves with increasing operational time. This is consistent with the wear characteristic of the feedback ball. As the ball wears in its groove on the spool, the spool is required to move further for the feedback wire to cancel the torque motor's armature torque. Note that the data points for the hysteresis and leakage for the 100 hour data point may be erroneous. The general trend for both valves was a general decrease in thresholds and pressure gain and an increase in the flow gain.

TABLE 1.
PWM Data Summary

VALVE/TEST POINT, HOUR	FLOW GAIN		FLOW HYSTERESIS		LEAKAGE GPM	PRESSURE GAIN		PRESSURE THRESHOLD	
	+	-	+	-		+	-	+	-
	GPM/MA	GPM/MA	MA	MA		PSI/MA	PSI/MA	MA	MA
S/N 120 PWM									
0	0.87	0.95	0.40	0.20	0.9	2.6×10^3	1.8×10^3	1.05	1.5
100	1.05	0.98	0.02	0.05	1.0	1.8×10^3	1.9×10^3	0.7	1.1
200	1.05	1.05	0.16	0.16	1.2	1.9×10^3	1.3×10^3	0.8	1.5
300	1.00	1.05	0.08	0.16	1.2	1.3×10^3	1.3×10^3	0.80	1.3
S/N 128 ANALOG									
0	1.00	1.00	0.10	0.10	1.0	2.8×10^3	2.2×10^3	0.80	1.4
100	1.05	1.09	0.24	0.20	1.4	1.0×10^3	1.3×10^3	1.29	1.5
200	1.08	1.08	0.10	0.10	1.2	1.7×10^3	1.9×10^3	0.70	1.3
300	1.05	1.11	0.28	0.10	1.2	1.2×10^3	1.3×10^3	0.60	1.2

Physical inspection of both valves showed changes in the condition feedback balls and spool edges. At the end of the 300 hours of cycling, the control spool edges showed some erosion. In addition, a polished appearance over the first 25% of the pressure control lands was apparent. The remainder of the spool lands and the return lands had a burnished surface finish. Figure 90 shows the surface condition of the spool lands. The polishing effect was attributed to the high velocity of the flow metered by the control edges of the spools. The appearance of both the analog and PWM driven spools was similar. Both feedback balls had a similar wear pattern. The patterns were circular in shape and developed where the feedback balls contacted the control spool. The

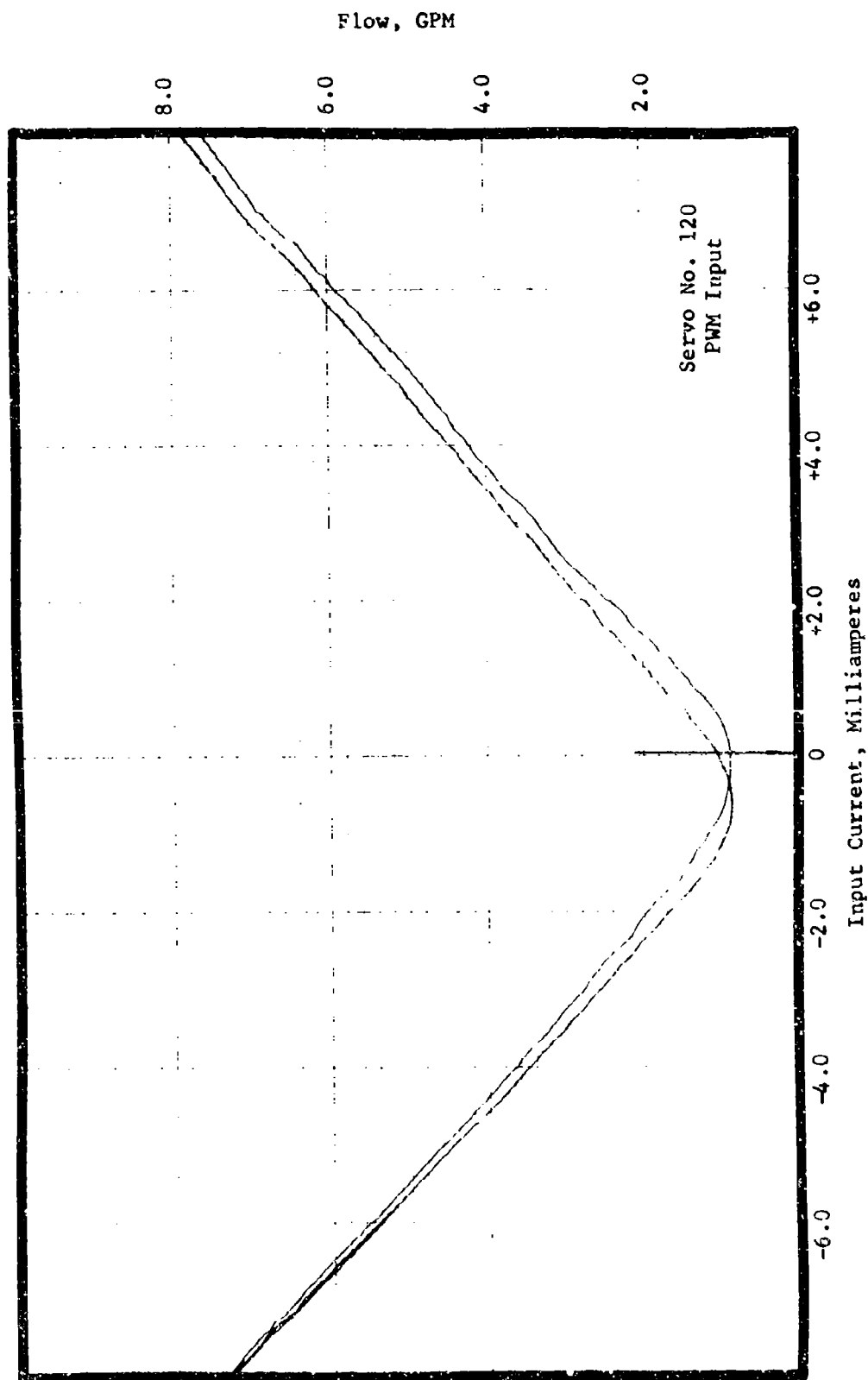


Figure 88. Base Line Flow Gain, S/N 120

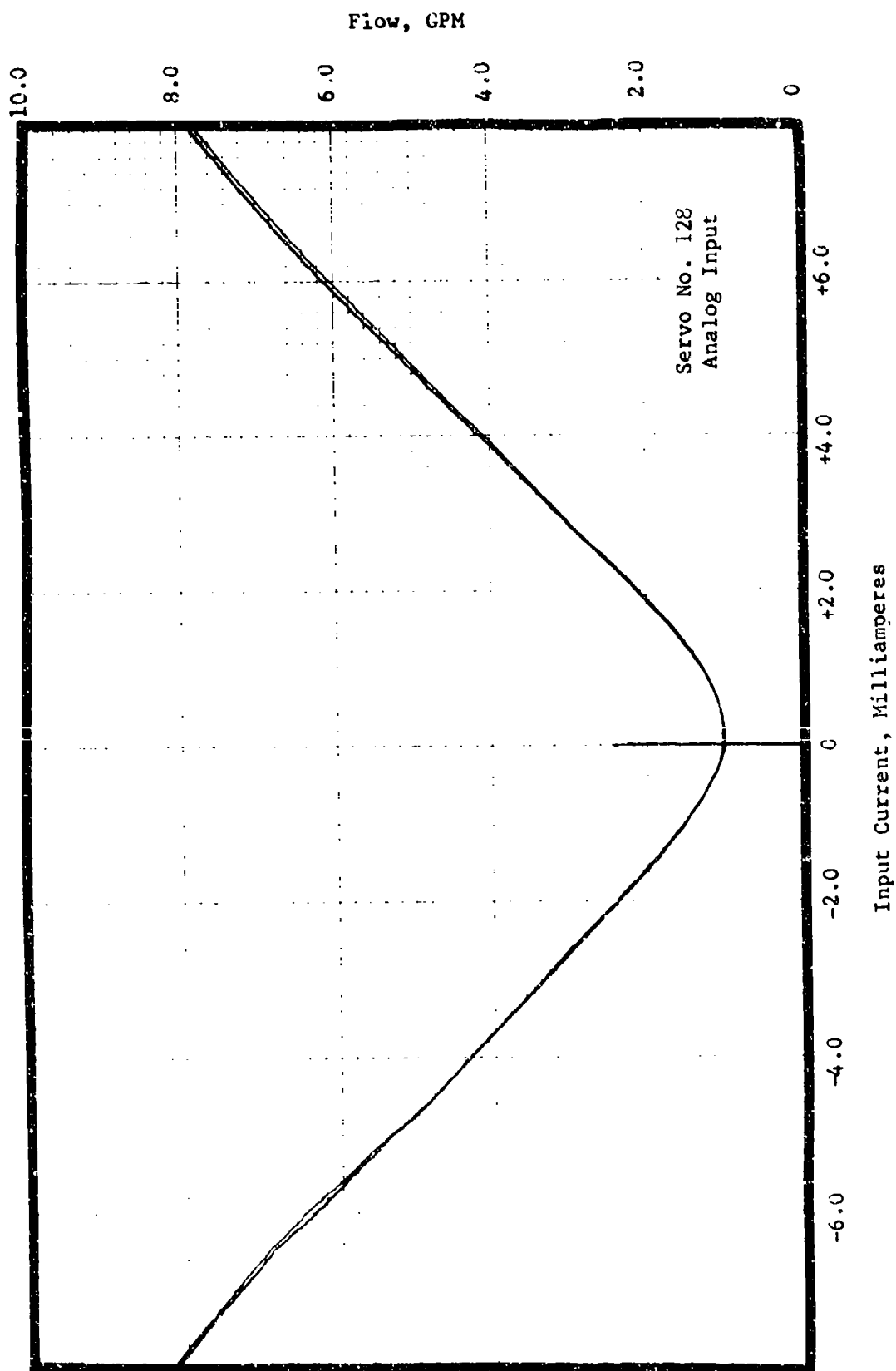
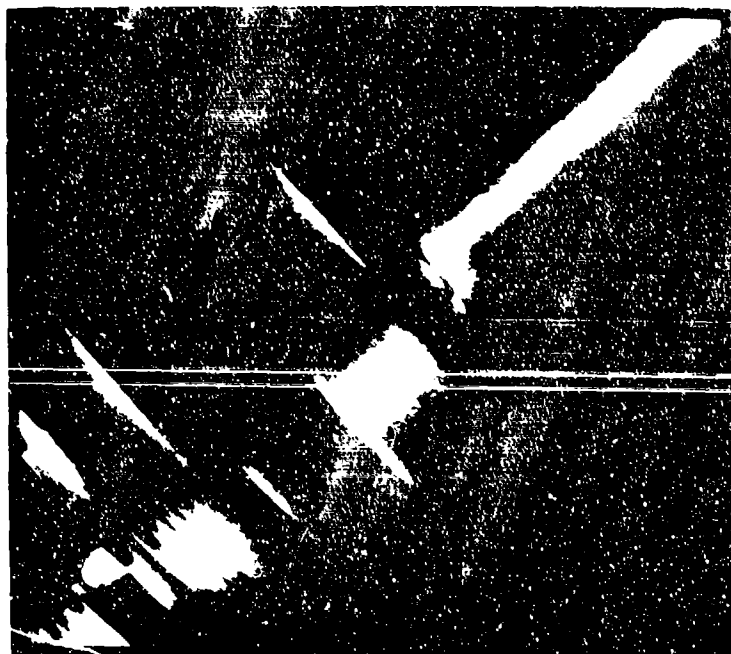


Figure 89. Base Line Flow Gain, S/N 128



S/N 120

Figure 90. Pressure Land Polishing Effect

wear pattern measured at 0.002 inches in diameter. The pattern resulted in a 0.0001 inch diametral difference between the ball diameter at the wear points and the diameter at 90 degrees from the wear patterns. The reduction in threshold shown on Table 1 measured during the sequence of data taken and the observed wear indicated that the valve spools were undergoing a reduction in mechanical friction during the testing. Photographic documentation of the ball wear was not successful because of lighting and equipment limitations.

Problems were encountered with portions of the test system during the 300 hours of testing. With both the analog driven valve and the PWM valve test setup, there occurred O-ring failures of the MIL standard straight thread fittings where they screwed into the test blocks. Failures of the face seals between the manifold and the servovalves also occurred. The O-ring failures were low leakage rate failures (weeping) rather than a steady stream. Examination of the failed seals revealed a nibbling wear pattern, apparently caused by pressure pulsations. There was no obvious difference in the O-ring failure characteristics between the analog and PWM driven valves. The cause of failure would appear to be the 10 Hz cycle frequency at 50% amplitude rather than energy associated with the 244 update frequency content. During the testing, one of the two manifolds used to mount the servovalves developed a crack between the threads of a fitting port and the surface of the manifold. The particular manifold that failed was a commercial off-the-shelf aluminum block that incorporated straight thread ports for 1 inch tubing. Reducers were used in the ports to adapt to 1/2 inch or 3/8 inch diameter tubing as required. The block failed after 196 hours of testing and was modified to allow completing the test sequence. The block that failed was used with the PWM driven valve. However, since the manifold block used with the analog drive valve was of a different design (smaller ports and 2024-T351 aluminum), the block failure cannot be attributed to PWM drive. The block failure does emphasize that the pressure variations associated with high frequency driving of hydraulic systems can fatigue components in the system and that the system hardware must be designed for that service.

Conclusions and Recommendations

Pulse width modulation as compared to the analog drive of the two stage electrohydraulic valve did not create any problems for the same operating time period. The 244 Hz update frequency for the PWM drive was low enough (less than 4 times higher than the frequency response rating for the valve) to have potentially excited the armature resonance of the valve. The low update frequency did not cause any apparent problem with the valve. However, it is recommended that a PWM update frequency 10 times greater than the upper bandpass frequency of the valve be used. This is high enough to minimize exciting any high frequency mechanical resonances in the valve or the system with which the valve is used. Since the servovalve response attenuates with increasing frequency, the higher the PWM frequency, the lower the pressure pulses introduced into the hydraulic lines because of the PWM control.

The digital controller's output which generates a PWM signal is two state, normally "zero" and 5 volts. The servovalve is bipolar, so that the "zero" output represents one analog input extreme and the 5 volts represents the other. If the digital controller fails, the output will then go to one state or the other, driving the analog system into a hardover failure. This characteristic should be addressed in the redundancy management of a system using PWM for control valve driving.

The PWM technique of interfacing digital controllers appears to be a viable cost effective alternative to digital/analog converters. Within the constraints of dynamic compatability and failure modes for a particular system, it is recommended as interface method.

SECTION VI. AIRCRAFT ENERGY STORAGE STUDY

Objective

The object of the energy storage study was to determine feasibility of reducing the pumping capacity of a current aircraft's hydraulic system by using accumulators to store hydraulic energy.

Background

The hydraulic power demands of the flight control system of an aircraft vary greatly during a typical flight. Normally, the hydraulic pumping system is sized to meet the peak flow demand of the flight control system (with the pressure of the pumping system maintained at a constant level). Variable displacement pumps are generally used to accommodate the changes in the flow demand on the pumping system. The hydraulic pump and connecting lines are sized for the peak demand on the pumping system. The pumps and lines are therefore larger than they would be if sized for average flow demand.

The flow demands from the pumping system supplying a flight control system are generally greatest during slow speed operation with air turbulence (such as during landing). Under these conditions, large surface movements are required to maintain a desired flight path. With the development of highly augmented aircraft (with aircraft motion sensors providing inputs to the flight control system), the flight control activity is increased over that of un-augmented aircraft. The motion sensors generate control inputs with higher frequency content than a pilot is able to produce. The motion sensors command large flight control surface motions, particularly when the aircraft experiences air turbulence. With the acceptance of Fly-By-Wire flight control systems and their ability to easily incorporate augmentation techniques, there is a trend for increased control system activity which places large short duration flow demands on the hydraulic supply system. This is particularly true for the pitch axis of control systems for aircraft designed with relaxed static stability.

The accumulators used in current aircraft are generally installed as a single accumulator for each hydraulic system. The accumulator is installed near the discharge port of the system's hydraulic pump and is sized to minimize pump related output pressure variations. Where more than one pressure source is provided to the system requiring hydraulic power, the accumulator is sized to minimize the output pressure drop during the startup of/or transfer time to a second system.

Using distributed accumulators for energy storage in order to allow the hydraulic lines and pumps to be sized for average flow instead of peak flow offers an attractive alternative design approach to aircraft hydraulic system design. The approach potentially allows using smaller hydraulic lines and hydraulic pumps. The approach does require establishing the flow demand profile for the particular aircraft design. If used in a new aircraft design, a simulation of the aircraft's control system power requirements for the most

demanding flight conditions would have to be run. The relationship between the peak and average flow for each control actuator would have to be measured as a time history, and each accumulator sized for the particular actuator based upon the acceptable pressure degradation during peak flow demands. Unless check valves are used to prevent reverse flow during peak demand conditions, the accumulators will tend to assist each other in providing the peak flow. The degree of assistance will be determined by the pressure/flow relationships for the interconnecting hydraulic lines. As with other aircraft design areas, the use of a simulation model as a tool is required to achieve an optimum design.

Investigation Technique

The General Dynamics F-16 airframe was selected as a study case since it was representative of a state-of-the-art high performance fighter. The F-16's flight control characteristics were available and the flight envelope defined.

Data for evaluating the peak and average flows for the F-16 aircraft was obtained from an AFTI/F-16 simulation conveniently being conducted on the TAMARS moving body simulator by the AFWAL/FIGD at the same time as the energy storage study. The flow demand of the flight control actuators was obtained from the control surface rates generated by the simulation with different pilots under various flight conditions.

For the investigation, the flow demand for each flight control actuator (as a function of control surface rate) shown in Table 2 was used. The values listed in Table 2 were obtained from AFFDL-TR-76-119.

Table 2.
Flow Demand

Control Surface	Flow Demand Each Surface GPM/Deg./Sec.	Maximum Rate Deg./Sec.	Maximum Flow Demand Each Surface in GPM	Surface Quantity	Max. Req'd Flow
Flaperon	0.139	60 Deg./Sec.	8.34	2	16.68
Horizontal Tail	0.128	18 Deg./Sec.	2.30	2	4.60
Rudder	0.036	120 Deg./Sec.	4.32	1	4.32
Leading Edge Flaps*	0.122	112 Deg./Sec.	13.40	2	13.40**

* The flaps on the normal F-16 aircraft are not continuously modulated. The particular simulation included modulation of the flaps to increase maneuvering capability. The flow demand for the leading edge flap drive was included in the total flow demand data.

** The flap drive is a central unit with two hydraulic systems supplying the hydraulic power. The maximum flow demand on each hydraulic system by the leading edge flaps is 13.40 gpm.

In addition to the flow demand related to the surface rate, the control actuators have a steady state flow due to servovalve first stage quiescent flow and internal leakage. For the first three control surface actuators listed in Table 2, the quiescent flow is 0.2 gpm (reference AFFDL-TR-76-119). This is a small percentage of demand flow and can easily be accounted for when designing an energy storage system by using a corresponding decrease in rating the available flow from the hydraulic pumping system.

The demand flow data to be analyzed was generated by adding the flows corresponding to the surface rates during the simulation runs. This allowed creating a time history of the total demand on the supply system during different simulated aircraft flying tasks.

Data Analysis

Figure 91 is a sample of the time history for the F-16 during a 3 g reversing target chase. Figure 92 is a sample of the time history for the F-16 during a landing with turbulence. Shown with the demand flow time history is the time history of pitch rate and normal acceleration. Note that the demand flow activity for the landing with turbulence is greater than that with the 3 g reversing turn. Note also that the pitch rate and normal acceleration time histories also show greater activity during the landing than with the reversing turn. Also shown on the two figures is the time history of the horizontal tail and flaperon control surfaces. Note that the surface activity (and corresponding flow demand activity) in Figure 92 is greater than that in Figure 91. This indicates that of the two flight tasks, the landing with turbulence creates the most severe demand on the hydraulic supply system.

The procedure used to analyze the data was to calculate from the flow demand time history the quantity of fluid used over successive 400 millisecond time intervals. The quantity of fluid used during each time interval is the area under the demand curve for that time interval. The chart paper used to record the time history has a grid which conveniently allows area determination by counting squares.

The flow supplied by the hydraulic pumping system is the sum of the pump flow and flow from the energy storage accumulator. For flow demands greater than the pump output flow rating, flow from the accumulator occurs. When the flow demand is less than the pump output flow rating, the pump recharges the accumulator.

The procedure used to evaluate feasibility of the energy storage technique was to assume a pump and accumulator size and plot the volume of fluid left in the accumulator as a function of time. The volume of fluid left in the accumulator can be expressed in equation form as follows in Equation 16:

$$V_a = V_a' + V_p - V_d \quad (\text{Equation 16})$$

Where: V_d is the volume demand during the incremental time interval considered.

V_p is the volume delivered by the pump during the incremental time interval considered.

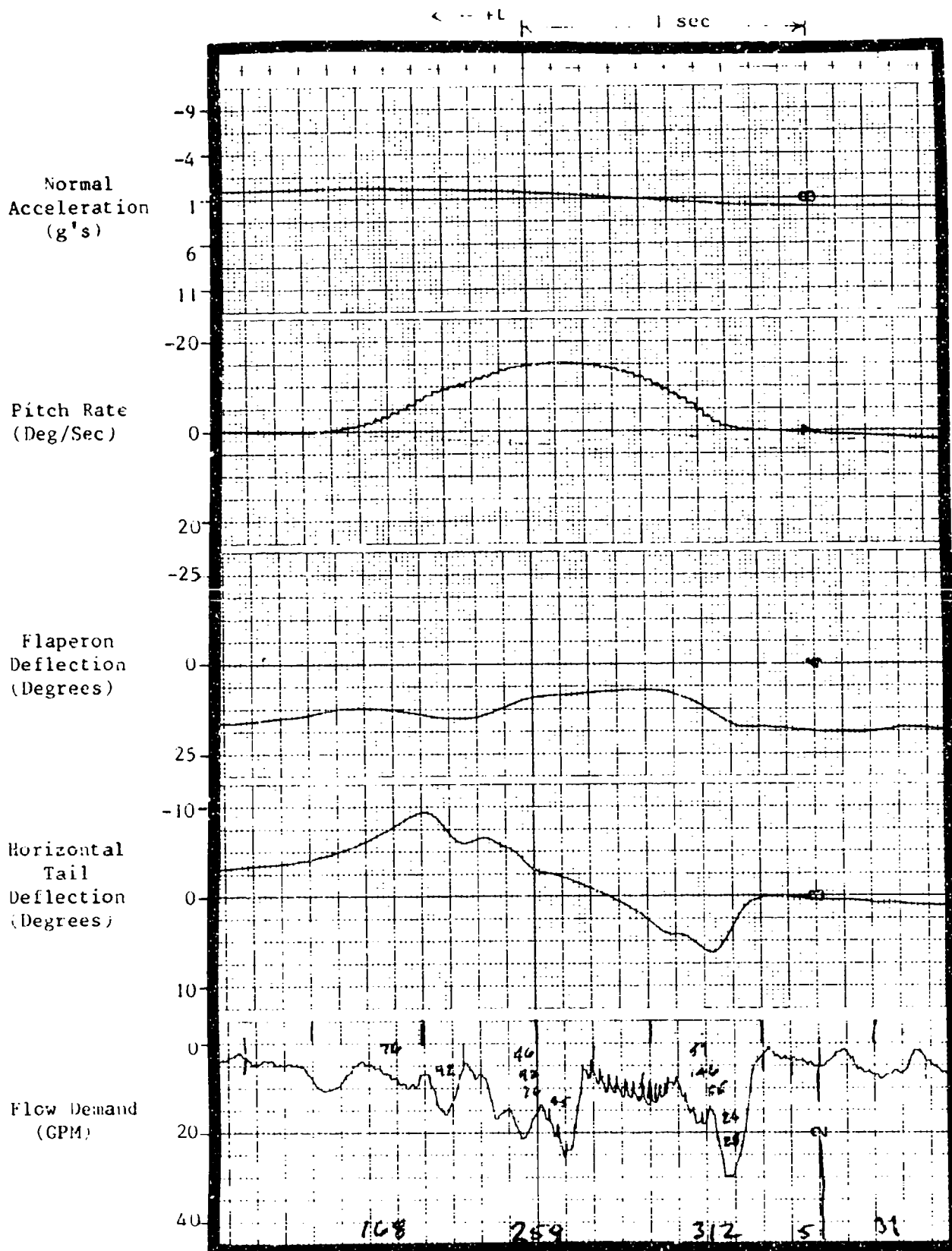


Figure 91. Sample History - 3G Reversing Target Chase

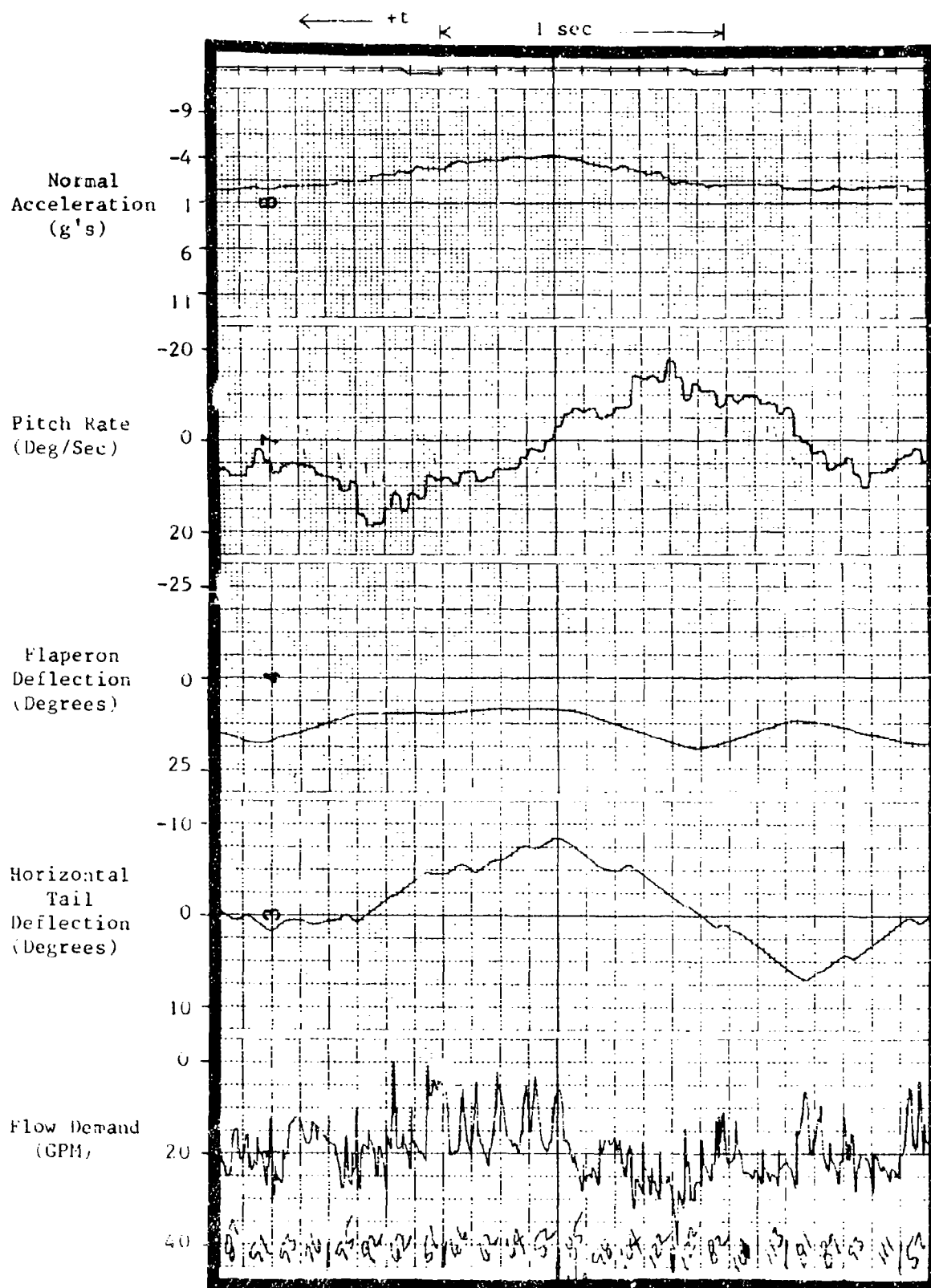


Figure 92. Sample History - Landing; With Turbulence

V_a is the volume available from the accumulator at the beginning of the incremental time interval considered.

V_a is the volume left in the accumulator at the end of the incremental time interval considered.

Note that the accumulator volume available to supplement the pump flow is dependent on the permissible pressure drop in the hydraulic supply line. The pressure head drop in the supply line is required for the accumulator to discharge into the line. The permissible pressure drop depends upon the particular aircraft and particular control surface. A pressure head drop results in a reduction of the hinge moment available from the control surface and a reduction in the maximum surface rate. In addition, the control actuators used in the flight control system may have pressure failure detection logic which has a preset trip level. The F-16 is such an aircraft since it uses failure logic that operates on pressure signals. The system is a 3000 psi supply system. The flaperon, horizontal tail and rudder actuators will detect supply pressure decay below 2000 psi as a failure. An energy storage accumulator for the F-16 must therefore be sized to deliver the required fluid volume for a pressure drop less than 1000 psi.

For the data evaluation, the time history for the flow demand of all simulation runs was inspected to find "worst case" time histories for detail examination. The aircraft maneuvers for which data was obtained were combat and landing maneuvers. The combat maneuvers were chases of a 3 g reversing target. Two different pilots' runs were recorded. The landing maneuvers were approaches from 4.7 nautical miles and 1500 feet altitude with and without turbulence. Ten landing maneuvers were recorded, six with turbulence and four with still air.

Data Analysis Results

Several combinations of accumulator volume delivery and pump size were iteratively tried in order to establish a pump and accumulator size where:

- a. The pump had sufficient delivery to recharge the accumulator during low flow demand time periods.
- b. The accumulator had sufficient volume to meet the peak flow demands.

The final selection for the variable volume pump size was 22 gal/min. The final selection for accumulator size was 115 in³. The presented results for the data analysis uses this pump and accumulator size.

Figures 93 through 94 show the time history of the flow demand of the aircraft during the 3 g reversing target chase run. Figure 93 covers the first 20 seconds of the run, and Figure 94 covers the second 20 seconds. Note that both the accumulator discharge volume and the system demand flow are presented on the figures. At the start of the run, the accumulator is considered to be fully charged. Note that the demand flow curve reflects the 0.400 second time increment used in applying Equation 16 to the simulation test data.

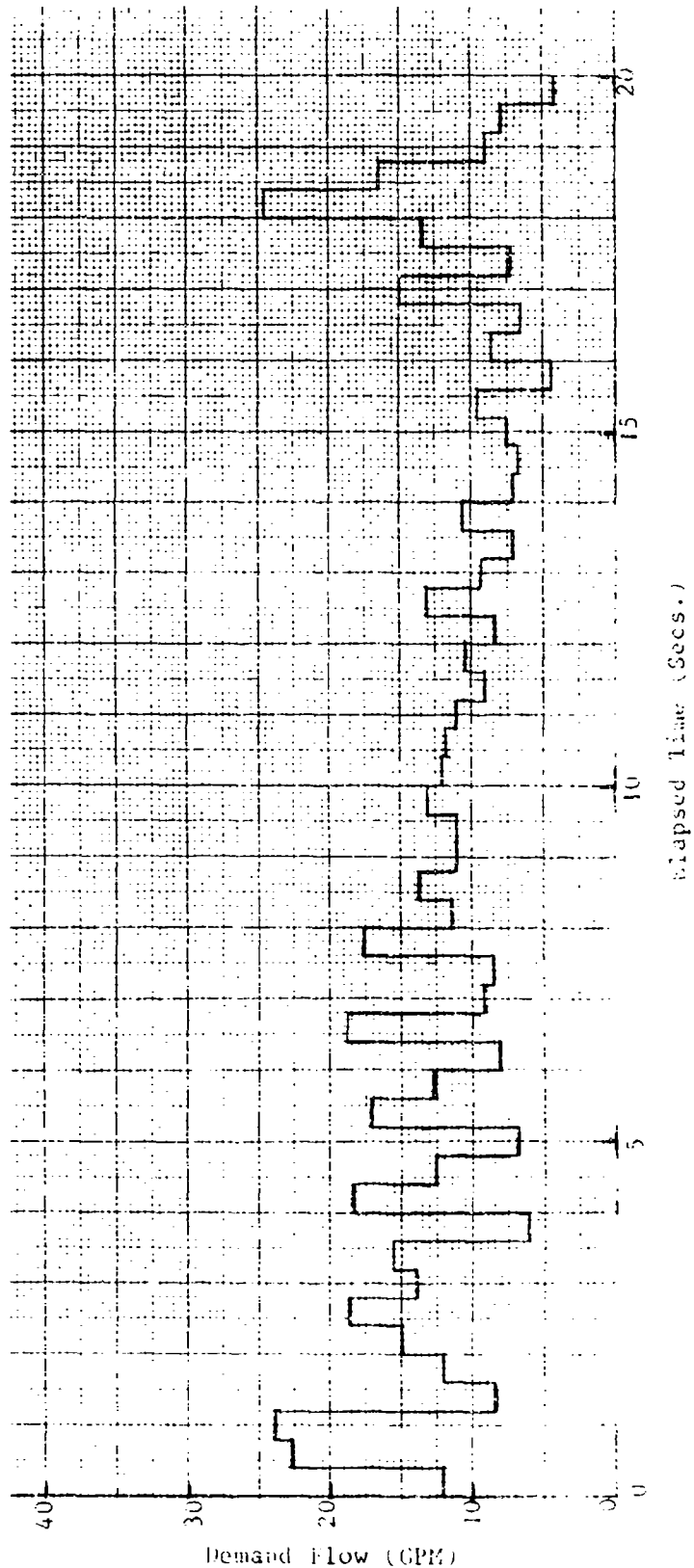
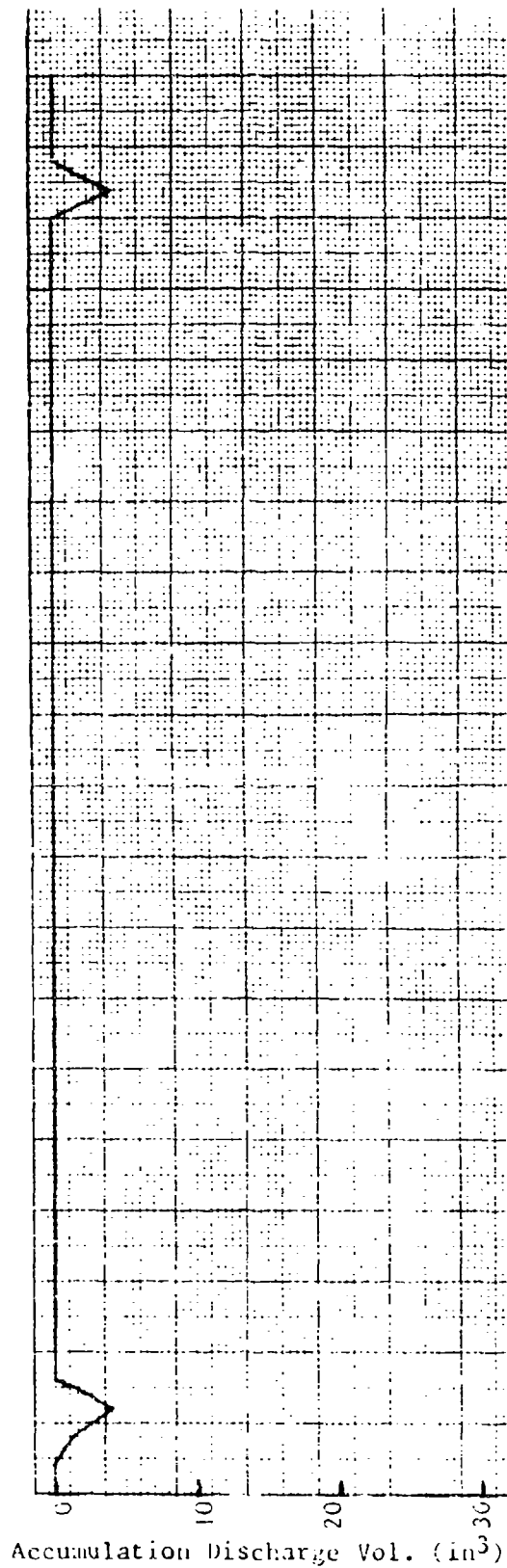


Figure 93. 0-20 Seconds, 3G Reversing, Target Chase

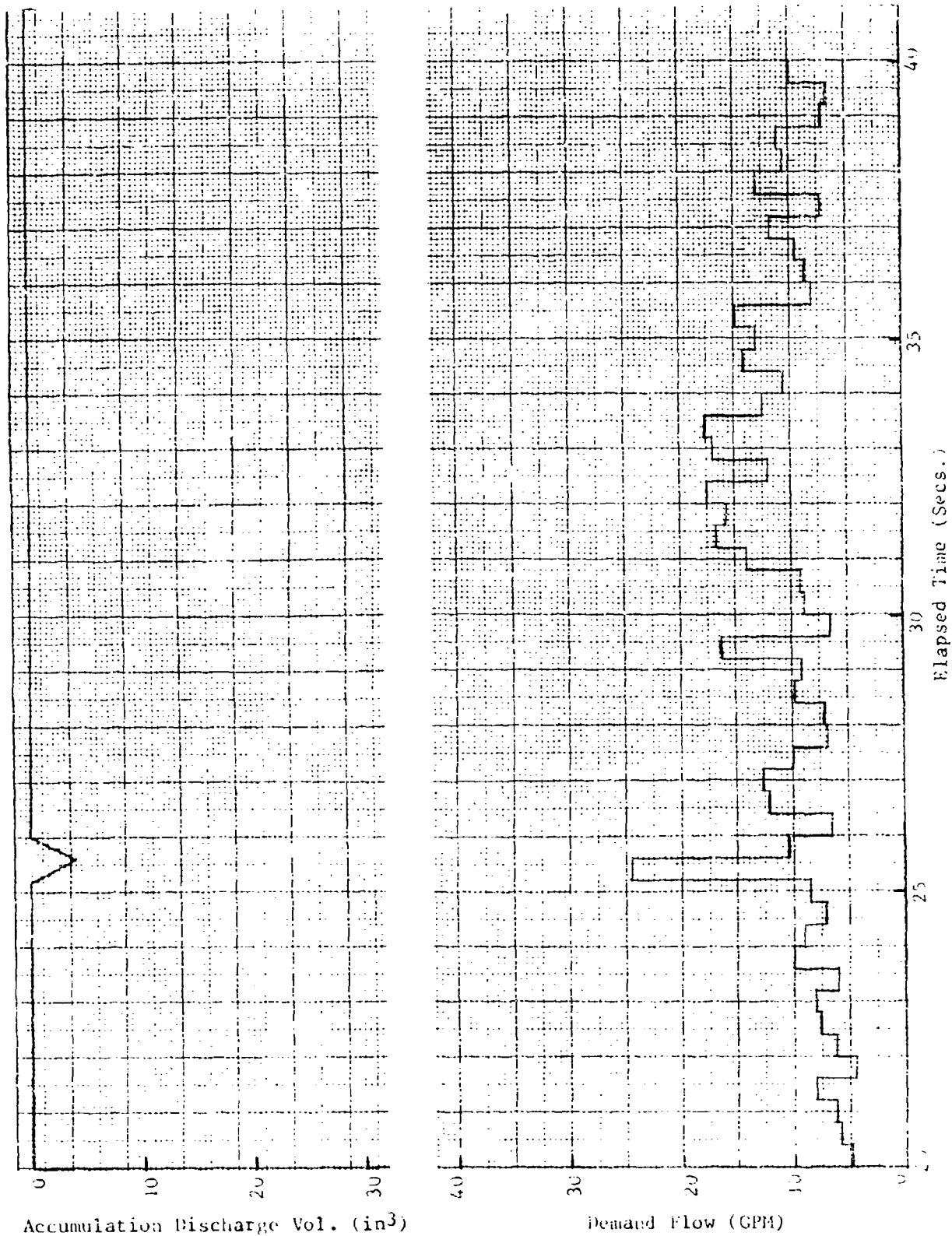


Figure 94. 20-40 Seconds, 3G Reversing Target Chase

Note that for the maneuver used for creating Figures 93 through 96, the demand flow was totally supplied by the pump for most of the run. The accumulator was discharged only 4 times during the 70 second run and then recharged almost immediately during the subsequent low flow demand intervals. The most severe demand occurred at $t = 50$ seconds with an average demand of 32.45 gpm for the 400 millisecond interval. Note that at $t = 52$ seconds, the accumulator had been recharged.

Figures 97 and 98 show the time history of the accumulator volume available and pump demand flow during landing with turbulence. The landing run lasts 40 seconds. As shown on Figure 98, the accumulator volume was discharged by 22 cubic inches at $t = 32.8$ sec. The accumulator was not recharged completely before touchdown at $t = 40$ seconds. The maximum delivered volume from the accumulator was therefore 22 in³ for the entire landing run.

To supply a given volume of fluid, the size of the accumulator can be calculated from the following equation for adiabatic conditions (Reference Greer Olaer Products, "Sizing Accumulators For Their Use As An Auxiliary Power Source"):

$$V_1 = \frac{V_x (P_3/P_1)^{1/n}}{1 - (P_3/P_2)^{1/n}} \quad (\text{Equation 17})$$

Where: V_1 = Volume of the accumulator necessary to supply the required volume of hydraulic fluid.

P_1 = The gas precharge pressure in the accumulator.

V_x = The volume of oil to be supplied by the accumulator.

P_2 = The maximum system operating pressure

P_3 = The minimum system pressure

n = Gas constant (1.4 for N_2)

Figure 99 graphically represents the relationships of Equation 17 with $n = 1.4$ for nitrogen and 3000 psi for P_2 . Each straight line on the figure corresponds to a different precharge pressure. Note that Equation 17 indicates that the smallest accumulator size for a given minimum system pressure occurs when the precharge pressure is set at the minimum system pressure ($P_3 = P_1$). For Figure 99, the straight lines correspond to different precharge/minimum system pressures.

From the graph of Figure 99, for the minimum system (and precharge) pressure of 2000 psi and a discharge flow of 22 in³, the accumulator size would be 0.175 gallons (40.4 in³). If a safety factor of two on the amount of discharge volume were used and 44 in³ was considered as the required discharge flow, the required accumulator size would be 0.5 gallons (115 in³).

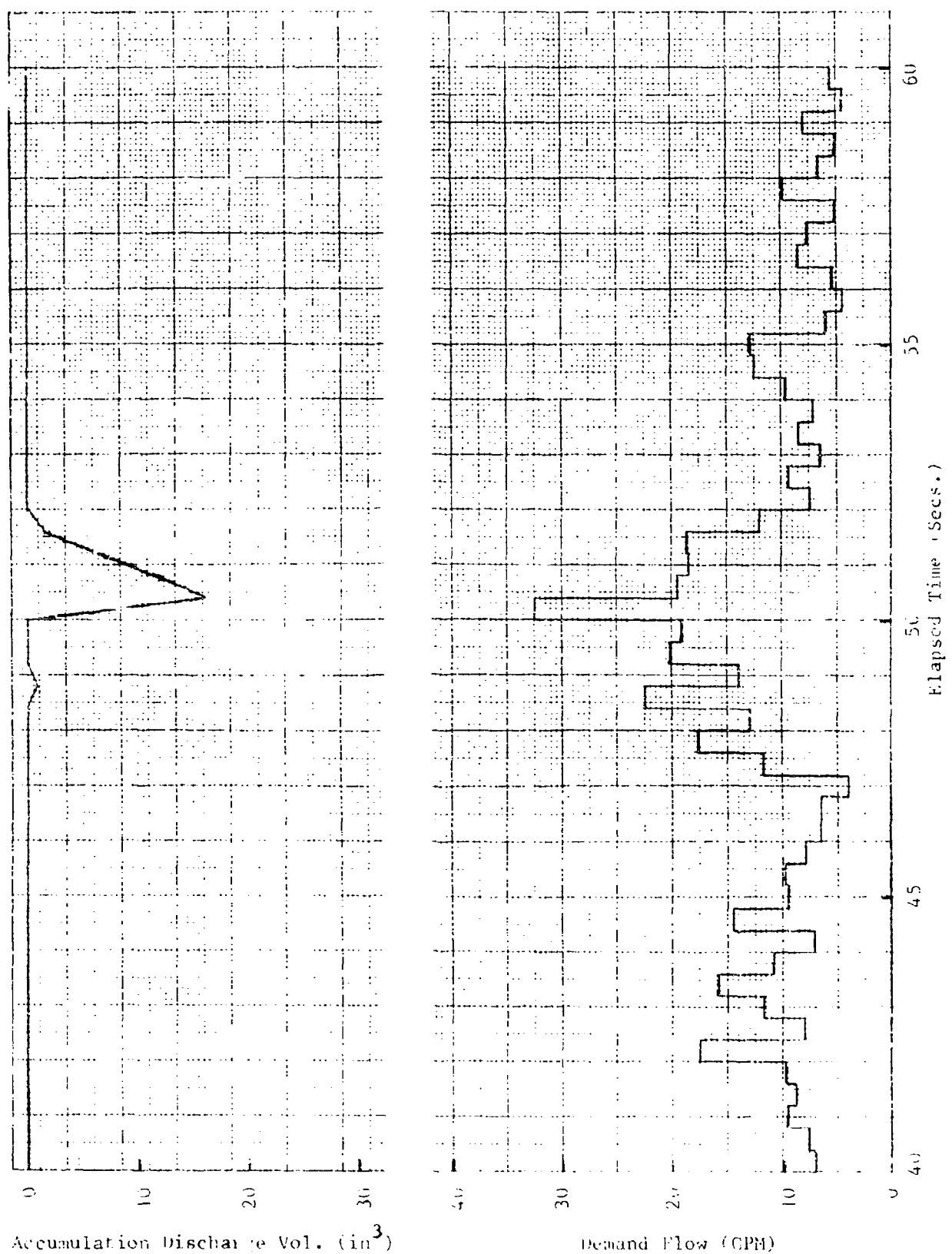


Figure 95. 40-60 Seconds, 3G Reversing Target Chase

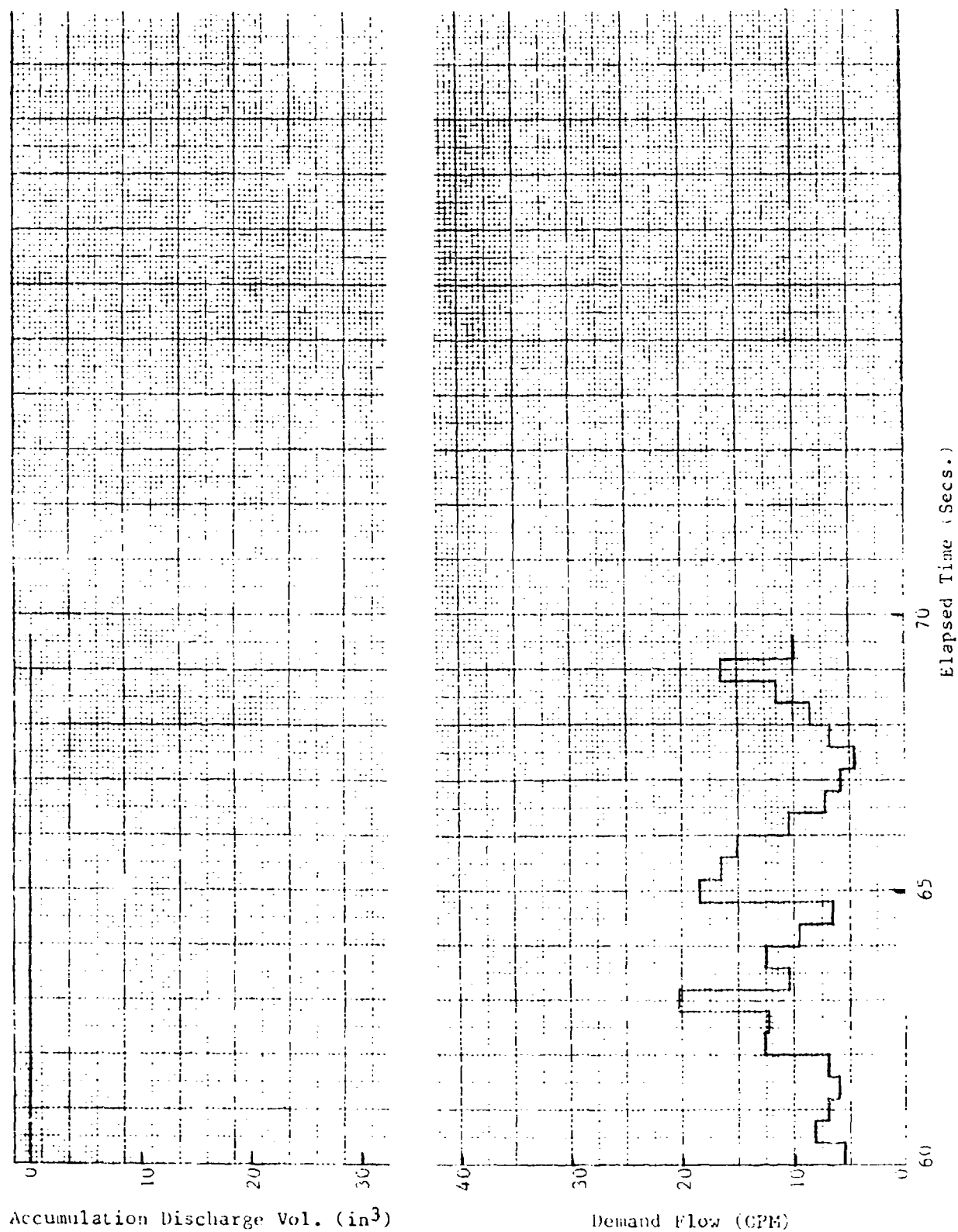
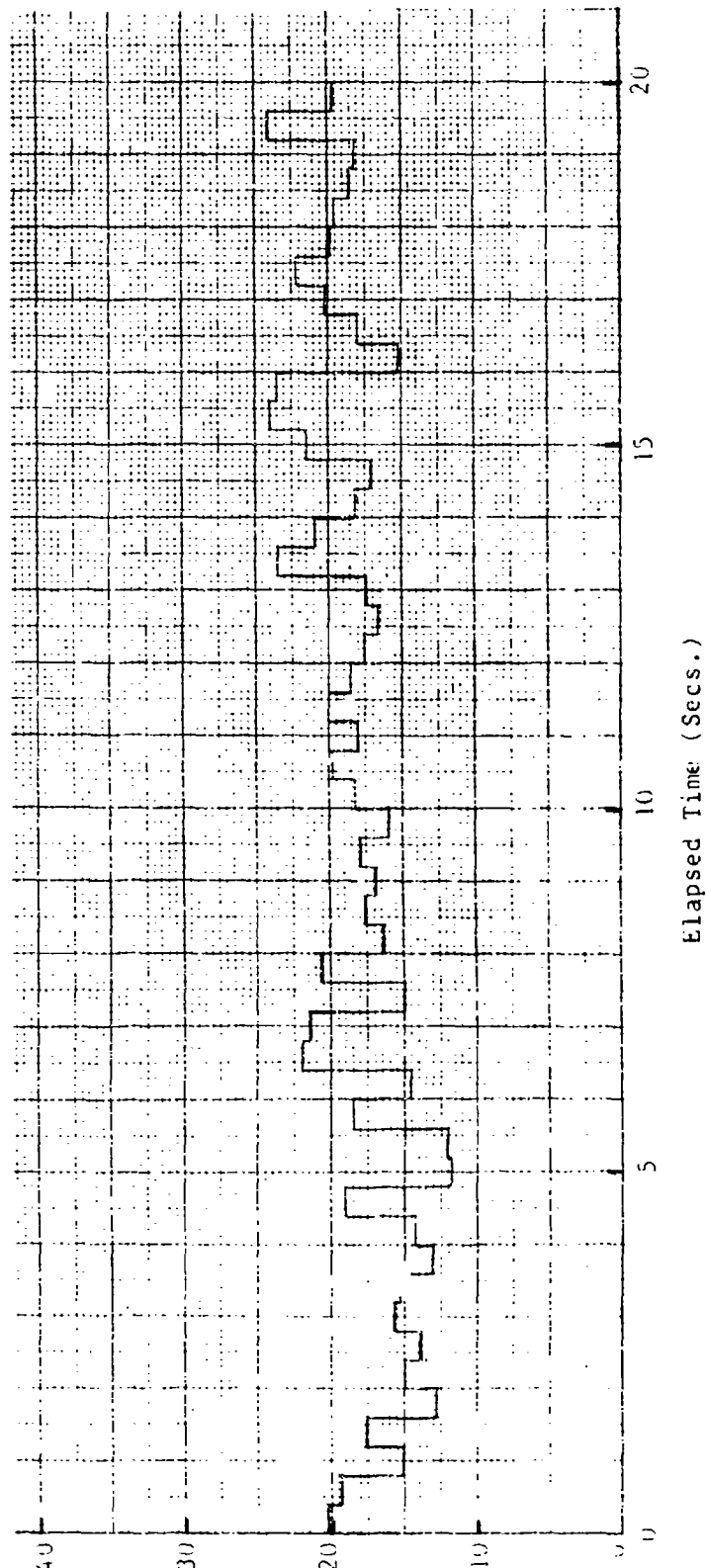
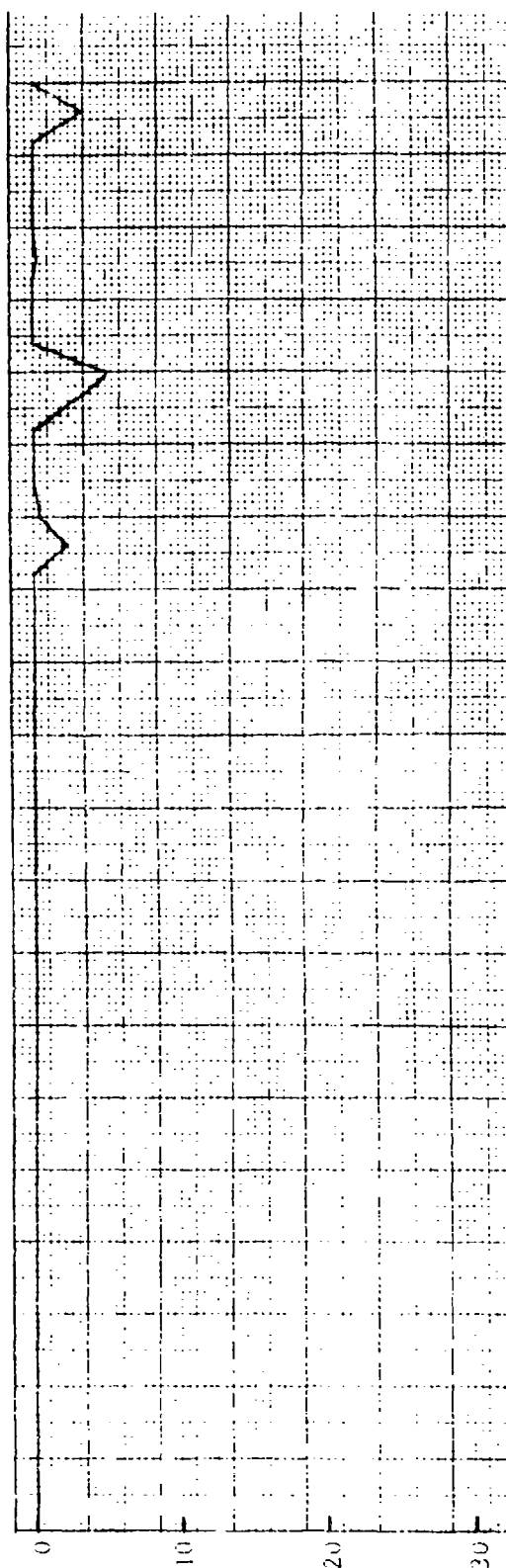


Figure 96. 60-70 Seconds, 3G Reversing Target Chase



Accumulation Discharge Vol. (in³)

Demand Flow (GPM)

Figure 97. 0-20 Seconds, Landing with Turbulence

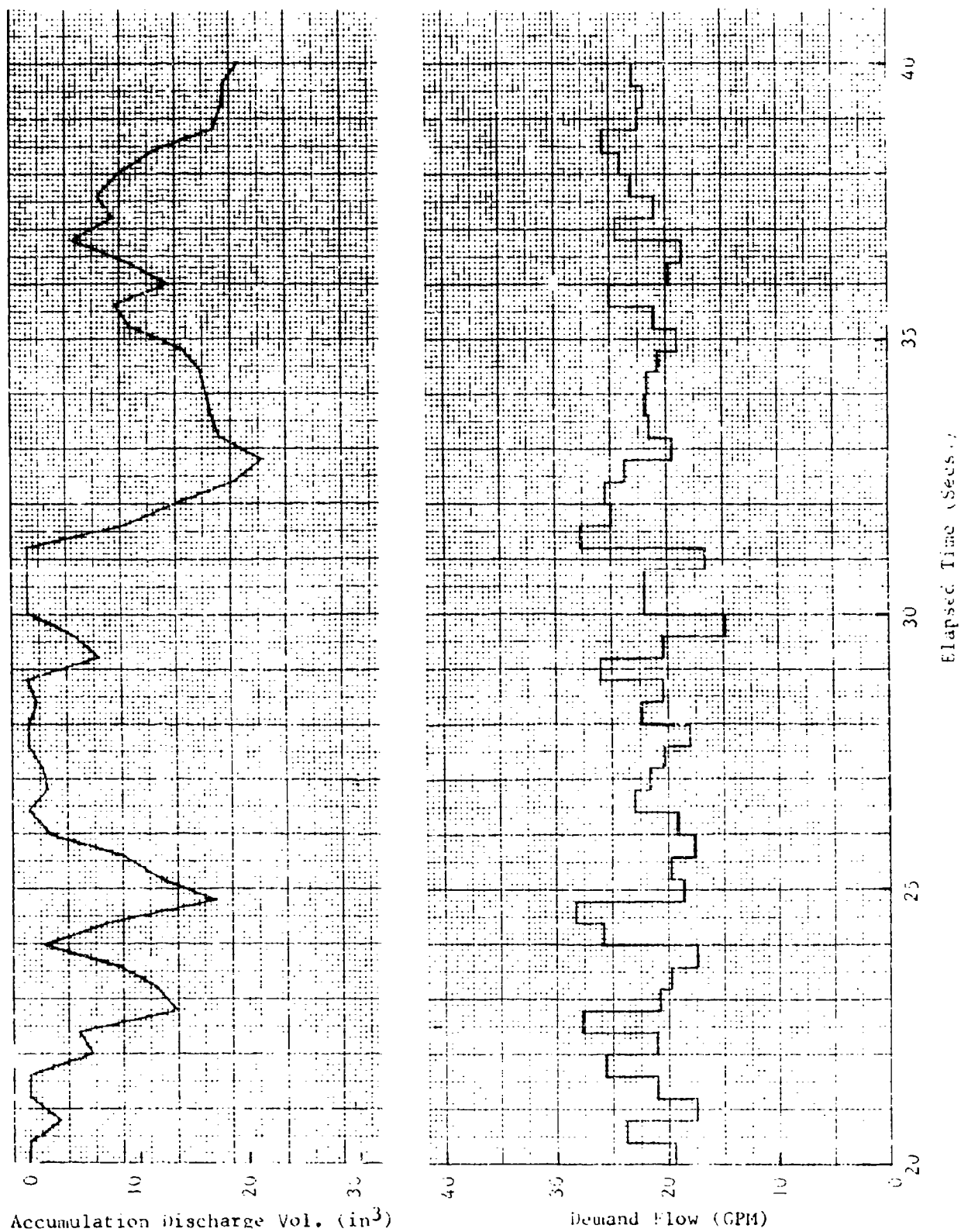


Figure 98. 20-40 Seconds, Landing with Turbulence

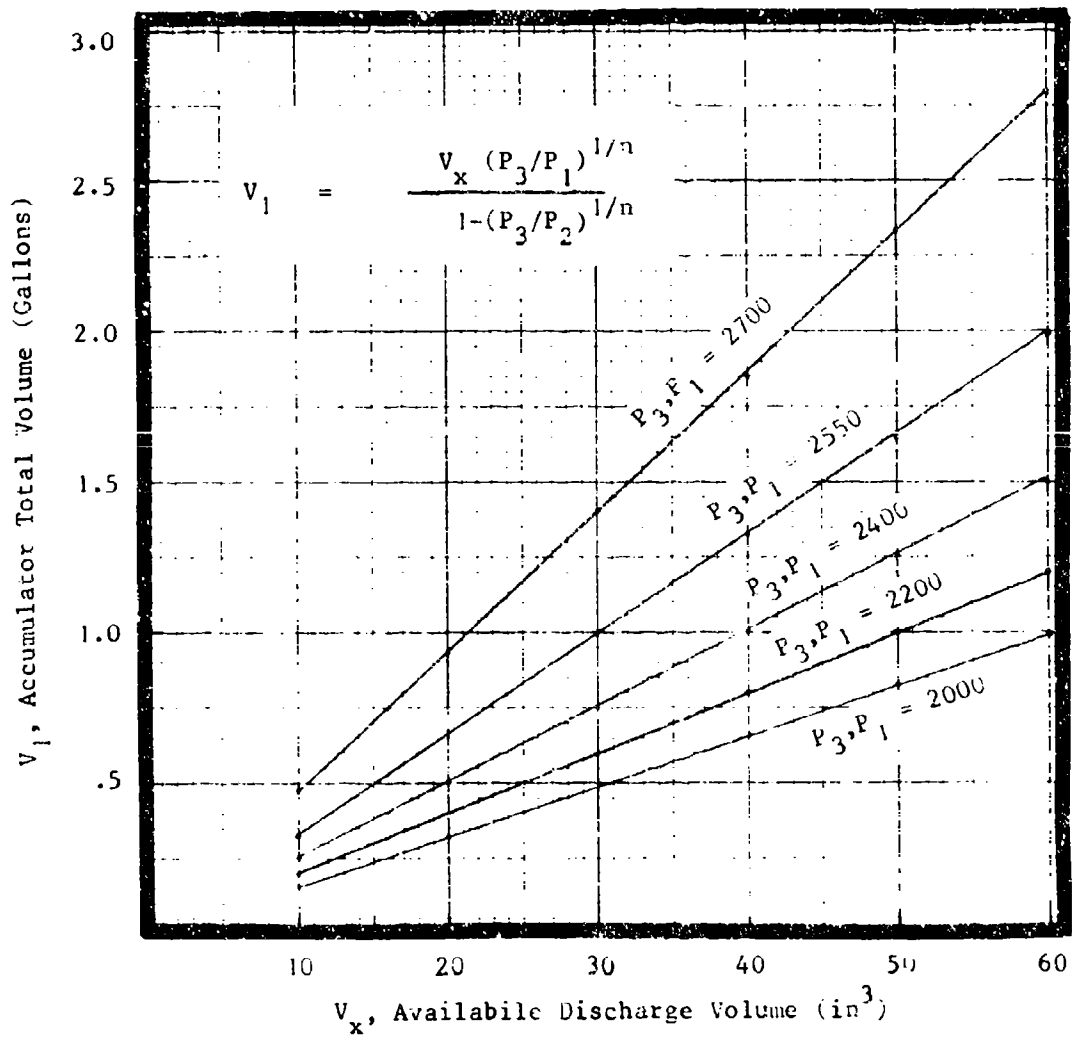


Figure 99. Accumulator Sizing

Discussion of Results

The pump and accumulator size for the energy storage system for the F-16 are dictated by the particular flight simulation results. The simulations used were representative of two severe demand flight tasks. The landing task with turbulence gave the greatest flow demand for the flight tasks used. Other simulations may generate greater flow demand requirements and would have to be explored for a final system design.

The pump size of 22 gpm for the energy storage system is considerably smaller than the normal F-16's engine driven pump size of 42.5 gpm. The pump size more closely matches the F-16 Emergency Power Unit's output flow of 22.5 gpm at 3000 psi. The accumulator size of 115 in³ is slightly larger than the normal F-16's accumulator size of 100 in³.

With a central accumulator energy storage design, the line sizes to the flight control actuators are the same size as the normal systems line sizes, since the flow through the lines does not change with the approach. The approach allows trading off pump size with accumulator size. However, if a distributed system of accumulators is used for the energy storage design, the line sizes are affected. If the accumulators are located at or near the flight control actuators, the hydraulic lines between the pump and actuators are required to handle only the pump flow, rather than the pump + accumulator flow. For example, if the pump delivery is reduced to 50% of the peak flow requirement (with the accumulators making up the balance), the inside line diameter for the lines to the accumulator can be reduced to the square root of 0.50 (0.707) for the same velocity of fluid. For example, for 3/8 in. outside diameter tubing (such as used on the normal F-16 for pressure and return lines), the inside diameter for 0.046 wall tubing is 0.277 inches. The hoop stress in the wall for 3000 psi fluid pressure is 8,479 psi. For 1/4 in. outside diameter tubing with 0.027 inch wall (which gives an inside tubing diameter of diameter of 0.195 or 0.707 of the 3/8 in. tubing inside diameter), the hoop stress in the wall for 3000 psi fluid pressure is 10,800 psi.

There are several advantages in reducing the pressure line tubing size. The 3/8 in. diameter tubing weighs 2.6 times as much as the 1/4 in. diameter tubing, not counting the weight of the fluid. Since the internal cross section area of the 1/4 inch tube is 1/2 that of the 3/8 inch tube, the volume of the fluid in the pressure lines is reduced by 50%. For steel tubing with a density of 0.28 lb/in³ and aircraft hydraulic fluid with a density of 0.031 lb/in³, the 3/8 inch tubing weighs 0.191 lb/ft. The 1/4 inch tubing weighs 0.0757 lb/ft for a weight savings of 0.115 lb/ft. An additional advantage of the smaller tubing is enhanced survivability. The smaller tubing is more easily routed (because of size and smaller allowable bend radii) into "protected" locations and the smaller size reduces the target area of the hydraulic lines.

The use of the smaller pump size has both a weight and volume savings (as well as reducing the peak loading on the aircraft engine). A smaller pump will normally have lower pump leakage flow than a larger one. This leakage flow is continuous and is similar to the quiescent leakage flow of the control actuator's electrohydraulic servovalves. Reduction of the leakage reduces the load on the aircraft's oil-to-fuel heat exchanger.

Using distributed accumulators will require using the same simulation procedure as with a central accumulator to establish the peak and average flow requirements of each control surface. The flight task simulation yielding the most severe demand on one control surface will not necessarily produce the most severe requirements for other surfaces. Therefore, in designing an energy storage system, care must be taken to ensure reliable flow demand data is generated by the simulations are run.

Conclusions and Recommendations

1. The analysis of the simulation results gave the indicated reduction in pump size with only a slight increase in the accumulator size over the normal F-16 hydraulic system indicates that the F-16 supply system is conservatively sized with respect to flow demand. This is consistent with the design of the F-16 flight control actuators which detect low supply pressure as a hydraulic system failure.
2. The use of the energy storage approach has the most potential payoff with distributed accumulators for each flight control actuator. The potential payoff is in reduced supply tubing size, resulting in a weight and target size reduction and a peak horsepower demand reduction on the engine.
3. The landing with turbulence simulation gave the greatest flow demand, as expected. In designing an energy storage system, simulations with low air speed and turbulence appear to provide the most severe demands on the hydraulic supply system for the flight control.
4. For future aircraft systems, sizing the hydraulic systems to simultaneously supply flow to all control surfaces moving at maximum rate at the same time may be impractical. The energy storage approach does provide an alternative approach that appears feasible and to have sufficient advantages to be considered on a new aircraft design.
5. It is recommended that further investigation be conducted, particularly with the distributed energy storage system, to better define advantages and potential problems.